The Application of Aperture Synthesis to Satellite Radar Altimetry

by

Behruz Purseyyed

A thesis submitted to the University of London for the Degree of
Doctor of Philosophy in Electronic Engineering

Department of Electronic and Electrical Engineering

UNIVERSITY COLLEGE LONDON

March 1990

abstract

Radar altimetry over the ocean is now a well established discipline of satellite remote sensing, providing measurements of mean height, significant waveheight and surface wind speed. In contrast, radar altimetry over non-ocean surfaces, to obtain topography of land and polar ice sheets, is still a new idea. The difference between these two situations is that the ocean surface is essentially flat with a very small vertical extent, so a broad-beam pulse-limited mode radar altimeter having a relatively small antenna is sufficient to give very accurate measurements of the ocean mean height. However for topographic surfaces, variations in the elevation can be much higher, and using a conventional altimeter causes serious problems, such as interpretation error and misregistration of a measured range, which cannot be normally corrected.

To avoid these problems, a considerably narrower beam antenna has to be used to localise the surface under observation. This requires very large antenna structures, which would be both complex and costly. This thesis investigates the application of aperture synthesis techniques to narrow-beam altimetry as an alternative to physically large antennas, to achieve high along-track resolution. It considers the analysis of the involved factors and design parameters, errors, data handling and signal processing requirements and methods for fixing the antenna beam accurately with the ultimate goal of providing a dynamic global altimetric database.

In the second half of the thesis, an experimental aircraft-borne altimeter is examined. Details of the design, construction and evaluation of a prototype system are described. This radar includes several novel features, such as aperture synthesis with full-deramp range processing, digital chirp generation, bistatic FMCW operation and off-line digital signal processing. Also a series of experiments are arranged for this radar to examine its performance to process the signature of corner reflector targets, and consideration is given to the extension of these ideas to a satellite-borne instrument.

To my wife Fatemeh, for di her dedication,
support and encouragement,
and to our little boy ?amid Wcza, who is the joy of our fife.

Acknowledgements

I would like to express my sincere gratitude to my supervisor, Dr. H.D. Griffiths, for unlimited guidance and support that he provided me throughout this work. His advice, comprehension and friendship which have been constantly with me from the first day that he accepted me as his student up to now are never to be forgotten and for me it has been a pleasure and privilege to work under his guidance.

My special thanks are due to Professor K. Milne, Dr. D.J. Wingham, and Professor R. Benjamin for allowing me to discuss different aspects of this work with them on numerous occasions, and giving me many invaluable suggestions.

Also I would like to thank R.A. Villa, W. Titze and especially my dear friend A. Khosrowbeygi for their contribution to some of the hardware needed for this work.

I am grateful to the European Space Agency for supporting part of this work.

I am also in debt of Dr. M. Movahedi for helping me in correcting the manuscript.

Finally I am grateful to all my friends at the Antennas and Radar Group of University College London for accepting me amongst themselves and sharing with me their pleasant and friendly environment.

Contents

Chapter 1. Remote sensing and sateflite aitimetrti

Chapter 2. Radar and aftimetry, basic concepts

Chapter 3. Synthetic aperture aftimetry

Chapter 4. Design of an experimental - synthetic aperture altimeter

Chapter 5. Experiments and signal processing

Chapter 6. Summary and conclusions

Appendices

List of Figures

List of Tables

List of principal-symbols

A	Target's scattering area;
B	Bandwidth of the signal;
BD	Doppler bandwidth;
D_{az}	Antenna along-track dimension;
D_{ac}	Antenna across-track dimension;
DR	Dynamic range;
F	Noise figure;
F_k	Sampling frequency;
G	Antenna gain;
L_s	Radar system loss;
M	Number of range bins;
N	Number of along-track samples;
N_B	Number of bits;
N	Number of looks;
P_t	Peak transmit power;
PRF	Pulse repetition frequency;
PRI	Pulse repetition interval;
R	Range of the radar to the target;
SLL	Sidelobe level;
(SNR)	Signal-to-noise ratio;
SW	Swath width;
T	Pulse length;
T	Time duration of the chirp signal;
T_o	Ambient temperature . 290K;
T_o	Target's two-way time delay relative to nadir return;
c	Speed of light - $3x10^{10}$m/sec;
d	distance of two successive samples;
0	Radiated power density;
f	Carrier frequency (co = 27uf);
f,	Clock frequency;
f_r	Fourier domain range variable;
g	Acceleration of free fall - 9.8m/sec^2;
h	height of the satellite;
k	Boltzmann's constant;
(	Synthetic aperture length;
p	Frequency precision;
p	= W_{in}, Off-set frequency;
r_{eq}	Earth's radius ..• $6.38x10^6$m;
td	Two-way time delay;
t_o	Time variable of the **nth** pulse;
x.	Aperture synthesis variable;
v	Orbital velocity of the satellite;
veq	Earth's equatorial velocity;
vi_{rx}	along-track component of the Earth's velocity;
v_{Ty}	across-track component of the Earth's velocity;
v_7	Earth's velocity at latitude y;
a	Surface slope;
13	Phase shift;
y	Latitude;
S_a	Along-track resolution;
S_c	Across-track resolution;
6.	Range resolution;
A4	Phase noise/error/difference;
Ah	Maximum height variation;
AT	Overlap time;
0_f	Frequency error;
t	Compressed pulse length;
ti_n	Time domain range variable;
X	Wavelength;
.t	LFM slope = B/T;
a	Phase noise standard deviation;
a°	Backscatter coefficient;
ae	Beam pointing standard deviation;
x	Radar along-track position relative to target;
6	Antenna off-nadir angle;
0b	Antenna beamwidth;
$0'(t_d)$	Phase noise at IF stage;
$(1)_0$	Maximum phase noise;
li	Antenna efficiency;
12	Along-track safety factor.

Chapter 1

Remote sensing and satellite altimetry

1.1 Introduction

Remote sensing may broadly be defined as collecting and interpreting information without actual contact with the object or area being investigated (Sabins, 1987; Clark, 1985).

The roots of present-day remote sensing go back to the early 1960s, when the development of spaceborne remote sensing probes began. Since then the subject has grown very fast, both in techniques and applications.

Nowadays remote sensing is used to observe and study the Earth's surface and atmosphere on a global and continuous scale, and proper interpretation of the acquired data provides a considerable amount of useful and even vital information for (for example), oceanography, glaciology, geology and geophysics, hydrology, forestry, agriculture, surveying and cartography.

Remote sensing probes cover the entire electromagnetic spectrum, from low frequency radio waves to microwaves, infrared, visible, ultraviolet and beyond, to collect as great a variety of data as possible. The collected information from different regions of the electromagnetic spectrum tend to complement each other, and the combination of such data is more useful than the sum of the individual contributions. However, sensors that operate at microwave frequencies have particular importance, in that they are much more able than the other regions of the spectrum to penetrate clouds, rain, vegetation and even ground and ice. They also do not rely on the Sun as a source of illumination. So microwave sensors are all-weather probes which can provide continuous observation of the Earth and its atmosphere, in day and night and in any weather condition.

Active microwave sensors, or in other words 'radars', which are used in remote sensing mainly fall into three categories:

1 - imaging radars, which use real or synthetic apertures to obtain high resolution images of the backscatter properties of the Earth's surface and its resources;

2 - scatterometers, which are non-imaging radars for recording backscatter of terrain as a function of incidence angle;

3 - radar altimeters, which are used for the measurement of the surface height, surface roughness, and backscatter coefficient.

The study of satellite radar altimetry, which forms the subject of this work was initiated in the early 1960s, with the goal of global geodetic measurements to accuracies of ±10 m, and later ±1 m and ±10 cm. The first experimental system, launched in 1973, was the Skylab S-193 altimeter, designed primarily for obtaining radar measurements necessary for designing improved altimeters. GEOS-3, carrying the second satellite altimeter, was launched in April 1975, and was the first globally applied altimeter system.The third satellite altimeter was carried by the SEASAT-1 satellite, launched in June 1978, and was the first altimeter system to provide a measurement precision of better than ±10 cm. Although the SEASAT satellite failed after only 90 days, many scientists are still engaged in the processing and interpretation of the huge amount of data collected by it. The next probes after SEASAT were Geosat in 1985 and Cosmos-1870 in 1987, which are still continuing their missions.

The importance of satellite altimetry can be better appreciated when it is realised that from about eleven remote sensing satellites that are planned for the last decade of the twentieth century (Brus, 1988; Carter and Challenor, 1988) at least eight will definitely carry radar altimeters. These are: ERS-1 in 1990 or early 1991, Topex/Poseidon in 1991, ERS-2 and NROSS both in 1992, Columbus, JERS-1, Spectrasat and EOS all in the mid 1990s.

1.2 *Satellite altimetry over topographic surfaces*

A satellite altimeter is a radar which transmits a narrow pulse towards the surface and makes three basic measurements of the target within its footprint: the two-way propagation delay, the echo shape, and the echo strength (figure 1.1). From these measurements a variety of geophysical parameters may be inferred about the solid Earth, oceans and the atmosphere.

Up to now, remote sensing radar altimeters have been optimised primarily for operation over ocean, which compared to the land can be assumed to be a flat surface. The basic extracted parameters from these altimeters are the ocean surface elevation, ocean surface roughness and surface wind speed. Today, however, scientists are also interested in using radar altimeters over topographic surfaces (i.e. land and polar ice sheets). If such altimeters are introduced to remote sensing satellites, they can provide a wealth of topographic data to be used in all disciplines of Earth sciences, from the study of the formation and evolution of the Earth's surface, investigation of the present state of the polar regions and consequences of the greenhouse effect, to the assessment of the future of this planet as an ecological system.

One of the major problems associated with land and ice altimetry is that the existing remote sensing altimeters work on the broad-beam (beamwidth of about 1.5°) pulse-limited mode concept and are almost only useful for ocean measurements. Compared to typical land topography, the ocean surface is essentially flat with very small vertical extent (less than ±20m). Even during the highest seas, the surface is locally very homogeneous. Figure 1.2 shows the situations over different types of surface. For the ocean, the first backscattered signals tend to come from nadir, and since the first returns are responsible for the generation of the leading edge of the received waveform, it is obvious that in this case the height measurement

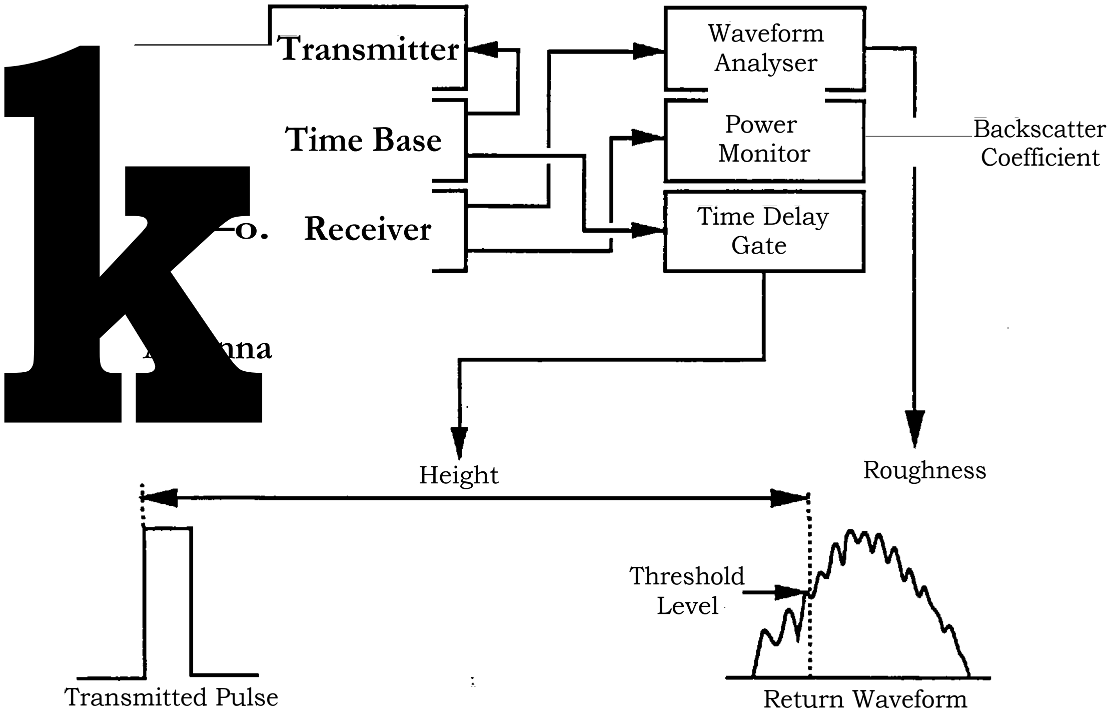

Figure 1.1- General block diagram of a radar altimeter

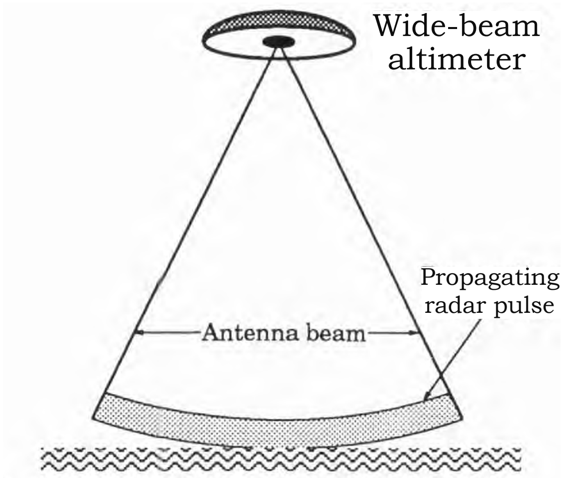

(a) First return at nadir over ocean.

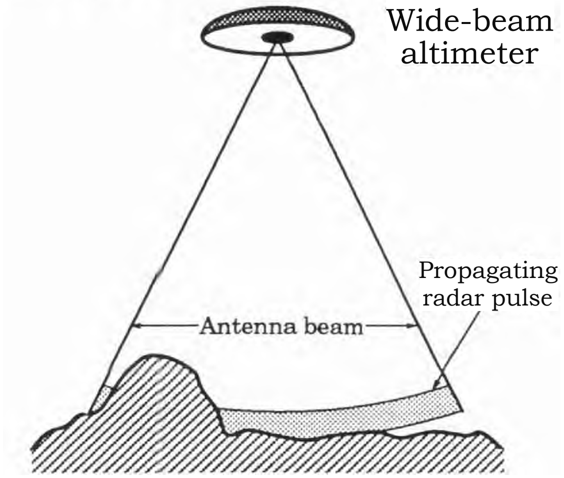

(b) First return may be off-nadir over land features.

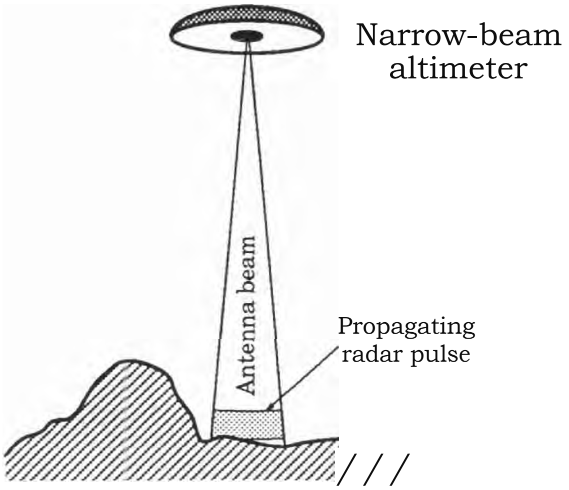

(c) Location of first return does not depend on terrain features.

Figure 1.2- Altimeter over different surfaces.
(after McGoogan & Walsh, 1978)

corresponds directly to the nadir point. In contrast, over topographic surfaces, the range measurement is made not necessarily to the nadir point, but to the nearest point to the altimeter (within the antenna beam) and this causes interpretation error and misregistration of the measured range. So the broad-beam pulse-limited mode altimeter is not usually suited to operation over topographic terrains, and it is more desirable to use a very narrow beam antenna to localise the footprint, which means that the location of the first backscattered signal does not depend on the topography of the terrain (figure 1.2).

1.3 *Objectives of the study*

Following the discussions of section 1.2, it is clear that to obtain meaningful altimetric measurements over land to provide as closely as possible, undistorted information about the topography within the footprint of the radar altimeter, the illuminated area has to be very localised, which means that the antenna beam has to be considerably sharpened. Figure 1.3 gives the altimeter antenna size needed to achieve a particular spatial resolution (i.e. footprint size) for two different altitudes: 250 km (suitable for Space Shuttle missions) and 800 km (suitable for permanent remote sensing satellite missions). The results *are* given at frequencies of 13.5GHz, 37GHz and 96GHz, corresponding to the frequency windows that possess the minimum attenuation due to Oxygen and water vapour absorption. These graphs show that to obtain high spatial resolution (the required spatial resolution for land altimetry will be discussed in Chapter 2), very large antennas are needed to be deployed in space, which would be both complex and costly. It is, however, possible to employ a thin, long antenna for the altimeter, similar to the antenna of an imaging synthetic aperture radar conventionally used in the remote sensing missions, to provide a narrow across-track beam. Then by using the technique of aperture synthesis, a narrow along-track beam is also obtained. To make such a synthetic aperture altimeter an effective tool for spaceborne remote sensing purposes, beam scanning can be added, in order to obtain wide swath coverage to be used for global and regional topographic mapping. There are also other

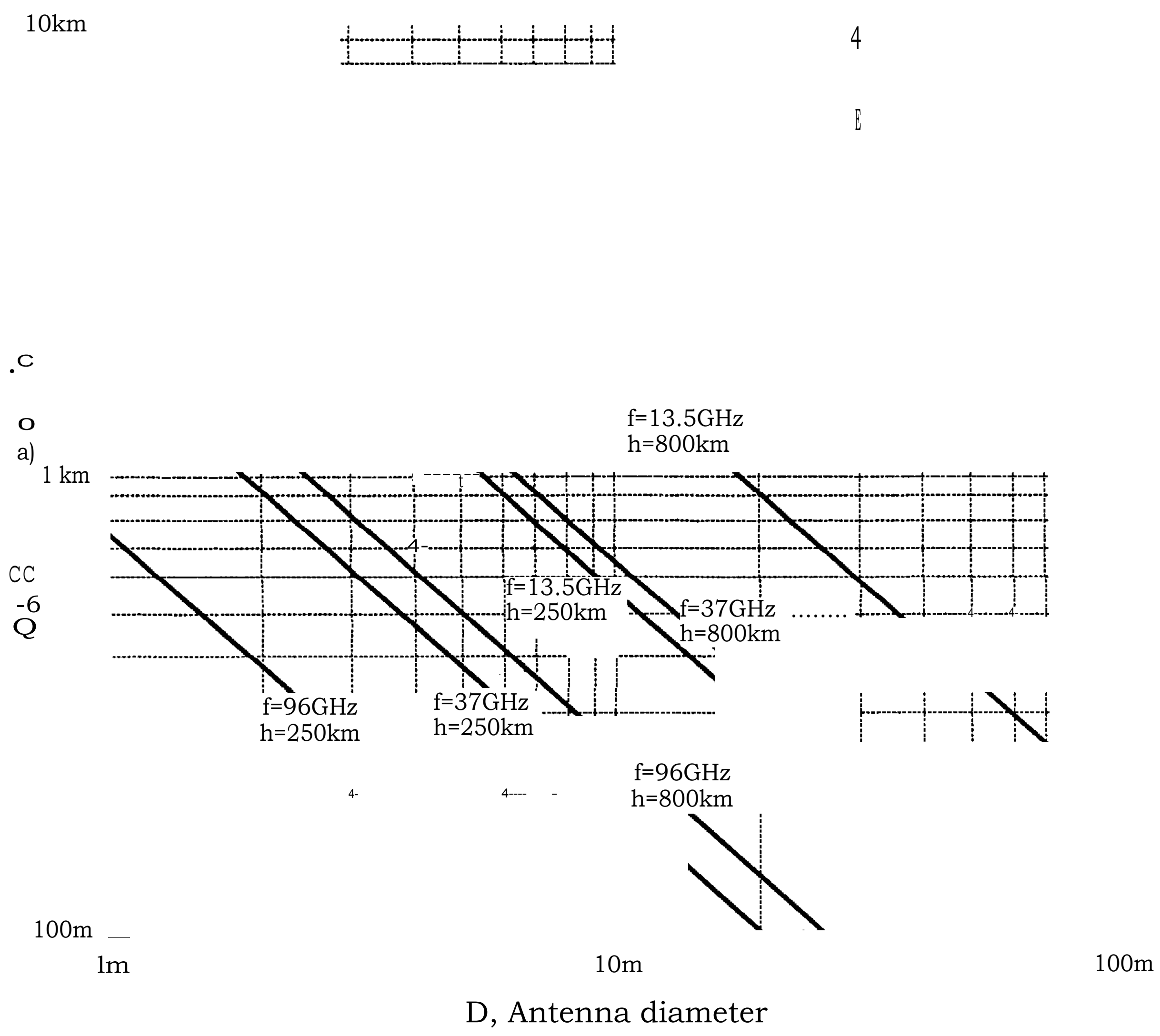

Figure 1.3- Spatial resolution versus antenna diameter.

techniques to recover the topography of terrains, namely: optical stereo imagery, stereo SAR, interferometric SAR and laser altimetry, each of which have their own merits and drawbacks. But it will be shown in Chapter 2 that the synthetic aperture altimeter is the one which can provide the maximum benefits, as a single remote sensing instrument, to the different activities of Earth sciences. The other methods can be used as a complement to synthetic aperture altimetry for the purpose of local scale topographic mapping of selected areas of the Earth's surface.

In conclusion, the main objective of this study is to investigate the application of synthetic aperture processing techniques to narrow-beam altimetry as an alternative to physically large antenna structures. This includes: the basic features, main design parameters, requirements for real-time signal processing, data telemetry , accurate attitude control and several other features such as the use of scanning beam systems to provide a dynamic and regularly updated database of global altimetric information in a short period of time. To complete the study, comprehensive examples of satellite-borne and aircraft-borne configurations are discussed, and the design, construction, laboratory testing and evaluation of an experimental system are explained in detail along with discussions about possible new approaches in the design of future altimeter systems.

1.4 *Thesis layout*

This thesis is the result of investigations into the theoretical and experimental aspects of applying aperture synthesis to radar altimeters from an engineering point of view. The study has been carried out at University College London in parallel with work by scientists at the Jet Propulsion Laboratory, California Institute of Technology, on the feasibility study of the LORA instrument (Land and Ocean Radar Altimeter), with the aim of deploying a scanning radar altimeter in orbit and this parallel work is acknowledged.

Chapter 2 of the thesis is concerned with the basic concepts of radars as applied to the radar altimeter, and which are of key importance to the analysis and design of such a system.

Chapter 3 gives the analysis of aperture synthesis applied to a full-deramp altimeter, and the associated signal processing requirements. Further details are also given about beam pointing control, and the extension of the basic idea to a scanning-beam altimeter.

Chapter 4 gives a comprehensive discussion of the design of an experimental aircraft-borne system and its requirements. It then explains the design, construction and analysis of a prototype system in which a number of novel ideas are used. Different sections of the system are discussed and an error analysis is given in detail.

Chapter 5 explains the experiments arranged for the prototype radar and the signal processing of acquired data, in order to demonstrate that the designed system has the expected performance. Also further investigations of some other relevant topics are presented.

Chapter 6 gives a summary of the study and discussion of the results, as well as suggestions for future work such as across-track real beam scanning, the use of other frequency bands and the extension to an aircraft-borne experiment.

Chapter 2

Radar and altimetry, basic concepts

2.1 *Introduction*

Synthetic aperture altimetry is an idea which employs various radar signal processing techniques to generate three dimensional high resolution pixels containing height information of the terrain under observation. For this purpose, range resolution is obtained by the full-deramp pulse compression method, across-track resolution by a narrow real beam and along-track resolution by the coherent correlation method. This chapter establishes several basic concepts as applied to a synthetic aperture altimeter, which are of key importance to the analysis and design of such a system. It also discusses the advantages and limitations of different processing methods, and summarises the applications of topographic mapping to different disciplines of Earth sciences. Finally it discusses the current state and trend of microwave technology for these purposes, considering as well a number of complementary techniques, leading to a basic specification for a satellite-borne synthetic aperture altimeter.

2.2 *Spatial resolution in radars*

Spatial resolution is a measure of the ability to determine whether only one or more than one different target elements are being observed. Two objects are said to be resolved if the radar system can tell that there are in fact two rather than one (Ulaby et al., 1982). For a radar altimeter, spatial resolution is divided into horizontal or ground resolution (i.e. along-track resolution and across-track resolution) and range resolution.

Along-track resolution, 5_a, and across-track resolution, 8_c , are the measures of the ability to differentiate between two targets placed on a line parallel (for 8_a) and on a line perpendicular (for 8_c) to the trajectory of the

satellite. To be resolved, these targets must be separated by a distance greater than the antenna footprint at a given range, R. So for a real aperture, Sa and Sc are given by:

$$8_a R 9_, = \frac{RA'}{D_{az}} \qquad ...2.1$$

$$\delta_c \approx \frac{R\lambda}{D_{ac}} \qquad ...2.2$$

where **el, ?JD** is the along-track or across-track antenna beamwidth, D_{az} is the along-track antenna dimension and D_{ac} is the across-track antenna dimension. The antenna beamwidth is directly proportional to the wavelength of the transmitted signal, X, therefore for a given antenna size, the ground resolution is higher for shorter wavelengths. On the other hand, for shorter wavelengths the amount of signal attenuation due to atmospheric absorption can become very significant, and the desirable weather-penetration capability decreases. As the beamwidth is inversely proportional to antenna size, Daz and **Dac,** resolution improves with larger antennas, but again there are practical limitations to the maximum antenna size in terms of mechanical complexity and cost. To avoid this problem in the along-track dimension, an alternative method known as aperture synthesis exists, and this will be explained in section 2.3.

Range resolution, S_r, is the ability of the radar to differentiate between targets in the range dimension. In a basic pulse radar, range measurement is done by transmitting a simple pulsed carrier having a pulsewidth T, and measuring the two-way propagation delay of the pulse. Two targets with a range separation of S_r can be resolved if their returns occur in two adjacent range gates (either in time or in frequency, B = 1/1'), giving the range resolution:

$$\delta_r = \frac{cT}{2} = \frac{c}{2B} \qquad ...2.3$$

From basic radar theory (Levanon, 1988), the signal-to-noise ratio at the radar receiver input is given by:

$$(SNR)_i - \frac{P,G^2\,X,^2\,a^0\,A}{(4/c)^3\,R^4\,L_s k T_0 B F}$$

...2.4

where G is the transmit/receive antenna gain, A is the illuminated area and L_s (.1) is the net loss at the receiver input, including plumbing losses as well as losses due to atmospheric absorption. Now, assuming that for a basic pulse radar the pre-processing and the output signal-to-noise ratios are the same, i.e. (SNR)i = $(SNR)_0$, and that the receiver bandwidth is equal to the inverse of the transmitted pulsewidth, B — 1/T , equation 2.4 is modified to:

$$(SNR).-- \frac{ptG^2x^2O^0AT}{(4n)^3\,R^4\,L_s k T_o F}$$

...2.5

This is the basic pulse radar equation, which relates the output signal-to-noise ratio to the peak transmitted power Pt and the pulsewidth T. A high range resolution with a basic pulse radar requires a very short transmitted pulse (equation 2.3). If the pulse is very short, then it is obvious from equation 2.5 that the peak power must be very high so that it contains sufficient energy to obtain the required SNR. However, there is another method which provides the required high range resolution without the need for narrow high power pulses. This is the well-known technique of pulse compression, which permits the use of longer, low power pulses.

The most common pulse compression technique is based on using a linear chirp signal. In chirp radar, a linear frequency sweep (modulation) is applied to the transmitted carrier signal, and in the receiver the obtainable resolution is determined by the bandwidth over which the frequency has been swept, rather than by the transmitted pulsewidth. Signal processing of the chirp signal can be done either in the time domain by matched filtering, or in the frequency domain via the full-deramp process.

Figure 2.1 shows the matched filter concept. The transmitted pulse has a width of T and is swept over a frequency band from fl to f2 with a total bandwidth of B, and a modulation slope of 1.t. = B/T. After the usual time delay, the received signal from a point target is received as a replica of the transmitted chirp. This signal is passed through a matched filter which compresses the received chirp into a very narrow pulse. Basically, the received signal has the form of:

$$v_i(t) = a.\exp[\, 2n(f_o + \frac{1}{2} gt)t \quad , -\frac{T}{2} < t < +\frac{T}{2}$$

...2.6

where a is its peak amplitude. This signal is applied to a filter having an impulse response h(t), which is the time inverse of the signal (Appendix 1):

$$h(t) = \quad .\exp j[27c(f0 - \frac{}{2} p.t)t = \sqrt{F} - \frac{B}{T} \exp j\,[27c(f0 - \frac{gt}{2})t]$$

...2.7

Therefore the output of the matched filter has the following form:

$$v_o lt) = v_i(t)*h(t) = \int_{\frac{T}{2}}^{+\frac{T}{2}} v_i(T).h(t - T)\cdot cit = \frac{\sin(np,Tt)}{(7tp.Tt)} \exp io(t)$$

...2.8

From equation 2.8, the matched filter output is a sinx/x function with a time width which is the reciprocal of the chirp bandwidth, 1/(11T) = 1/B ==. ti . Therefore, the range resolution associated with the matched filter technique is given by:

$$Sr = \frac{}{2} \text{ or } \frac{c}{2B} \qquad ...2.9$$

The processing gain of the matched filter is defined as the ratio of the output power to the input power. From equations 2.6 and 2.8 this ratio is given by:

$$\frac{P_{oi}}{P.} = \frac{(a.117\text{-}r.)^{2}}{2\ a} = BT \qquad ...2.10$$

Equation 2.10 also means that the matched filter in a chirp radar provides a processing gain of B.T over the basic pulse radar. Therefore, the SNR at the output of the matched filter is B.T times the SNR given in equation 2.4:

$$(SNR)_0 = B.T. \ \frac{Pp^2X^2a^\circ A}{(47r)^3 R^4 L_s kT.BF} \ \frac{P G^2 X^2 a^o AT}{(470^3 R^4 L_s kT_0 F} \qquad ...2.11$$

This equation is apparently the same as equation 2.5 describing the basic pulse radar. However, it should be noticed that to obtain the same range resolution and SNR for both the pulse and chirp radars, the pulse length T in equation 2.5 has to be reduced to the reciprocal of the chirp bandwidth. Moreover, P_t in equation 2.5 has to be increased to B.T times the chirp transmitted peak power.

Another important method of achieving high range resolution is the full-deramp technique. In this technique (figure 2.2), the signal reflected from a point target, which is a replica of the transmitted chirp signal, is mixed with a local oscillator signal of the same chirp slope as the transmitted signal. The mixing process removes the linear frequency modulation of the received signals and gives an output which has a constant frequency proportional to the range of the target. After passing this output through a spectrum analyser the range information is mapped to the

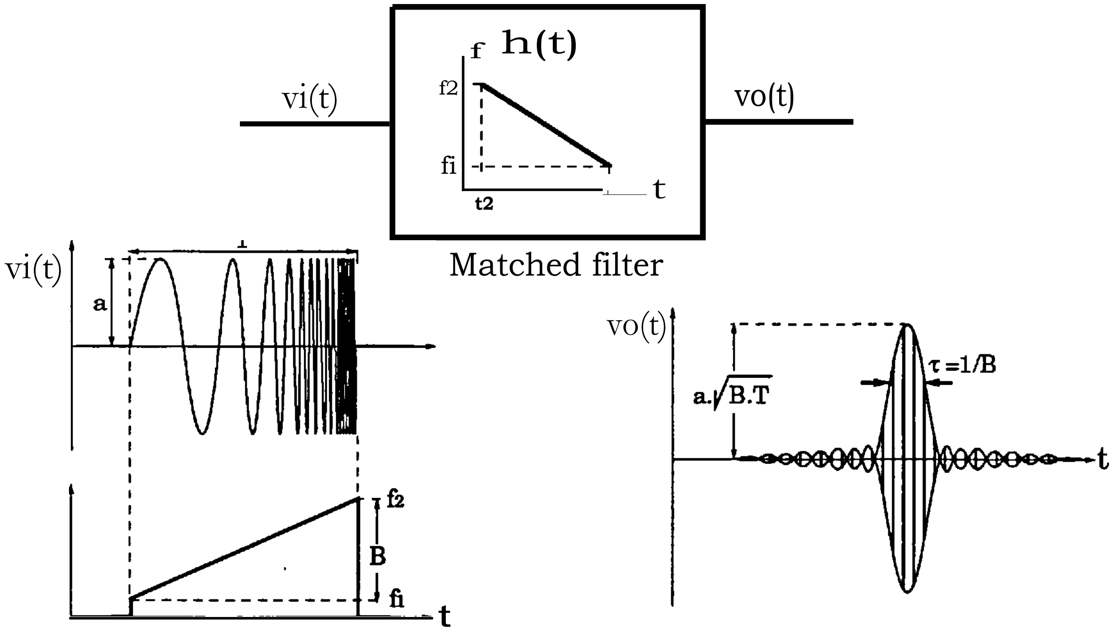

Figure 2.1- Matched filter pulse compression .

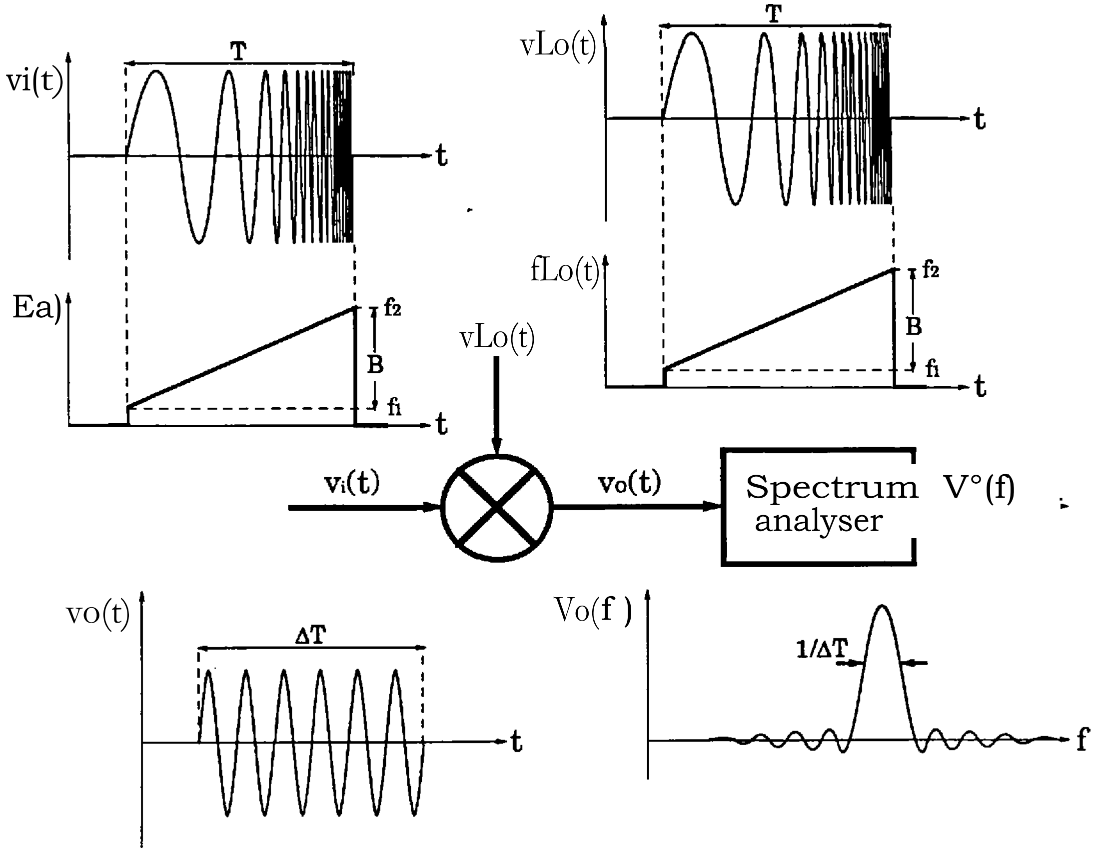

Figure 2.2- Full-deramp pulse compression .

frequency domain and the range resolution becomes frequency resolution. Mathematically, the signal to be processed is similar to the matched filter input, equation 2.6. This signal is mixed with a replica of the transmitted chirp, triggered at an appropriate time t_o:

$$v_{LO}(t) = \mathrm{expj}2/r[f_o(t - td + \frac{1}{2} igt - t_0)^2 1 \qquad \ldots 2.12$$

The output of the mixer is $v_o lt) = a.\mathrm{expj}[cD_i(t) - 011{:}1_{1,O}(t)1$, where the output phase is the difference between the received signal phase, equation 2.6, and the local oscillator signal phase, equation 2.12. It should be noted that this output exists only during the overlapping time of the received and local oscillator signals, AT, and outside this interval the output is zero. The resultant signal is then fed to a Fourier transformer, giving:

$$V.(0.)) = \underset{AT}{S} V0(t).\mathrm{exp}\text{-}j(27tft).dt = a.AT \frac{\mathrm{sinn}(i.a-f)AT\ 1}{Tc(gto-f)AT}.\mathrm{expjet}_o \qquad \ldots 2.13$$

As illustrated in figure 2.2, in the full-deramp method compression, the wideband input signal transforms into a very narrow bandwidth output signal and high range resolution is achieved in the frequency domain. The effective width of this frequency compressed signal, which has a sinx/x form, is equal to the reciprocal of the overlap time, Af = 1/AT, as can be seen from equation 2.13. If AT tends to zero (i.e. no time overlap of received and local oscillator signals), the effective frequency width tends to infinity (i.e. no resolution). Therefore the application of the full-deramp method requires that the total time (or range) span of the signals being processed should be much less than the transmitted pulsewidth, otherwise truncation and loss of resolution result. An important case to which the full-deramp process can be applied is altimetry, in which the time (or range) extent of all the surface features within the altimeter footprint is much less than the transmitted pulsewidth, and it can therefore be assumed that the overlap *time* is equal to the transmitted pulsewidth, i.e. AT = T.

To calculate the range resolution in the full-deramp technique, two received chirps corresponding to two point targets with a range separation of S_r are considered. At an appropriate instant, the local oscillator is triggered to generate a single chirp pulse which has different time delays with respect to individual received chirps, t_o = t for the first point target and t_o = t + At for the second one. From equation 2.13, the expressions associated with the centre frequency of the two adjacent signatures are:

TU [III - fl AT = 0 and It[igt +At) - (f +AMAT= 0

where of is the frequency separation of the two signatures. Knowing that two targets are said to be resolved if their frequency separation is at least equal to the effective width of one of them, 1/AT, and also by using 11 = B/T and Sr = c.AtJ2, the difference of the above equations results in the following expression, which is the same resolution provided by the matched filter:

$$S_r = \frac{C}{2B} \qquad ..2.14$$

In a radar altimeter, the range window consists of a series of contiguous range bins, or a bank of digital filters, either by means of hardware or via software, and the bandwidth of a single bin or filter is equal to 1/T. From equation 2.5, the output SNR associated with an individual range bin is given by:

p G2 X2GO A n r121 AT
(SNR) — it — u
° (47c)^{3}R^{4}L$_s$kT$_o$+ F (470^{3}R^{4}L$_s$ kT F

...2.15

This SNR is exactly the same as that achieved by the matched filter method.

Although, for the case of the altimeter, the matched filter and full-deramp methods are identical in terms of range resolution and transmitted power, there is still a very important difference between them. In the matched

filter method, the time domain compressed output has the same bandwidth as the transmitted chirp signal, which means that the radar receiver should be very wideband, and since radar signal processing is generally performed digitally, very high sampling rates and very high speed processing hardware would be required. In contrast, the important advantage of the full-deramp process is the compression of the bandwidth required to process the return signals, from the bandwidth B of the chirp pulse, to a bandwidth much smaller than B, within which the reflections from all surface facets will fall. Therefore, the full-deramp process requires much simpler and very much slower signal processing hardware.

2.3 *Synthetic aperture processing*

Synthetic aperture processing is a method of obtaining high along-track resolution. In a synthetic aperture radar (SAR), the radar platform moves along a straight path which does not intersect the target, and collects at different spatial points backscattered signals from the target. Then using a signal processing technique, very high along-track resolution can be synthesised without requiring a physically large antenna.

Figure 2.3a shows the SAR/target geometry. The radar passes over the target and intercepts its backscattered signals. The maximum receiving interval is limited by the visibility range L of the target, or equivalently the along-track real beamwidth of the radar antenna. Now, suppose a SAR observes a target at x = 0 and R = Ro . As the platform moves, its range to the target is given by:

$$R = \sqrt{R_0^2 + x^2} \longrightarrow R \approx R_0 + \frac{x^2}{2R_0} \quad \text{for } R_0 \gg x \qquad \ldots 2.16$$

From equation 2.16, the range of the radar to the target has a parabolic variation, and the two-way phase variation of the received signal that can be sensed by the radar during the interval for which the target is visible is given by:

$$4)(X) = \frac{27c}{A,}[2(R-R_{o}), = \frac{2xx^{2}}{R_{o}X,}$$

...2.17

This function (figure 2.3b), is known as the phase history of the target, expressed as a function of radar along-track position, x. The synthetic aperture technique is basically the correlation process of the complex signal $v_s(x)$ = expj4(x), which carries the phase history of the target with a suitable reference function $v_r(x)$. This can be described by the following integral:

$$v_{o}(x.) = \underset{\substack{r\\-2}}{\overset{+\frac{C}{7}}{1}} v_{s}(x).v{:}(X+X_{a})\,dx$$

...2.18

where x_a is the correlation variable, and *Cis* the integration length (*Cs* L). It is obvious that during the course of target interception, the radar sends and receives a series of individual pulses and not a continuous uninterrupted signal. Therefore, in the actual signal processing, instead of a correlation integral there has to be a discrete correlation process. However, under the assumption of having many spatial samples across the processing interval, the summation is replaced by the correlation integral in this section and a more elaborate analysis will be given in Chapter 3. Accepting this assumption, there is still a noticeable difference, in that a discrete synthetic aperture, like any sampled waveform, has a periodic pattern and may generate grating lobes (explained later in this section).

A search for a suitable reference function to be used in the synthetic aperture correlation leads to two distinct situations: unfocused processing, where $v_r(x)$ is assumed to have no phase variation and in its simplest form $v_r(x) = 1$; and focused processing, where it is assumed that for any target a known phase history exists, so a reference function showing a similar phase variation as the signal under the correlation process can be used. This function, in its simplest form, is $v_r(x) = v_s(x)$ = expj4(x).

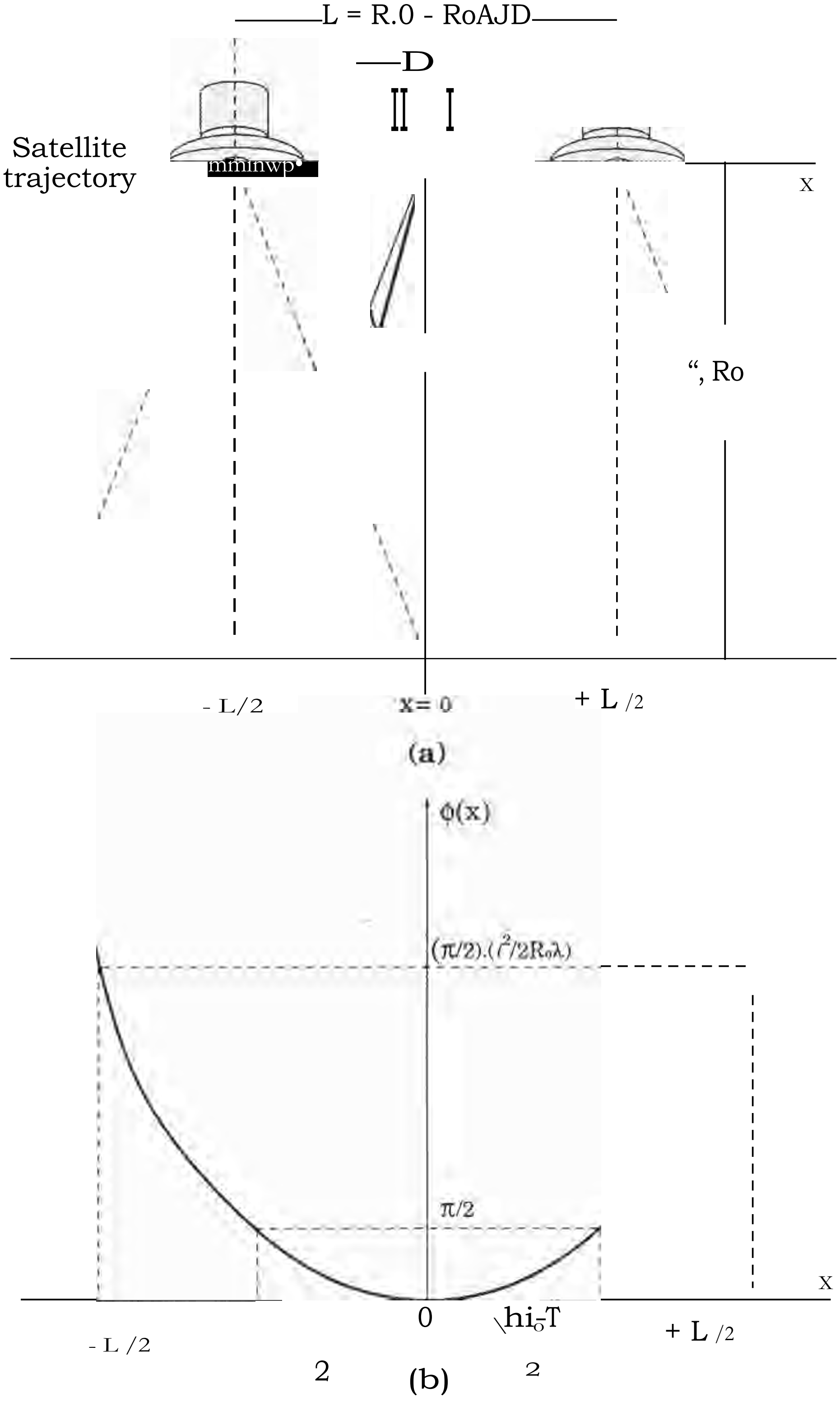

Figure 2.3- Geometry and phase history of a point target observed by synthetic aperture radar.

In unfocused processing, inserting equation 2.17 into equation 2.18, and taking $\mathbf{v_r(x)=1}$, gives:

$$V_o(X_a)=\int_{\frac{1}{2}}^{+\frac{r}{2}} \mathrm{SeXpi}^{\frac{27C(X+X0^2}{\underline{R}_0}} \mathbf{dx}$$

This integral can be solved in terms of Fresnel sine and cosine integrals, resulting the following power function:

$$|V_0(X_a)|^2 = \frac{1}{2}\,\mathbf{9}^2\, t\,[C(11+4)+C(11—W^2+ [S(11+4)-1-S(1—)]^2\}$$

...2.19

where:

$i = f/\mathit{II}$ **and** **= $2x_a$/VR7t**

...2.20

and, C(.) **and S(.) are the well-known Fresnel integrals defined as follows:**

$$\mathbf{C(z) = icos(\,f\,s^2).ds}\quad\Big|_0^z \qquad \textbf{and} \qquad \mathbf{S(z) =}\,\mathrm{fsin}(\tfrac{1}{2,}\,s^2).\mathrm{ds}\quad\Big|_0^z$$

...2.21

Equation 2.19 **is the detected signature of a point target, or equivalently the two-way synthetic aperture *gain* pattern, generated by the unfocused processing. The numerical evaluation of equation 2.19, for different values of ii, or in other words different synthetic aperture lengths 1, is depicted in figure 2.4a. From this figure (or figure 2.4b which shows more detail), it is clear that although $\mathbf{_{Ti}}$ - 1.2 gives the greatest absolute gain, the optimum synthetic aperture pattern in terms of main lobe peak and sidelobe level occur at i - 1. As a result, the optimum synthetic aperture length 1 is given by:**

$$Ti = f / 1 7, \; -i \; 1 \longrightarrow f_u = ji. \qquad \ldots 2.22$$

From figure 2.4b, the synthetic beamwidth, which determines the along-track resolution of unfocused processing 8_u, can be calculated as:

$$4 = 2x./ J1, .--. 0.5 \quad \_4 \qquad 8_u = 2x..-- 1 \, _1F, \qquad \ldots 2.23$$

For a focused process, inserting equation 2.17 in equation 2.18, and taking $v_r(x)$ = expj0(x), gives:

$$v_o(x.) = \int_{-\frac{C}{2}}^{\frac{C}{2}} 1 \exp j \, \frac{7cx^2}{I'OP.} 7.-7r \; \exp -j \, \frac{A(X + X_a)^2}{R.i,} \, dx - t: \frac{\sin k \left(\frac{27C}{ROA.} \, fX_a \right)}{\left(\frac{2,7c}{IT:27} \, fx_a \right)} \exp i \, \frac{2,xx^2}{RoX}$$

Therefore, after normalisation to unity, the output has the following power function:

$$\left| V A) \right|^2 = \left| \frac{\operatorname{Si71}\left(r \, \frac{1}{A} \, f X_a \right)}{\frac{27C}{R_0 A,} \, r_x a} \right|^2 \qquad \ldots 2.24$$

This (sinx/x) squared expression is the signature of a point target detected by the radar, or equivalently the two-way synthetic aperture gain pattern generated by the focused processing. Figure 2.5 shows the focused two-way gain pattern for different synthetic aperture lengths, and it can be seen that the narrowest beam is achieved when the synthetic aperture length is at its maximum (i.e. 1= L = 110AJD, the visibility range). For this situation, from figure 2.5, the -3dB width is approximately equal to 1.4. Therefore, from equation 2.24, the along-track resolution of the focused processing 8f can be calculated as:

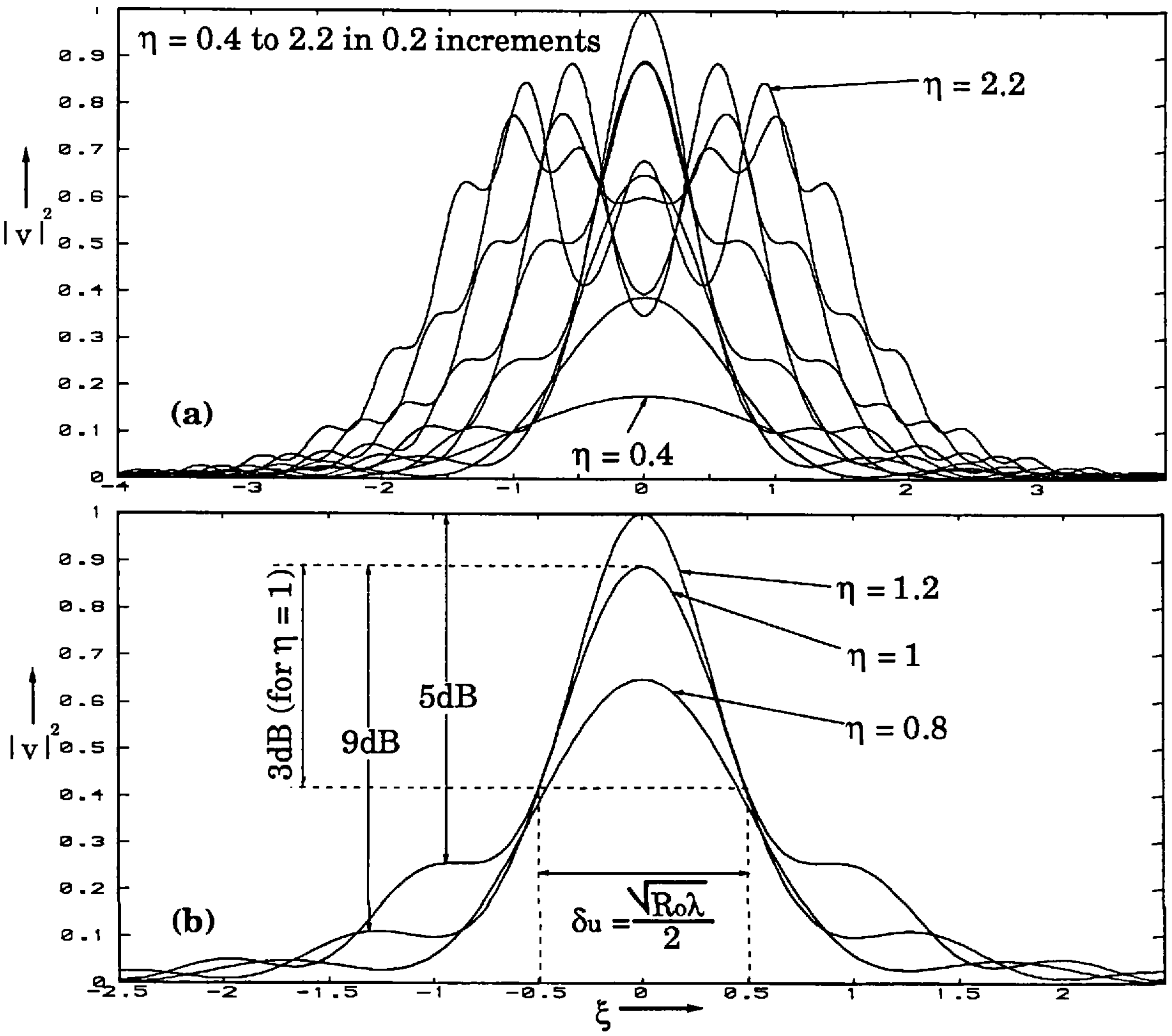

Figure 2.4- Unfocused synthetic aperture beam patterns.

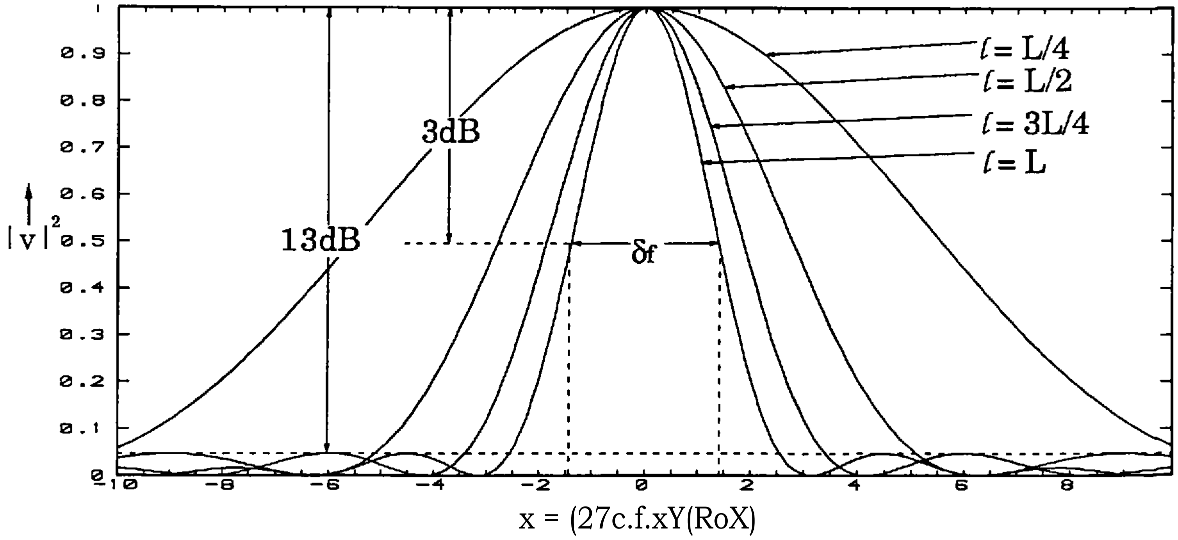

Figure 2.5- Focused synthetic aperture beam patterns.

$$\frac{27c\bullet f.x_a}{o} \quad 1.4 \longrightarrow) \qquad S_f = 2x \ 1.^{4x \ D} \quad 2 \qquad ...2.25$$

Comparing equations 2.23 and 2.25 shows that the optimum unfocused process provides an along-track resolution which is half the synthetic aperture length, $\mathcal{C}_u$. In contrast, in the focused process the finest along-track resolution is half the real aperture length D. This means that a smaller real aperture provides a higher along-track resolution.

So far it has been explained that to synthesise an aperture, a series of along-track spatial samples are needed to be used in a correlation process. The length of the correlation integral is constant and its equivalent time T, assuming that the platform moves with a constant velocity v, is given by:

$$7= \qquad \text{(where } C = R_o d \text{ for unfocused and } f = \frac{R}{i}\text{-fl for focused)} \quad ...2.26$$

If n samples are needed for the correlation process, the number of samples per second (i.e. the pulse repetition frequency, PRF), using equation 2.26 and by taking d as the distance between two successive samples, is:

$$\text{PRF} = \frac{}{T} = \frac{}{t} = \frac{}{d} \qquad [\text{where } d = t/(n\text{-}1) = \text{tin}] \qquad ...2.27$$

As is well-known, for any radar there is a maximum limit for the PRF which is governed by the ambiguity in detecting targets in the range direction. To understand the situation, figure 2.6a illustrates a timing diagram for a transmitted chirp signal having a pulsewidth T and the composite received waveform (associated with all the targets within the beamwidth of the antenna) starting at t1= 2Rn/c and ending at t2= T+2Rf/c (R_n is the range of the nearest target and Rf is the range of the furthest one). Therefore, to avoid overlapping of any part of a return waveform and

its two neighbouring transmitted pulses, the PRF should have an upper limit given by:

$$PRF_h = \frac{1}{PRI} < \frac{1}{2T + \frac{2}{C}(R_f - Rd} \qquad ...2.28$$

For a synthetic aperture radar, as well as the higher limit of PRF, there is also a lower limit which is governed by the ambiguity in detecting targets in the along-track dimension (caused by the grating lobes of the discrete correlation process). From figure 2.6b, the spatial sampling interval is d, so the discrete synthetic array repeats its pattern with a period XJ2d (compared to ?Lid for real arrays), and the distance between the two grating lobes lying on either side of the main lobe, is found by substituting for d from equation 2.27:

$$A = 2 \times \frac{LL}{2d} \therefore \frac{X}{d} - \frac{A.PRF}{v} \qquad ...2.29$$

Again from figure 2.6b, the position of the first nulls of the along-track real beam pattern, assuming uniform excitation, is given by:

$$A_I = \frac{2X}{D.} \qquad ...2.30$$

To attenuate the grating lobes, they must fall outside the real beam main lobe; therefore using equations 2.29 and 2.30, the lower limit of PRF is:

$$(A_r \; D_{az}) < (A \quad ..\underline{PRF)} \underline{\quad} > PRF > 2v \qquad ...2.31$$

Combining equations 2.28 and 2.31 gives the two bounds of the PRF:

$$\frac{2v}{D_{az}} < PRF \quad \frac{1}{2T + \frac{2}{c}(R_f - R_n)} \qquad ...2.32$$

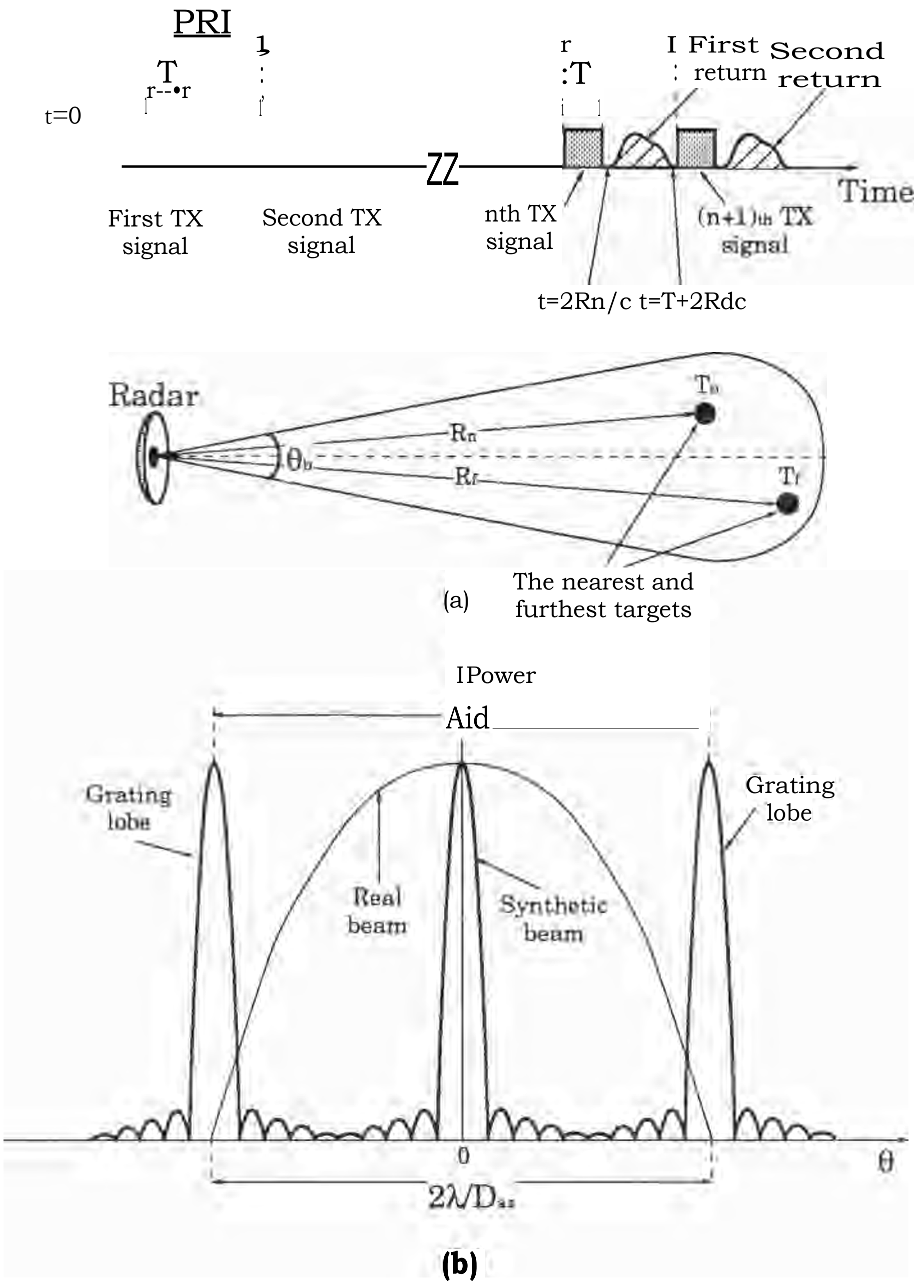

Figure 2.6- Range and along-track ambiguities in synthetic aperture processing.

To close this section, it is worth mentioning that having only one transmit/receive element along the aperture effectively doubles the phase sensitivity of the synthetic array in comparison to a real array of the same length (more details are given in Chapter 5). In other words, a synthetic aperture radar with a correlation length of I[t] provides half the beamwidth of a real aperture radar with an aperture a this can be clearly seen in the synthetic aperture patterns, figures 2.4 and 2.5). So, the general equations for the beamwidth 0_a and resolution Sa of a synthetic aperture radar are given by:

$$0_a \, a \, 2(\qquad \text{and} \qquad 8_a = Tr \qquad \text{...2.33}$$

2.4 *Radar altimetry, pulse-limited and beam-limited modes*

Two operating modes are envisaged for a radar altimeter: the pulse-limited mode and the beam-limited mode. In the pulse-limited radar altimeter, the size of the footprint is limited by the effective width of transmitted pulse T. As the antenna is designed to illuminate an area larger than the footprint, the footprint is pulse-limited and not beam-limited:

Figure 2.7a shows the intersection of a narrow pulse from a pulse-limited radar altimeter on a sea surface whose waveheight is small compared to the compressed pulsewidth. It also shows the evolution of the radar footprint and the corresponding received power.

The leading edge of a pulse having a width ti and transmitted at time t = 0, first hits the surface at time t = h/c, where h is the satellite height. The circle of illumination then grows linearly with time over the surface until t+t, at which time the trailing edge of the transmitted pulse intersects the surface. After time t+t, the centre of the growing circle (i.e. nadir point) is no longer illuminated and the illuminated surface becomes an annulus of constant area. The backscattered signal is received by the altimeter from

---

[t] [N.B. throughout this thesis the term 'correlation length' has been taken to mean synthetic aperture length, rather than its more usual meaning.]

the nadir point from time 2t = 2h/c until 2t+T. The distance d to the furthest points from which backscatter can also be received at time 2t+t, is obtained from 2d/c = 2t-vr. Thus, d = h+cT12, and from the geometry of figure 2.7b, the radius r and the area A of the fully developed pulse-limited footprint are (Brooks et a1.,1978):

$$r = .\backslash/(h+\frac{ct}{2})^2\text{-}h^2 \approx 4717 \text{ and } A = 7Cr^2 = \text{nein} \qquad \text{...2.34}$$

After this, the illuminated region is an expanding annulus of constant area and the expansion of this annulus continues until the received power is attenuated by the antenna pattern. The received waveform at the altimeter is processed in a series of range bins, each providing a time resolution of 'C. The inner radius and the area of the **nth** annular footprint corresponding to the nth processing range bin (figure 2.7b), are given by:

$$r_n = \quad (h+\frac{nct}{2})^2 h^2 - \text{rnchr and } A_n = nr^2_{n+1} - nr^2_n = \text{In} \qquad \text{...2.35}$$

Equation 2.35 shows that the area of the annulus is constant and is equal to the area of fully developed pulse-limited footprint (i.e. equation 2.34).

Now, assume that the transmitted pulse encounters a rough sea with wave heights which are large compared to the compressed pulse width. The first returns begin to arrive earlier than that of the calm sea, because the pulse leading edge first hits the wave crests and is scattered from them. From this moment the illuminated area begins to grow until the trailing edge of the transmitted pulse intersects the wave troughs at nadir. So the evolution time and the area of the footprint on a rough sea are greater than those on a calm sea, which suggests that the slope of the leading edge of the received waveform can be used to infer the waveheight of the ocean surface.

As mentioned in section two of Chapter 1, if a broad-beam pulse-limited altimeter operates over topographic surfaces, the range measurement is

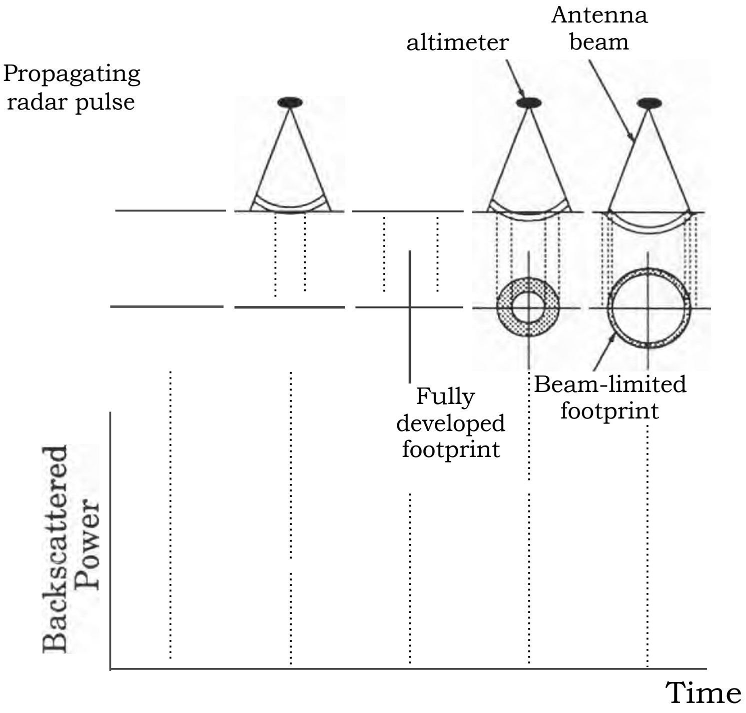

Figure 2.7a- Interaction between radar altimeter pulse and a diffused surface, showing evolution of footprint as a function of time (after Francis, 1984).

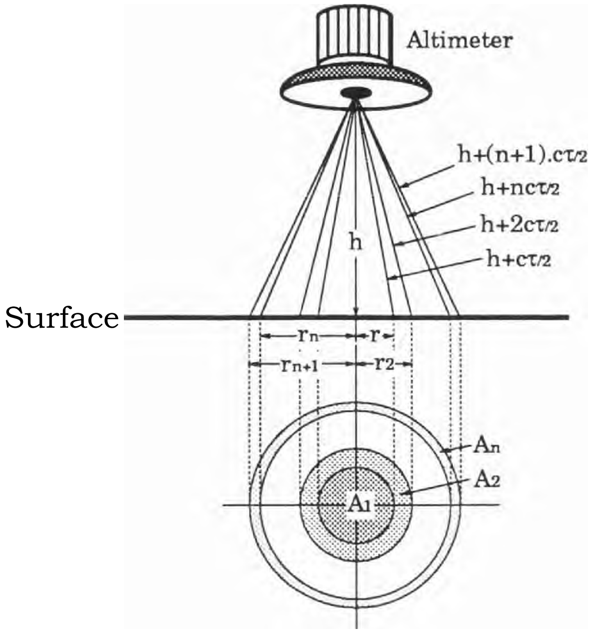

Figure 2.7b- Pulse-limited mode footprint geometry.

made not to nadir but to the nearest point to the altimeter within the antenna beam, and this causes error in the range measurement at nadir and an error in the surface location of a correct range measurement. Even for a flat sloping surface, the range measurement is made to an off-nadir point within the antenna beam which is displaced upslope either along-track or across-track, depending on the direction of the slope. This error is known as slope-induced error, and was first pointed out by Robin (1966). The magnitude of the slope-induced error, including error in the range measurement of the nadir Ah, and error in the horizontal displacement of a correct range measurement Ax, can be derived from the geometry of figure 2.8:

$$Ah = h - h' = h(1 - cosa) \quad \text{and } Ax = h \bullet sina \bullet cosa \qquad ...2.36$$

where h' is the measured height of the nearest reflecting point to the altimeter, h is the desired height above the satellite nadir and a is the slope of the surface. The magnitudes of these errors can be quite large, even for seemingly insignificant slopes. For example, for a satellite altimeter at a height of 800 km, a surface slope of 0.5° causes a nadir range measurement error of -30 metres and a horizontal displacement error of -7 km.

For a planar surface having uniform along-track slope, slope-induced error causes a constant bias of Ah in the height measurement which can be detected and corrected for. However, this is not normally the case and a topographic terrain cannot be treated as a plane surface. Therefore, the broad-beam pulse-limited mode altimeter is not usually suitable for operation over topographic terrains and it is more desirable to use a very narrow beam antenna to localise the footprint. The ultimate form of a narrow-beam altimeter is the beam-limited mode, in which the transmitted pulse should simultaneously illuminate the entire footprint. In other words the beam-limited footprint should be smaller than the pulse-limited footprint. Hence, the difference between the maximum and minimum ranges within the footprint has to be less than the range resolution er/2:

$$Ar = r_{max} - r_{min} < FL\frac{c}{2} \qquad \text{...2.37}$$

The footprint of a beam-limited mode altimeter, is the area illuminated by the antenna beam. The radius r and the area A of the beam-limited footprint generated by an antenna having a diameter D are thus given by:

$$r = \frac{la}{213} \text{ and } A = \text{TCP} \; {}_{2D}{}^{1} \qquad \text{...2.38}$$

For an altimeter which operates over sloping surfaces, two different beam-limited situations can arise as shown in figure 2.9. From equation 2.37, they result in:

$$Ar = h.coscc[sec(\frac{-1}{2D} -+ a) - 1] \quad \frac{a}{2} \qquad \text{for } 0 <\_a < \frac{0_h}{2} \qquad \text{...2.39}$$

$$Ar = h \bullet cosa[sec(1 - a) \; - sec(\; /T \; \circ C \; i- \qquad \text{for } a > \frac{Ob}{2} \qquad \text{...2.40}$$

The ocean surface slope relative to the equipotential geoid surface (for geostrophic balance) is very small, of the order of 2 arcsec (Robinson, 1985). Using this nominal value, also taking h = 800km and X. = 8mm (i.e. f = 37GHz), from equation 2.39, the antenna size is -1.5m, which is about 50% larger than that of a conventional pulse-limited altimeter. However, over land, slopes of several degrees can be encountered. As an example, for a surface with only 1° slope, from equation 2.40, the antenna size will need to be about 38m. Equations 2.39 and 2.40 have been obtained for terrains with roughness of the order of the range resolution. For a land radar altimeter, the required range resolution is of the order of a few metres, but the surface roughness even for a small footprint (a few tenth of a square kilometre) is normally much greater than the range resolution. This implies that although for topographic mapping, the beam-limited mode is the ideal mode, it is still hard to find terrains that satisfy the beam-limited condition,

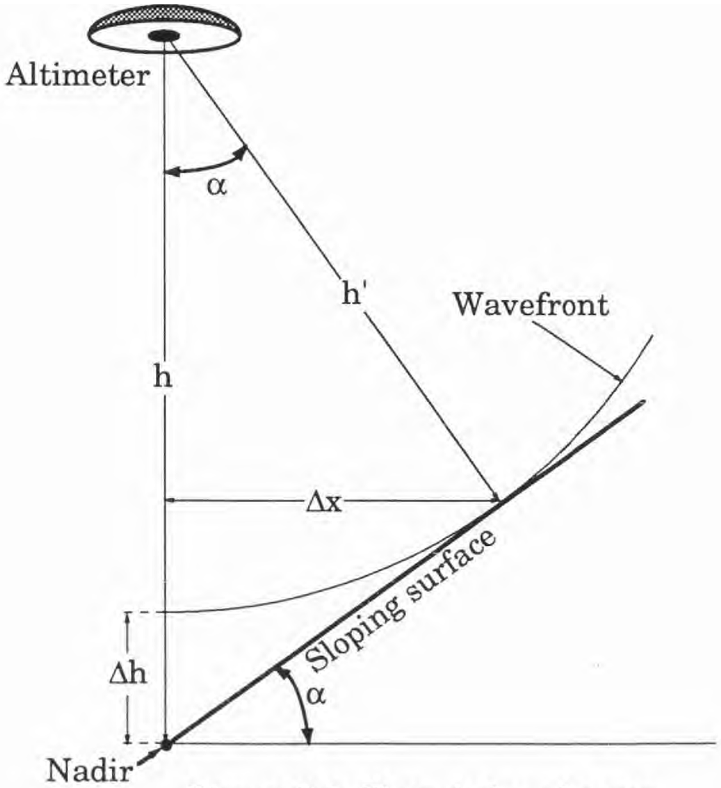

Figure 2.8- Slope-induced error.

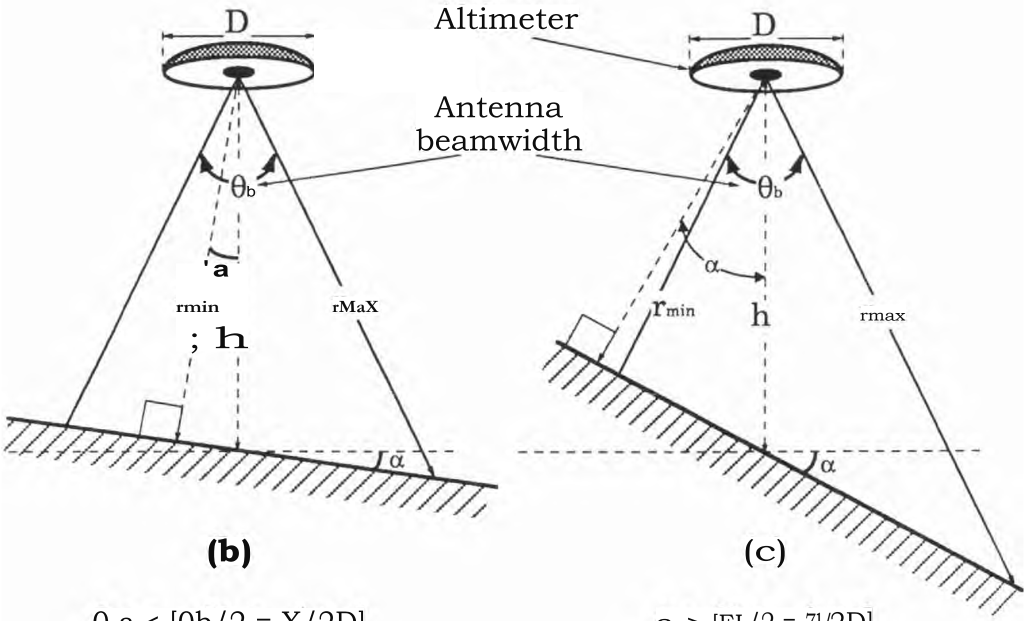

(b)

(c)

0 a < [0b/2 = X/2D]

a > [EL/2 = 7l/2D]

Figure 2.9- Altimeter over sloping surfaces.

and even for smooth terrains, the beam-limited mode only works over near zero slope surfaces, for otherwise the antenna size becomes impractically large. Therefore, the only option is an antenna having a beamwidth as narrow as possible to alleviate the problems of the broad-beam pulse-limited mode. The footprint of such an altimeter then depends on the terrain topography. For some surfaces it might be beam-limited but the dominant mode will be the narrow-beam pulse-limited mode.

2.5 *Topographic data and Earth sciences*

Topographic data (i.e. elevation, slope and slope orientation) have extensive applications in different branches of Earth sciences, namely: hydrology, vegetation and ecology, geology and geomorphology, continental geophysics, and polar science. Under any of these disciplines there are several scientific activities requiring different spatial resolutions, coverage and repeat intervals. A recent study (Burke and Dixon, 1988) prepared for NASA, has attempted to identify the applications of topographic data in Earth sciences and their associated requirements. The following few paragraphs summarise some of these applications.

Topography has important effects on hydrologic processes of the Earth's surface. These include: influence on water deposition, water runoff by means of overland and ground flows, soil moisture after drainage of the excess water, loss of moisture by evaporation, solar radiation and variation in temperature. The direct result of all these processes have a large effect on the vegetation of different areas of the Earth.

Topographic data provide enormous information for different activities of geology and geomorphology. These include: study of the formation and evolution of the Earth's surface, investigation of valley networks, volcanic regions, glacial valleys and deposits, landslides, floods and earthquakes. Another interesting application is the monitoring of alpine glaciers. This is attractive for the purpose of the study of the greenhouse effect, since such glaciers have significantly less thermal inertia than the polar ice caps and are thought to be more responsive to changes in temperature due to the greenhouse effect.

Topographic information of the Earth's surface combined with information about the gravity field provides fundamental data for research into continental geophysics. This includes the study of the motion of the continents and interaction between their boundaries, and the deformation of the Earth's crust and earthquake activities.

Polar ice sheets, consisting of Antarctica and Greenland, have a great influence on the Earth's surface and its atmosphere. The polar regions contain 80% to 90% of total fresh water of the Earth and can be of great importance as a future resource. At the present, it is not known whether polar ice sheets are stable, growing or shrinking, but it is thought that there is a feedback from the greenhouse effect which may cause the ice sheets to shrink, resulting in a sea level rise with the direct effect on the coastal regions of the world. It is therefore very important to monitor the mass balance and dynamics of these ice sheets. Also information about the thinning of the ice shelves, their grounding lines and margins, investigation of various polar features such as: ice domes, ice divides, drainage basins and ice streams, all require topographic mapping of the polar ice sheets. It is however obvious that under the severe polar conditions of darkness, remoteness and cold, only satellite remote sensing probes can provide the required data.

Different activities of Earth sciences require a variety of resolutions, repeat intervals and coverages, and table 2.1 summarises some of these requirements. Although the enormous diversity of the applications of topographic data makes it most unlikely to find a common data set to meet all the demands, it is still possible to classify the requirements into three groups: local problems, requiring very high resolution data; regional problems, requiring high resolution data; and global problems, requiring moderate resolution data. Figure 2.10 summarises these categories and for comparison also shows the best presently-available global data set. This

[illegible]	Requirements				Application examples
	Data set scale	Horizontal resolution	Vertical resolution	Repeat interval	
[illegible]	Global			-10 years	Global vegetation, hydrologic and ecosystem studies and modeling.
	Regional	[illegible]		-yearly	Regional-scale vegetation studies, water deposition and run off, mesoscale circulation.
	Local			-yearly	Erosion,hydrologicrouting, snow accumulation.
Geology and geomorphology	Global		[illegible]	5-10 years	Global geomorphic mapping, tectonic studies.
	Regional	[illegible]	[illegible]	1-5 years	Volcanic activities, major landslides, deltas, valley networks. _
	Local		[illegible]	1-5 years	stream channels, river floods, small landslides.
Continental geophysics	Global			[illegible]	
		[illegible]		5-10 years	Study of polar large-scale features.
		[illegible]	[illegible]	1-5 years	

implies that the existing information is considerably coarser than that required by the different branches of Earth sciences.

2.6 ***An altimeter for the remote sensing of topographic surfaces***

So far, the methods for obtaining spatial resolution applicable to a radar altimeter have been explained. Also, feasible applications of topographic data provided by radar altimetry and their requirements have been summarised. This section attempts to quantify some of the basic parameters of satellite-borne radar altimeters for the near future.

By considering figures 1.3 and 2.10 (the first gives the size of a real antenna, either in the along-track or across-track dimensions, for different frequencies and altitudes to obtain a particular spatial resolution; the second shows the classifications of the horizontal and vertical resolution needed for different disciplines of Earth sciences), and also by considering the state of technology and the trend of progress in the design of space qualified high frequency components, a very close link can be deduced between them in dictating the limits of achievable spatial resolution for a practical satellite radar altimeter.

There is apparently no severe technological problem to limit the maximum range resolution that can be achieved by a radar, as it is proportional to the bandwidth of the modulated chirp on a microwave carrier.

For horizontal resolution, it seems that high along-track resolution is relatively easy to achieve because, by means of aperture synthesis, it is possible to provide extremely fine resolutions down to a few metres. However, in the across-track dimension, the real beam of the radar antenna is used, which means that high resolution needs a very narrow real beam. The beamwidth is inversely proportional to both frequency and antenna size, so to provide a narrow beam both the frequency and antenna size need to be increased.

Technology is gradually advancing from microwave to millimetre-wave (mm-wave) frequencies. This is because mm-waves have many advantages over microwaves, including: the ability to support broader bandwidth, higher spatial resolution, greater immunity to interference and small antenna and equipment size. These features make mm-waves attractive for communications, radars and electronic warfare. For spaceborne applications however, selective resonances of Oxygen and water vapour molecules cause severe attenuation of the mm-waves in certain frequency regions (figure 2.11 shows the amount of attenuation for frequencies up to 100GHz). Therefore, only particular mm-wave frequency windows which possess low attenuation (such as: 37GHz, 96GHz, 140GHz and 220GHz) are usable for long range applications. Nowadays, mm-wave active and passive devices such as low-noise amplifiers (LNAs), power amplifiers, oscillators, mixers, filters and phase shifters are available, covering the entire mm-wave band, from 30GHz to 300GHz. However, one of the obstacles that limits the use of available mm-wave components in satellite applications is the long-term reliability requirement, which is vital for any spaceborne electronic system. This is because in the case of any malfunction or failure, repair and maintenance of the electronic components of a satellite are virtually impossible. Some recent papers (Bierman, 1989; Kamal, 1989) have assessed the state of technology in space qualified mm-wave devices. With today's technology (1990) mm-wave passive components that meet space standards are more or less available. Of the active devices, GaAs FETs can provide low-noise amplification for lower mm-wave frequencies of up to 60GHz, but the advent of high electron mobility transistors (HEMTs) show a lot of promise towards attaining very low-noise (noise figures of the order of 1 to 3 dB) amplifiers at least up to 100GHz, and with their trend of development, space qualified mm-wave LNAs will emerge very soon. In contrast, the availability of mm-wave transmitter power amplifiers is a major concern. Power amplifiers have been developed both as thermionic and semiconductor devices, realising that high power higher frequency amplifiers are still confined to thermionic devices such as TWTs. The main concern with these amplifiers is their operating lifetime, which is an important factor for spaceborne applications, and although very reliable

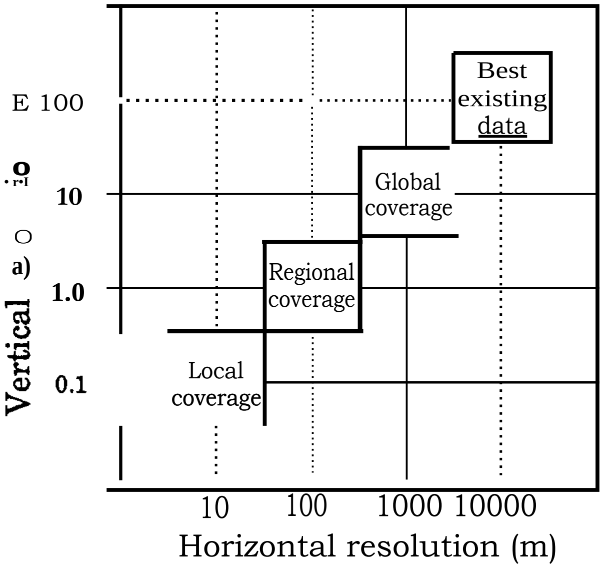

Figure 2.10- Categories of spatial resolution.
(Burke and Dixon, 1988)

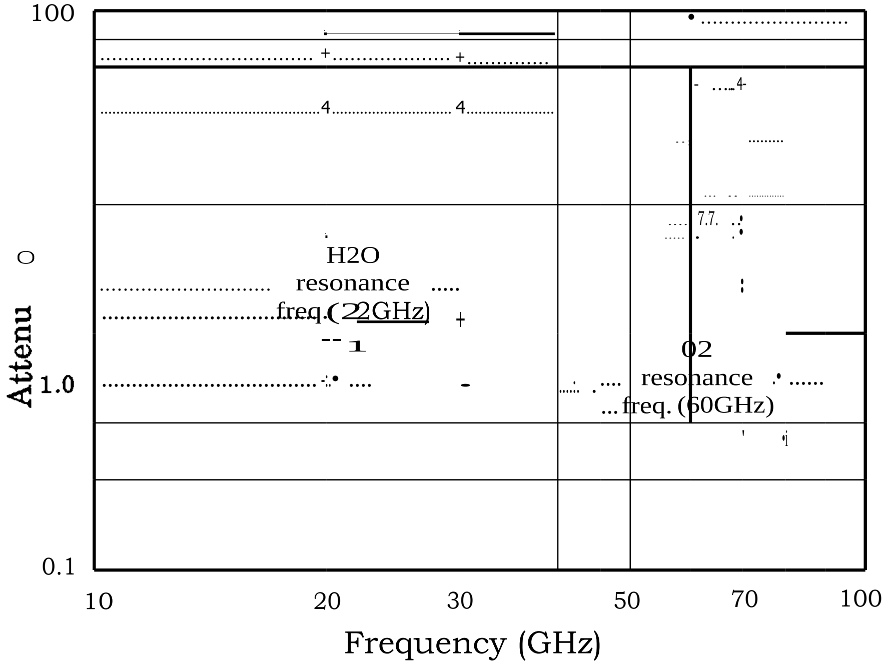

Figure 2.11- Total two-way attenuation of electromagnetic waves through the Earth's atmosphere. (after Long, 1975)

and long life microwave band TWTs exist and are conventionally used in remote sensing and communication satellites, there is still a gap for similar mm-wave band amplifiers. As an example, today's long-life 94GHz TWTs have —5000 hours (- 200 days) of operating lifetime which is rather short for a remote sensing satellite mission. As an alternative, research on MESFET and HEMT power amplifiers is going on and recently space qualified HEMT amplifiers for 42GHz providing 0.5W output power have been introduced (Bierman, 1989). A series of these low-power amplifiers arranged in a phased array antenna system could provide an effective high transmit power suitable for long-range mm-wave applications.

Considering the state of technology in the 1990s and its trend of progress, very soon all passive and active components necessary for a spaceborne remote sensing system operating at 37GHz will be available. Subsequently it seems reasonable to expect the introduction of a whole range of space qualified devices for frequencies up to 100GHz. However, for remote sensing missions in the near future, and for the purpose of this study, 37GHz is chosen as the frequency of the radar altimeter.

Antenna size is the other parameter which dictates the achievable spatial resolution of a radar altimeter. Present day spaceborne radars have small and moderate size antennas, and the longest ones used in SARs are around 10 metres. Even if it is assumed that a 20m long antenna (ignoring all the mechanical complexities) is feasible to be deployed in space, for a radar altimeter operating at 37GHz and 800km altitude, equation 2.1b gives the across-track resolution as only about 330m. Therefore, out of vertical resolution, along-track resolution and across-track resolution, the third one is the hardest to improve, and as a result, from figure 2.10, the feasible horizontal resolution falls in the upper limit of the high resolution regional scale altimetry. This limitation in obtaining high across-track resolution, which is the result of technological shortcomings, does not obstruct the enormous applications of synthetic aperture altimetry which can still cover most of the global scale and regional scale data sets. On the other hand, for the local scale data set, since there is no need for large coverage, some optical or radar methods, such as: optical stereo imagery, stereo SAR, interferometric SAR and laser altimetry are proposed to be used as complementary techniques.

Optical stereo imagery is similar to the aerial stereo photography which is conventionally used in surveying and cartography. In this method, by using an optical camera, a pair of images of the same area of terrain but taken from different spatial positions are overlapped and the stereoscopic parallax (i.e. apparent displacement) of points from one image to the other one are measured. The parallax of any point is directly related to the elevation of the point, so either (i) having the height of the platform h along with the height of a reference point in the image with respect to a reference level, or (ii) having the height of the platform with respect to a reference level and the focal length of the camera f, as well as the distance between the two photographs along the flight path X, the height of any desired point of the photographed area can be calculated by measuring its parallax (Wolf, 1983). For these two cases, and from figure 2.12, the following equations are derived:

$$h_b — h \quad \frac{P_a(h - h_a)}{P_b} \qquad \text{(for case I)}$$

$$h_b = h - \frac{f}{P_b} * X \qquad \text{(for case II)}$$

$$\ldots 2.41$$

where $P_a = X_a - X'_a$ is the stereoscopic parallax of the reference point a, $P_b = XE, - X'_b$ is the stereoscopic parallax of the under measurement point b, and h_a and h_b are the heights of points a and b with respect to the reference level. The spatial resolution offered by optical stereo imagery is very high, but the height extraction precision is limited by the geometry of the observing system. For example, the HRV imaging instrument on board the SPOT-1 satellite (launched by CNES in 1986) provided 10m ground resolution and -10m height extraction precision. Other near future missions have similar specifications, such as the Metric Camera instrument on board Atlas-1 which will be launched by NASA in 1991, to

provide 5m ground resolution and —10m height extraction precision (Burke and Dixon, 1988). In addition to the moderate height resolution, optical stereo imagery has another important disadvantage, which is its sensitivity to weather condition and solar illumination, making it unable to operate whenever the area under observation is covered by cloud or fog, or when it is night. Despite the above-mentioned problems, spaceborne optical stereo imagery has been extensively used in recent years, and a number of missions are planned by different space agencies for the near future.

An alternative method to optical stereo imagery is the stereo SAR which is less sensitive to weather condition, and also it is independent of solar illumination. In this method, using the same principle as was explained for optical stereo imagery, a pair of radar images of the same area are used for parallax measurement of points. Some recent results from SIR-B stereo images (flown on a Shuttle mission in 1984) have shown —25m ground resolution and —50m height extraction precision (Thomas et al., 1986). Therefore, despite some advantages of stereo SAR over optical imagery, it offers less horizontal and vertical resolution as well as requiring considerable signal processing to generate the basic images.

To extract the height information, there is also another method which uses the direct phase measurement of similar pixels in a pair of images, instead of amplitude detection and parallax measurement. This technique is known as SAR interferometry. Figure 2.13 depicts the basic geometry of such a system. As can be seen, the signal sent by a single transmitter is intercepted by two receivers with a time delay between them corresponding to the differential range to the target. This time delay between the two channels gives rise to a phase difference that can be measured at the complex output of the processor. This phase difference, Aci), provides the depression angle of the baseline to the target, i), by the following equation:

$$= {}^{2t}_{2L} d.\cos(15+T) \pm 2nn \qquad \text{...2.42}$$

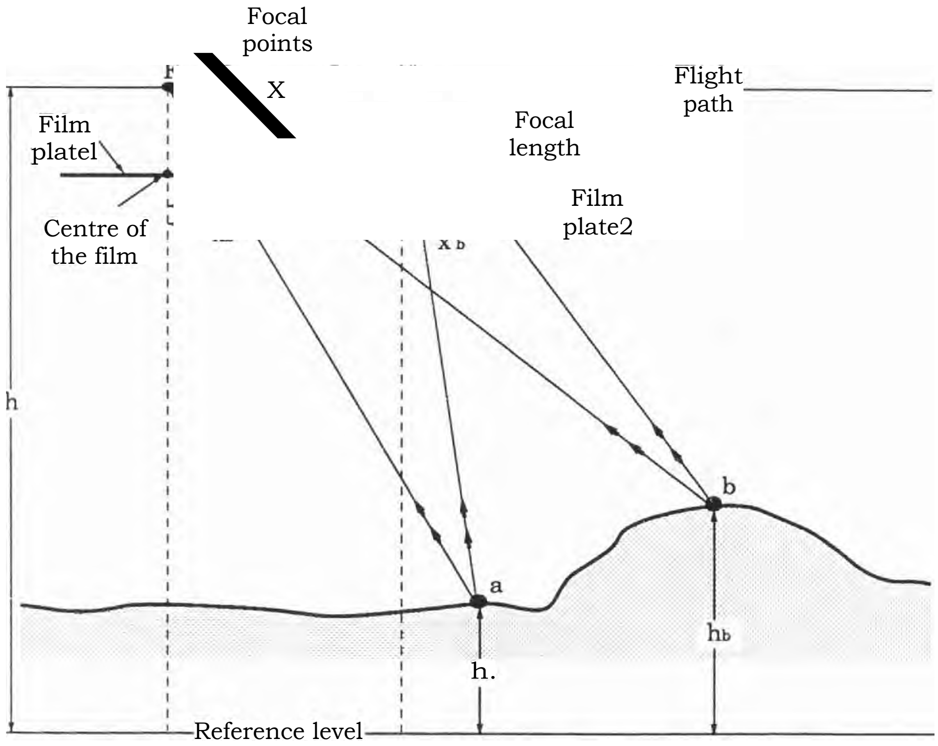

Figure 2.12- The geometry of optical stereo imagery.

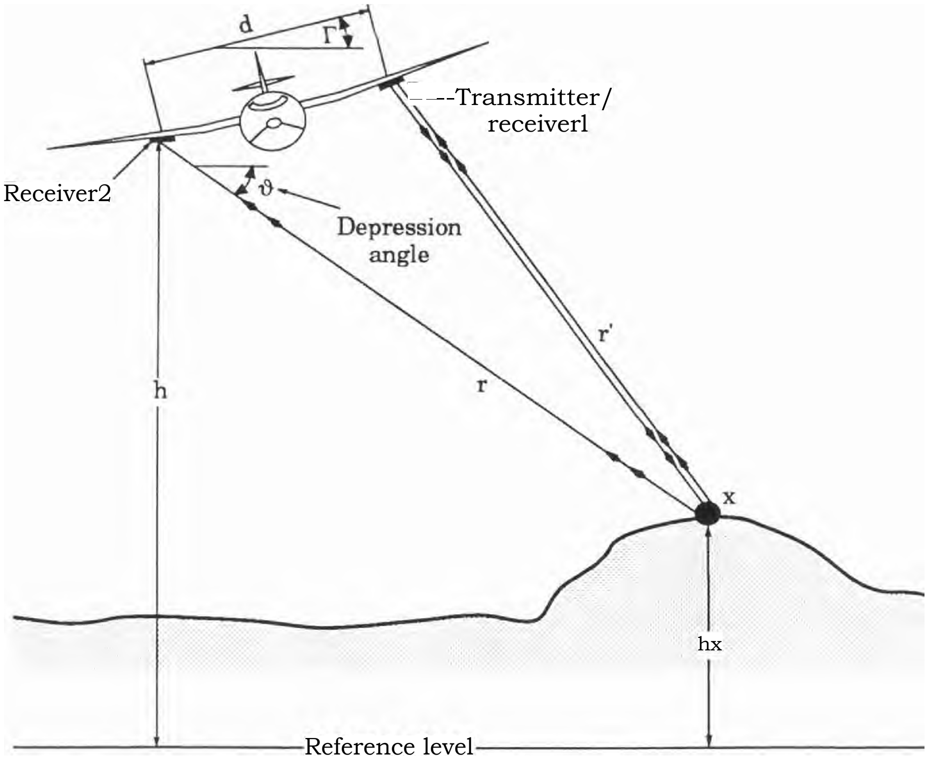

Figure 2.13- The geometry of interferometric SAR.
(after Zebker and Goldstein, 1986)

where d is the distance between the two antennas forming the interferometer (i.e. the length of the baseline), T is the angle of the baseline with respect to horizontal, and 2nit is the phase ambiguity which exists in determining the true phase difference. Extracting the range, r, of the target from the processed image and knowing the height of the platform with respect to a reference level, h, from equation 2.42 the following expression can be derived for the height, h., of the target (Zebker and Goldstein, 1986):

$$h_{-} = h - r.\mathrm{sim}5 = h - r.\mathrm{sin}_{r}\cos^{-1}[\,_{2}X_{Ta}(AO \pm 2nrc)] - r\,\Big| \qquad ...2.43$$

From equation 2.43 the height of any desired point of the complex image can be calculated. However, there is still a problem in determining the value of which provides the phase ±2nir. To overcome this problem, at least one reference point with known depression angle should exist within the image. Then, after determining the value of for that reference point, the trend of phase variation has to be tracked pixel by pixel for the entire image which at the end provides the true value of the phase difference for any pixel. This procedure is called phase unwrapping.

It has been explained that the SAR interferometry is in effect a method of extracting depression angle of the targets with respect to the radar from a pair of coherently processed images. But to find the height of the target, its absolute range, r, and the baseline angle, I', have to be also measured. This means that the error in the height determination of the points is related to the errors in measuring the absolute range, the baseline angle and the phase difference. Therefore, even if the phase difference and baseline angle could be determined exactly the height resolution is still restricted by to the range measurement resolution. As a result, interferometric SAR cannot provide finer height resolution compared to a synthetic aperture altimeter which only uses the range measurement of footprint through a very narrow beamwidth antenna and a precision attitude determination, as will be explained in detail in Chapter 3. Furthermore, considering that the interferometric SAR requires more extensive signal processing in terms of image generation, phase extraction and phase unwrapping, it does not seem a suitable choice for global and regional scale altimetric purposes. It is however, necessary to mention that as a sideways-looking radar, interferometric SAR can provide greater across-track resolution by mapping its range resolution into ground range resolution, in contrast to a synthetic aperture altimeter which uses an across-track real beam. Therefore, like imaging SARs, resolution cell sizes of about 25mx25m are achievable by focused processing, which obviously introduces more complexity to an altimeter. But this capability, along with better height resolution, makes interferometric SAR more attractive than stereo imagery for the purpose of local scale topographic mapping. Here it has to be mentioned that, recently, a new idea has been proposed by Wingham (1988), and is currently under investigation. This is based on processing the square-law detected signals of a SAR, and is consequently an example of incoherent aperture synthesis. It is thought that a number of stringent constraints of conventional SAR processing, such as PRF and precise location of the platform, can be relaxed by this new approach.

A powerful substitute for the optical and radar stereo imagery and also SAR interferometry, in terms of offering very high ground and height resolutions as well as simpler signal processing requirements, is laser altimetry. In the laser altimeter, very short pulses of a laser beam are sent towards the surface, and by measuring the arrival time of the reflected pulses received by an optical receiver, very high range resolution can be achieved. For spaceborne remote sensing applications, several pulsed laser sources are now available. Some of these sources offer beam divergences of the order of 0.1 milliradians and pulsewidths of less than 0.3nsec (Measures, 1984). Such pulsed lasers, on a platform at a height of 800km above the Earth's surface, can provide -80m footprint (ground resolution) and -50cm height resolution. These characteristics, which satisfy most of the requirements of the local scale data sets needed by different disciplines of Earth sciences, provide a promising capability for very high resolution topographic mapping of selected local areas. However, an obvious problem with laser altimetry is the obstruction of the laser beam whenever the area under observation is covered by clouds. Apart from this, the important concern is the short lifetime of laser sources (with current technology a lifetime of about $5\text{x}10^7$ pulses seems feasible (Chase, 1987). Assuming a footprint area of -0.01 km^2 corresponding to a ground resolution of -100m, $5\text{x}10^7$ laser pulses can only cover $5\text{x}10^4$ km^2 in comparison with 150 million square kilometres of the total non-ocean area of the Earth's surface. This huge shortcoming makes laser altimeters unsuitable for regional and global scale applications (at least for the near future). [N.B. another problem with the spaceborne laser altimetry is the power consumption]. In conclusion, any of the optical and radar techniques explained in this section to be used for topographic mapping of the Earth's surface, have their own merits and drawbacks, and any individual technique could form the subject of a separate study. However, considering the current state of technology and likely trends for the next few years, synthetic aperture altimetry appears to be the one which can provide the maximum benefits, as a single remote sensing instrument, and in terms of resolution and coverage, to the greatest number of activities of Earth sciences. For this purpose, a technologically reasonable trade-off for near future satellite-borne altimetry, appears to be to design a radar to provide around 500mx500m horizontal resolution and a few metres (say 3m) vertical resolution, operating in the 37GHz frequency band and at 800km altitude, for permanent monitoring of the Earth's surface. Table 2.2 summarises the basic specifications of the proposed satellite-borne radar altimeter.

Altitude	800 km
Carrier frequency	37 GHz
Along-track resolution	500 m by aperture synthesis
Across-track resolution	500 m by narrow real beam
Height (range) resolution	3 m by full-deramp technique

Table 2.2- Basic specifications of the satellite-borne radar altimeter.

Chapter 3

Synthetic aperture altimetry

3.1 *Introduction*

Aperture synthesis is a method of processing radar echo waveforms in a two-dimensional space, to obtain high spatial resolution. The synthetic aperture altimeter is similar in many ways to a conventional SAR, but there are some important differences - indeed, it is one of the aims of this chapter to explore the similarities and differences. The purpose of the altimeter is to provide a map of the surface elevation, either along the sub-satellite track, or ideally over a two-dimensional swath. The surface elevation is derived from the propagation delay of the radar signal, and it is convenient to use full-deramp processing for this purpose. Horizontal resolution is provided by restricting the antenna beam, using real (across-track) or synthetic (along-track) apertures. The purpose of the conventional SAR, on the other hand, is to provide a two-dimensional map of surface reflectivity to one side of the sub-satellite track. Azimuthal discrimination is provided by aperture synthesis, and across-track discrimination by range gating of the received echoes, (Griffiths and Purseyyed, 1988).

This chapter aims to use the raw material provided by Chapter 2 to analyse the synthetic aperture full-deramp altimeter and its capabilities, while considering the power budget, digital signal processing, data telemetry, and beam pointing stabilisation, extending the basic idea into a scanning-beam altimeter along with several other features.

3.2 *Spaceborne altimeter*

First, the time or phase history of a point target illuminated by the radar altimeter is derived. As was explained in Chapter 2, the synthetic aperture provides the along-track signature of the target by means of phase-coherent processing of backscattered signals, sampled at different points in space. These samples generate a parabolic phase history which is symmetrical with respect to the centre of the synthetic aperture, so by correlating this phase history with a suitable reference function, the processed signature of the target is placed at the minimum of the phase parabola (i.e. the boresight of synthetic aperture). It is usually considered in the analysis of a SAR that the nth transmitting and receiving points are both at the same spatial position. This leads to the usual two-way time delay equation td = 2R/c. This is generally acceptable for an airborne radar, but for a spaceborne radar the range can be of the order of 800km and as a result td is about 5.3msec. Also the orbital velocity of the satellite carrying the radar is —7000 m/sec, and therefore the displacement of the radar platform between the nth transmitted signal and the reception of the corresponding echo will be 37m. This, for a spaceborne synthetic aperture altimeter with a correlation length l= 6.5m to provide 500m along-track resolution, means that when the ground track of the satellite is still about 20m away from the along-track centre of the target the radar altimeter has to start sending a series of pulses towards the target for a distance of 6.5m. After this period, transmission has to stop while the radar is moving and after passing over the centre of the target by about 20m, the radar altimeter starts receiving the backscattered signals for a period of 1= 6.5m. Hence by processing the collected echoes over this period, the along-track signature of the point target is obtained and placed at the centre of the receiving period which is in fact the centre of synthetic aperture [N.B. along-track sampling and correlation are performed during the reception period so the aperture provided by the motion of the radar during the reception period is the synthetic aperture length]. This discussion suggests that a spaceborne synthetic aperture altimeter is a bistatic radar both in space and in time.

Now to return to the derivation of the phase history of a point target, figure 3.1 depicts the appropriate geometry of the calculation. The radar altimeter on board the satellite travels with velocity v in the (x,z) plane parallel to the x-axis at a height h above the surface. The point x is the position of the radar at the instant of receiving the nth backscattered waveform, which was

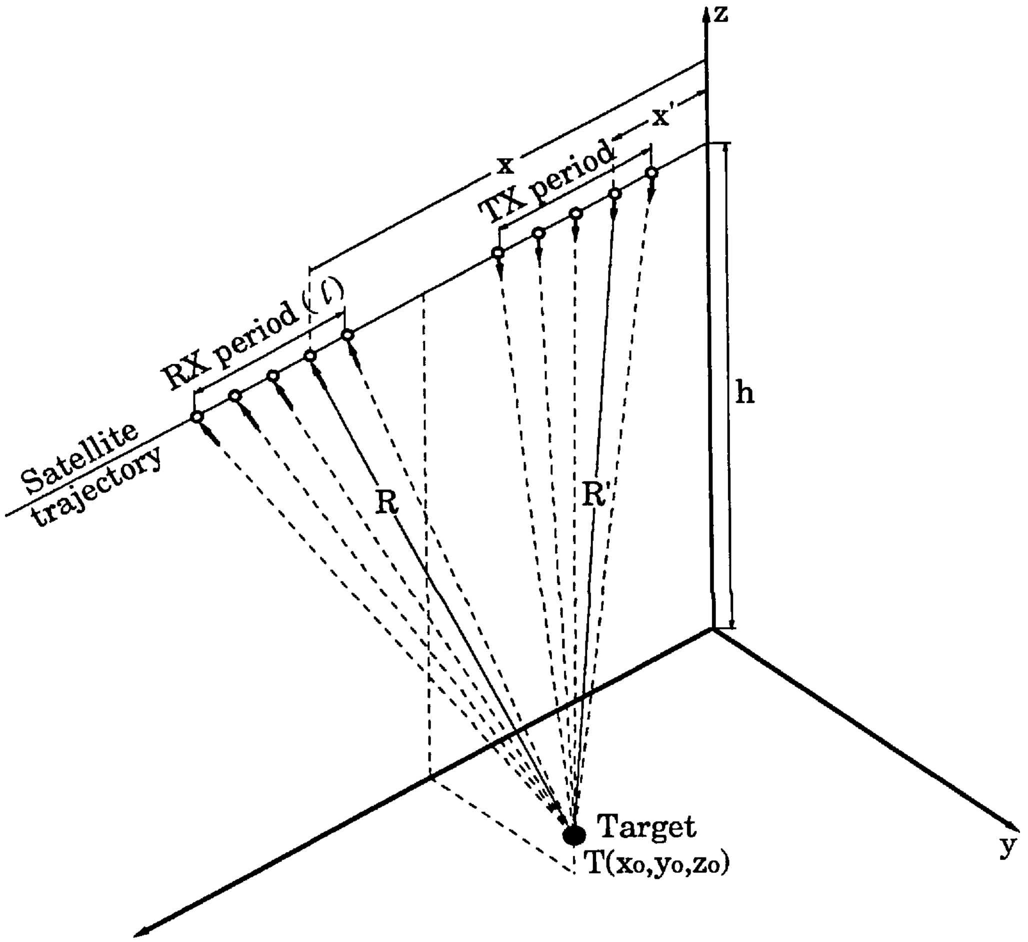

Figure 3.1- Geometry of satellite and target, shoWing conceptual formation of synthetic aperture and in particular, that the locations of the 'synthetic aperture' are different between transmission and reception.

transmitted when the radar was at x-vtd . So the range, R', of the radar to the target during the transmission of the nth pulse and the range, R, of the target to the radar during the reception of the **n**th backscattered signal are given by:

$$R' \ldots \overline{j[(x-vt_d)\,\mathbf{-x_0]}^2+y_0^2+(h-z_0)^2} \qquad \ldots 3.1a$$

$$\mathbf{R}= \mathbf{j}^{(x-xO)^2+\,y\theta^2+\,01.20)^2} \qquad \ldots 3.1b$$

In the above hyperbolic equations, $(x_o,y_0,4)$ is the location of the target in the (x,y,z) coordinate system, and t_d is the time taken for the transmitted pulse to be received by the radar (i.e. two-way time delay). td is also equal to:

$$t_d= \frac{R'+R}{c} \qquad \ldots 3.2$$

Inserting equations 3.1a and 3.1b in equation 3.2, and solving for t_d ,gives:

$$t_d= \frac{\underline{2}\quad {}^{1}7\text{—}}{c\,[1-v/c2]}\,[2C./\;(x-x_0)^2+y_0^2+(h-z_0)^2\;-\,2v\,(x-x0)1 \qquad \ldots 3.3$$

Similar to other synthetic aperture radars, the Fresnel approximation can be applied to above equation, since h^2 is always much larger than the other terms under the square root. This leads to the following parabolic expression:

$$t_d\cdot\frac{X^2}{hc}+\dot{m}\,i_0+\frac{2h}{c} \qquad \ldots 3.4$$

where:

$$X:\text{----}\;x-x-0\frac{hv}{c} \qquad \ldots 3.5$$

$$T_o= [y_o^2+ z^2- 2hz_o]/[hc] \qquad \ldots 3.6$$

In the derivation of the above equation another assumption made was that $[(v/c)^2 \ll 1]$, since $(v/c)^2 = 6\times10^{-16}$. [N.B. Numerical comparison of equation 3.4 with equation 3.3 shows a phase deviation of the order of ten microradians in the worst case, at the aperture edges. This is very insignificant especially for unfocused apertures where spatial samples are summed without any phase compensation up to E/2 radians].

From the two-way time delay, equation 3.4, and also from equation 3.2, the phase history of the target can be written as:

$$= {}^{7c}\ (I24\text{-}R) = {}^{27c}\ x^{2} \qquad \ldots 3.7$$

$$2_{2}7\ \mathrm{To}+\ 47ch \qquad \ldots 3.8$$

From equation 3.7, it can be **seen that the minimum of the phase history, which is the location of the processed signature of the target, is at x = 0 or equivalently $x = x_0$-1-(hv/c) during the receiving period. From the above equations an expression can also be derived for the square of the two-way time delay, which will be useful in the following sections:**

$$td = [\ \overset{4}{\underset{c}{+}}\ 2\overset{o}{\underset{hc}{T}}\ I\ X^{2}\quad [\ T_0 + \overset{2h12}{7^{1}} \qquad \ldots 3.9$$

In deriving **the above expression, the term $(X^2/hc)^2$ has been ignored because it is about 10^{16} times smaller than the other terms.**

3.3 *Aperture synthesis using linear* ***FM*** *signals*

The transmitted signal used for the synthetic aperture altimeter, as explained in Chapter 2, is a linear frequency modulated chirp waveform with pulse repetition interval Tp and duration T. The radar altimeter moves

in the along-track direction and sends a series of these chirp pulses towards the surface. The backscattered signals are processed by a two-dimensional processor to extract the signature of the target in the range and along-track directions. The third dimension, which is the across-track dimension, is inherently included by using a very narrow real across-track antenna beam.

The nth transmitted signal thus has the following form:

$$v_{\cdot rx}(t_n) = A_T.\mathrm{expj}O_{rx}(t_n) = A_T \bullet \mathrm{expj}2n(f_o t_n + 4\ t_n) \qquad -\frac{T}{7} < t_n < \frac{1}{2}$$

...3.10

where t_o is the time measured from the centre of the **nth** transmitted pulse, **AT** is the peak amplitude, Lis the carrier frequency and p. is the chirp rate. The backscattered signal from a point target is given by:

$$\mathbf{VRX(tn'td= A^{R}{}'eXpjO_{Rx}(t_n,t_d) = A_R\text{-}eXpj27[f_o(t_n\ t_d)+2\,(t_n\ t_d)^2]}$$

$$t_d - \frac{T}{2} - t_n \le t_d + \frac{T}{2}$$

...3.11

where **AR** is the peak amplitude of the received signal. Substituting for **td** and t_d^2 from equations 3.4 and 3.9, the received signal in equation 3.11, is modified to:

$$\mathbf{V_R x(X,T_n) = A_R \bullet eXpj27C[[\frac{[IT\ -f}{11C\ \ 0}\, x^{2}\, 1+[-\frac{II}{7}\, x^{2}\, t_n]+[f_o t_n 1.1.T_o t_n + \frac{1}{4} T_n^2]+[\frac{1}{2} T_0^2 - f_0 T_0]])}$$

$$t_d - \frac{2h}{C} - z. \le t_n < td - \frac{2h}{-}\, 4 - T,$$

where:

...3.12

$$t_n = t_h^{f} - \frac{2h}{c}$$

...3.13

Equation 3.12 is the two-dimensional received signal,in which the first square bracket is the along-track parabolic phase history generated during

the reception period by the range variation between the radar and the target when radar moves in along-track. The second square bracket is the cross-product of the range and along-track variables, and the third bracket is the parabolic phase term introduced by the linear frequency modulation of the transmitted signal, which is perturbed by the range information of the target due to the time delay between transmitted and received signals. The fourth bracket is a constant phase. This received signal is then mixed with the signal of a local oscillator (LO) which is a replica of the transmitted chirp signal having an appropriate time delay. So the nth LO signal is given by:

$$v_{io}(t_n) = A_L\text{-}\mathrm{expj}2n[f_o(t_n - t_o)+14\,(t_n - t_o)^2 1$$

where AL is the peak amplitude and to is an arbitrary time corresponding to the LO triggering instant. Taking t_o as 2h/c and using equation 3.13, the LO signal becomes:

$$V_{w}(T_n) = \mathrm{Acexpj}2n[f_oT_n + \overset{1.1.}{2}\text{-}\,\mathrm{tin}\} \qquad ...3.14$$

In this analysis the LO signal has the centre frequency of the transmitted pulse. This is because in the final stage of the receiver, before the range/along-track processing, the received signals are down-converted to zero-IF frequency using an in-phase/quadrature demodulator, so the negative and positive frequency components corresponding to the targets with ranges lower and higher than 2h/c can be unambiguously extracted.

Mixing the local LO and received signals (equations 3.12 and 3.14) and using a low-pass filter to select the down-converted spectra, gives:

$$V_o(X\,'T_x) = A_o\mathrm{expj}2n\,(\,[\,\frac{f_o\text{-}p.T.}{he}\overset{2}{x}\ 1\pm E\ \overset{11}{t7}\ X2T_{n}{}^{i+EgT}{}_{o}t_{n}{}^{i+Ef}{}_{o\,T\,o}-\ \overset{ii}{T}{}^{T}{}_{o^{1}\ 1}$$

$$\mathbf{d}\,\frac{2h}{\mathbf{C}}\ \frac{T}{2} < t_n \leq \mathbf{td} - \frac{2h}{C}\ \frac{4.}{2} \qquad ...3.15$$

This signal is the input to the two-dimensional range/along-track processor. The cross-product term in equation 3.15 represents a coupling between the range and along-track operations due to the range curvature effect. Under conditions where the maximum phase variation caused by the cross-product term is much less than the phase variation of the other terms in the exponent argument of equation 3.15, the two-dimensional signal processing is then separable in range and along-track, and the processing can be performed by two one-dimensional processing steps. Therefore,to examine the contribution of the different phase terms of equation 3.15, the following typical values of the parameters involved can be used:

1- f_o = 37 GHz (= 8 mm)
2- h = 800 km
3- X(max) (hX)/(2$8_a$) = ±3.25m for 8a = 500m
4-1.1 = BIT = (50 MHz)/(20 psec) = 2.5 x 10^{12} Hz/sec^2
5- T_r, (max) = **chirp duration T = ±10 gsec**
6- $T_o$tinin) [for a smooth terrain with the roughness "Az: of only 1cm at the nadir] = 6.7x10^{-11} *sec*
7- T_o(max) [**for a very rough terrain with the roughness "Az: of more than 3000m for an off-nadir beam at y_0=10km] = 2x10^{-5} sec**

Substituting these quantities in equation 3.15, shows that the cross-product term is —1500 times less than along-track and range terms, so the phase contribution of the cross-product term in the range and along-track processes is negligible. There are also other modifications that can be carried out for equation 3.15. Firstly, in the along-track bracket, the second term is —750 times less than the first term, and secondly, in the constant phase bracket, the second term is —1200 times less than the first term. So after omitting all the insignificant terms from equation 3.16, the output signal becomes:

$$v_o(X,T) = A_0.\mathrm{expj}2/ \quad x^2 \text{-1-1.1}T_o t_n + 0T^0] \qquad t_d \frac{}{c} - \frac{T}{2} \le - < t_d - \frac{2h}{c} + \frac{T}{2}$$

...3.16

Range processing is performed on any individual nth received waveform by applying a Fourier transform to equation 3.16 in the range (or equivalently t_n) domain:

$$V_o(X, f_r) = \overset{T2}{\text{Si)}}(\text{LT}).\ \text{eXP}\ (-\ \text{j27C}\ f_r t_n).\text{th}_n$$

...3.17

where f_r is the frequency variable of the Fourier transform and, T1 and T2 are the limits of the Fourier integral. In the general case T1= td-2h/c-T/2 and T2 = td-2h/c+T/2 , where td is given by equation 3.4, providing a time delay which is a function of the along-track variable x. However, following the discussion of the negligibility of the cross-product term, the range variation of the target to the radar from the time at which the target is at the minimum of the phase history parabola, to the time that the target departs from this minimum by ±3.25m (i.e. the edges of synthetic aperture) is less than 0.001X. In terms of the variation in the time delay, this range variation is equivalent to 5.4 $x10^{-14}$seconds, which is 10^9 times less than the Fourier transform integration length (i.e. ±lOgsec). Therefore the time delay td in the range Fourier transform can be very well approximated by the time delay at the aperture boresight (i.e. x = 0), which gives (using equations 3.4, and 3.6):

$$T_1 = t_{do} - \frac{2h}{F} - \frac{T}{7} = \text{To}- \frac{T}{7} \quad \text{and} \quad T2_2\, t_{do} - \frac{2h}{C} + \frac{T}{2} = T + 2$$

Now, inserting the above limits in equation 3.17, and also substituting for $v_o(x,t_n)$ from equation 3.16, the range Fourier transform becomes:

$$V_o(x,f_r)= (\text{T.Asexpj274}\, \frac{fo}{7} X^2 + (fo+ \text{ilTo-fr}\rangle\, ro \quad \frac{\sin[n(\text{tTo}-fr)T]}{[n(\text{IIT}}$$

...3.18

The (sinx/x) factor of equation 3.18 is the expected range signature of the point target, which will be explained later. Rearranging equation 3.18

results in:

$$V_o(x,f_r) = [A„T.exPic1)][FT)\ ][exPi_{i}\ {}^{c}\ x^2]$$

...3.19

$$Pr(f) — \frac{\sin [7c\ (p.T.-f_r)T1}{Dr(p.T.-fdT]}^{2}$$

...3.20

where (1) = 27a0+ gTo- fr)To is a phase factor independent of the along-track variable, Pr(fr) is the power (gain) pattern of the range processed output and X = c/f_o is the carrier wavelength.

Now it remains to consider the along-track phase history, shown in the third square bracket of equation 3.19, which has to be used for the synthetic aperture correlation process. It is obvious that the range variable ti_n is originally a continuous variable. In the signal processing, range processing can be done either by continuous analogue or discrete digital methods, whereas the along-track variable x is a discrete variable in nature. This is because a series of pulses, rather than a continuous transmission, are sent towards the target and the returns of these discrete pulses are used in the synthetic aperture correlation process. Therefore the unfocused correlation integral is modified to an unfocused correlation summation:

$$F(C) = I_{\frac{t}{2}}^{+\frac{(}{2}} F(X+X_a).dX = \mathbf{Ax./}\sum_{\mathbf{n=i}}^{N}\mathbf{F[n(Ax)+x_a]}$$

...3.21

$$\mathbf{N\text{-}1} = \frac{f}{\mathbf{v}} \cdot \mathbf{PRF}$$

...3.22

$$\mathbf{AX} = \frac{C}{\mathbf{N\text{-}1}}$$

...3.23

where x_a is the correlation variable, N is the number of samples, *I* is the integration length (equation 2.26) and Ax is the sample spacing. Inserting

the along-track factor of equation 3.19 in equation 3.21. and ignoring the constant factor of the summation also substituting for Ax from equation 3.23, the synthetic aperture correlation becomes:

$$F(x.) = \sum_{n=1}^{N} \exp j \frac{2\,11.}{hA} En \frac{-j-}{N\;1} + x_a \; {}^{2}$$

...3.24

Also the power pattern of synthetic aperture process will be:

$$[F(a)]2 = \left| \sum_{n=1}^{N} \exp j \; 129t \left[n \frac{1.}{N-1} + x_a \right]^2 \right.$$

...3.25

In the general case of an unfocused continuous process, as was explained in Chapter 2, the resultant pattern is a combination of Fresnel sine and cosine integrals. On the other hand, in a real situation when the signal processing reaches the stage of equation 3.25, although this summation can be easily performed numerically, no closed form expression can be found for it. However, for the particular case of a synthetic aperture altimeter, the integration length (I) compared to the optimum unfocused process (equation 2.22), is very short and the corresponding phase curvature across the aperture is very small, so it can be assumed that the aperture is focused at infinity (similar to the far-field criterion of an antenna). Therefore, such a synthetic aperture is approximated by a linear synthetic array having the following power pattern:

$$[f(x_a)]^2 - \left| \frac{\sin \frac{27ENC}{(N-1)h?,} x_a}{N\sin \frac{27c\,t}{(N-1)h?.} x_a} \right|^2$$

...3.26

Equations 3.25 and 3.26 have been numerically evaluated, and the patterns have been plotted in figures 3.2, 3.3, 3.4 and 3.5. All the plots are for a

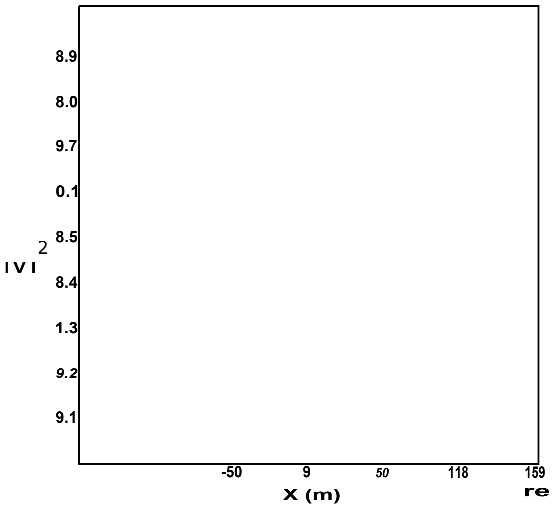

Figure 3.2- Sinc approximation of discrete unfocused aperture for very short correlation length.

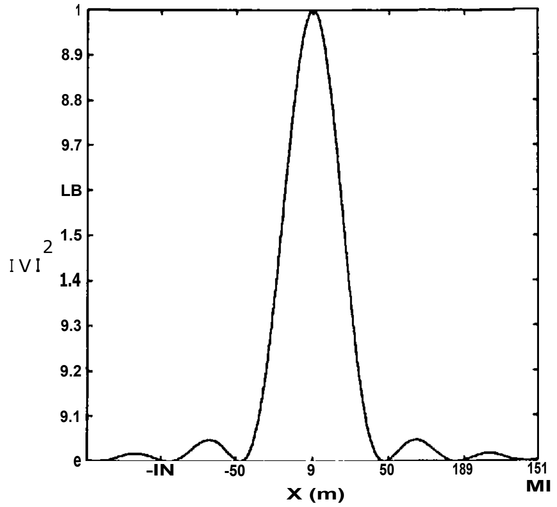

Figure 3.3- Fresnel integral representation of discrete unfocused aperture for very short correlation length.

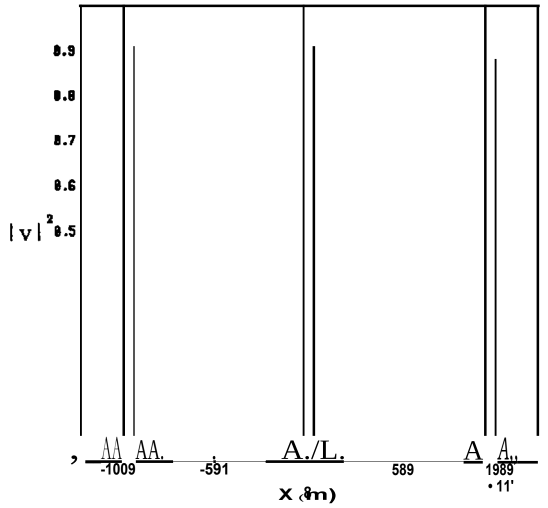

Figure 3.4- Sine approximation of discrete unfocused aperture for very short correlation length.

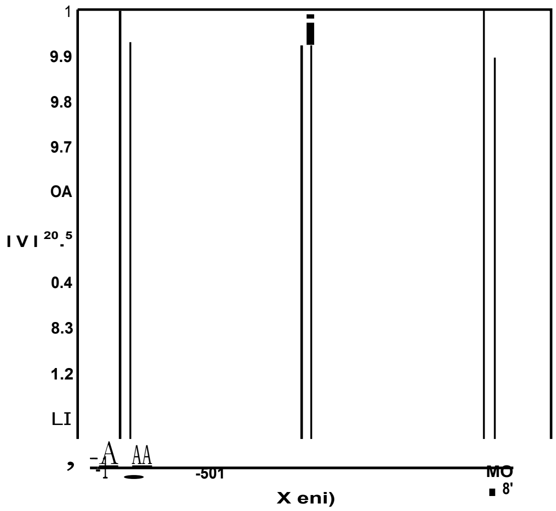

Figure 3.5- Fresnel integral representation of discrete unfocused aperture for very short correlation length.

synthetic aperture length of ±3.25m, giving 500m along-track resolution and with a PRF =10kHz (from equation 3.22: N40). Figure 3.2 shows the power pattern using the summation of equation 3.25 and figure 3.3 shows the power pattern using equation 3.26. Both give 500m along-track resolution and 13dB suppression of the first sidelobes. The two results are identical and will exactly overlap each other. Figure 3.4 is a compressed version of figure 3.2 for equation 3.25 which shows the first two grating lobes on either side of the main synthetic lobe, and figure 3.5 is the compressed version of figure 3.3 for equation 3.26 which shows the same grating lobes. Hence for short length unfocused processing, equation 3.25 can be replaced by equation 3.26, and in fact equation 3.26 can be treated as the closed form expression of the unfocused correlation summation. To examine to what extent this argument is true, the power pattern has been numerically evaluated for different lengths of synthetic aperture, and it has been found that for up to 5 times the nominal length, (i.e. 5 x 6.5 = 32.5m) the difference between equations 3.26 and 3.25 is insignificant. However, for longer synthetic apertures, the sidelobes start rising and the equivalence of these two equations become invalid. Different plots in figure 3.6 show the synthetic aperture power pattern for integration lengths of 8, 11, 15 and 18 times the nominal synthetic aperture (i.e. 6.5m) evaluated using the summation of equation 3.25, which demonstrate how the sidelobes rise.

Having completed the along-track and range processing, from equations 3.19, 3.20 and 3.26 the normalised two-dimensional power pattern of a point target becomes:

$$|V_0(x_a,f_r)|^2 = \left[\frac{\sin[\pi(\gamma T_0-f_r)\tau]}{\pi(\gamma T_0-f_r)\tau}\right]^2 \left[\frac{\sin\left(\frac{2\pi h f}{(N-1)h\lambda}x_a\right)}{N\sin\left(\frac{2\pi f}{(N-1)h\lambda}x_a\right)}\right]^2 \qquad \text{...3.27}$$

The first bracket of equation 3.27 is the range signature of a point target processed by the full-deramp technique, followed by a Fourier transform..

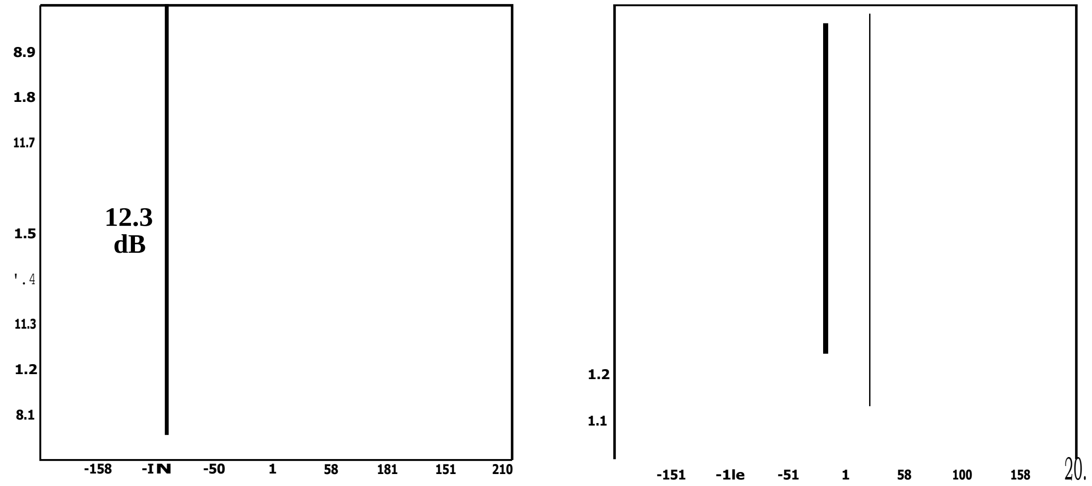

Correlation length (f) = 50m

Correlation length (= 75m

Correlation length (*f) =100m*

Correlation length (*f)* =120m

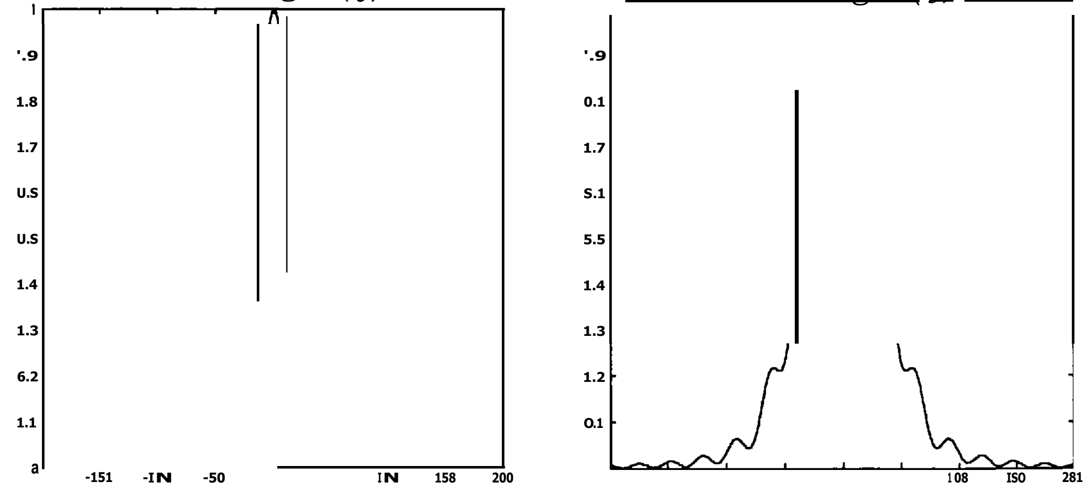

Figure 3.6- Fresnel integral representation of discrete unfocused aperture for different correlation lengths, when the optimum unfocused aperture length is 80.5 metres.

Therefore the signature of a target located at $T(x_e y_o, z_o)$ will be mapped to a centre frequency f_r:

$$p,T_o\text{-}f_r = \mathbf{0} \qquad \longrightarrow \qquad f_r = \frac{\text{il}}{hc}\,[y_o^{2}\text{-1-}\,z_o^{2}\text{-}2hz_o] \qquad ...3.28$$

From this frequency the height information of the point target can be inferred. The width of the range processed pattern gives the frequency resolution (i.e. the translation of c/2B range resolution in the frequency domain in a full-deramp altimeter) and can be calculated numerically from equation 3.27 (for $T_{(,}$= 0 and T= 20 p.sec) giving:

$$8_r = 2f_r = \frac{1}{T} \text{ .-- 50 kHz} \qquad ...3.29$$

This result is exactly what is expected from an FM radar, as previously obtained in Chapter 2.

The second bracket of equation 3.27 is the along-track signature of the point target processed by unfocused aperture synthesis. This process puts the signature of the target at the boresight of the synthetic aperture (i.e. x = 0). The width of this pattern gives the along-track resolution and can be calculated numerically from equation 3.27:

$$8_a\text{a } 2x_a\text{=} \frac{hX,}{2/\text{-}} \qquad \text{[for large N: (N-1) – NI} \qquad ...3.30$$

$$S_a = \frac{\text{800km x 8.108mm}}{\text{2 x 6.5m}} \text{ – 500m}$$

This result is what is expected from a 6.5m synthetic aperture, as previously obtained in Chapter 2, equation 2.33.

Figure 3.7 illustrates the two-dimensional processed signature of a point

x_a= along-track response, in 2m increments,

f_r= range response, in 10kHz (0.6m) increments,

li = (B = 50MHz)/(T = 201.isec)

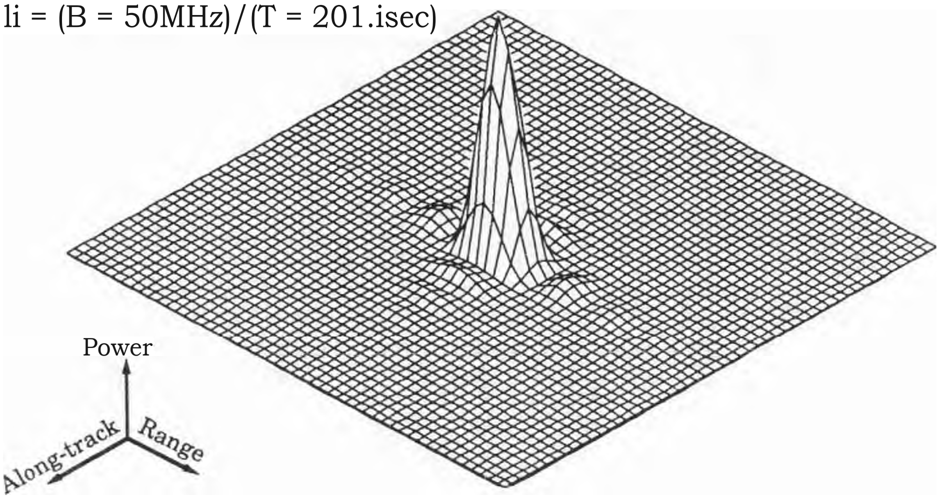

Figure 3.7- Two-dimensional signature of a point target, for a correlation process of 0.5 times the optimum unfocused aperture

x_a= along-track response, in 2m increments,

f_r= range response, in 10kHz (0.6m) increments,

li = (B = 50MHz)/(T = 201.tsec)

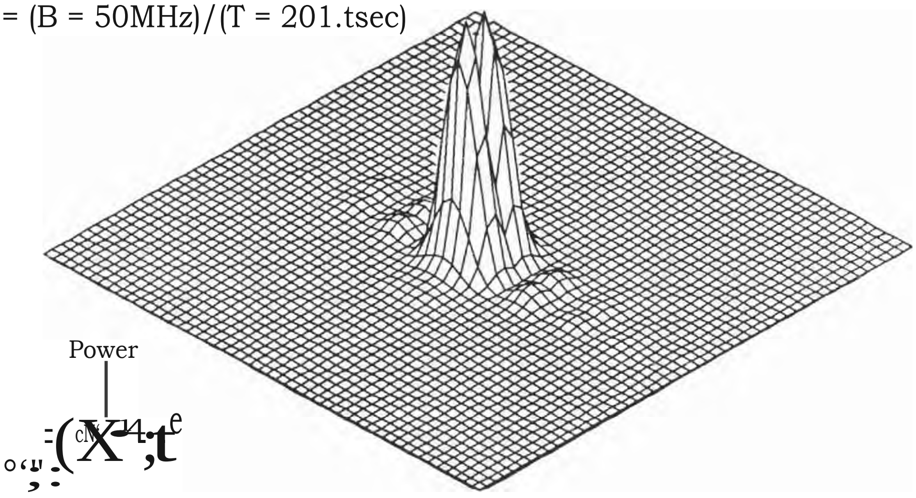

Figure 3.8- Two-dimensional signature of a point target, for a correlation process of 2 times the optimum unfocused aperture.

target using equation 3.27 which shows the [sinx/x] pattern in both range and along-track directions. For comparison, figure 3.8 shows the two-dimensional processed signature of a point target for a long unfocused aperture, where the along-track Fresnel pattern is noticeable.

At this stage it is important to mention that in the analysis of the synthetic aperture radar it is assumed that when the radar wants to transmit or receive a pulse it stops. Therefore the motion of the satellite has a fictitious stop-start pattern, stationary during the course of transmission or reception of a signal and moving in between. For a long focused synthetic aperture (for example the SEASAT SAR, having *1*= ±8km, h = 800km, v = 7000m/sec, 21, = 23.5cm and T= 33.8gsec) equation 3.7 shows that the stop-start assumption gives about 7° phase error at the edges of aperture which might cause defocusing in the along-track processing. But in a synthetic aperture altimeter, having *1*= ±3.25m, h = 800km, v = 7000m/sec, X. = 8 mm and T= 20psec, equation 3.7 shows that the stop-start assumption gives 0.05° phase error, which is insignificant in the unfocused aperture synthesis.

3.4 ***Errors in a synthetic aperture altimeter***

A satellite is an extremely stable platform, and its position and velocity can be precisely determined and controlled in order to make the effect of platform motion anomalies on the target-radar range vector, and as a consequence on the radar signal processing, insignificant. However, despite the fact that the land features which are the targets for the radar are stationary, the Earth's rotation causes a noticeable deviation in the target-radar range vector. Figure 3.9 depicts the geometry for the analysis. In this figure, arc A represents the ground-track of the satellite having an inclination angle i (i.e. the angle between the ground-track of the satellite and the equator). Point M is the equatorial crossing of ground-track of the satellite. Arc B is the meridian circle passing from point M. T is the crossing point of the boresight of the altimeter and the ground-track at any instant (i.e. the nadir point of the altimeter). Also the latitude which crosses point T is shown having an angle 7. a is the angle between this

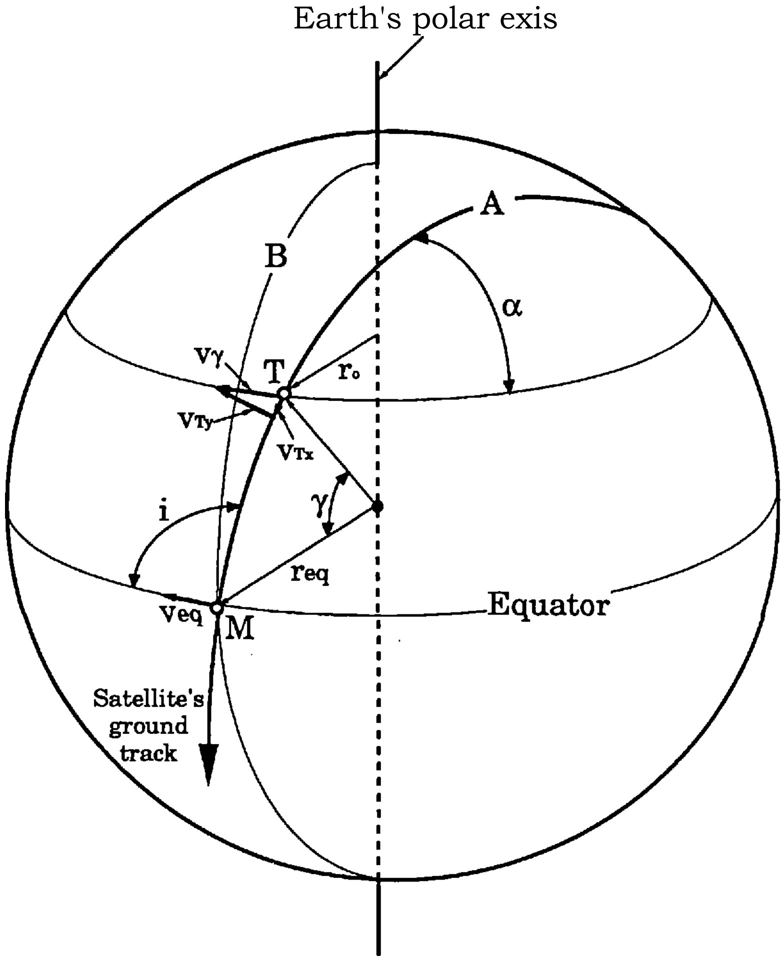

Figure 3.9- The geometry of rotating Earth and orbiting satellite.

particular latitude and the ground-track. From the geometry of the diagram it is clear that a is zero (minimum) at the maximum latitude and (n-i) at the equator (maximum) ,(Elachi, 1987):

$$o\ 5.\ a\ 5\ (Tc-i) \qquad \text{...3.31}$$

v_{eci} is the Earth's linear velocity at the equator and v_y is the linear velocity at that latitude having angle T. First, the equatorial velocity is given by:

$$V_{eq}\ \frac{2nr_{eq}}{24hour \times 3600\ sec} — 464\ m/sec\ [\ r_{eq}(earth\ radius) = 6380k]\ \text{...3.32}$$

and from the geometry, the relationship between v_{eq} and v_y is given by:

$$v_Y = v_{eq} cosy \qquad \text{...3.33}$$

Knowing the angle between the latitude and ground-track circle a, the along-track and across-track velocity components of the Earth's rotation (v_{T}. and vT_y) at point T can be calculated:

$$V'_{Tx'=}\ V_y.cosa = V_{eq}\bullet cosy.cosoc \qquad \text{...3.34}$$

$$V_{Ty} = v_7 \bullet sina = v_{eq} \bullet cosy \bullet sina \qquad \text{...3.35}$$

From the limits of a (equation 3.31), the maximum of v_{T}. and v_{Ty} occur at the equator (i.e. y = 0°), so assuming i = 98.8° (the inclination angle of the ESA polar platform 'Columbus' planned for mid 1990s), vT. and v_{Ty} are:

$$_{Tx(max)} = 464\text{-}cos(0°)\bullet cos(180°-98.8°) = 71m/sec$$

$$N^{T}_{Ty\ (maxi=} 464 \bullet \cos(0°) \bullet \sin(180° - 98.8°) = 459 m/sec$$

The satellite orbital velocity is of the order of v = 7000m/sec and the velocity vector is considered to be in the x direction. Unfocused processing is performed by summing a constant number of along-track spatial samples. So an extra along-track velocity component, vrr_x , equation 3.34, causes the synthetic aperture correlation length f to become shorter (if vi;, < 0) or longer (if vn, > 0). As a result the synthetic beam pattern and the along-track resolution are altered. As mentioned above, vm($_{max}$) occurs at the equator which is 71m/sec. But this velocity is small compared to the velocity of the satellite, v = 7000ra/sec, and it only causes 1%(max) change in the synthetic aperture length, which is negligible.

It has been explained that the boresight of the synthetic aperture beam is centred at the correlation interval and perpendicular to the motion vector of the satellite or x-axis. Any extra velocity component in the y direction, vi_{ry} equation 3.35, causes the motion vector to deviate from the x direction, which means a rotation of the boresight of the synthetic beam around the z-axis of the satellite (i.e. yaw). The rotation angle is given by:

$$0\,0/_{Ty}) = \tan^{-1}[\frac{V_{Ty}}{v}] \qquad ...3.36$$

As mentioned above, v $_{y}$($_{max}$) occurs at the equator which is 459m/sec. This velocity is large enough to rotate the synthetic beam around the z-axis of the satellite by $\tan^{-1}$[459/7000] =3.75°. This is much larger than the synthetic beam which is only [A./2/] = [8 mm/2x6.5m] = 0.624 milliradians = 0.036°. To cancel this beam rotation an appropriate phase correction can be applied to the down-converter of the altimeter receiver. This correction could also be applied during the digital signal processing by using an appropriate shift in the processed image.

Synthetic aperture processing is based upon the coherent summation of a series of spatial samples, so any frequency drift introduced by incoherency between the transmitter and the receiver causes error in the processed output. To explain this, the phase history of a target is considered from equations 3.7 and 3.5:

$$4) = \frac{27CX^{2}}{h2t.} \text{-I-} 4)_{o} = \frac{27c}{Wt.} [X-X_{o} - \frac{hv}{c}] + 01)_{o} \qquad ...3.37$$

where x is the spatial location of the radar during the receiving interval. Since the satellite moves in the along-track direction with an orbital velocity v, x can be expressed as: x = v.t, where t is the temporal location of the radar during the receiving interval. Using this expression in the phase history gives:

$$4O = \frac{2TC}{h2.} V^{2} t^{2} - \frac{4ir}{hX,} [x_{o} \pm \frac{hv}{c}] Vt - F \frac{27c}{hX} [x_{o} 4- \frac{hv}{c}]^{2} \pm 4)_{o} \qquad ...3.38$$

Now, the phase history has become a function of along-track time, and a frequency function can therefore be defined:

$$f_{Li}(t) = - \frac{1}{27C} \frac{DOW}{at} = - \frac{2^{2}t}{ha,} + \frac{2}{h?.} [x_{o} + \frac{hv}{}].v$$

or:

$$f_{D}(x=v0 = - \frac{2vx}{hX,} 4- \frac{2v}{hX,} [x_{o} -F \frac{by}{c}] 1 \cdot - \frac{2v}{hx,} [x - x_{o} - \frac{1.,}{c}]$$

$$\rightarrow \quad fp(X) = - 17, X \qquad ...3.39$$

fp(x) is considered as the Doppler frequency shift generated by the target-satellite range variation during the correlation period (figure 3.10). From this frequency function, the bandwidth of the along-track processing is given by:

$$B_{D} = f_{D}(x=+\frac{f}{2}) - f_{D}(X= -\frac{c}{2}) = \frac{2 \cdot v.I'}{X.} \qquad ...3.40$$

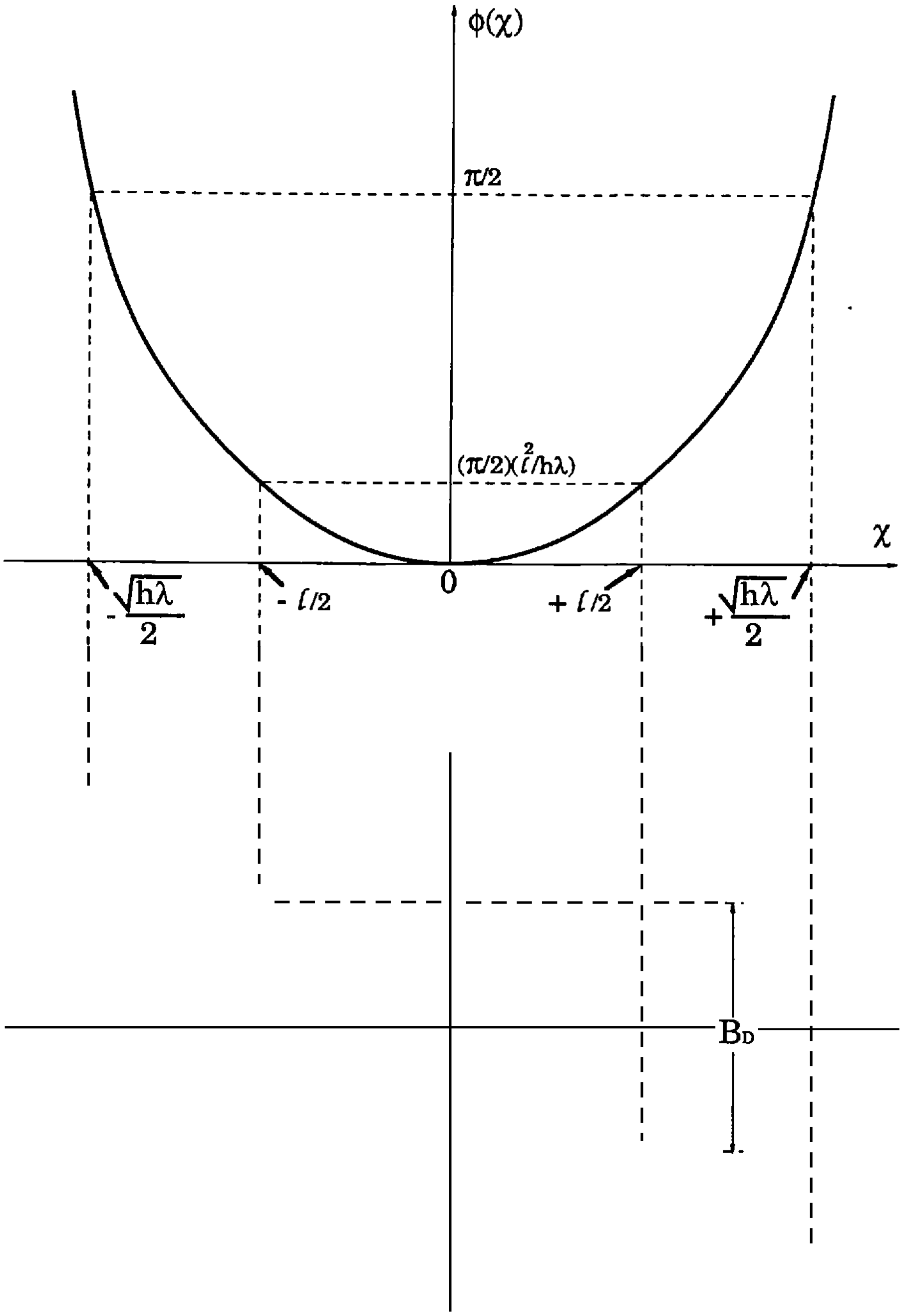

Figure 3.10- Phase history of a point target and its associated frequency variation.

At any spatial point, the radar transmits a single pulse towards the target and receives its echo after a time delay td = 2h/c. Therefore, if there is any incoherency between transmitter and receiver (i.e. frequency drift in the master reference oscillator of the radar) during the time delay td, in order to keep the backscattered signal of the target within the limits of the Doppler bandwidth, frequency drift should be a fraction e_f of the value in equation 3.40 (Ulaby et al., 1982). As a result, the allowed frequency drift is efx BD Hz around the radar carrier frequency f_0 = cik over the time td, and the frequency precision p of the reference oscillator is given by:

$$P = \frac{EfX\ B_D}{t_d x\ f_e} \quad p\_ \frac{2v f}{hA,\ .s.} \quad \frac{e p v f}{h^2} \quad \text{(Hz/Hz)/sec}$$

...3.41

For a synthetic aperture altimeter (h = 800km, v = 7000m/sec, C= 6.5m) and assuming that Ef = 1%, equation 3.41 gives a precision of $7x10^{40}$ or $7x10^{-4}$ ppm/sec for the reference oscillator. This requirement is well within the capabilities of today's drift compensated crystal oscillators (-10^{-9} ppm/sec).

3.5 *Design parameters of a synthetic aperture altimeter*

In Chapter 2, it was shown that the limits on the PRF of a synthetic aperture radar are given by:

$$\frac{2v}{az} < PRF:c. \frac{1}{2T+\frac{2}{c}(R_{f'} R_n)}$$

...3.42

The PRF upper limit is governed by the range ambiguity, as with all types of radars. The PRF lower limit is governed by the along-track ambiguity. This lower limit can also be calculated from the along-track beam pattern of the synthetic aperture altimeter using equation 3.26. From this equation the first grating lobe is found by making the argument of the sine in the

denominator equal to n :

$$\frac{27ct}{(N\text{-}1)10_{,,}} \; x_{a} \qquad \text{...3.43}$$

Using equation 3.22 in the above expression and solving for x_a gives:

$$x_{a} \_ \frac{\text{hA.-PRF}}{2v} \qquad \text{...3.44}$$

So if the main synthetic beam is centred at xa = 0, the first grating lobes are at xa=±(hX.PRF)/(2v), or in terms of an angle, their location is:

$$0_{g}= \tan\text{-}1(\quad) \quad (\text{x}\!\!\text{t} \quad \frac{h?VPRF}{2v} \; \frac{1}{F.} = \frac{X\bullet PRF}{2v} \qquad \text{...3.45}$$

On the other hand, the first nulls on either side of the real along-track beam occur at angles 9r = ±X/Daz . To attenuate the grating lobes as much as possible, they must fall outside the real beam nulls, which means that:

$$_{g} \; r \; \overrightarrow{2v} \; \doteq \overline{D_{az}} \text{ --> } \mathbf{PRF} \; \frac{2Y\text{-}}{Daz} \qquad \text{...3.46}$$

This is the same result as found previously in Chapter 2 (equation 2.31).

In the design of a radar, keeping the PRF as low as possible is important, otherwise the data handling and signal processing require very high speed hardware which in some cases may not be feasible. Therefore, the lower limit of equation 3.42 is more important. However, for a spaceborne radar, the platform velocity is very high and for a reasonably small real aperture, the calculated PRF is of the order of tens of kHz, which is still much higher than the PRF of conventional altimeters. In some cases it is possible to relax the lower bound of PRF. Figure 3.11a shows the geometry of the

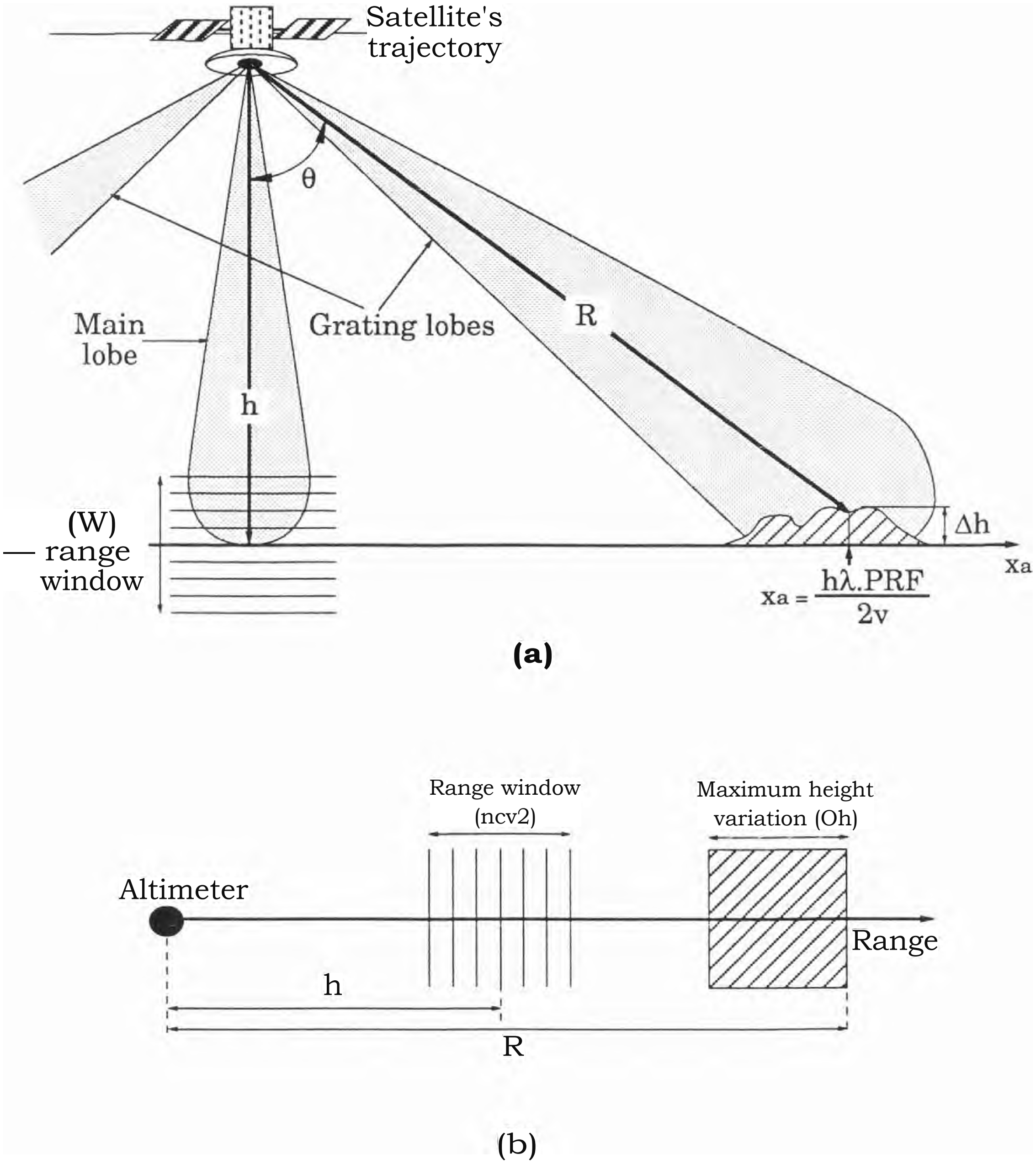

Figure 3.11- Unwanted return signals through grating lobes.

synthetic main beam and the first grating lobes. As can be seen, the range R of the region illuminated by a grating lobe is longer than the range of the main beam which is about h. So by range/time gating, the backscattered signals coming from the grating lobe area can be disregarded. From figure 3.11b, the maximum range applicable to the radar altimeter is h+(1/2)(nct/2), where (nct/2) is the length of the processing range window, and the minimum range from where a signal can be backscattered from the grating lobe is -R-Ah, where Ah is the maximum vertical extent of the surface. To avoid any coincidence between the unwanted signal and the useful data, the following inequality should be satisfied:

$$rh+\frac{nCT}{4} < [R\text{-}Ah = \backslash H\text{-}7\text{-}Ah\ h+\overset{2}{2h}$$

Using equation 3.44 in the above expression and solving for the PRF gives (Griffiths, 1987):

$$PRF \quad 2v \quad \frac{ncT+4Ah}{2h} \qquad \ldots 3.47$$

Combining equations 3.47 and 3.42, assuming **Rf** ˉ$\mathbf{R_n}$ Ah, provides:

$$\min \substack{12N1 \\ D_{az}}\ \text{an}d\ \substack{2v \\ r}\ '' \overline{\frac{nct+4Ah}{2h}}^{1} \quad PRF \quad \frac{\underline{1}}{2T+\frac{}{c}Ah} \qquad \ldots 3.48$$

So for different applications the value of PRF has to be decided by the minimum of the two quantities inside the lower limit bracket.

For very smooth terrains with a vertical extent of a few metres, range/time gating gives a PRF of a few kHz, however for land altimetry the vertical extent within the footprint is usually much higher and can easily reach hundreds of metres, and sometimes a couple of kilometres. For this case, range/time gating gives a PRF of the order of 100 kHz which is unacceptable and as a result the PRF has to be determined from equation 3.46.

Another quantity that can be inferred from equation 3.42 is the minimum along-track dimension of the real aperture, which is:

$$2v < \frac{\underline{1}}{2T+ 2Ah} \quad \text{-->} \quad D_{az} \overset{?}{\underline{4}}v[T+ Ah]$$

...3.49

Assuming Ah = 3km as the maximum vertical extent within the footprint of a radar, with T = 20i.tsec, from equation 3.49 the aperture size is D_{az} . 85cm.

The task of the synthetic aperture processor is to coherently sum a certain number of signals that have been sampled along-track. If N signals are coherently added, the resultant SNR is N times the SNR of an individual signal. Therefore the output SNR of the synthetic aperture altimeter in which the range processing is performed by the full-deramp technique, will be the SNR of the full-deramp process (equation 2.15) multiplied by the number of samples over the length *f*(equation 3.22):

$$(SNR)^{\circ}= \frac{P_tG^{22}\ O^{0} A T}{(4n)^{3}R^{4} L_skT_0F} \ \frac{r}{v} \ PRF$$

...3.50

The antenna gain G (assuming that $_{X11}$ is its efficiency) is given by:

$$G = {}_{1}\frac{47ED\ D_{az_2}\ \underline{ac}}{x}$$

...3.51

The reflecting area (the projection of the resolution cell area on a plane normal to the boresight of the antenna) is A, so if the antenna off-nadir angle is 0 and the surface slope within the footprint is a, this area will be:

$$A = 8_{8z}\;{}_{C}cos(0+ a) \qquad ...3.52$$

The maximum area A occurs when the footprint is beam-limited and the off-nadir angle and surface slope are zero. Using equations 2.2_and 2.33:

$$Amax= \overset{2}{\overset{h}{21}}.D_{ac} \qquad ...3.53$$

However the dominant mode for a satellite altimeter is the pulse limited mode. Therefore the area A is:

$$A \quad \frac{RA,ct}{4\;t.tan(9 + cc)} \qquad ...3.54$$

Also from equation 3.48,assuming that $n,$ is the along-track safety factor (Ulaby et al., 1982), the PRF is given by:

$$PRF\;11_{2}[2v/D_{az}] \qquad .\text{-}3.55$$

The slant range R can be given in terms of the nadir height h and off-nadir angle 0:

$$R = h/cos0 \qquad ...3.56$$

Using equations 3.51, 3.53, 3.54, 3.55, 3.56 in equation 3.50, the maximum and nominal output SNRs of a synthetic aperture altimeter are given by:

$$(SNR)_{max}-\frac{P_{t'}a^{o}_{max'}{}^{T'}{}^{i}l1'{}^{TI}{}^{2}_{.2'}D_{az}.D_{ac}}{4x.h^{2}.L_{S}.kT\;F} \qquad ...3.57$$

$$(\mathrm{si}_{s}\mathrm{TR})\ \_\ \frac{\underline{\mathrm{COS}}^{3}\,\underline{0}}{t\,\mathrm{an}(e+ot)}\quad\frac{P_{t}\mathrm{ou}^{t)}.\ T\ .\ {}^{2}.11_{2}.D_{az*}\,D^{2}_{ac}.C't}{87c.h^{3}\ .X.L_{s}.kT_{O}^{F}}$$

...3.58

The dynamic range of the radar, DR, is the ratio of the maximum to the minimum signal-to-noise ratios, hence from equations 3.57 and 3.58:

$$DR - \frac{(SNR)_{max}}{(SNR)_{min}}\quad\frac{\tan(e+a)\ 211A.}{-\epsilon I}\ {}_{cti}\ ac\bullet\frac{a0_{max}}{a6_{rm}}$$

...3.59

The dynamic range given in equation 3.59 determines the maximum variation in the return signal which the receiver has to cope with.

The maximum backscattering area before any range/along-track processing is the ideal beam-limited footprint $A_1 = (h^2X^2)/(D_{az}D_{ac})$• Substituting this area, and also the antenna gain from equation 3.51 in equation 2.4, and using the fact that the input $(SNR)_i = P_i/(kT_oBF)$, the maximum return power at the input of the radar receiver will be:

$$\mathbf{p}_{imax}\ \frac{P_{t}.a0_{max}\ .r_{1}^{2}\,\frac{1^*}{2}\,D_{az*}\ D_{ac}}{47t.h\ .L_{t}}$$

...3.60

where Lt is the total loss in the system excluding the receiver loss. The processing of signals in the synthetic aperture altimeter consists of Fourier transformation and correlation integration, which are linear operations, so the dynamic range at the receiver input is the same as the dynamic range of the processed output. By this argument the minimum return power at the input of the radar receiver is simply given by the maximum received power, equation 3.60, divided by the dynamic range of the signal, equation 3.59:

$$\text{mun} \quad \frac{\cos 0}{\tan(0+a)} \quad \frac{P_{t:\ \min}{}^{T1,}\ {}_{3}1D_{az}^{2}.D_{ac}^{2}.CT}{87c.h\ .X.L_t}$$

...3.61

To start the signal processing, the output of the full-deramp mixer has to be converted into its in-phase (I) and quadrature (Q) components. This conversion has two purposes. Firstly, because of the flexibility and simplicity of digital signal processing, the trend of present day signal processing is mainly towards digital methods using DSP chips and computers, and normally all coherent digital algorithms need I and Q components. Secondly, to process analogue signals by means of digital methods, they have to be sampled at a sampling rate which is at least twice the maximum frequency component of the input analogue signal (Nyquist's criterion). However, extracting in-phase and quadrature components of a signal at zero-IF frequency halves the required sampling rate without occurring any ambiguity between the negative and positive frequency components. This means slower sampling and processing, which are important advantages, (Brigham, 1989).

If the output of the full-deramp mixer is assumed to be $S = A(t).\cos[co_o t\text{-}1\text{-}0(t)]$, from figure 3.12, the signals at the outputs of I/Q converter have the following forms:

$$S_1 = A(t)(\cos[2co_o t + cp(t)] + \cos[0(t)]) \;\&\; S_2 = A(t)(\sin[2o)_o t + 1{:}0(t)] + \sin[0(t)])$$

S1 and S2 are passed through low-pass filters to eliminating the sum frequency components generated by the mixers, as well as band-limiting the baseband signals to avoid aliasing. The outputs are:

$$I = A(t)\bullet\cos[.(t)]$$

...3.62

$$Q = A(t)\bullet\sin[O(t)]$$

...3.63

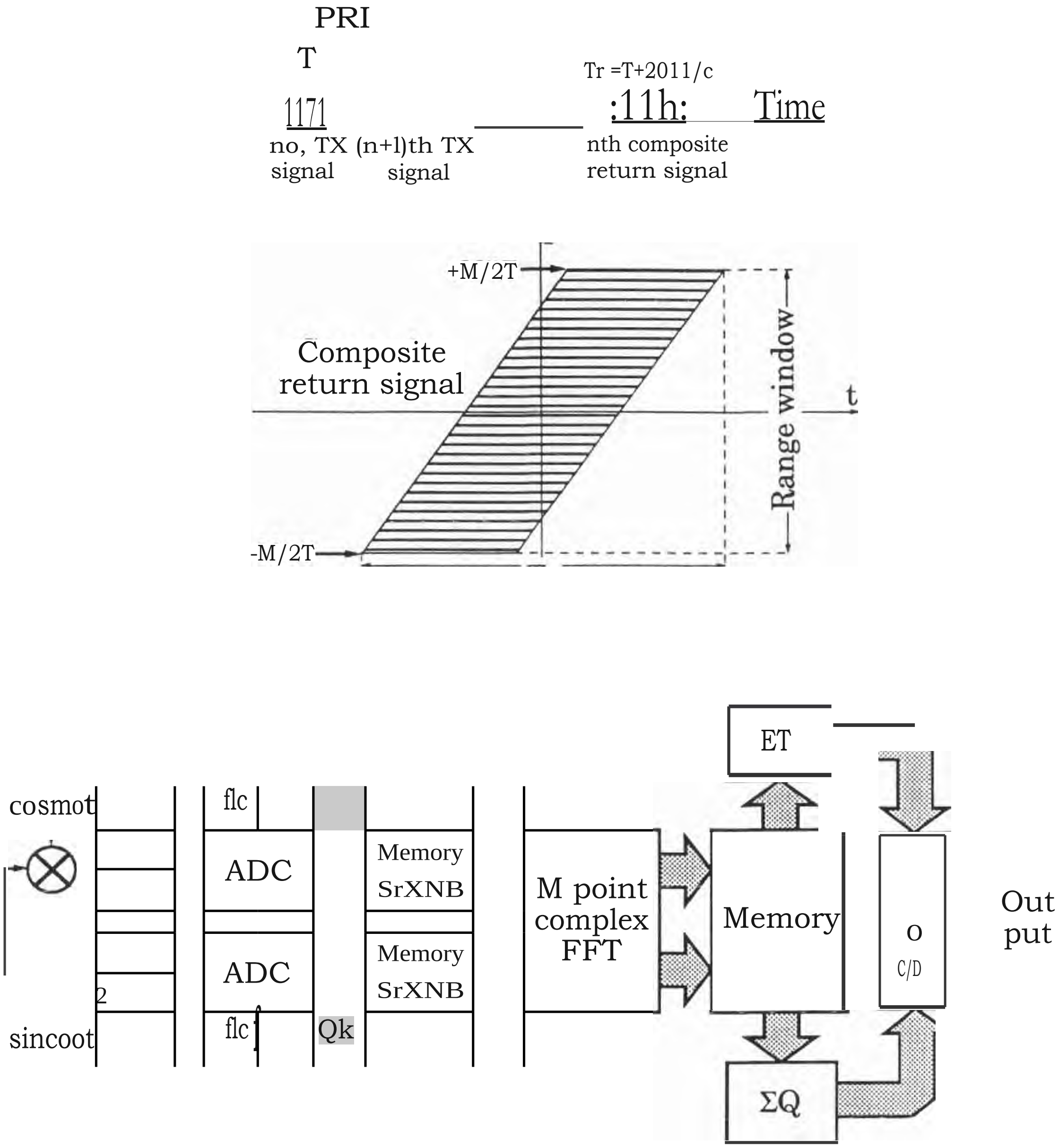

Figure 3.12- Digital signal processing.

Now the two outputs have to be sampled (at successive sampling times t_k) and digitised by analogue-to-digital converters (ADCs), which result in:

$$A(t_k)\bullet\cos[O(t_k)] \qquad \text{...3.64}$$

$$Q_k= A(t_k)\bullet\sin[O(t_k)] \qquad \text{...3.65}$$

Assuming that there are M range bins in the range processing window, the bandwidth of each range bin using the full-deramp technique is equal to the inverse of the chirp sweep width T. Therefore the bandwidth of the zero-IF range window is [±M/(2T)], and the sampling frequency (Fk) is given by:

$$F_k > \frac{M}{T} \qquad \text{...3.66}$$

The output of each ADC consists of NB bits. The number of quantised levels is 2NB, and this represents the ratio of the maximum level to the minimum level of the signal that could be sensed and digitised by the ADC. In other words the number of bits is determined by the dynamic range of the receiver:

$$(DR)_{dB}= 20\mathrm{1og}2^{NE} = 6.02\mathrm{x}\,N_B \;-3\; NB= \frac{(DR)dB}{6.02} \qquad \text{...3.67}$$

Another important parameter is the speed or bit-rate of the ADCs, which is given by:

$$R_{te}= F_k.N_B \quad \text{bit per second} \qquad \text{...3.68}$$

For each pulse sent by the radar transmitter, the radar receiver receives the backscattered signals for a period of (from figure 2.6 or figure 3.12):

$$T_r = T + \frac{2Ah}{C} \qquad \text{...3.69}$$

$\mathbf{T_r}$ is the time which has to be allocated for receiving the echoes from all the targets within the footprint. The amount of buffered samples S_r and digital binary data $\mathbf{D_r}$ obtained from the return signals of a single transmitted pulse are given by:

$$S_r = F_k \text{-} T_r \text{ samples per TX pulse, } D = R_{AOc}.T_r \text{ bits per TX pulse} \qquad \text{...3.70}$$

All the samples corresponding to an individual transmitted pulse are stored in a memory with a capacity of Dr **bits.** The next stage is Fourier transformation of these time samples for the purpose of range compression. In this case, where the signal processing is carried out by digital methods, a fast Fourier transform (FFT) is applied to the contents of all memories. In fact S_r. time samples, each of $\mathbf{N_B}$ bits, are transformed to M frequency samples, each having N_B bits via an M point FFT. Bellanger (1980) gives some expressions for the number of complex operations, CFFT needed to perform the 1/Q FFT (when S_r and M are powers of 2):

$$C_{FFT}\ 2M[0.51og_2(S_r/2) + 2] \qquad \mathbf{if\ S_r{*}\ M}$$
$$\mathbf{C_{m}{\cdot}x}\ M\log_2(M/2) \qquad \text{if } S_r = M \qquad \text{...3.71}$$

The FFT computation has to be carried out in the total time allocated for one transmitted pulse (i.e. 1/PRF), so the computation rate RFFT is given by:

$$\mathbf{R_{FFT} = C_{FFT}.PRF} \qquad \text{Computations per second} \qquad \text{...3.72}$$

After the FFT, the mth in-phase and quadrature frequency components of the nth transmitted pulse are $\mathbf{i_{nni}}$ and Q_{nmi}. It was explained that for a synthetic aperture altimeter, along-track correlation is simply performed by summing a certain number, N, of range processed along-track samples:

$$I_m = \sum_{n=1}^{N} I_{n,m} \text{ and } Q_m = \sum_{n=1}^{N} Q_{n,m} \quad \left[\text{where } N = \frac{C.PRF}{v} + 1\right] \qquad ...3.73$$

The FFT of any composite waveform must be stored in a memory, and after filling this memory with N range processed waveforms, the contents of similar frequency points belonging to successive along-track samples have to be superimposed. Therefore the capacity of this memory, MEM, and also the number of along-track computations, C_{az}, are:

$$MEM = N.M.N_B \text{ bits and } C_{az} = N.M \qquad ...3.74$$

Finally, the power in the **mth** along-track processed range bin is given by:

$$P_m = I_m^2 + Q_m^2 \qquad ...3.75$$

Other aspects of synthetic aperture altimeter signal processing will be discussed in Chapter 4 and Chapter 5.

3.6 *Scanning synthetic aperture altimeter*

The orbital velocity, v, of a satellite is dictated by its distance from the Earth's centre. Using some of the basic laws of physics (laws of gravitation, motion and centrifugal force), a simple equation can be derived for the velocity of the satellite in order to provide a stable orbit. This is given by:

$$v = r_{eq} \cdot \sqrt{\frac{g}{r_{eq} + h}} \qquad ...3.76$$

where $g = 9.8 m/sec^2$ is the acceleration of free fall. From equation 3.76, having r_{eq} = 6380km, for a satellite at h - 800km, the orbital velocity is about

7500 m/sec. Having the velocity and height of the satellite, the time T_{sat} needed by the satellite to complete one rotation around the Earth is:

$$T_{sat} - \frac{27c(r_{eq} + h)}{v} \quad \text{sec} \qquad \text{...3.77}$$

While the satellite is orbiting around the Earth, the Earth rotates with an equatorial velocity of 464 m/sec (equation 3.32). So after a certain time, the across-track swath of the satellite altimeter can cover the entire surface of the Earth. A synthetic aperture altimeter has a narrow across-track real beam, which implies a narrow swath width. Having an across-track resolution of a few hundred metres, a satellite altimeter has to spend several years, more than the lifetime of a normal satellite, in order to be able to cover and map all the Earth's surface. It would in principle be possible to use many satellite missions at the same time (each having a synthetic aperture altimeter on-board), to reduce the required mapping time, but a simpler and cheaper method can be adopted, which is to use a scanning or multiple beam synthetic aperture altimeter. If a radar altimeter can provide an across-track swath width of about 50km by means of a multiple beam antenna or mechanical/electronic across-track scanning of the beam, it will be possible to map the Earth's surface in about two months, which is quite reasonable.

A wide swath multiple beam configuration needs parallel receivers with simultaneous fixed antenna beams. Each receiver and its related beam work like a normal synthetic aperture altimeter, in a similar fashion to that explained in the previous sections.

A scanning synthetic aperture altimeter needs a single receiver, and a phased array antenna which has to be scanned across-track to generate a wide swath. A simple form of scanning is depicted in figure 3.13. As was explained earlier in this chapter, the synthetic aperture altimeter is bistatic both in time and space. To synthesise a narrow beam, the radar

transmitter sends a series of pulses, and after a relatively long delay due to the long distance between the radar and the Earth's surface, the radar receiver receives the return signals of all the transmitted signals one after another. There is thus a time gap between the transmitted and received periods. Also it is evident from figure 3.13 that as the required along-track synthetic footprint Sa is much longer than the integration length *f,* there is another time gap between the transmit/receive periods of two consecutive along-track resolution cells. These two time gaps can be used to scan the real beam of the synthetic aperture altimeter across-track. From figure 3.13, the total time gap, T_g,between two consecutive resolution cells is given by:

$$T\,g = \frac{hX,}{2(}\frac{1}{V} \qquad \text{...3.78}$$

The required time, T_{res}, for the radar to generate one synthetic beam is the transmitted time plus the received time for one synthetic beam:

$$T_{res} = \frac{2/}{V} \qquad \text{...3.79}$$

So the number of scanning steps, N_{scan}, is given by:

$$N_{scan} = \frac{\overset{T}{S}}{T_{res}} = \frac{h2,}{(2O^2} = \frac{\overset{2}{5a}}{hk} \qquad \text{...3.80}$$

Having a 500m along-track resolution, for a radar at 800km elevation and 37GHz carrier frequency, the above equations give 38 scanning steps which provides 19km total swath width. It is also possible to increase the number of scanning steps by multiple linear phase weightings of the received samples in order to generate a series of along-track synthetic beams rather than only one. Figure 3.14 depicts the geometry, including a target at the centre of the along-track real beam. In a synthetic aperture altimeter, the along-track real beam can intercept any individual target for a time Treat ,

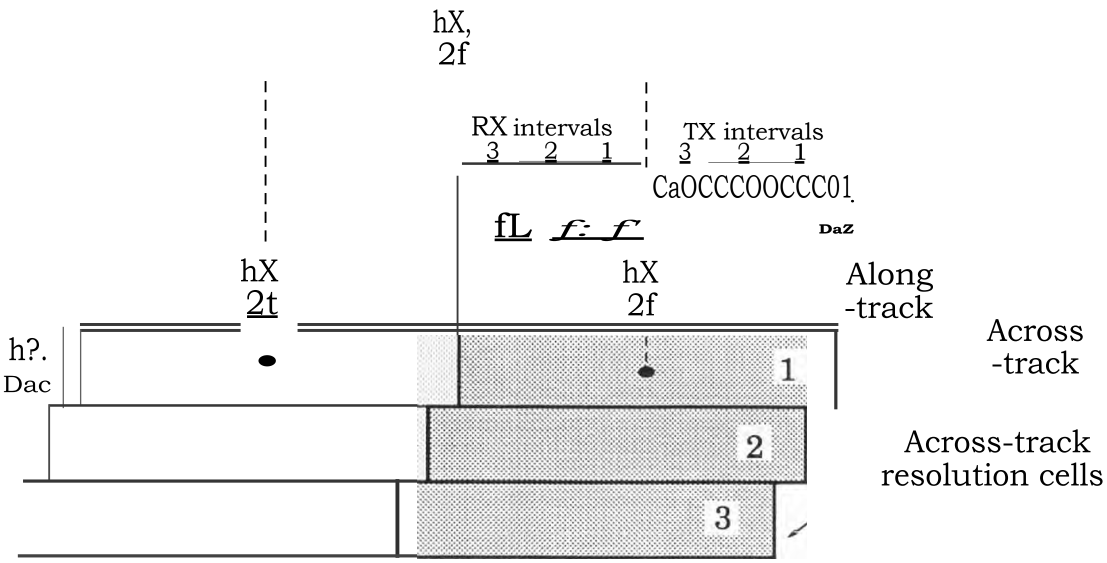

Figure 3.13- Across-track real beam scanning.

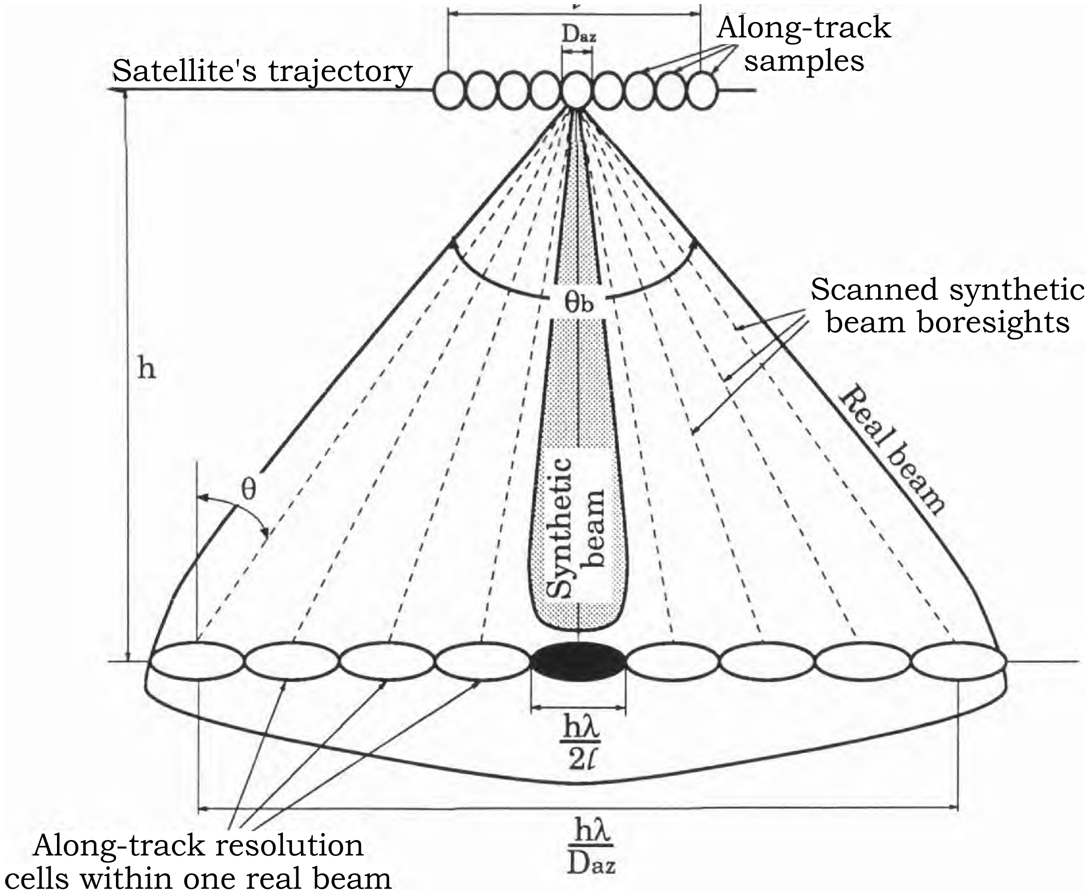

Figure 3.14- Along-track synthetic beam scanning.

which is determined by the real aperture D_{az} and the satellite velocity v. This time is given by:

$$T_{real}\quad \frac{RI}{D_{az}} \bullet \frac{1}{v}$$

...3.81

The radar transmits and receives a series of pulses for a period of T_{res} given by equation 3.79, and as the received samples obtained during this time include the returns from all targets within the real beam of the antenna, by a method which may be called "synthetic phased array processing", the synthetic beam can be centred at any individual along-track resolution cell [N.B. signal processing of the synthetic phased array will be discussed in Chapter 5]. In fact, by this method the parabolic phase variation across the unfocused synthetic aperture is approximated by a linear phase variation applied to along-track samples. To find the condition for the validity of this argument, the worst case geometry is considered, when the samples are used to generate a synthetic beam on a resolution cell at the edge of the real beam. In this situation the maximum two-way parabolic phase excursion across the synthetic aperture is given by:

$$^{A4)}1 = {}'X^{I.}\,[N \quad h^2 + \left(21\,\overset{IA,\ ,2\_}{,\text{--}}\right)_{az} \quad - h^2\left(hX \frac{}{2D_{az}}\right) -\text{''}\ f\backslash^2 \quad -\ h)\ \frac{27c}{}\left[\frac{lar}{\mathbf{D_{az}}}\right] - t^{,-2}1$$

...3.82

Applying synthetic linear phased array processing means that the target is assumed to be in the far-field of the array. Therefore the maximum two-way linear phase excursion across the synthetic array is given by:

$$2\quad \frac{4 7c}{} \bullet f\bullet\sin\ \overset{I}{\tan}\quad \frac{h2t.}{2D}\ \bullet\ h \quad = \frac{27}{L_{iaz}}\, r,^{r}f$$

...3.83

To have unfocused processing, the remaining two-way phase error after

linear phase processing which is caused by the phase curvature (i.e. 02-OD should be less than, say, 7c/2, therefore from expressions 3.82 and 3.83:

$$\mathrm{AO}_2 - 4_1{}^{53}2 \quad -) \qquad 4,F:x \qquad \text{...3.84}$$

This result is just what is expected from an unfocused SAR. The appearance of the factor 1/2 in this equation is because the synthetic aperture is squinted and the maximum phase excursion is the two-way phase difference at the two ends of the array.

The above discussion shows that the required time to sample and generate all along-track synthetic beams within any individual along-track real beam is equal to T_{res} (equation 3.79). Therefore the ratio of the available time for the real beam to sweep one footprint (i.e. T_{reat} given in equation 3.81) and the time T_{res}, provides the maximum number of across-track scans N_{scar},

$$N_{scan} \quad \frac{T_{r\ al}}{T_{res}} \quad \frac{112}{2\overline{TT}).} \quad \frac{8.}{D_{az}} \qquad \text{...3.85}$$

Having a 500m along-track resolution and 1.3m real aperture size, the above equations give 384 scanning steps and a 192km total swath width.

It is important to note that as in a scanning synthetic aperture altimeter, along with scanning the real beam electronically across-track, the synthetic beam is scanned along-track by means of signal processing. It is thus likely that a grating lobe enters in the along-track real footprint. Therefore to avoid reception of any unwanted echoes from the surface through a grating lobe, the PRF has to be high enough to increase the distance of the grating lobes from the main synthetic beam. Moreover, the real antenna pattern has to provide very low sidelobes to keep the grating lobes as low as possible.

Coherent processing of the received signals from a surface containing many independent, randomly spaced scatterers results a pattern which shows a variation in the processed detected level per pixel. This is known as speckle noise (as explained in Appendix 2). In SAR, speckle noise can be reduced by using independent data sets to estimate the same area of the terrain. When only one data set is available, multilook processing can be applied by dividing the available synthetic aperture into subapertures which generate independent looks at the target area, based on the angular position of the targets (Fitch, 1988). Dividing the available aperture *(into* N subapertures means reducing the coherent integration length by a factor of Nand widening the synthetic beam by the same factor, which results in a corresponding loss of resolution. Therefore, to obtain the same resolution as a single synthetic beam, the time required for the radar to observe one real **footprint** T_{res}, has to be increased to wtimes the time needed to sample one synthetic beam:

$$T_{res'}\ N.^{2t} \qquad \text{...3.86}$$

Equation 3.85 provides the number of across-track scanning steps N_{scan} for the single look situation. For the multilook situation, the number of scan steps is the ratio of the real beam time T_{real} (equation 3.81) and T_{res} (equation 3.86):

$$N_{scan} = \overset{8}{ND}{}^{a}_{az} \qquad \text{...3.87}$$

From this equation the maximum achievable across-track swath width is given by:

$$SW = N_{scan} . 8_c \qquad \text{...3.88}$$

3.7 ***Example of a scanning synthetic aperture altimeter***

In this section a numerical example of a scanning synthetic aperture altimeter is given and during the calculations a number of new issues are presented and discussed. The initial assumptions are as follows:

Satellite altitude: h = 800km
Carrier frequency: f = 37GHz (i.e. carrier wavelength A, = 8 mm)
Transmitted pulsewidth: T = 20gsec
Along-track resolution: S_a = 500m
Across-track resolution: S_c = 500m
Range (height) resolution: S_r - 3m

On the basis of the above quantities the main design parameters of the altimeter are calculated. First from equation 3.76, the velocity of the satellite for a stable orbit is: v = 7450m/sec.

From equation 2.2 the across-track antenna size is: $\mathbf{D_{ac}}$ = 13m. This is rather a long antenna but not unusual, since for example the SEASAT SAR and SIR-B SAR both had 10.7mx 2.2m antennas, and all the planned spaceborne SAR systems for the last decade of the twentieth century have large antenna structures, even up to 18mx 4m (Elachi, 1987).

From equation 2.33 the synthetic aperture integration length is: C= 6.5m. From equation 2.23, the maximum unfocused integration length $_4$ (when the pixel is centred at the transmit/receive interval) is: G_u = 80.5m, and from equation 3.84, the maximum unfocused integration length f_a (when the pixel is not centred and the synthetic beam is directed to it by means of signal processing) is: G_u = 40.25m. Hence in any case (C= 6.5m) < C_u and for the along-track processing there is no need for phase compensation.

The altimeter transmits linear chirp pulses and the range processing is done by the full-deramp technique. Having the range resolution, the bandwidth of the chirp (from equation 2.14) is: B = 50MHz. Also as the length of transmitted chirp is 20.tsec, from equation 3.29 the bandwidth of each range bin is: BW = 50kHz.

It is assumed that the maximum height variation MI within a moderate antenna footprint (i.e. less than say 5km along-track and 500m across-track) is less than a few kilometres, say 3-4km. Thus from equation 3.49, the length of the antenna along-track should be more than: D.> 1.2m. Also from equation 3.48, the limits of the PRF are given by: 12400Hz < PRF < 16700Hz. For the time being, the PRF is assumed to be 15000Hz, and D. to be 1.5m. This provides an along-track safety factor of $1_2 = 1.5$ (equation 3.55): D. = 1.5m, PRF = 15000Hz ($1_2 = 1.5$).

From equation 3.87, assuming $N.$ 4, the maximum across-track scanning steps are: $N_{scan} = 83$, and from equation 3.88, the maximum swath for the scanning altimeter is: SW = 41.5km = ±20.75km. This means ±1.5° scanning or off-nadir angle for the altimeter and the required time for global coverage is about ten weeks. Figure 3.15 illustrates the scanning scheme and swath geometry of the synthetic aperture scanning altimeter.

The required stability of the reference oscillator of the altimeter is given by equation 3.41, and for this particular example, assuming E f = 1%, it gives:
$p = 7.5\text{x}10^{40}$ (Hz/Hz)/sec = $7.5\text{x}10^{-4}$ ppm/sec which is easy to achieve.

From equation 3.22, the number of samples for processing one synthetic beam is: N = 14, and the number of samples for one real beam and for $N.$ 4 is: N = 53.

From equation 3.51 (assuming 50% antenna efficiency, and 3dB loss due to the phased array components and waveguides) the antenna gain is:
G = 60dB. also the total system loss is assumed to be: L. = 6dB.

The noise figure of the receiver is assumed to be: F = 2dB (or equivalently, the noise temperature of the receiver is: F = 1+ (T/290) --> T = 170 Kelvin. Apart from parametric amplifiers, nowadays HEMT (high-electron mobility transistor) amplifiers can provide this noise figure (and even lower values) at millimetre-wave frequencies (Mishra et al., 1989; Bierman, 1988; Jabra, 1988).

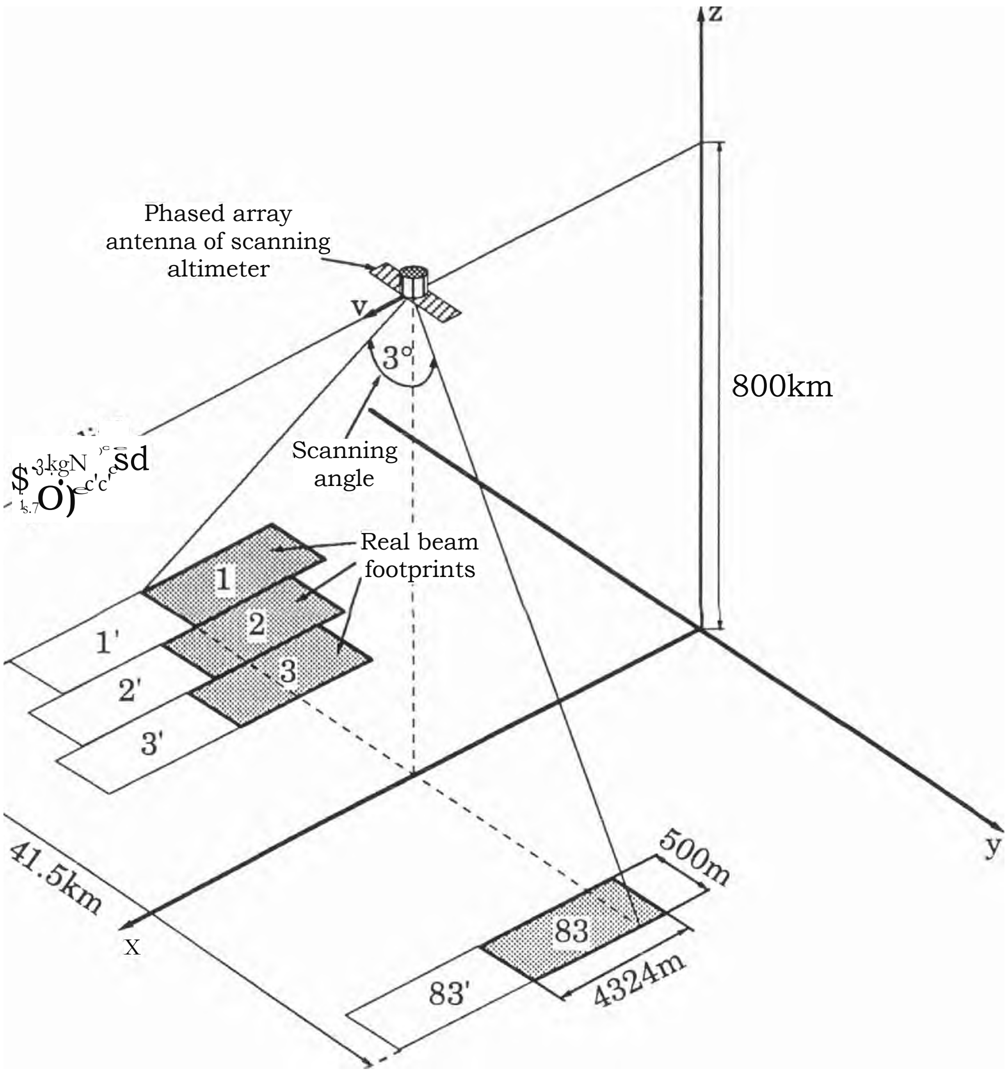

Figure 3.15- Geometry of scanning altimeter.

The backscatter coefficient range of interest, at 37GHz for different terrains, is assumed to be: -10dB < a°< +10dB, and on the assumption of a maximum height variation of Ah = 3000m in a 5000m footprint, the maximum surface slope will be a - 30°.

Assuming an SNR of 20dB for one range bin, from equation 3.58 the required transmitted peak power is : P_t= 183Watts (52.6dBm), and from equation 3.57, the maximum SNR of one range bin is: (SNR)max = 62dB. From equation 3.59, the receiver dynamic range is: DR = 42dB, and from equations 3.60 and 3.61 the maximum and minimum received powers, assuming a total loss of L_t = 3dB, excluding the loss of receiver input, are: $P_{i.}$ = -61.4dBm, and P_{iniin} = -103.4dBm.

Having a dynamic range of 42dB, the number of digital bits is given by equation 3.67: NB = 7bits. Also having a range resolution of S_r = 3m and height variation of oh = 3000 means that there are 1000 range bins within the processing range window (i.e. M = 1000). Therefore from equation 3.66 the the baseband In-phase and quadrature sampling rate is:
Fk = 50MHz.

The time allocated for receiving all the echoes of one transmitted pulse is given by equation 3.69: T_r = 401asec. From equation 3.70, the number of samples per transmitted pulse and the required memory before FFT processing are: $S_{i.}$ = 2000 samples/TX pulse and D_r = 14000 bits/TX pulse.

From equation 3.71, the total number of operations needed to perform the FFT for one transmitted pulse is (assuming $S_{i.}$ = 2048 and M = 1024 which are powers of 2): CFFT = 15000 operations. These operations have to be carried out in one PRI, so from equation 3.72 the computation rate inside FFT processor is: $R_{FFT} = 200\text{x}10^6$ operations per second. The present state of the art in high speed digital technology can provide 1024-point FFT processing in less than 40gsec (Curtis and Rees-Roberts, 1989). This is less than the required FFT time, which is equal to PRI = 661.tsec. Therefore the real-time range processing can be performed on-board the satellite without any particular difficult ,(but subject to power consumption limitations).

After this stage there is a memory which stores the FFT processor outputs for N along-track samples (N = 53) , so from equation 3.74 the capacity of this memory is: MEM = 371kbits. To generate a single synthetic beam, from equation 3.74, the number of required operations is: C_{az} = 53000 operations.

For the scanning synthetic aperture altimeter under investigation, the total number of scanning steps is N_{acan} = 333, and these have to be completed in the time T_{real} required for the radar to move by one real beam, as given in equation 3.81. Therefore there have to be C_{az}x N_{scan} computations to generate all the synthetic beams within the time Treat = 0.58sec. This means $17.6x10^6$ operations with a rate of $30.4x10^6$ operations per second.

At this stage, after the range/along-track processing, an area of **(hX/Daz) x SW = $1.8x10^8m^2$** is mapped, and this is composed of 500mx500m pixels each having 1000 range bins and 7 bits per range bin. This means 5 megabits of data storage is required for any $1.8x10^8m^2$ area. The total area of land and polar ice sheets is about 150 million square kilometres, which means that global mapping of the Earth's surface excluding the oceans needs $4x10^{12}$ bits of data. This amount of data (or a part of it) can be stored temporarily and when the satellite comes within range of an earth station, the stored data are transmitted to that station through a down-link (telemetry) channel. Since there are a number of earth stations, it is not necessary to store all $4x10^{12}$ bits in the satellite. Data recording can be performed on erasable optical disks which can store large amounts of data. Today, the state of the art in optical disk technology is about 10^{10} bits (i.e. 10 gigabits) recording capacity, but the trend of development shows that in the near future this will reach to more than $6x10^{10}$ (i.e. 60 gigabits) on one $5^1/4$-in optical disk (Freese, 1988). Therefore a digital data recorder equipped with ten to fifty erasable optical disks can provide enough space to store the acquired topographic data for the period that the satellite cannot see an earth station. Also, a high recording data rate is feasible; as mentioned above 5 megabits of data corresponds to a $1.8x10^8m^2$ area and the time related to this area is the time of one real beam (equation 3.81) which is 0.58sec. Hence the data rate is less than 8.6 megabits/sec. At the present time the data rate of optical disk recorders is more than 5 megabits/sec and in the near future it will reach 500 megabits/sec (Freese, 1988).

To avoid huge amounts of on-board data processing which need very high speed hardware as well as a lot of electric power consumption, it would be possible to record the raw data on optical disks. As has been calculated, there are 14000 bits of data per received waveform and 53 waveforms to process one synthetic beam. There are also 83 scanning steps in the time Treat . There are thus $6x10^{7}$ bits per $1.8x10^{8}m^{2}$area. To obtain global mapping, 50 gigabits of memory is hence required. This amount of memory can be divided into several sections depending on the number of times that the satellite can transmit the raw data to different earth stations.
[N.B. recently it has been announced that, the state of the art in optical storage technology in June 1989 was $8x10^{12}$ bits on a single optical tape (Abbott, 1989). This huge capacity is twice the required memory to store the processed global mapping data (i.e. $4x10^{12}$ bits). Also, only six optical tapes would be needed to record the unprocessed (raw) global topographic data (i.e. $50x10^{12}$ bits). Therefore, different options are feasible for storing and transferring the obtained information to the earth stations.]

As depicted in figure 3.16, the radar altimeter transmits chirp signals with a 50MHz bandwidth and 2011sec duration, with PRF = 15000 Hz, and the receiver has to collect all the echoes for about 40psec (equation 3.69). This 40p.sec received waveform is mixed with a local oscillator signal which has a chirp slope equal to the transmitted pulse chirp slope. If the time length of the local oscillator chirp is the same as transmitted chirp (i.e. 201.1.sec), it will not be able to cover about half of the received composite waveform and this causes serious degradation in the range resolution. Hence the time length and bandwidth of the local oscillator signal are:

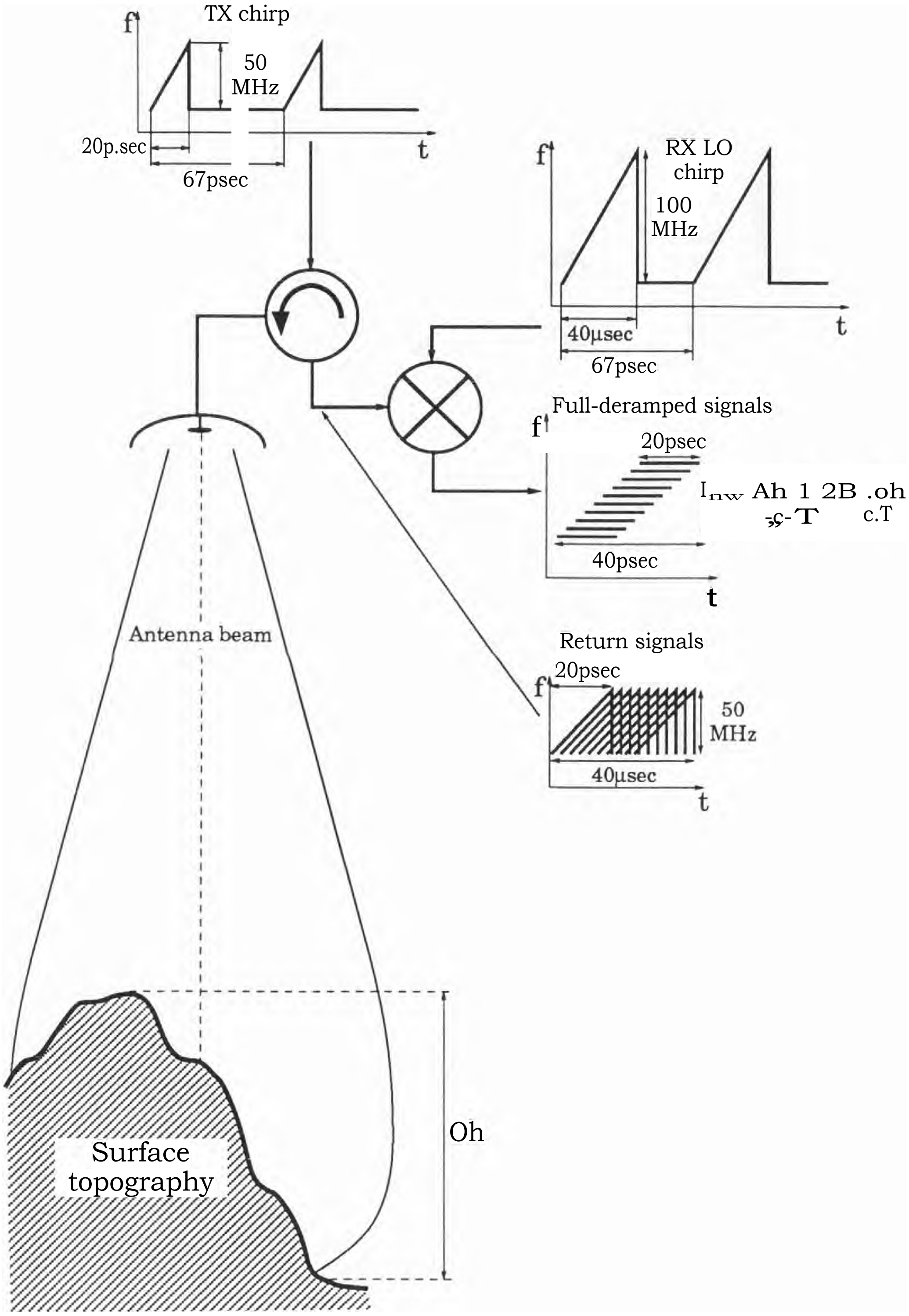

Figure 3.16- Waveforms of the different sections of the altimeter.

$$T\text{in} = T_{r} = T + 2.? \qquad \text{and} \qquad B_{LO} \cdot B.TL0 \qquad ...3.89$$

This means that the local oscillator should generate a chirp signal of 100MHz bandwidth in 401.bsec in order to cover the entire received waveform.

When the synthetic beam is scanned along-track by means of signal processing, grating lobes are also scanned and there is the danger of having a grating lobe inside the real beam. To avoid this, the PRF has to be high enough and also the antenna real pattern has to provide sufficient low sidelobes. Figure 3.17 shows the situation for the current example. From equation 3.44, the first grating lobes are at: x = ±6530m. Also the nulls of the real beam are at:

$$x''' + \frac{IA}{D_{az}} + \frac{8x\,10^{5}\,x0.008108}{1.5} — \pm 4324\text{m}$$

The maximum along-track scanning is when the synthetic beam reaches the edges of the real beamwidth, which is at (x = +4324/2 = +2162m) and at (-2162m). In this situation the negative grating lobe also moves by this amount to x = -6530m+2162m = -4368m. As can be seen, this grating lobe is still outside the real beam null, which is at -4324m. Therefore there is no problem due to the along-track synthetic beam scanning and the only condition is to provide sufficient real beam sidelobe rejection, of say -30dB.

When the real beam of the altimeter is scanned across-track to obtain a wide swath, it encounters a curved Earth. Figure 3.18 depicts the geometry, from which the actual across-track resolution and swath for the maximum off-nadir angle can be calculated. For this purpose the basic expressions are:

$$\frac{\text{sine}}{r_{eq}} \equiv \frac{}{h+r_{eq}} \qquad \text{and} \qquad 0\text{i} = {}^{0}{+}{}^{7}1$$

$$\frac{\sin(e+e_{b})}{r_{eq}} - \frac{\sin 0_{2}}{h+r_{eq}} \qquad \text{and } 0_{2} = {}^{1}3+0_{b}+72$$

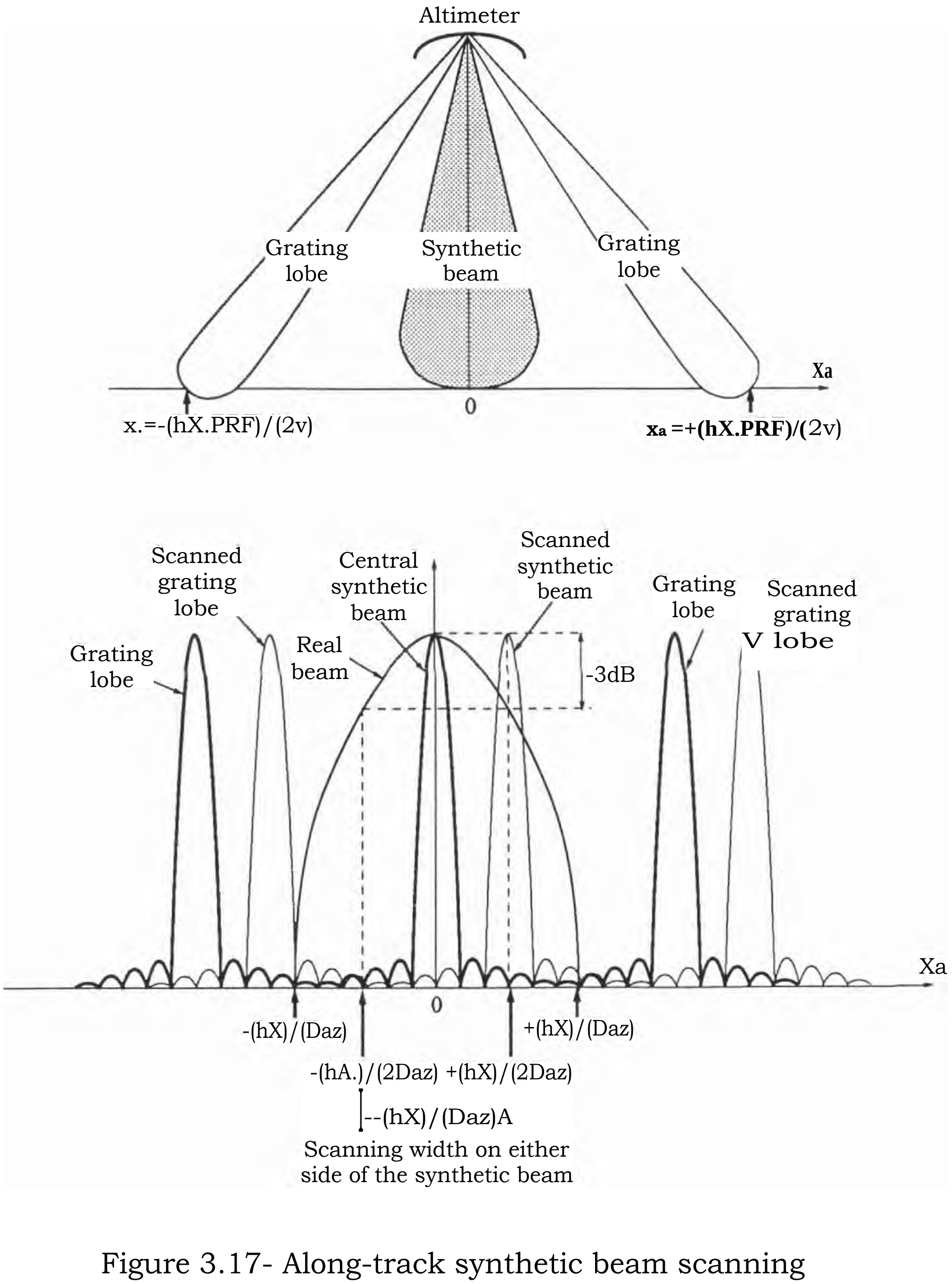

Figure 3.17- Along-track synthetic beam scanning

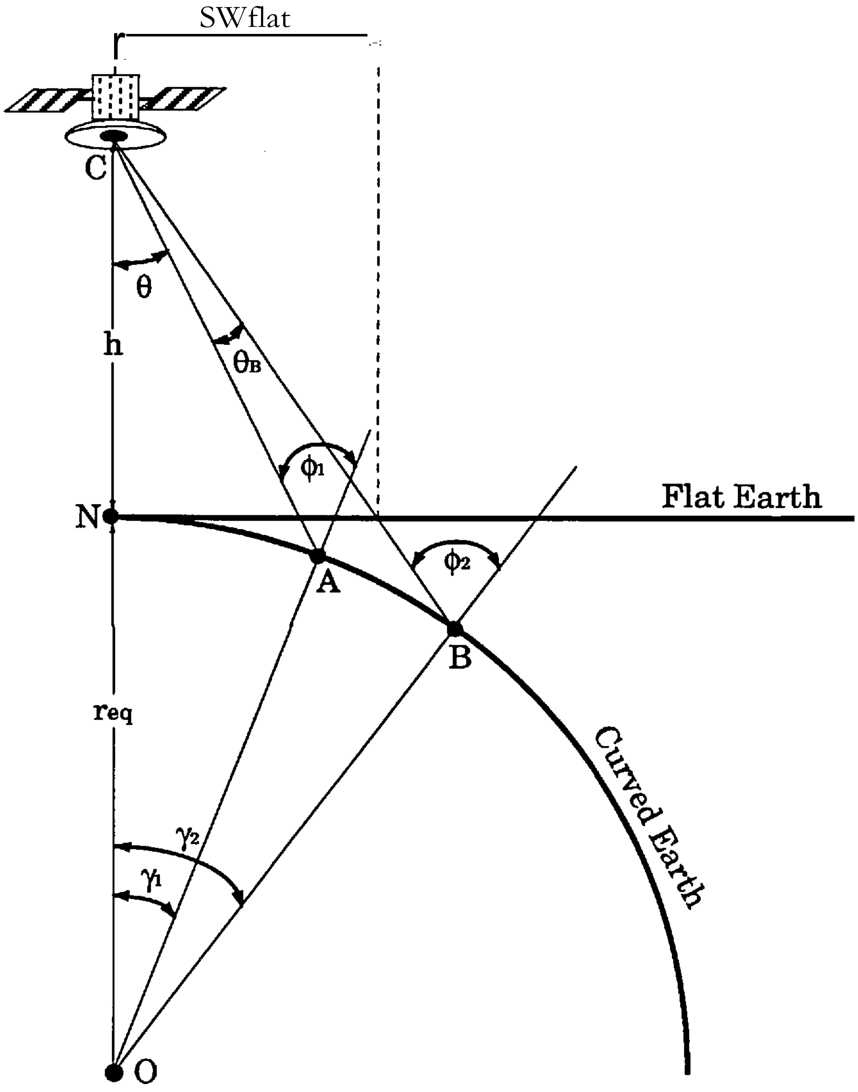

Figure 3.18- Geometry of swath operation over the curved Earth.

where 0 is the off-nadir angle of the across-track beam inner edge, and Ob is the across-track beamwidth. From these expressions the worst case across-track resolution 8,(curved) and swath SW(curved) are given by:

$$8_c(\text{curved}) = r_{eq} . \text{ sm } \frac{h+r}{eq}\text{eq} \sin(0+0_b)\mathbf{)1} -\text{si}\mathbf{n1} \frac{h+r_e}{eq}\text{q sine} -0_b \quad \text{Radian} \qquad ...3.90$$

$$SW(\text{curved}) = r_{eq} . \left| \sin \left| \frac{h+r_e}{eq}\text{qsin}(0+0_b) \right| -0 -0_b \right|_{\text{Radian}} \qquad ...3.91$$

Comparing **the results of the above equations with the results pertaining to a flat Earth shows a 10cm difference in across-track resolution and** 3m **difference in the total swath width, which are negligible. Using a similar procedure, the off-nadir range, r, to the last across-track pixel over the curved Earth can also be calculated:**

$$r = \frac{r}{\text{sine}}\text{q} \cdot \text{sin} \left| \text{sin}^{4} \left| \frac{h+r_e}{eq}\text{a sine} \right| - 0 \right|$$

Comparing the result of the above equation, which provides the true range, and the flat Earth range, gives rise to a difference of more than 34m. A similar situation exists for the along-track pixels.

Altimetric measurements with high spatial (horizontal) resolution will not provide any useful information, unless the acquired data are related to actual illuminated footprints. In other words, it should be exactly known which part of the terrain has been really observed by the remote sensing probe (i.e. altimeter). Having completed this stage, it is then possible to generate an accurate topographic map of the area under investigation. The

footprint track of the altimeter antenna on-board the satellite, while it is orbiting the Earth, is governed by the attitude dynamics of the satellite including gravitational force, magnetic field, gravitational irregularities, Solar and Lunar gravities, pressure due to solar wind and radiation, atmospheric drag, micrometeorite impact and even the torques caused by the moving parts within the satellite. The required spatial resolution for topographic mapping of land and polar ice sheets is 500mx500m, which is equivalent to a beamwidth of 0.036° both in along-track and across-track directions. Hence, despite all the above-mentioned phenomena which affect the dynamics of satellite, at any instant the orientation of all three axes (x,y,z), (i.e. attitude), of the satellite relative to a reference coordinate system (for example the geocentric coordinate system) should be determined and controlled to a precision of the order of 0.036°.

In addition to what was explained above, there is another factor which further restricts the precision of satellite attitude determination. A radar altimeter can measure the range of a target with a resolution of $\mathbf{S_r}$ (range resolution of the radar). Assuming that at an off-nadir angle 0, it is possible to measure the mean range Rof the footprint with a resolution of S_r, to estimate the mean height *51;* of the footprint, the mean range has to be projected on the local vertical of the footprint (figure 3.19):

$$91 = Rcose \qquad \ldots 3.92$$

This expression shows that the estimate of Jldepends on the measurement of Rand 0 (Griffiths et al., 1985). To estimate a quantity z which is a function of two measurements x and y (i.e. z = f(x,y)), the estimation error can be expressed in terms of errors in measuring x and y via the propagation of errors (Bevington, 1964):

$$a_z^2 = a_z^2 . [\, af(x,y)^{\,2} + \overset{2}{a}_y \mathbf{i} \, af(x,y) \,]^2 \qquad \ldots 3.93$$

where a_z^2 is the variance of z (i.e. a_z is the error in extracting z from x and

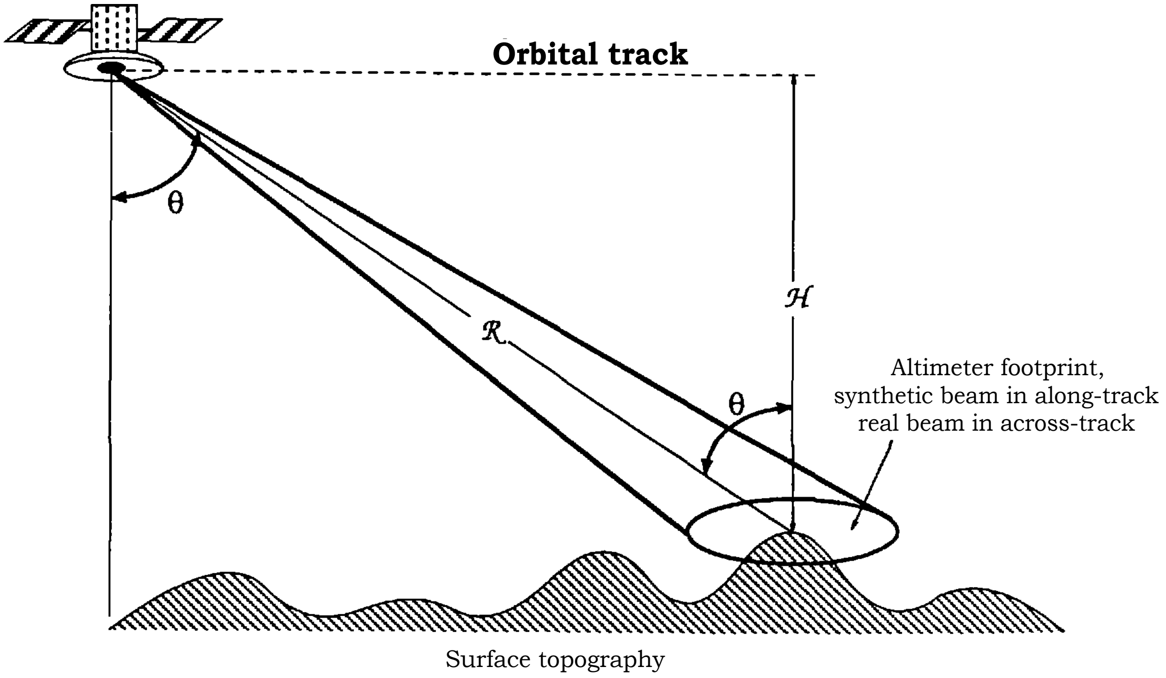

Figure 3.19- Extracting height from range information.

y), 6_x^2 and 6_y^2 are the variances of the individual measurements of x and y, and the two measurements are assumed to be uncorrelated. Applying equation 3.93 to equation 3.92 results in:

$$a^2_{91-} - a^2_{R}.\cos^2 0 + a^2_e \mathrm{igome}]^2 \qquad ...3.94$$

For the current example, the worst mean height error occurs at the maximum scanning angle (0 = 1.5°). Having $a_{9c} = S_r$ = 3m, if it is assumed that when mean range measurement is translated to the mean height a precision loss of 50% is acceptable (i.e. a_H= 4.5m), from equation 3.94 the acceptable error in the off-nadir angle a_o will be:

$$4.5^2 = 3^2 \text{ x } \cos^2(1.5°) + a_0^2 \text{x } [8\text{x}10^5 \text{x } \sin(1.5°)]^2$$

$$—) \quad a_e = 1.6\text{x}10^{-4} \text{ Radians} = 33 \text{ arcseconds}$$

Therefore, the attitude of the satellite carrying the altimeter has to be stabilised and controlled with a 33 arcsec angular precision. With this requirement in mind, in this part of section 3.6, the problem of attitude determination is discussed.

The knowledge needed to establish three-axial orientation of the satellite with respect to a desired coordinate system is obtained by a combination of instruments on-board the satellite, known as attitude sensors (Berlin, 1988). The outputs of these sensors are processed to provide the instantaneous attitude of the platform and the errors which need to be compensated. The error signals are then injected to the attitude correction section to adjust all three axes of the platform in order to reach a desired attitude with respect to the reference coordinate system. Various attitude sensors are used in satellites, such as gyroscopes, magnetometers, Sun sensors, Earth sensors and star sensors. However, for permanent high precision attitude determination and control, to the degree which is required in high spatial

resolution altimetry only the last one is particularly suitable.

Figure 3.20a shows the basic block diagram of a star tracker, which is comprised of the following sections: (i) an optical system, which collects and focuses light on the photosensor and reduces stray light from other bright sources; (ii) the photosensor, which transforms light information into electrical signals; (iii) the signal processor, which receives signals corresponding to bright sources and carries out all the computations and decision making. These provide some feedback data for the optical system and photosensor sections and some output data to be used for attitude determination and control.

To find a known reference coordinate, the stars to be tracked must be identified. The most useful signatures of stars are the magnitude of their brightness, their emitting spectra, fixed or predictable angular relationships between stars, and predictable angular relationships relative to the observer. Of these four properties, the last two are the most useful because they are unique. For example, in astronomy the angular separation of bright stars are precisely known and they can be stored, as a lookup table, in the star tracker processor. Now, if the angle between two of the bright stars which can be seen by the star tracker is measured, and the result is correlated with the contents of the lookup table, the star pair can be identified as stars A and B. The question will be which star is A and which B? To resolve this ambiguity, if the angle measurement is repeated for star A and a third star, by correlating the angular separation of this second star pair with the contents of the lookup table and the feedback from the result of the first star pair, all three stars can be individually identified, because only star A was common to both measurements. Knowing the location of three stars establishes a known reference coordinate frame. There are enough bright stars in the celestial sphere and their distribution is uniform, in order to make practical the use of continuous star tracking. It has to be noted that as the satellite is orbiting the Earth outside the atmosphere, the star tracker can detect stars during day or night, since scattered sunlight does not enter its field of view (Quasius and McCanless, 1966).

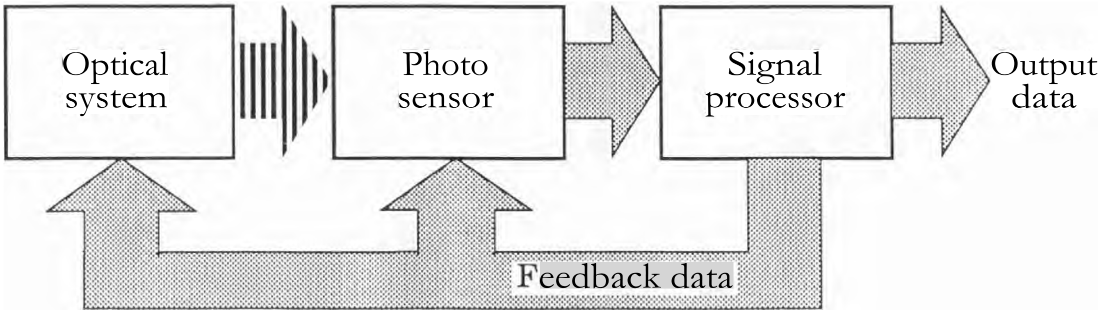

Figure 3.20a- General block diagram of a star tracker.

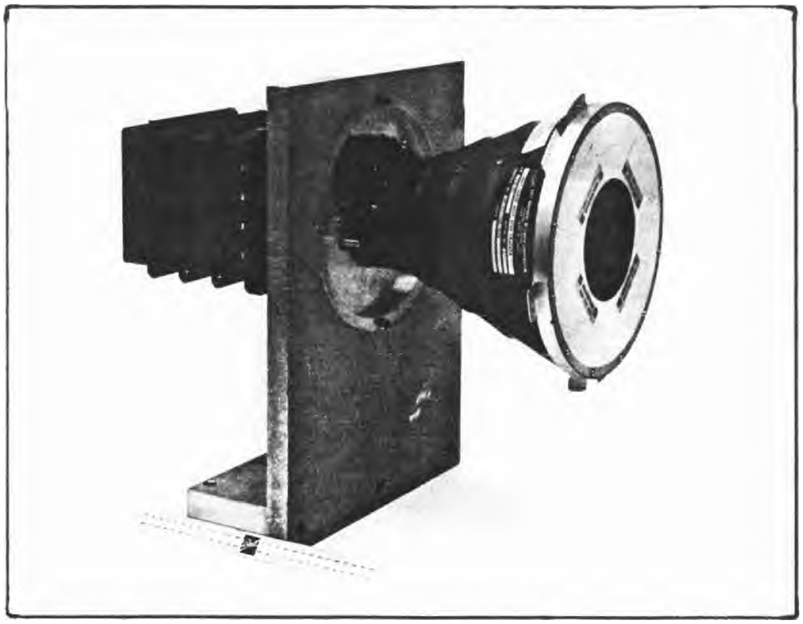

Figure 3.20b- CT411 star tracker, (Gutshull & Deters, 1979).

Many different types of star trackers have been used in space missions, such as: the BBRC CT-411 star tracker (shown in figure 3.20b) for the Space Shuttle missions with 10°x10° field-of-view and angular precision of 60 arcsec, the Bendix OAO fixed head tracker with 8°x8° field-of-view and angular precision of 10 arcsec, and the Honeywell HEAO-C tracker with 2°x2° field-of-view and angular precision of 3 arcsec (Gutshull and Deters, 1979). In recent years, CCD (Charge Coupled Device) and CID (Charge Injection Device) array sensors have been introduced in star trackers, yielding an angular precision of 1.7 arcsec and 8° field-of-view. Star trackers which were built for an experiment in one of the Space Shuttle missions in 1983 had CID array sensors of 256x256 pixel chips providing a 19.3°x19.3° field-of-view and a precision of 7 arcsec (Kollodge and Sand, 1984).

Therefore angular precision of the star trackers can easily reach a few arcseconds. This makes them ideal for attitude determination and stabilisation of a high spatial resolution altimeter. To control the three-axes angular orientation of the altimeter antenna three star trackers can be mounted on the platform.

Another possibility for determining and controlling the attitude of a spaceborne platform is the use of the NAVSTAR Global Positioning System (GPS) which has been primarily planned to provide worldwide precise location of any user who has a GPS receiver. By the year 1995, the GPS project will provide a constellation of 24 satellites around the Earth with an orbiting period of 12 hours at an altitude of —20000km. Each GPS satellite is precisely time and frequency synchronised with the others, and continuously transmits streams of navigation information about the precise position of the satellite at the instant of each transmission with an uncertainty of less than 10m. This uncertainty is expected to be reduced to about 1-2m when GPS becomes fully operational by 1995 (Yunck et al., 1985). The constellation of the satellites is arranged in such a way that there should always be at least four satellites visible to the user's GPS receiver, regardless of the hour or the location. Since all the GPS satellites transmit on the same carrier frequencies, the GPS receiver receives a composite signal of all the visible satellites. To find which part of this composite signal belongs to which GPS satellite, any individual satellite puts its own identification in the form of a unique pseudo-random sequence modulation on its transmitted signal. Therefore, by a series of properly time-aligned correlations between the composite received signal and the replicas of the expected pseudo-random sequences generated in the receiver, the position of any intercepted satellite and its range to the receiver can be individually extracted. By extracting position and range information of the four GPS satellites at the same time, and using them in a system of four range equations which relate the coordinates of the GPS receiver and the satellites, the position of the receiver can be easily calculated with a precision of 15m, and the clock error of the receiver with a precision of 0.11.tsec . Therefore GPS signals can be used by a GPS receiver on-board the remote sensing satellite to obtain position information for the synthetic aperture altimeter, and even carrier Doppler tracking can provide the velocity of the GPs receiver with a precision of 0.1m/sec. But how is it possible to determine the angular orientation of the remote sensing satellite by GPS? This may be achieved by an interferometric method. Figure 3.21 shows two parallel GPS receivers with their antennas separated by d metres. Receiving signals from a common GPS satellite via an incoming angle 0, causes a relative one-way phase difference 0 = (2n/X).d.sin0 between the two channels. These signals are correlated against the same pseudo-random sequence in the two parallel channels to distinguish them from the signals of the other GPS satellites. The two outputs are then mixed together to generate the interferometric voltage pattern (cos4)), which reveals the orientation of the interferometer baseline with respect to the wavefront of that particular GPS satellite. All the GPS satellites operate on two common carrier frequencies, with the higher one being 1575MHz (i.e. X = 0.19m). If the baseline is assumed to be d = 13m (equal to the across-track dimension of synthetic aperture altimeter antenna), to control the orientation of the antenna in across-track with a precision of 33 arcsec, the phase difference between the two channels of the interferometer will be 0 = 4° and this is not difficult to measure. However, if the interferometer

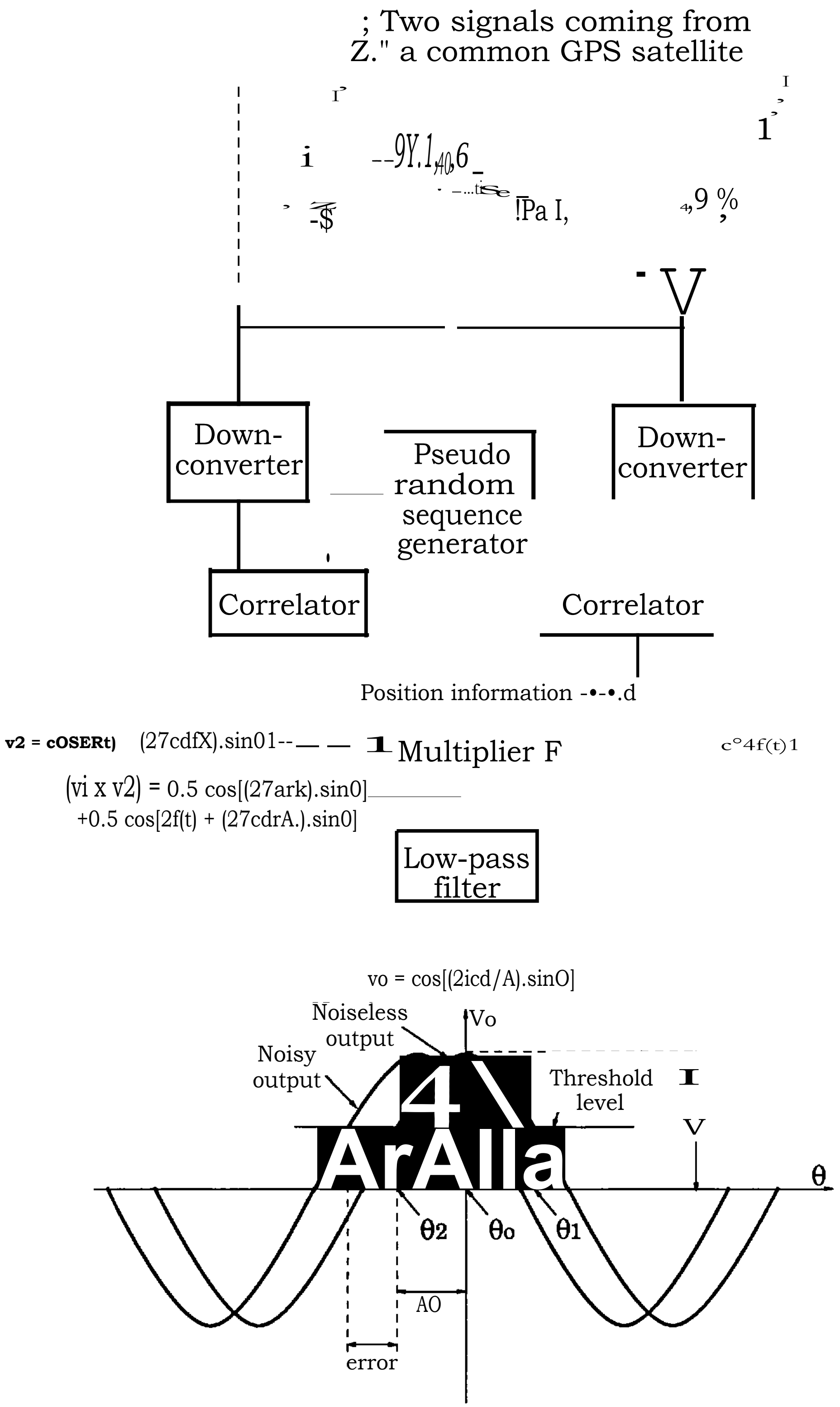

Figure 3.21- Interferometric GPS receiver.

baseline is assumed to be d = 1.5m (equal to the along-track dimension of synthetic aperture altimeter antenna), to control the orientation of the antenna in along-track with the same precision (i.e. 60 = 33 arcsec), the phase difference between the two channels of the interferometer will be = 0.46°. This fine phase measurement seems difficult but not impossible. It is also feasible to increase the length of the baseline along-track to obtain a higher phase difference, and as a result easier phase measurements.

Following the discussion of the last paragraph, here a simplified treatment of the achievable precision in the angle measurement using a GPS interferometric receiver is given. Figure 3.21 shows the voltage pattern of the interferometer, in which it is assumed that the particular lobe which is centred at the geometrical line-of-sight can be distinguished from the other lobes, since the knowledge of GPS satellite location and also the determination of the position of GPS receivers provide this information. In figure 3.21, two patterns are illustrated, one for the ideal noiseless case, and the other one in the presence of finite signal-to-noise ratio which causes a shift in the apparent direction of the arrived signal and consequently degrades the achievable angular precision. Now, a threshold detector has to be used to detect the voltage level of a particular angle. If the two crossing points of the voltage pattern and the threshold level are detected, which correspond to two angles 01 and 02, the location of the boresight of the pattern oo **will be:**

$$0_0 = (8_1 + 0_2)/2 \qquad \text{...3.95}$$

Since in the presence of noise, an error is involved in the measurement of 01 and 82, **the standard deviation of** oo **can be calculated by applying the propagation of errors, equation 3.93, to equation 3.95 (assuming that 01 and 02 are two independent measurements having similar standard deviations,**

$Ge_1 = ae_2^{-}$ no):

$$o^2_{00} \quad (O^2_{01} + (5^2_{O2})/4 = (2(5^2_{e} \;,(4,1 \; -p \qquad a_{o0} = a/_{0},17$$ ...3.96

Therefore, the error in the determination of the boresight angle, $_{\mathbf{Geo'}}$ is related to the error in measuring angle at the threshold levels,a_e. On the other hand, using a threshold detector to detect a prescribed voltage level related to a particular angle means that the error in measuring angles is equal to the RMS voltage noise, a_n, at the threshold level, considering a proportionality factor which is the slope of the voltage pattern at the threshold level (Steinberg, 1976). This means that a higher slope increases the sensitivity of the level detection. Thus placing the threshold level at the maximum slope of the voltage pattern which is approximately the ratio of the pattern peak, V, to half the null-to-null width of the pattern, A0, provides the following expression:

$$a_e = \frac{a_n}{(V/A_e)} = \frac{A_e}{(V/a_n)}$$ ...3.97

In equation 3.97, V is the voltage level and a_n is the voltage noise, which can be related to the receiver output SNR. As a result, equation 3.97 becomes:

$$(SNR) = \frac{2}{a_n}; \longrightarrow \qquad a_9 = \frac{A}{I\,(SNR)}$$ ...3.98

Now, inserting equation 3.98 in equation 3.96 gives (Steinberg, 1976):

$$a_{o0} = \frac{A_e}{I2(SNR)}$$ ...3.99

The above expression gives the maximum achievable precision in the determination of the boresight of a GPS interferometric receiver, as a function of the pattern width and output SNR. If N received signals are averaged to increase the signal-to-noise ratio, the angular precision can be improved and equation 3.99 becomes:

$$ao - \frac{A_e}{2/\text{-}7(81\backslash ir)} \qquad ...3.100$$

From figure 3.21, $(A_o)_{inax}$ which is half the null-to-null width is given by:

$$co^{2nd}\ sine = 0\ \text{-}*\ ^{\underline{2nd}}\ sin() = \frac{1L}{2}\quad \text{-}4\quad A = sin^{1}[\frac{1-1}{4d}$$

Using this expression in equation 3.100, gives the final result as:

$$a - \frac{sin^{1}\ \underline{441}}{00\ .1 \bullet T.(S1s,2)} \qquad ...3.101$$

The SNR at the output of pseudo-random correlator of the GPS receiver is about 30dB (Spilker, 1978), so having = 0.19m and an across-track baseline d = 13m, to achieve an angular precision of about $a_{e.}$ = 33 arcsec in the attitude control of the synthetic aperture altimeter, equation 3.101 shows that it is sufficient to have only one (N = 1) received GPS signal. However, in the case of an along-track baseline d = 1.5m, to provide the same angular precision at least N = 20 received GPS signals have to be averaged. [N.B. Increasing the baseline length from d = 1.5m to d = 3m reduces the number of averaged signals from N = 20 to N = 5]. Consequently, by proper arrangements it is possible to employ GPS interferometric receivers for the high precision attitude determination and control required for high spatial resolution synthetic aperture altimeters. Similar to star trackers, to control the three-axes angular orientation of the altimeter antenna three GPS interferometric receivers can be mounted on the platform.

Chapter 4

Design of an experimental synthetic aperture altimeter

4.1 *An aircraft-borne altimeter*

Following the theoretical study of the application of aperture synthesis to satellite radar altimetry, it is proposed that the next stage in the development of such an instrument would be an aircraft-borne 'proof-of-concept' synthetic aperture altimeter which can be realised rather simply and cheaply (Purseyyed and Griffiths, 1988; Griffiths and Purseyyed, 1989). In this chapter, the requirements of such a system are examined, and the design and construction of a prototype system are described. This radar altimeter, whose general block diagram is shown in figure 4.1, includes a number of Technologies, such as aperture synthesis with full-deramp range processing, digital chirp generation, bistatic FMCW operation and off-line digital signal processing. This instrument will use unfocused along-track aperture synthesis, and obtaining its across-track resolution from a real across-track aperture. The other parameters of the system are discussed and listed below:

The operating frequency has been taken as 13.5GHz (A. = 2.2cm). Whilst higher frequencies would allow improved resolution, the hardware involved would certainly be more expensive. Therefore increasing the frequency does not seem reasonable when the aim is only to demonstrate the practicality of an idea. The 13.5GHz carrier is swept by an LFMCW (linear frequency modulated continuous wave) signal with a bandwidth of 50MHz (equation 2.14) providing 3m range resolution. The PRF of the LFMCW signal is taken as lmsec, equivalent to a 1kHz range bin.

The mean height and velocity of the aircraft platform are assumed to be:

h = 300m and v = 55m/sec respectively. Assuming 32 bins in the range window, the altimeter can measure height in the range of 300m±48m.

The variation of backscatter coefficient for a nadir-looking land altimeter at 13.5GHz is taken as: -20 dB < a° < +10 dB (Ulaby et al, 1982; Long, 1975; Elachi, 1987; Somma and Thompson, 1981).

The dimensions of the transmitter antenna are: Dac = 2m and D_{az} = 0.5m (D_{az} satisfies the lower limit of PRF, equation 3.55). The across-track dimension provides 3.3m across-track resolution at h = 300m. The antenna along-track length of 0.5m gives a 13.33m real footprint. The along-track processing generates a synthetic beam with the same resolution as the across-track real beam, so from equation 2.33 the synthetic aperture length will be about lmetre. Having similar resolutions for height (range), across-track and along-track provides an approximately cube shaped resolution cell. The transmitter antenna gain (equation 3.51), assuming an efficiency of 50%, is 12700 (41dBi). The receiver antenna is a simple horn, and as long as the illumination is limited by the narrow-beam of the transmitter antenna, the beamwidth of the receiver horn antenna is not important and can be very wide. Therefore the dimensions of the receiver antenna are taken to be D_{az} = 17cm and D_{ae}= 13.5cm providing a gain of 290 (24.5dBi), for an efficiency of 50%.

At the front-end of the receiver there is no microwave low-noise amplifier since it is not necessary from signal-to-noise considerations and it is rather an expensive component. So the received signals are directly down-converted to IF using a passive microwave mixer. Figure 4.2 illustrates the front-end of the receiver, from which the noise figure of the radar receiver can be calculated using the well-known Friis formula (Pettai, 1984):

$$F = F_{=2} \quad E[F.-1]_{4} \overset{-}{\vdots} 1_{J=2} G.I. \; 48 = 17\mathrm{dB}$$

[S is the number of sections.]

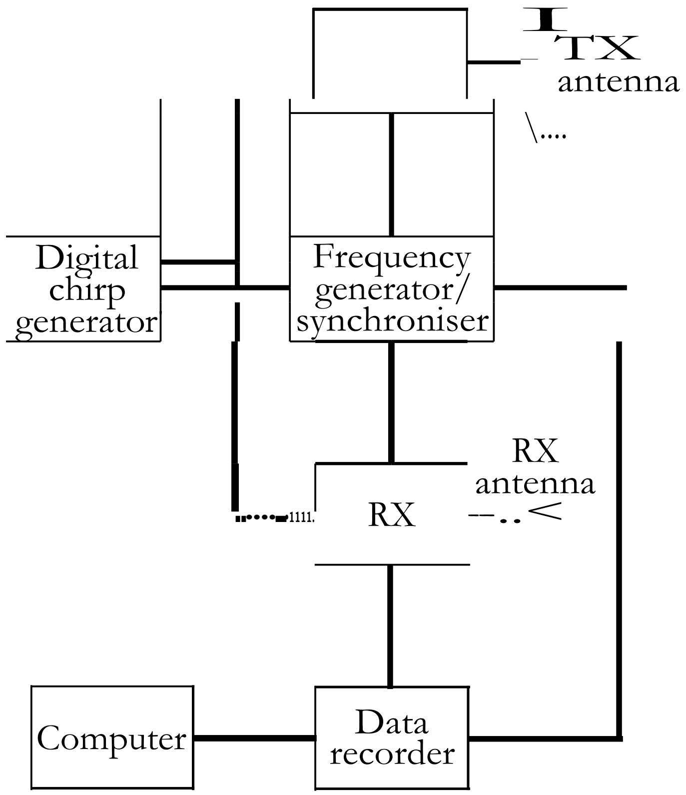

Figure 4.1- General block diagram of the experimental radar altimeter

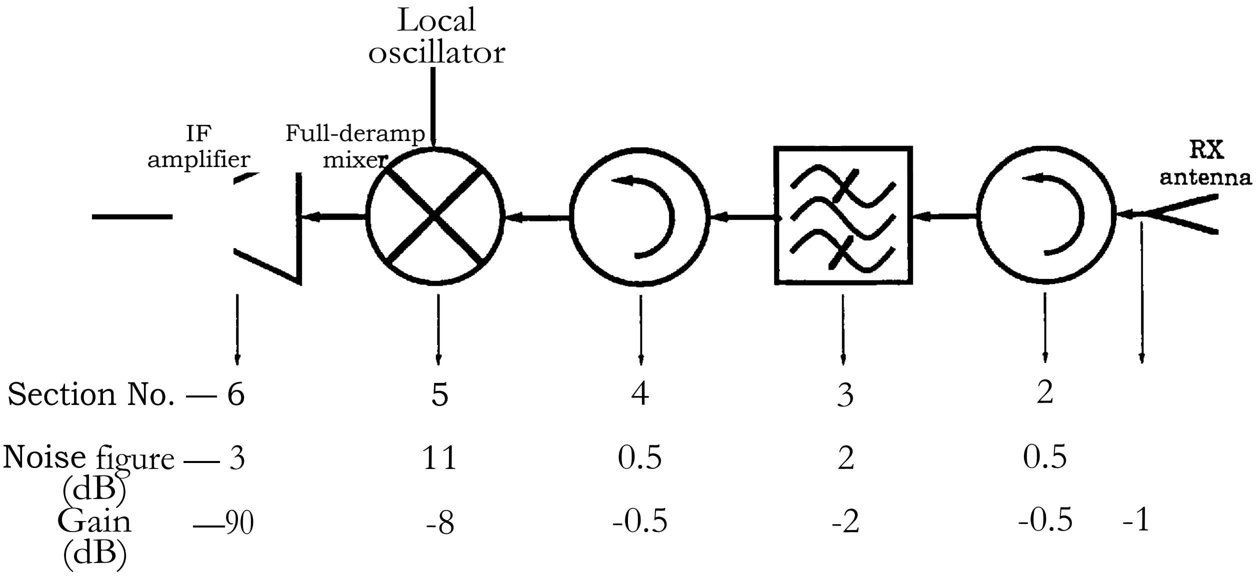

Figure 4.2- The experimental radar altimeter receiver front-end

Since this experimental system operates in a beam-limited mode and has a bistatic configuration with two separate antennas (i.e G_t GO, from the relevant equations of Chapter 3, some modified versions of the equations for the transmit power, received power and dynamic range can be derived:

$$P_{t(max)} \quad \frac{2vD^{lx}(SNR)\ .\ (47c)^{3}\ \underline{R}^{2}_{\underline{maz}}\ L_{s}\ kT_{o}\ F.}{G_{t}G_{r}X^{4}\ Cr^{o}_{nun}}$$

...4,1

$$(SNR).- \frac{PtGtG_{2r}\quad a^{4\ o}\qquad 1}{(47t)^{3}\ R\ \ L_{s}kT_{o}F\ 2vD:}$$

...4.2

$$DR = \frac{R^{2}_{max}\ max^{o}}{R^{2}_{min}\ a^{o}_{mm}}$$

...4.3

$$P.— \frac{\underline{P}_{\underline{t}}\underline{G}_{\underline{t}}\underline{G}_{\underline{r}}\ 2k,\ G^{4\ o}}{(470^{3}\ R^{2}\ L_{t}D_{a}^{1DC-1X}\mathbf{P}_{ac}}$$

...4.4

where D_{az}Tx and D_{a}.Tx are the along-track and across-track dimensions of the transmitter antenna. Inserting the required values into the above equations (assuming SNR = 20 dB for one range bin), give:

P_t = -9dBm and $(SNR)_{tnaï}$--- 53dB

DR = 33dB and $P_{i(nin)}$.. -113dBm

The required transmit power is -9dBm, which is very low. This implies that there is no need for a microwave power amplifier in the transmitter.

As has already been mentioned, the radar operates in an FMCW mode. This is because the time-of-flight of the radar pulses is approximately -21.ts (at an aircraft height of 300m). Thus, unless the transmitted pulse length is less than this, 'aliased' operation (transmitting and receiving

simultaneously) is inevitable. This design takes a different approach, and increases the pulse length to a 100% duty cycle with the result of a very low peak transmit power. Thus the transmitted pulse length is (1/PRF) = 1ms. A consequence of using such a long pulse length is that the digital sampling rate required for the range bin formation is extremely low. Each range bin filter corresponds to (1/1ms) = 1kHz, and if a range window of 32x3m = 96m is taken, the required sampling rate of the ADCs is only of the order of 32kHz. Another consequence of this is that no tracking is required - with a range window of 96m from an aircraft at 300m, the range window can stay fixed. The transmitter and receiver antennas are used in a quasi-bistatic configuration, separated by a few metres. This helps obtain high isolation between them, and this, together with the very low transmit power requirement afforded by the 100% duty cycle, means that there will certainly be no receiver overload problem - only a point target due to the reception of the direct transmit signal, and this can be arranged, by suitable choice of intermediate frequency, to fall outside the range window (Griffiths and Purseyyed, 1988).

The transmitted chirp provides the same bandwidth adopted for the scanning radar altimeter system described in Chapter 3, and it has the merit that the chirp can be generated easily by digital means (the digital chirp generator will be explained in section 4.4). For the proposed system, suitable parameters would be a 1.5625MHz baseband chirp in two quadrature channels, which can be easily generated using 'NI, integrated circuits and with a clock rate of 8MHz. Then by up-conversion and x16 frequency multiplication, the final chirp with a bandwidth of ±25MHz around the carrier will be obtained. All the SSB modulator and frequency multiplier circuits are at RF rather than microwave frequencies, so the hardware is relatively cheap and uncritical.

Only one transmit/receive chirp generator is used. This is because the time taken for the transmitted chirp to travel from the radar to the target and return is very short, 2.32psec two-way time delay for maximum range of 348m, compared to the length of the chirp which is one millisecond.

Therefore the received waveform is almost overlapped in time with the transmitted chirp with a time difference of only 2.32usec. This gives 1.5cm loss in 3m range resolution which is very insignificant. For this configuration, the only parameter that should be properly adjusted is the fIF to translate the echo signal of the central target (i.e. h = 300m) exactly at the IF amplifier centre frequency. This frequency shift between the transmit chirp and the receive local oscillator chirp, for an IF amplifier which is centred at 70MHz, is [70MHz - (1kHz/3m)x(300m)] = 69.9MHz.

Moreover, the same microwave oscillator is to be used for both transmitter and receiver to simplify the required frequency synchronisation inside the system and more importantly, reduce the costs. To select a suitable microwave oscillator, Appendix 3 describes the phase noise requirements of such an oscillator resulting in the following expression:

$$N^{0}\; E\; C^{P1}_{f_{,,,}(\mathrm{max})} = \mathrm{201og}\,\frac{``\mathrm{td})}{4\sin[7cf_{m}t_{d}]}\quad \mathrm{dB/Hz} \qquad \ldots 4.5$$

Equation 4.5 gives the maximum permissible phase noise sideband density at the frequency offset f_m. This means that if the maximum permissible phase noise at the IF stage EV(t_d), which is equivalent to the acceptable phase error in the synthetic aperture processing, and also the time delay t_d are known, then the required phase purity of the master oscillator at any particular offset frequency f_m can be calculated. For this experimental radar, substituting all the necessary quantities in equation 3.7 (the synthetic aperture phase history), gives the maximum uncompensated phase excursion across the aperture:

$$A. = [27tx\,(2)^{2}]/[252mx0.022m] = 0.28\ \mathrm{Radians} = 16^{\circ}$$

Assuming that an unwanted phase error or phase noise of 0.28×10^{-3} Radians is acceptable for the oscillator in order not to affect the synthetic beam pattern, and also taking t_d = 2.3p.sec, the required phase purity of the oscillator can be calculated from equation 4.5:

$$C\ fm = 20\log \frac{0.28\text{x}10^{3}\ \text{Radians}}{4\sin(2.3\text{usecx}1\text{txf}_m)}\ \text{dB}/\text{H}_z \qquad ...4.6$$

The above equation gives the permissible phase noise of the oscillator for an offset frequency f_m. As an example for f_m = 30kHz the permissible phase noise is -70dB/Hz. For a fairly modest commercial 13.5GHz Gunn oscillator **(**Marconi Gunn oscillator model DA8909), the residual phase noise in a 1Hz bandwidth at 30kHz offset from carrier is less than -100dB which is much better than what is needed for the experimental radar.

4.2 *The effects of phase error on a synthetic aperture*

In section 4.1,to calculate the required phase purity of the radar oscillator it was assumed that the acceptable phase noise is less than a very small fraction of the maximum uncompensated phase excursion of the unfocused synthetic aperture. In this section, some simple expressions are obtained to evaluate the effect of phase noise on the synthetic beam.

From antenna theory, the aperture excitation A(x), the far-field radiation f(v) and the power pattern I f(v) 1^2 of a 1-dimensional antenna having a length L in the x direction can be related to each other by the following well-known Fourier transforms:

$$f(v) = SA(x)\exp(jvx)dx$$

$$\text{I}\,f(W)\,\text{I}^2 = f(v)f^{*}(v) = \underset{LL}{11}A(x_i)A(x_2)\exp[jv(x_f - x_2)]dx_i dx_2 \qquad ...4.7$$

where: v = [(27r/7L).sin0], and 0 is the angular variable of the pattern. Also

recalling from Chapter 3, the along-track pattern of the unfocused synthetic aperture altimeter is equivalent to the pattern of a linear synthetic array. Therefore, from equations 3.26 and 4.7, the normalised along-track far-field radiation and power pattern of an ideal synthetic aperture altimeter are given by:

$$f_0(11) = \overset{N}{\underset{n=1}{\mathbf{TIeXp(UX)}}}$$

$$I\, f_0(U)\, I^{2} = f_o f_o^{*} = \underset{N}{\mathbf{iT}}\,\overset{N\ \ N}{\underset{n=lm=1}{\mathbf{nexpljU(X_{n}\text{-}X_{III})]}}} \qquad \text{...4.8}$$

where:

$$u = \frac{41\ c}{11X,}\mathbf{x_a} \quad \textbf{and } x_n = \frac{\mathbf{n\ t}}{N\text{-}1} \qquad \text{...4.9}$$

Now, if a series of independent zero mean and equal variance (= a^2) phase errors, *$8_{,1}$*, are applied to the system, the far-field radiation and power pattern of the synthetic array will become:

$$\mathbf{f(u)} = \frac{\mathbf{l}}{N}\overset{N}{\underset{n=1}{\mathbf{E}}}\mathbf{explj(ux_n+8_n)})$$

$$I\, f(u)\, 1^{2}\mathbf{-\,fe=}\ \frac{1}{N^{2}}\overset{N\ \ N}{\underset{n=1\ m=1}{\mathbf{1\ 1}}}\text{exp}[ju(x_{n}\text{-}x_{m})]\text{exp}\,[j_{(6\text{-}}\mathbf{8}_{m}))] \qquad \text{...4.10}$$

From equation 4.10, the expected or mean power pattern of the synthetic array is:

$$\mathbf{ER\%\ fl = \text{-}71\ 1\ exp[ju(x,\ x_m)]\bullet E[expj(8_{,r}\text{-}\ 8_m)] =}$$
$$\quad \mathbf{N\ \ n=1\ m=1}$$

$$= \frac{\mathbf{1}}{N}(\,1\text{-}(E[\text{expj}8]\,)^{2})+\frac{\mathbf{.1_{i}}}{N}\,{}_{\text{‹}}E[\text{expjo}]\,)^{2}\overset{N\ \ N}{\underset{n=1\ m=1}{\mathbf{1,\ 1}}}\text{exp}[ju(x_{n}\text{-}{}^{3}c_{m})] \qquad \text{...4.11}$$

Expanding [expj8] for small phase errors and inserting it into (E[expj8])^2,

results in:

$$[E[\exp j8]]^{2} .\text{--}. 1- a^{2} \qquad \text{for } a < \tfrac{1}{2} \text{ Radians}$$

...4.12

where a^2 is the variance of the phase errors. Inserting the expectations from equation 4.12 into equation 4.11 and using equation 4.8, the mean power pattern of the synthetic array affected by the phase noise is given by:

$$E[\bullet f^{*}] = (1-a^{2}) f_{o} G + 4$$

...4.13

Equation 4.13 shows that the mean power pattern is a combination of the ideal pattern and the phase noise variance, as illustrated in figure 4.3. From this figure it is evident that any phase noise causes changes in the level of both the main lobe and the sidelobes. The sidelobe level relative to the peak of the main lobe can be found from equation 4.13 and figure 4.3, (knowing that the ideal main lobe peak is at u=0 and in normalised form it is equal to unity, and also its relative sidelobe level is b^2):

$$(SLL)dB -=: 1011 + {}^{2} + \frac{CY^{2}}{N(1-a^{2})} \, i$$

...4.14

Another consequence of the phase error, as seen from the expected power pattern, is a change in the beamwidth of the array. From equation 3.26 the ideal synthetic pattern is given by:

$$fof{:}(x) - \left| \frac{\sin\left| \dfrac{27cNf}{(N-1)11A,} x_{a} \right|}{N.\sin\left[\dfrac{27c\, i}{(N-1)h2t,} x_{a} \right|} \right|^{2} \longrightarrow f_{o}f{:}(0 - x_{a}/h) - \left| \frac{\sin i \dfrac{27EN\, i}{(N-1)A,} e^{1}}{\frac{1}{N}\bullet\sin\left[\dfrac{f}{(N-1)?,} i\delta \right]^{1}} \right|^{2}$$

The above equation can be used for the calculation of the ideal pattern

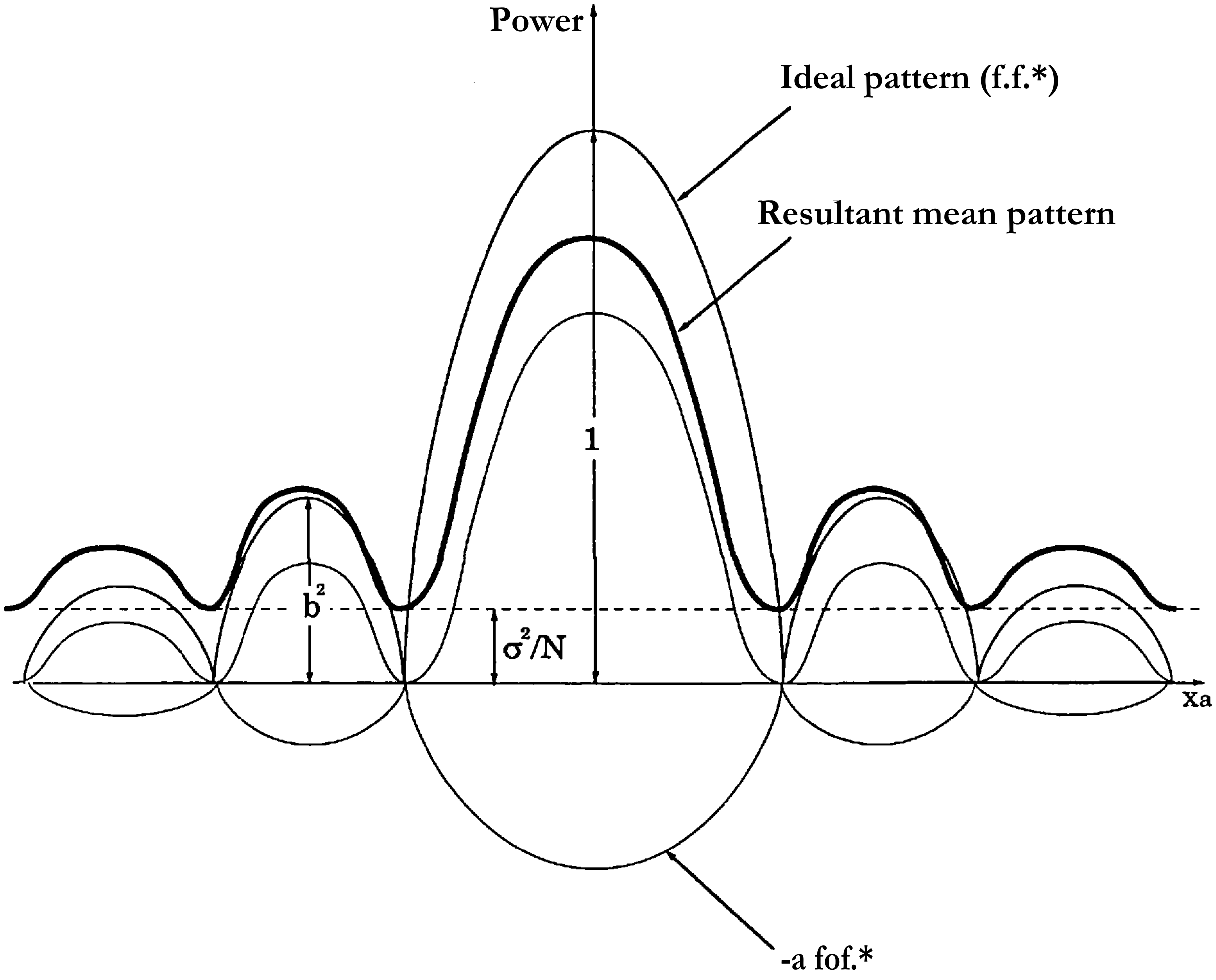

Figure 4.3- Effect of phase error on synthetic aperture beam pattern

beamwidth, 0_{bo}. Also by inserting the expression for $f_o f_o^*$ from this equation in the expected pattern (equation 4.13), the mean pattern beamwidth, O_b, can be obtained. After the calculation of the two beamwidths, the ratio of them OW which is a measure of deviation in the beamwidth of the synthetic array from the ideal case to the phase noise affected array is given by:

$$R_b = \frac{b}{0_{bo}} . 1 \frac{1}{J.} - \frac{G^2}{N(1-cy2)} \quad 1$$

...4.15

Phase error can also change the synthetic pattern beam pointing. To find the location of the main beam of a synthetic array (i.e. the location of the main lobe peak) affected by phase noise, the derivative of the power pattern (equation 4.10) with respect to the along-track variable u, must be set to zero:

$$\frac{a(f.f^*)}{au} - \frac{2}{N^2} \underset{n\ m}{II} (x_n - x_m)\sin[u(x_n - x_m) + (5_n - 8_m)] . 0$$

Assuming small phase errors and a very narrow synthetic beam, the sine in the above expression can be replaced by its argument (when the aim is finding the main lobe peak). Therefore from this modified equation, solving for u gives:

$$\underline{u} -E \underset{n\ m}{E/}(xn - xin)(5n - Elm) \underset{n\ m}{HE/}(xri \; x.)21$$

...4.16

u is the instantaneous location of the synthetic boresight, which has a zero mean (since the phase errors have zero means). The variance of u however, provides the amount of beam fluctuation around this zero mean boresight:

$$(Y_u^2 = EN^2 i = Ei \underset{n\ mrp}{IIN} X_r d(X_r - x_p)(8_n - c)(8_r - S_p) lit / \underset{n\ m}{E}(x. - X_m)^2 1$$

In the above expression, n = m and r = p produce zero terms, also for (n or m) # (r or p) the expectation terms become zero because the phase errors are uncorrelated. By these considerations, the above equation results in (Steinberg, 1976):

$$(5_{u}^{2} \_ I 4N^{2}a^{2} \underset{n}{\underset{Zd}{7}} x^{21}_{n\ i} / \ 2N \underset{n}{\underset{Zrf}{7}} X^{2}_{n} \_^{2} \underset{n}{y} d_{--n} \ {}_{=} \Big|^{2} \qquad \ldots 4.17$$

Substituting for x_{ri} from equation 4.9, and knowing that for n =1 to N the summation over x_n^2 is equal to N(N+1)(2N+1)/6, and also assuming that N » 1, which is normally the case, equation 4.17 is simplified to:

$$a_{u}^{2} = E \overset{i_r}{L}u = \frac{47t}{hki}^{x} \ 1\,{}^{2}4\,1 \ - \ {}^{\text{"A}}{}^{er2}\frac{'1}{Nr} \quad -) \quad a = \underset{x.}{\ } h\underset{4n}{X}.A._{171}a \qquad \ldots 4.18$$

Equation 4.18 provides the standard deviation of the beam pointing of synthetic array, a.. , as a function of phase noise standard deviation a.

Assuming that as a result of the phase error, 0.5dB increase in the sidelobe level is acceptable, and also assuming a beam pointing error, a_{xa} , of 1% of the along-track resolution and a beamwidth ratio, $RI_{)}$, of1.01 (equivalent to 1% deviation in the beamwidth) are tolerable, the maximum acceptable phase error is obtained from the minimum of the standard deviations given by equations 4.14, 4.15 and 4.18. This provides a = 0.12 Radians. Thus the synthetic array phase noise has to be less than 0.12 Radians. This is much coarser than what was considered previously for the calculation of the required phase purity of the oscillator (i.e. 0.28×10^{-3} Radians). Therefore if desired, a noisier oscillator could be used for the experimental radar.

Another requirement for the microwave oscillator is its frequency stability (expressed by equation 3.41). Inserting the relevant quantities of the experimental radar into that equation gives:

$$p \quad \frac{\text{eta(55x1} \quad \underline{2}}{348} = E_f X \, 5\text{x}10^4 \text{ (Hz/Hz/sec) = (500x ed ppm/sec}$$

Assuming a tolerance of o_f =1% results in a frequency stability of 5ppm/sec. To achieve this degree of stability for a free-running microwave Gunn oscillator in the presence of a variation in the DC power supply voltage, modulation of the oscillator by various leakage signals inside the system, variation of load VSWR and also temperature variations is difficult. To avoid these problems, the obvious solution is to phase lock the microwave oscillator to a crystal reference oscillator. This gives very good frequency stability, as well as spectral purity and considerable reduction in phase noise. The reference oscillator of this experimental radar is a 70MHz crystal oscillator (Appendix 4), and in order to provide the synchronisation in the different parts of the transmitter and receiver all the required frequencies are generated directly from this crystal oscillator.

For the microwave oscillator in this system, a microwave signal generator (Hewlett-Packard 8620C sweep oscillator) is used in a phase locked loop (PLL) configuration. The reference signal of this PLL is 275.33 MHz which is directly extracted from the 70MHz crystal oscillator. This signal (its 48th harmonic) is mixed with the microwave signal in a harmonic mixer resulting in a 20MHz IF. This IF signal is then injected to a phase synchroniser (Hewlett-Packard 8709A) along with a 20MHz reference signal generated from the 70MHz crystal oscillator. The output of the synchroniser is a DC control voltage which is used to correct the phase/frequency drift of the microwave oscillator. Figure 4.4 depicts the block diagram of the phase locked microwave oscillator that was built for the experimental radar. Figure 4.5 illustrates the microwave oscillator output signal at 13.276GHz when stabilised only by its internal AFC system indicating significant frequency fluctuation. Figure 4.6 illustrates the microwave oscillator output signal at the same frequency when placed in

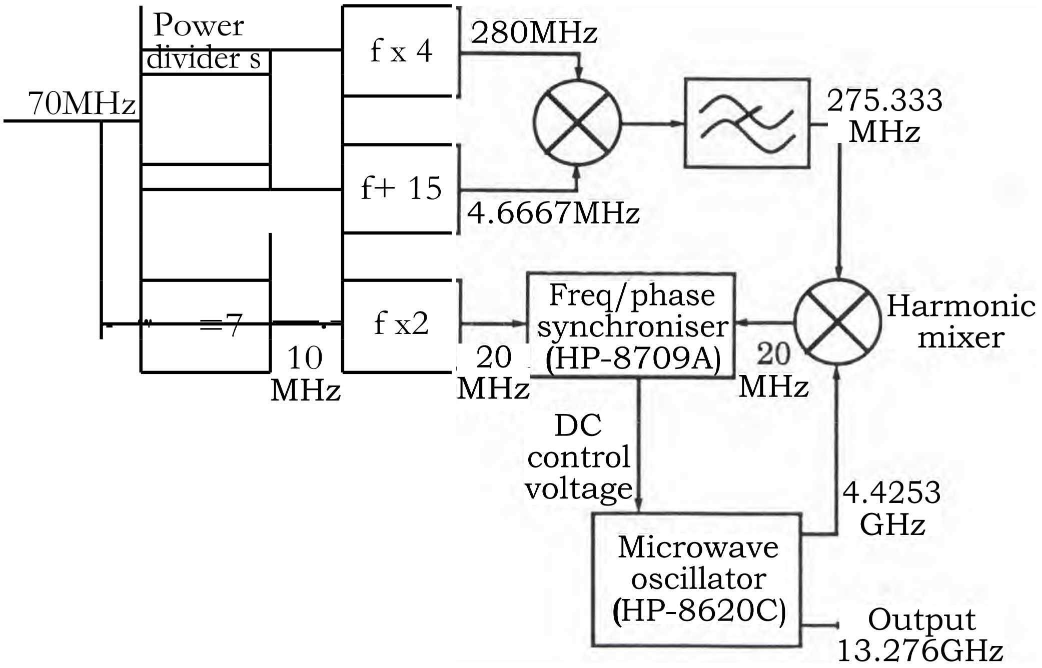

Figure 4.4- Block diagram of microwave phase locked oscillator

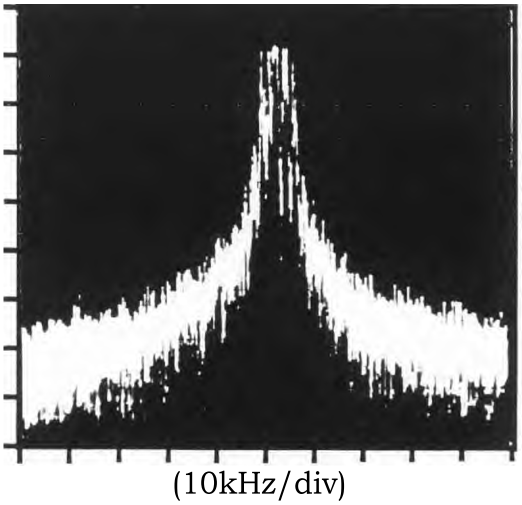

Figure 4.5- 13.276GHz signal of free running microwave oscillator, 1kHz resolution bandwidth.

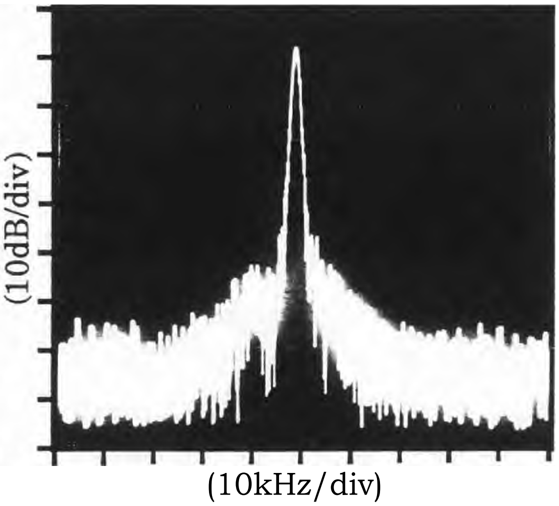

Figure 4.6- 13.276GHz signal of phase locked microwave oscillator, 1kHz resolution bandwidth.

phase locked loop of figure 4.4, providing a stable output signal.

The other signals which have to be generated from the 70MHz crystal oscillator are the signals for the chirp generator, its up-converter and frequency translator, the signals for the receiver IF-to-baseband down-converter, and the sampling frequency of the ADCs at the outputs of the receiver. The block diagram of the subsystem that provides all these signals is depicted in figure 4.7.

Having obtained all the frequencies inside the experimental radar, figure 4.8 illustrates the block diagram of the designed transmitter/receiver. This figure indicates some important features of the radar, which are a passive receiver front-end with no need for a microwave LNA, a passive transmitter with no need for a microwave power amplifier, and the use of a single microwave oscillator to provide the up-converting carriers for both the transmitter chirp and the receiver LO chirp.

4.3 Linear frequency modulated (chirp) signal

In Chapter 2, the merits of full-deramp processing were discussed. As was mentioned, the heart of this technique is the generation of linear frequency modulated (chirp) signals needed for the transmission and full-deramp down-conversion. It was explained that the full-deramp technique provides high range resolution, low transmit power and low sampling rate for a radar altimeter.

It was shown in Chapter 2 that if a uniformly amplitude weighted linear FM signal is full-deramped, the Fourier transform of the output which provides the range information will be a sinc function (sinx/x), equation 2.13. This means that the range sidelobe level is as high as -13dB relative to the main lobe of the transformed waveform, and this level is unacceptable for most radar applications, including radar altimeters. Range sidelobes appear as false targets, and can cause a weakly-reflecting target to be obscured by a nearby strongly-reflecting target. Thus it is usually important

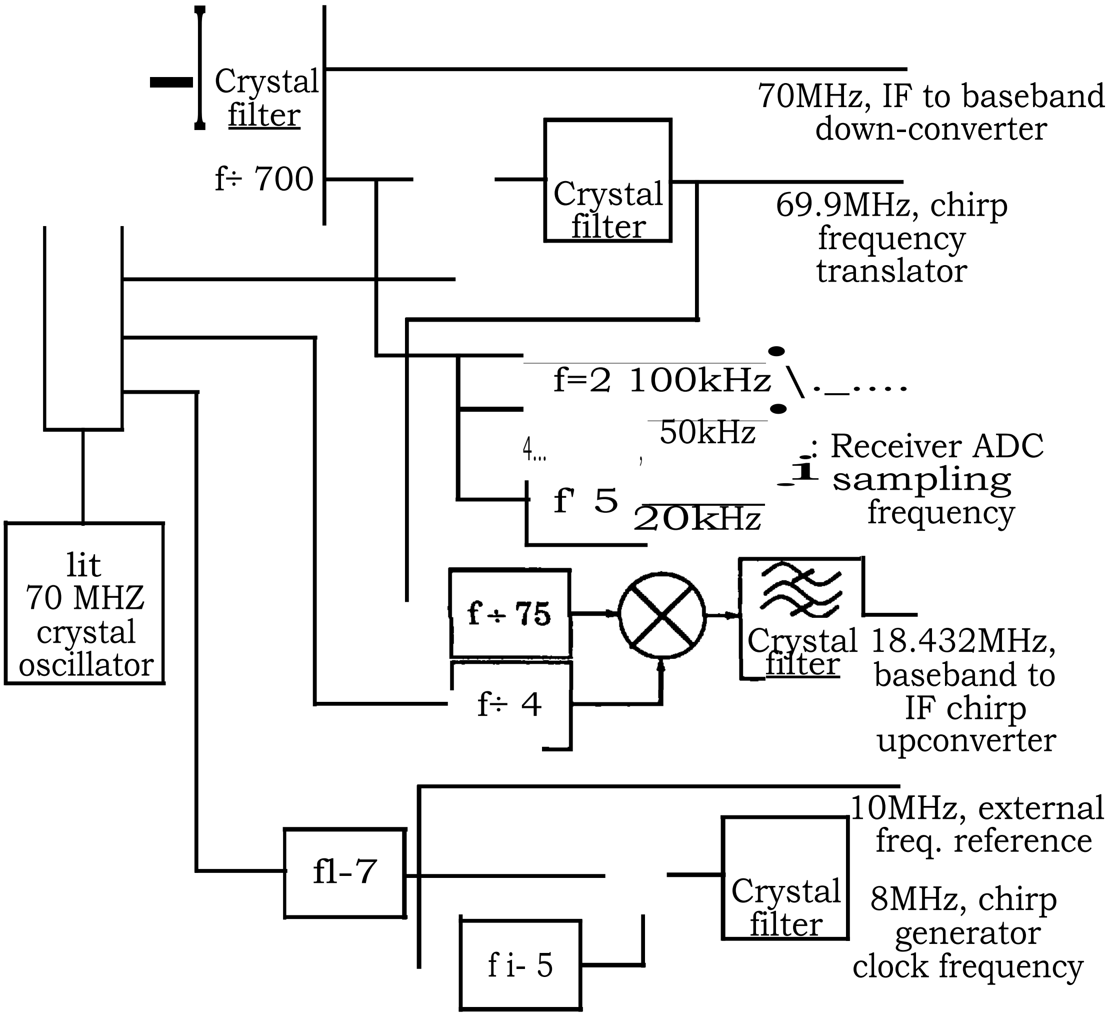

Figure 4.7- Block diagram of the master frequency generator

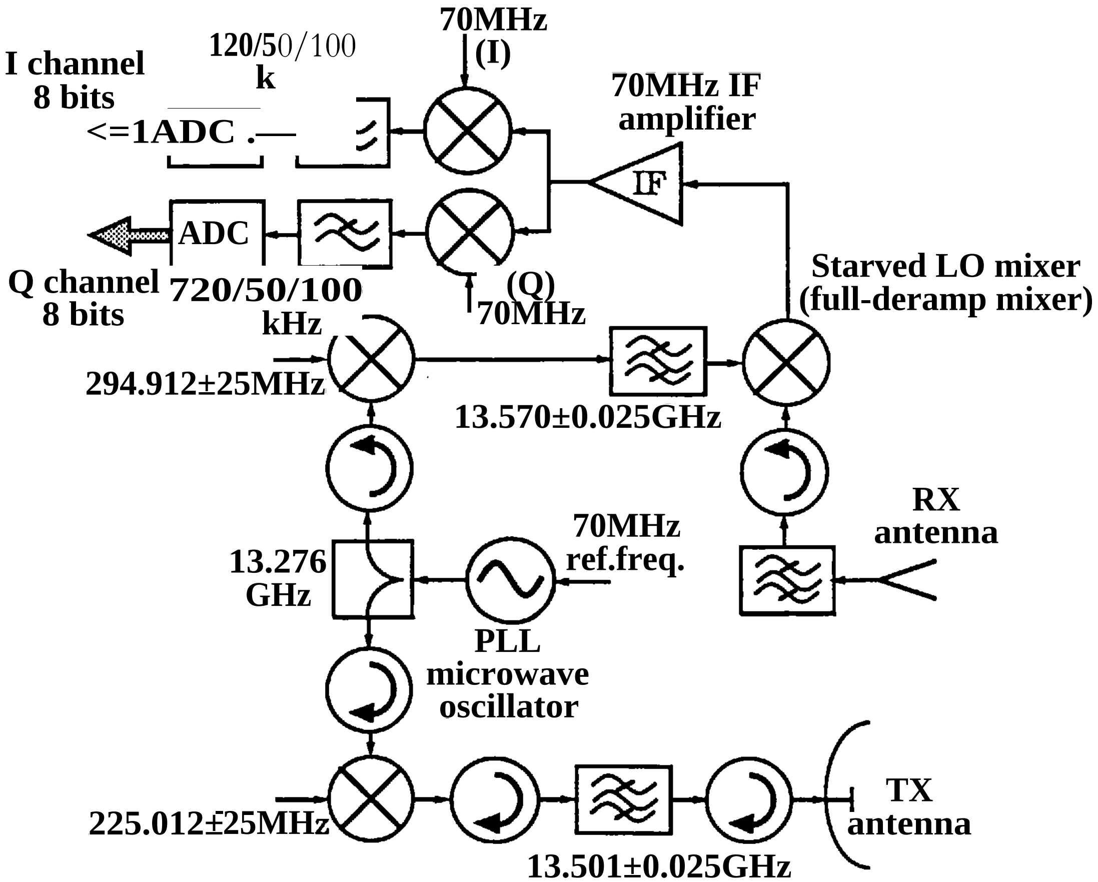

Figure 4.8- Block diagram of high frequency sections with all the important frequencies inside the system.

to ensure that the range sidelobes are adequately suppressed (Morgan, 1985). The required range sidelobe rejection depends on the application of the radar and the nature of the targets and their background or clutter, but a typical value is about -30dB or so (for example the SLL is -25dB for the ERS-1 altimeter).

The cause of the range sidelobes which appear in the Fourier transformed output is the sharp edge or discontinuity of the envelope of the chirp signal in the time domain. The solution to this problem is to apply an amplitude weighting on the waveform to give a maximum amplitude at the centre, decreasing towards the edges. The Fourier transform relationship between the time and frequency waveforms permits the use of a weighting function either in the time or frequency domains with the same result at the output. As a first choice, the weighting function can be applied on the generated chirp signal in the transmitter. However, amplitude weighting at this stage has the same effect as amplitude modulating of the signal. For most radar applications the transmit power is high and the transmitter power amplifier operates in saturation mode, which makes it difficult to taper the transmitted signal (Skolnik, 1985). It is therefore much easier to apply the amplitude weighting in the receiver which has exactly the same effect on the sidelobes. Moreover, the full-deramp technique is a linear process on the chirp signal and the weighting function can be applied anywhere during the process with the same output result. Thus it is much easier to apply amplitude weighting at the output of the full-deramp processor by multiplying the full-deramped output and the time domain weighting function or by convolution of the frequency domain weighting function and the Fourier transformed version of the full-deramp output. This last method is probably the best, since all the processing will be done digitally with considerable flexibility and ease.

Several weighting functions with different characteristics are available (Harris, 1978). However, in addition to reducing sidelobe levels, they increase the width of the main lobe, which means loss of range resolution. This though can be compensated for by increasing the chirp bandwidth in such a way that, in the end, the desired range resolution is obtained. Table 4.1 gives the performance of some conventional weighting functions. As an example, the Hanning function is a cosine squared window having zero amplitude at t = -±AT/2 and unit amplitude at the centre (t = 0) of the window:

$$a(t; It| < AT/2) = \cos^2\left[\frac{t}{T}\right] \text{ and } a(t ; It I > AT/2) = 0$$

Figure 4.9 illustrates the Fourier transformed output of the full-deramp mixer for the two cases of uniform and Hanning weighting functions, showing the differences in the main lobe width and sidelobe levels.

Several techniques are envisaged for generating a linear FM signal. The basic method is to use a voltage controlled oscillator (VCO), whose frequency is changed by a time varying voltage ramp. Although this method is very simple, it is however very sensitive to temperature and input noise voltage. Also the frequency stability can be very poor, and it is not very reproduceable.

To alleviate the above problems a programmable frequency synthesiser may be used. In this method, a VCO is locked to a very stable crystal reference oscillator. The output of the VCO is injected to a programmable digital frequency divider and the output of this divider is compared with the reference frequency and an error signal is generated. This is used to control the VCO in a phase locked loop (PLL) configuration, so the output frequency of the VCO will be exactly the reference frequency multiplied by the division factor. Thus by changing the division factor, the output frequency can be varied, which will finally provide a very stable and finely quantised version of the linear FM signal. The most notable difficulty of this method is the need for a very fast locking time for the PLL.

Another method for generating a chirp signal employs a dispersive delay line. A dispersive delay line is a linear passive device, giving a delay which

Weighting function	Peak sidelobe	Output loss	Relative main lobe width
Uniform	-13.2dB	OdB	1
Triangular	-26.4dB	1.25dB	1.43
Harming	-31.7dB	1.76dB	1.64
Hamming	-42.8dB	1.34dB	1.5

Table 4.1: Performance of various weighting functions

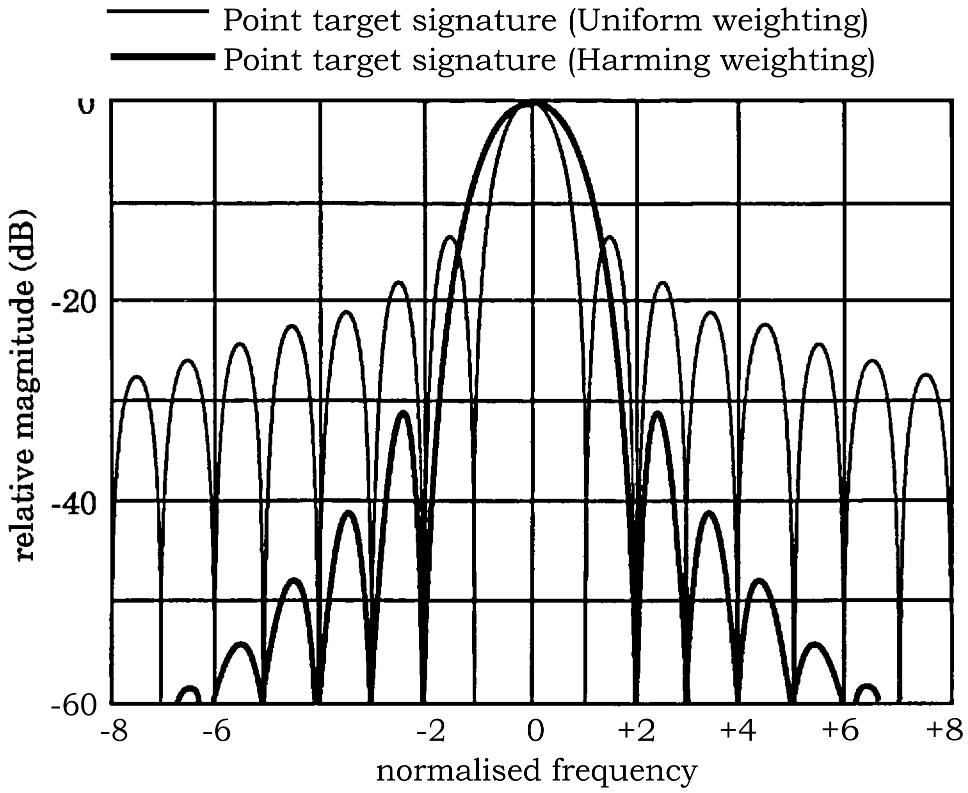

Figure 4.9- Full-deramp mixer output for a point target

varies substantially with frequency. In other words, its impulse response is a frequency-modulated pulse. Therefore, if a very narrow pulse containing a large number of closely spaced frequency lines is injected to the dispersive delay line, since different frequency components experience different time delays, they will not reach the output simultaneously, resulting in a chirp signal at the output. Up to now, this method has been the only technique which has been widely used in radar applications because it can provide highly accurate waveforms. However a dispersive delay line is very sensitive to temperature variations and special precautions have to be taken to minimise this effect. Another disadvantage of this method is that the expansion process reduces the power level of the signal, particularly if the time-bandwidth product is large. This may cause an inadequate SNR at the output (Morgan, 1985). In addition, the time-bandwidth product of waveforms generated by this method is limited (to — 10^4), although subsequent frequency multiplication may be used to increase the chirp bandwidth. Another important problem with dispersive delay lines is that when it is required to change the duration and/or bandwidth of the chirp signal, there is no way to control any parameter of the waveform. To cope with this problem separate delay lines have to be used for each waveform.

4.4 ***Digital chirp generator***

Recent advances in large scale integrated controllers, memory circuits and digital-to-analogue converters (DACs), have provided an opportunity for a new technique in generating waveforms, termed 'direct digital synthesis' (DDS). Figure 4.10 depicts the general block diagram of the DDS technique. The heart of the DDS is a central processing unit (CPU), comprising a digital phase calculator/accumulator, and several control sections which allow easy implementation of frequency, phase and amplitude modulations. Combinations of these modulation techniques allow the synthesis of nearly any type of waveform (Zavrel, 1988). From the input data, the CPU calculates the phase as a function of time in the form of a series of digital numbers. Then, by means of these numbers which act as addresses, the CPU cyclically accesses the contents of a memory. This memory acts as a waveform mapper, which simply converts the calculated phase position to the appropriate instantaneous sinusoidal amplitude value. In other words, the memory input address corresponds to time and phase while the memory output data corresponds to the appropriate amplitude value. Thus the memory is actually a digital phase-to-amplitude converter. Using the DDS technique for generating radar waveforms offers several advantages as follows:

1. Very large time-bandwidth products of more than 10^6 are very easy to achieve.
2. DDS is nearly insensitive to temperature variations.
3. In mass production, in terms of signal performance, DDS waveform generators are virtually exact unit-to-unit replicas of each other.
4. Any type of phase/amplitude codings can be easily applied to the DDS technique.
5. By controlling the amplitude modulation of DDS data streams, any kind of amplitude weighting can be superimposed on the generated waveform.
6. Pulse-to-pulse coherency is one of the important merits of this method which does not exist in analogue approaches.

After considering different methods of generating a chirp signal, the direct digital synthesis technique was selected for the experimental synthetic aperture altimeter. For this purpose a simple form of DDS has been adopted, which generates a primary chirp signal, and then by using analogue multipliers increases the bandwidth of the chirp signal to any desired final bandwidth. The general block diagram of this digital chirp generator is illustrated in figure 4.11. This waveform generator generates a baseband chirp in the form of two quadrature channels spreading from 0Hz to 1.56251V111z. To change the frequency linearly, which is equivalent to changing the phase parabolically, the parabolic phase values are computed and stored in a programmable read-only-memory (PROM). This is the phase memory of the chirp generator. Then by uniformly clocking a counter and using the output of the counter as an address for the phase

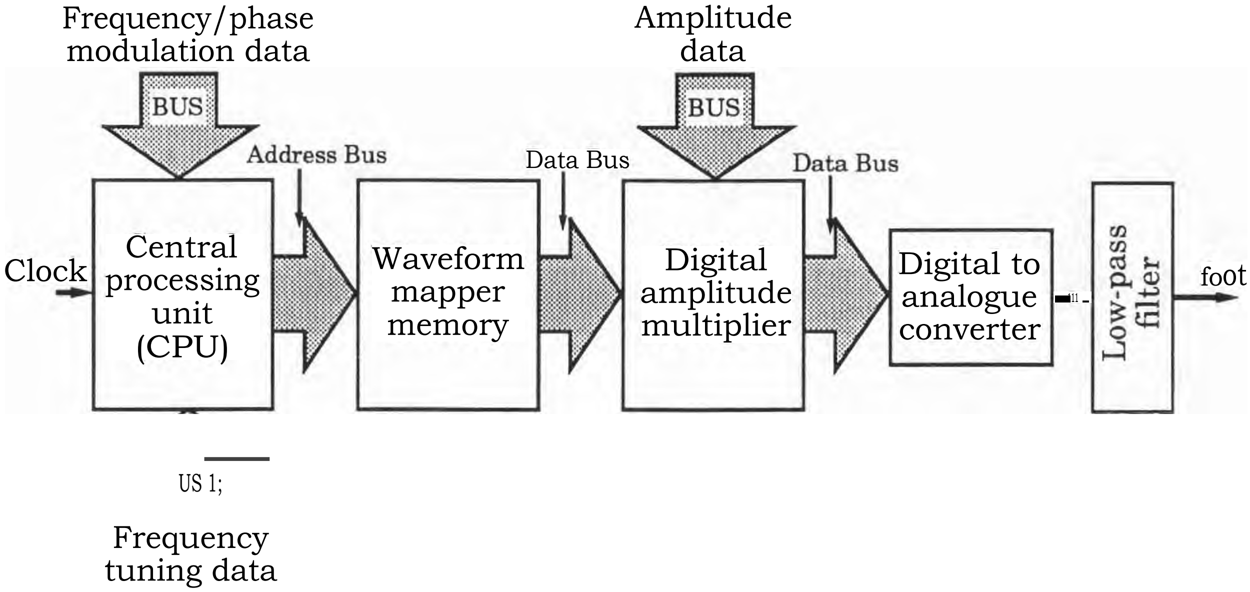

Figure 4.10- General block diagram of direct digital synthesis

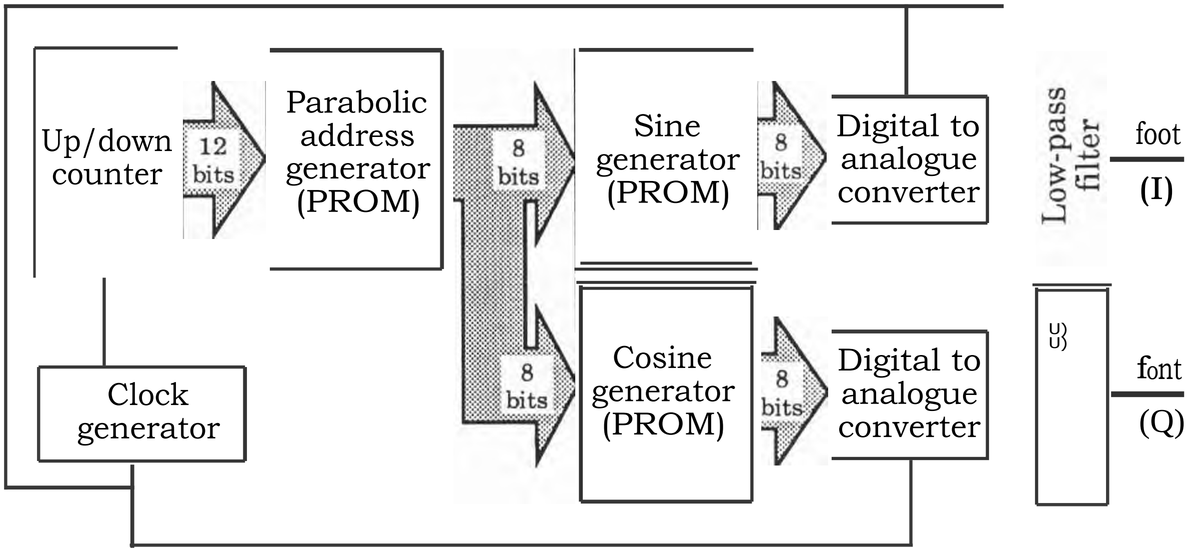

Figure 4.11- General block diagram of the experimental radar chirp generator

memory, different parabolic phase values can be accessed. These phase values are then used as addresses to access the contents of a pair of sine and cosine memories, whose outputs provide the I and Q amplitude values of the baseband chirp. Figure 4.12 shows the outputs (i.e. generated addresses) of the different stages of the chirp generator. To generate a symmetrical parabolic phase, the digital counter counts downwards for half the chirp period and counts upwards for the other half. From the frequency versus time characteristics of the primary chirp, the phase values which have to be inserted in the phase memory can be simply calculated:

$$f(t) = -\frac{B}{2} + \frac{B}{T}t \longrightarrow \qquad 4(t) = 2/Eff(t)dt = 27t[E\frac{r}{2}\left(\frac{1}{2} - \frac{t}{T}\right)^{2}]$$

where B is the primary chirp bandwidth (±1.5625MHz) and T is the chirp period (imsec). In quantised form, considering f_c as the clock frequency and n as the clock number at time t_n, the above expression is modified to:

$$0(n) = 2_{7r} \quad 2\,\frac{(}{2}\;\frac{1}{T.f_c}{}^{n} \qquad ,n = 1,2,3,,N$$

...4.19

From this equation, for any value of n (which also represents the address related to a particular time instant t_n) the corresponding parabolic phase value can be calculated. This phase value might contain an integer multiple of 2n, so after omitting this phase rotation from the calculated phase value the result can be stored in the phase memory. To generate a baseband chirp which covers 0Hz to 1.5625MHz, the minimum clock frequency has to be 2x1.5625MHz = 3.125MHz (Nyquist's sampling theorem). However this frequency is the start of the aliased spectrum which have to be filtered out by an ideal step-like filter. In practice, by increasing the clock frequency the aliased spectrum is frequency shifted in such a way that an implementable low-pass filter can sufficiently attenuate all the aliased components. For this experimental design, the clock frequency is

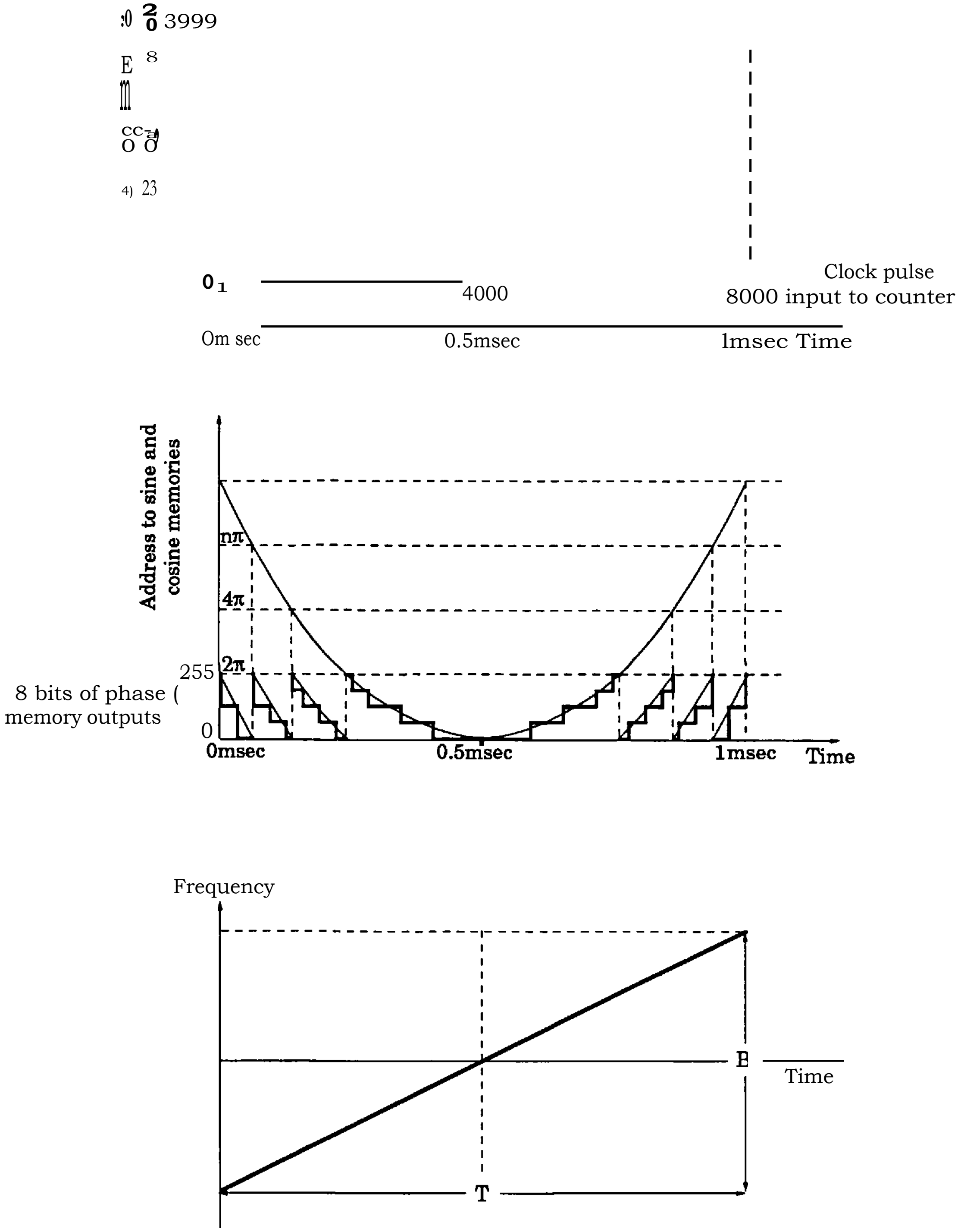

Figure 4.12- Waveforms and generated addresses in digital chirp generator.

assumed to be 8MHz which is more than five times the maximum baseband frequency. In this situation, by using eighth-order Bessel filters at the outputs of quadrature channels, the aliased spectrum is attenuated to more than 40dB below the baseband primary chirp spectrum. Choosing f_c = 8MHz, means that 8000 time samples are needed to generate the baseband chirp in a one millisecond period. These 8000 time samples are clocked by 8000 clock pulses. Since the digital up/down counter first counts downwards for 4000 pulses and then counts upwards for 4000 pulses, it needs 12 binary bits (2^{12} or 4096 potential addresses) to cover all the 4000 addresses required to access the parabolic phase memory. For the sine and cosine memories, any amplitude level corresponding to a particular phase angle between zero and 360 degrees has to be digitised to a certain number of binary bits, which means that there is always a phase quantisation error. Assuming that m bits are allocated for each channel, figure 4.13 shows the in-phase and quadrature channels on a complex (real-imaginary) plane and the unit radius circle with the rotating vector which represents the chirp signal at the output of the SSB modulator. The angular velocity of the rotating vector is linear with time, starting from $(co_o$-27cp.T/2) and increasing to $(co_o$+2nuT/2) after T seconds. The grid illustrated in figure 4.13 represents the allowed quantised levels of the I and Q DACs and the acceptable instantaneous states of the rotating vector. Having m digital bits for each quadrature channel, means 2m quantised levels with the following step size:

$$Ac = \frac{2}{2^m-1} \qquad \text{...4.20}$$

The maximum quantisation error is half Ac, because if the increment in the amplitude of either I or Q is less than AE/2, the rotating vector stays at its present state and if the increment is more than Ae/2, the rotating vector jumps to the next acceptable state. Thus from figure 4.13 and equation 4.20, the maximum phase uncertainty in the location of the rotating vector is (Griffiths, 1986):

$$AO = \tan^{-1}\left|\begin{matrix}Ac\\2\ \ 1\\1\end{matrix}\right| =\tan\ li\ \begin{matrix}1\ \ 1\\2^{m}-1\end{matrix}$$

...4.21

Figure 4.14 shows the amount of phase error versus the number of digital bits of the sine and cosine memories. Since the quantised phase error varies with the clock frequency f_c, it is assumed that this type of phase error has a dominant sinusoidal component given by the following expression:

$$Act{:}\bullet\,(t) = 64.\sin[27rf_{c}t] = [\tan^{-1}\ \frac{1,}{2^{,,}-1}\ \bullet\sin[27cf_{c}t]$$

...4.22

This periodic phase error is added to the parabolic phase function of the baseband chirp and the combined phase is expanded by the multiplication factor of the frequency multiplier. Apart from the phase error due to the digital generation of the chirp signal, other errors can also arise from the SSB modulator and frequency multiplier. Therefore, by considering all these phases, the final output of the chirp generator can be expressed as:

$$V(t) = \cos[2nft+2n\,\frac{P.}{2}\,t^{2}i\text{-}cb(t)]$$

...4.23

where (I)(t) is the total phase error (which is the sum of $AO_a(t)$ due to the analogue parts of the chirp generator and $Act,_d(t)$ which is the phase error AO(t) due to digital quadrature memories multiplied by the frequency multiplication factor N). Assuming similar transmitter and receiver chirp generators, the radar point target response is found by mixing expression 4.23 with a delayed version of its replica. This, after low-pass filtering, provides the following waveform at the output of the full-deramp mixer:

$$V(t) = \cos[mu_{d}t+[2nt_{d}+ngt_{d}^{2}]+(1)(t+t_{d})-001$$

...4.24

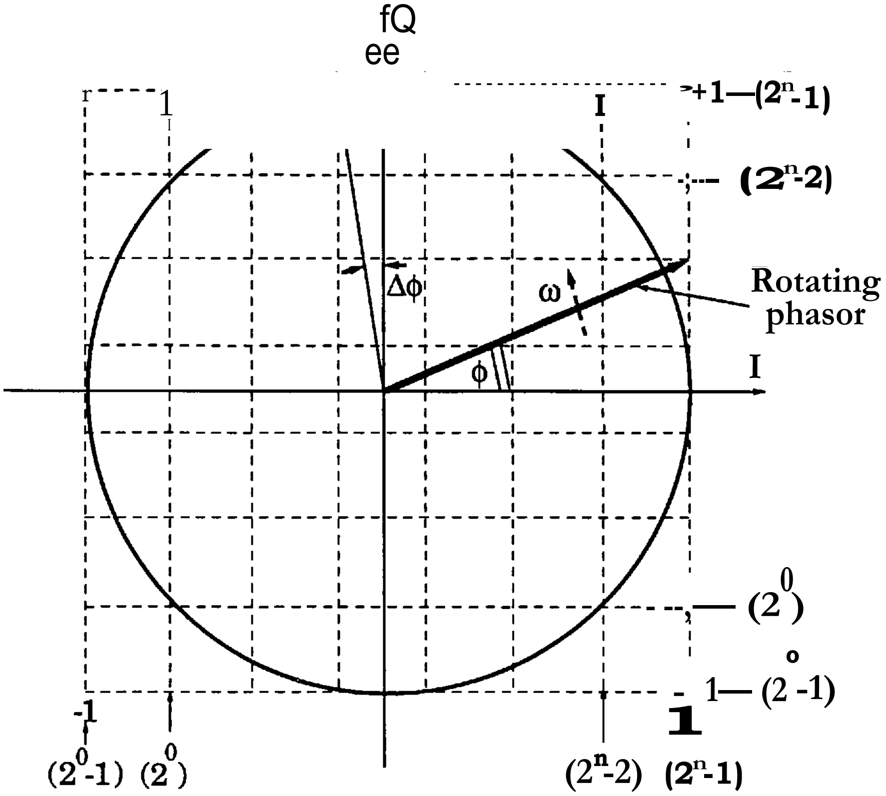

Figure 4.13- Quantised nature of I and Q channels

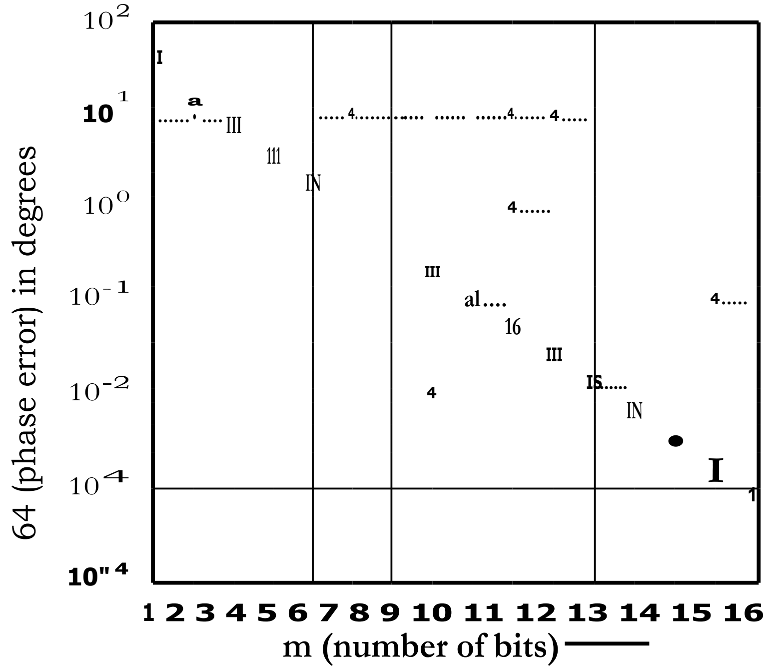

Figure 4.14- Phase error versus number of bits in a chirp generator

In this equation the first term of the cosine argument is the beat frequency of the point target which gives the sinc function in the frequency domain. The next two terms enclosed are constant phases and the last two terms are due to phase error. In the phase error analysis of a chirp radar which employs a matched filter, the classical method is based on the paired-echo concept (Klauder et al., 1960; Cook and Bernfeld, 1967) in which the phase error is assumed to be a periodic function with a dominant sinusoidal component. Adopting this concept for the full-deramp technique, which is the frequency domain equivalent of the matched filter method, b(t) is taken as:

$$OW = (D_o \sin(\bar{a} v_o t) \qquad \text{...4.25}$$

where (N**is the peak phase error and v_o is the frequency of the phase error function. In equation 4.24, which provides the general form of the phase modulation, the maximum sidelobe level of a pure phase modulation process occurs when the modulating function is at a maximum. This argument for the modulating function of equation 4.25, means that:**

$$\max[0(t+t_d)\ \_\ OW] = \max[Co\sin[2nv_o(t+t_d)]\ \_\ O_0\sin[27tv_o t]] = 2cD_o\sin(2nv_o t)$$

To obtain the worst case sidelobes due to phase error, the above expression is inserted in equation 4.24. Then after neglecting the constant phases terms, the result can be replaced by a Bessel function expression, yielding:

$$v(t) = J_0(20\ )\bullet\cos[nin_d t]\ -\overset{oo}{\underset{n=1}{\mathbf{D}}}_n(240(\cos[(p.t_d-2nv_o)nt]\ +(-1)^n\cos[(1.tt_d+2nv_o)nt])$$

...4.26

where Ji (20$_0$) **is Bessel function of the first kind and** ith **order. Equation 4.26 implies that the Fourier transformed output of the full-deramp mixer consists of infinite pairs of sinc-shaped spurious responses on either side of**

the main point target response. These spurious components are called paired-echoes. Figure 4.15 gives the first four Bessel functions for different arguments. From this figure, for a small peak phase error (i.e. $2cD_0 < 0.5$ Radians) J. and J_1 are the dominant terms and equation 4.26 will be reduced to:

$$v(t) = J_0(20_0)\bullet\cos[mAt_d t] - J_i(20\ )\cos[4a_d t - 2av_o t] - \cos[ngt_d t + 2/cv_o t]] \qquad ...4.27$$

Thus, under the condition of having relatively small phase error, only one paired-echo is present. In this situation the peak spurious level to the peak point target response is a measure of the tolerable phase distortion:

$$SLL = 20\log\frac{J,(2(1_o))}{J_0(2O_0)} \qquad ...4.28$$

Figure 4.16 illustrates the relative level of the paired-echo as a function of the peak phase error.

Spurious responses can also occur when there is an unwanted amplitude variation on the chirp signal. Taking a simple amplitude modulating signal $[a_0 + a_i\cos 2\ddot{n}iit]$, where a_o is a constant, a_1 is the peak amplitude of the signal and fl is its frequency; applying this signal to expression 4.27 gives the composite point target response affected by phase and amplitude errors:

$$\begin{aligned}
v_{AM,4)}(t) &= A(t)\bullet v(t) = a_o J_o(20_o)\cos(np.t_d t) \\
&0.5a_1 J.(20.)[\cos n(gt_d+211)t + \cos 7c(Rt_d-21)t] - \\
&a_0 J_i(2O_0)[\cos n(p.t_d-2v.)t - \cos 7c01t_d+2vdt] + \\
&0.5a_1 J_1(20)[\cos n(gt_d+211-2v.)t + \cos n(gt_d-21-2v_o)t1 + \\
&0.5a_1 J_1(20_0)[cosic(lt_d+271+2v_0)t + \cos n(i.tt_d-211+2v_0)t]
\end{aligned} \qquad ...4.29$$

This expression has one-paired echo corresponding to phase error, one paired-echo corresponding to amplitude error and two paired-echoes as a

result of having both amplitude and phase errors. Now, if there is only spurious amplitude modulation on the chirp signal, equation 4.29 is reduced to:

$$v(t) = a_o\cos(741t_dt) + \frac{a1}{2}[\cos(m.a_dt\text{-}1\text{-}27cnt)+\cos(m.a_dt\ \text{-}2/cit)] \qquad ...4.30$$

Figure 4.17 illustrates the relative peak level of the AM paired-echo [20log($a_1/2a_0$)] as a function of the spurious amplitude ripple (1+a_1/a_0). By using diagrams 4.16 and 4.17, the error budget in the design of the different sections of the digital chirp generator can be worked out.

The extent to which the spurious level has to be kept low depends on the dynamic range of echo signals from the altimeter footprint. It has to be noted that this is a local dynamic range which is different from the receiver dynamic range explained earlier. Assuming that the local dynamic range is less than 25dB, the spurious level has to be less than -25dB to avoid masking low reflectivity targets by spurious sidelobes. Keeping AM spurious sidelobes lower than say -30dB is not very difficult, since from figure 4.17 this level corresponds to 0.5dB amplitude ripple which is relatively easy to achieve by using proper amplitude limiters. However, controlling the phase error needs more attention. From figure 4.16, the relative spurious level of -25dB corresponds to 20_0= 7°, so the chirp generator should not introduce an output phase error of more than 4:1)$_0$= 3.5°. In the analogue section of the chirp generator, the precautions which have to be considered in reducing the phase error are as follows:

1 Employing wide-band devices to minimise phase nonlinearity,
2 Employing carefully designed linear-phase filters,
3 Employing suitable limiters to avoid amplitude modulation which might convert to phase modulation later because of system non-linearity,
4 Providing fine adjustment and control of amplitude balance and phase balance in the SSB modulator.

These precautions have been investigated in detail by Khosrowbeygi (1988).

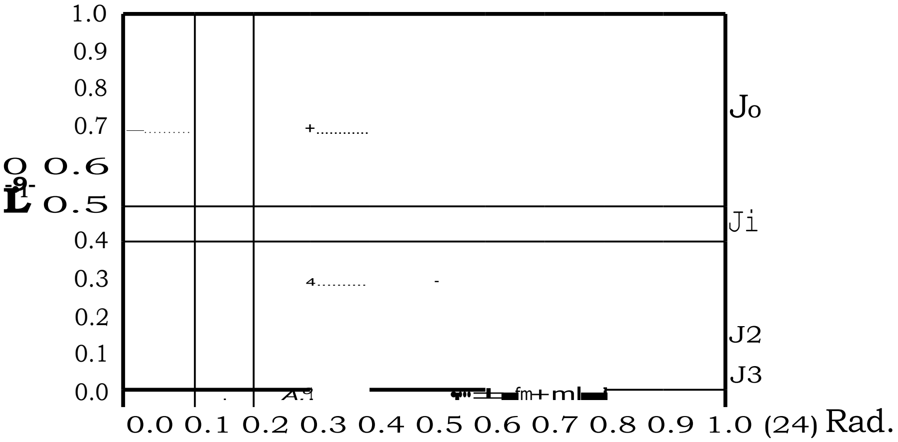

Figure 4.15- The first four Bessel functions, (after Klauder et al., 1960)

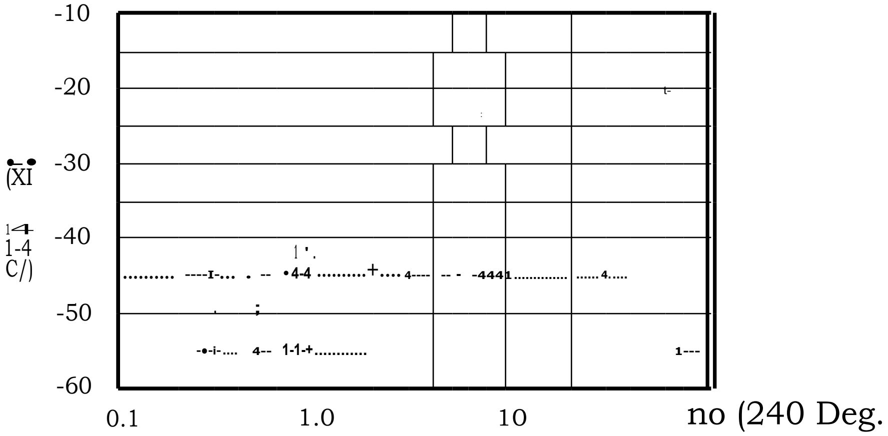

Figure 4.16- Relative level of paired-echo versus phase error, (after Klauder et al., 1960).

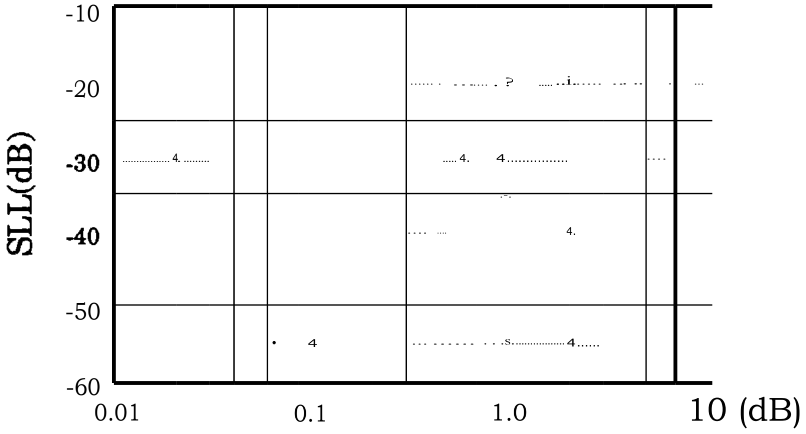

Figure 4.17- Relative level of paired-echo versus spurious amplitude error, (after Klauder et al., 1960)

For the digital section of the chirp generator, the quantisation phase error is sensitive to the number of digital bits of the quadrature memories (figure 4.14). Having 8 bits means 0.22° phase error at baseband. After a x16 frequency multiplication which takes the 1.5625MHz baseband chirp bandwidth to 50MHz bandwidth at the output of chirp generator, the quantisation phase error increases to b0=16 x 0.22°-= 3.5°. This amount of phase error is marginally acceptable to keep the spurious sidelobe level to less than -25dB. However as expressed by equation 4.22, this phase error has a frequency of f_c, so for the experimental radar (f_c = 8MHz) from equation 4.26 the first paired-echo corresponding to the quantisation phase error is at ±8MHz from the radar point target response. This distance is much larger than the frequency domain range window, so in effect there is little contribution from quantisation phase error on the range window spurious level. In any case, generally in the design of a chirp generator, the number of digital bits has to be sufficiently large and the clock frequency has to be much higher than the baseband chirp spectrum. Also using anti-aliasing filters along with interstage band-pass filters in the frequency multiplier chain considerably reduces the quantisation phase error.

To complete this section, the laboratory results of the experimental radar chirp signal generation and up-conversion at different stages from the baseband to the final microwave signal are given. Figure 4.18 provides the block diagram of the entire chirp generator with interstage amplifiers, filters and amplitude limiters. Figure 4.19 shows a detail of the I and Q channels of the baseband chirp signal as seen on the oscilloscope screen. In this figure the centre of the waveforms can be assumed as t = 0 (considering a single chirp interval -T/2 < t < +T/2). For the cosine signal, when the time approaches zero from t < 0, its frequency tends to zero. On the other side when time crosses zero towards t > 0, the frequency of the cosine starts increasing in a continuous manner having 0° phase difference compared to negative time. For the sine signal when time approaches zero from t < 0, its frequency tends to zero. However, on the other side when time crosses zero towards t > 0, the frequency of the sine starts increasing with a 180° phase difference compared to the negative time. Considering this behaviour, if

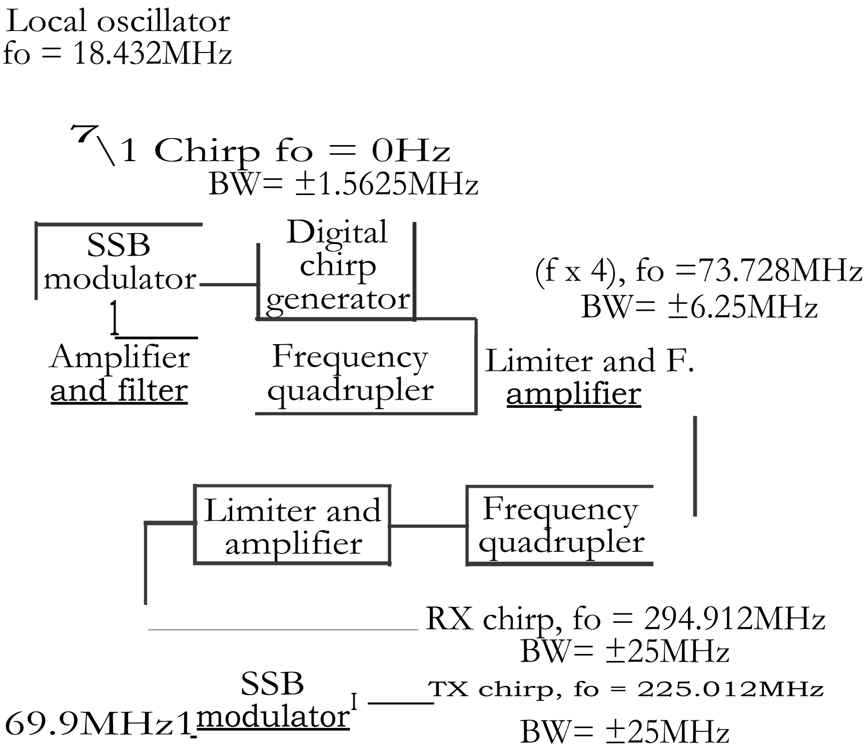

Figure 4.18- Block diagram of the experimental radar TX/RX chirp generator.

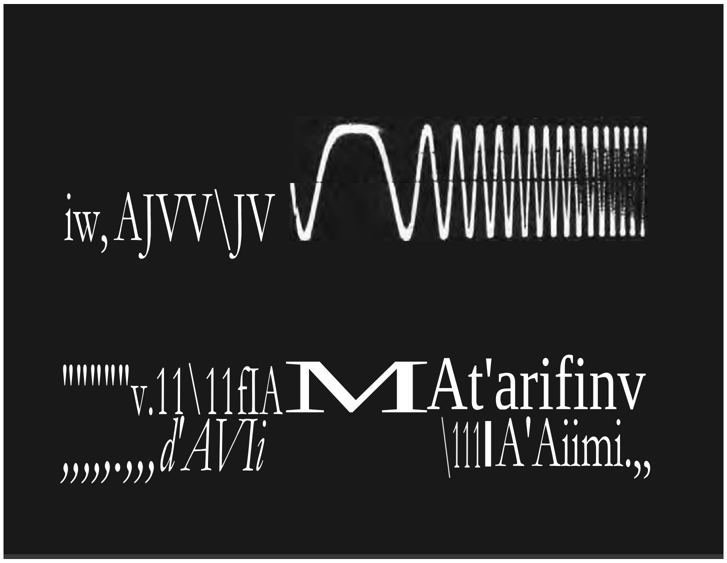

Figure 4.19- Baseband sine and cosine chirps as seen on the oscilloscope screen.

these I and Q baseband signals are injected into the SSB modulator the resultant output will be:

$t < 0$ —) $40 = \sin co_b t$ and $Q(t) = coscu_b t$

$v_{SSB\ (t)} = I.\sin co_i t + Q\cos co_i t = \cos[(cu_i - \mathbf{CO}_{dt}]$ ...4.31

$t > 0$ —) $I(t) = \sin (it + o)_b)t = -\sin co_i \mathbf{l}$ and $Q(t) = \cos co_b t$

$v_{S\ SB\ (t)} = I.\sin w_i t + \bullet \cos co_i t = \cos[(o)_i + co_b)t]$ ...4.32

where co_b is the frequency of the baseband **I and Q signals which varies linearly with time between 0Hz and 1.5625MHz, and co_i is** the LO frequency of the SSB modulator. The output frequency of the SSB modulator given in equations 4.31 and 4.32 shows that having a pair of baseband quadrature signals with a 180° phase shift for half the interval in one channel provides a sinusoidal output with an instantaneous frequency which varies linearly from $(co_i - co_b)$ to $(o1/2 + co_b)$ during the chirp interval. This means that effectively the bandwidth of the baseband chirp has been doubled.

Figures 4.20, 4.21 and 4.22 display the chirp spectrum at the output of the SSB modulator, at the output of the chirp generator after x16 frequency multiplication and at the output of the Ku band microwave up-converter.

To examine the point target response of a radar altimeter, the basic approach is to mix the transmitter microwave chirp, after applying a delay equivalent to the two-way range of the radar to the ground (i.e. 2psec), with the receiver LO microwave chirp. Thus the output of the mixer will be the point target response which can be investigated either in the IF band or at baseband, figure 4.23. To generate a 2gsec delay at 13.5GHz by using a long waveguide delay-line is not practical because of its huge weight and volume. The use of a long microwave coaxial cable is not suitable because it causes phase distortion which affects the whole point target response test.

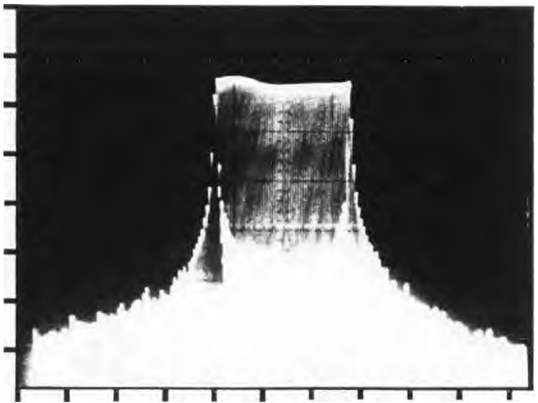

Figure 4.20- Chirp spectra at the output of the SSB up-converter, fo = 18.432MHz, BW= ±1.5625MHz

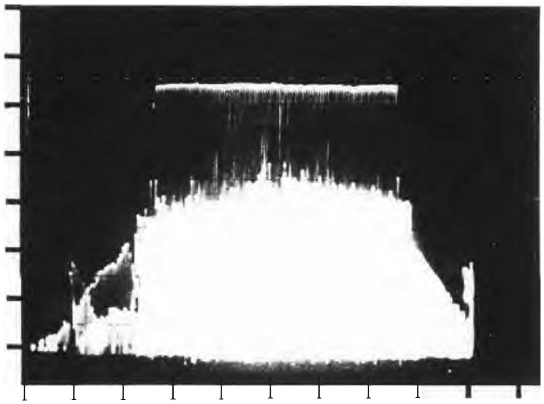

Figure 4.21- Chirp spectra at the output of the frequency multiplier, fo = 294.912MHz, BW= ±25MHz

Figure 4.22- Chirp spectra up-converted to microwave frequency, fo = 13.570912GHz, BW= ±25MHz

Consequently, for the experimental synthetic aperture altimeter, the primary point target response test has been carried out at RF by means of a very long coaxial delay line, and the microwave test has been performed by corner reflectors (as explained in Chapter 5). The result of test on the RF chirp signals is illustrated in figure 4.24 which gives both the linear and logarithmic scale versions of the point target response as seen on the spectrum analyser screen. This waveform, as expected has a sinx/x shape and the level of the sidelobes is a combination of the ideal point target response, phase and amplitude errors of the chirp signals and inherent amplitude tapering of the TX chirp because of the band-pass nature of delay line cable. As a result, although for the ideal rectangular weighting chirp, the sidelobe level is about -13dB relative to the main lobe, it was still possible to obtain a sidelobe level of about -23dB in the actual test [N.B. There is also another effect which is important in determining the sidelobe levels, and that is the periodic nature of the chirp signal, as discussed in Chapter 5].

4.5 *Receiver design*

In section 4.1, the receiver front-end (comprising a rectangular horn antenna with about 25dB gain, a microwave band-pass filter, and a microwave full-deramp mixer which directly down-converts all the received echoes to 70MHz IF frequency) was explained. It was also shown that the minimum received power is -113dBm, so after considering the loss of the passive components, the minimum power level at the input of IF amplifier is -123dBm. From the calculated dynamic range of the system (DR = 33dB), the maximum power level at this stage is -90dBm. The IF signal is amplified and down-converted to baseband to form a pair of I and Q channels. These two outputs are passed through linear phase low-pass filters to attenuate the unwanted frequency components outside the desired range window (i.e. ±16kHz) and to avoid aliasing problems in the digital signal processor. The resultant signals are then digitised by two ADCs, whose outputs are stored in a digital recorder to be used as input data of an off-line computer. This processes them by the FFT method to give the range information and by coherent correlation to generate the along-track narrow

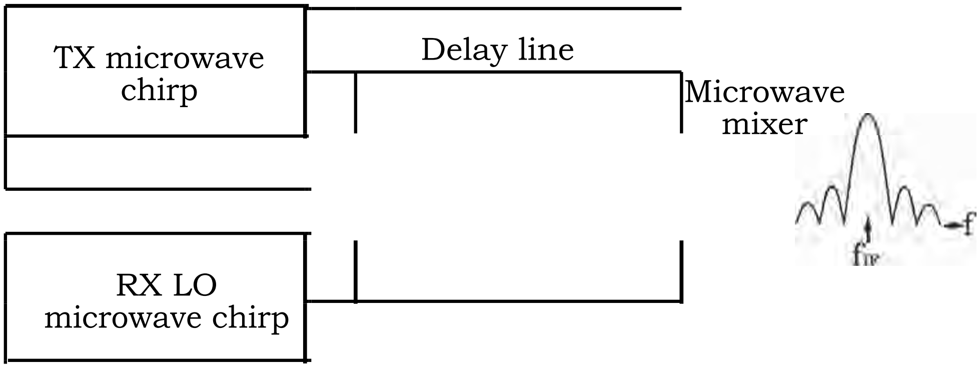

Figure 4.23- Point target test of a chirp radar

Linear scale

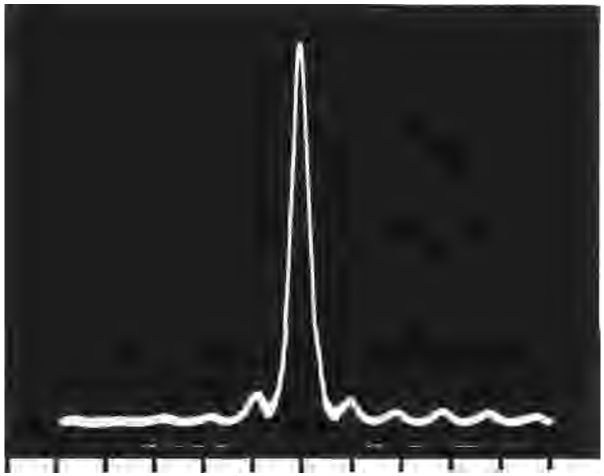

Logarithmic scale

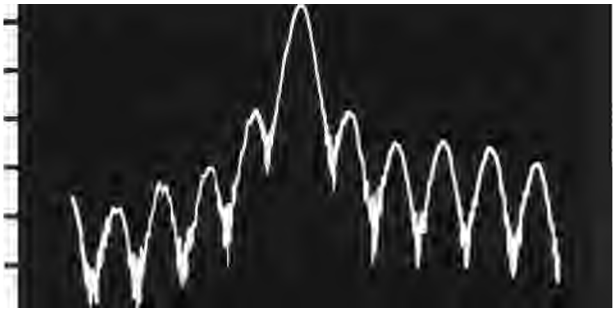

(1kHz/div)

Figure 4.24- Point target response of the experimental radar as seen on the spectrum analyser screen, fo = 69.925MHz, IF bandwidth = 0.3kHz.

beam (figure 4.25). The actual signal processing algorithms will be discussed in Chapter 5.

After all the analogue frequency conversions, amplifications and filterings, the I and Q composite signals are ready to be digitised for processing. The power level at the output of the baseband quadrature channels changes between a minimum and a maximum with a difference which determines the dynamic range. After amplitude quantisation, the phase of the i^{th} received waveform is given by the ratio of the digitised I and Q components:

$$Q_i = \tan^{-1}\Big[4 \Big| \qquad \text{...4.33}$$

The synthetic beam can be generated by storing the I and Q components of the n received waveforms and by coherently summing them (as explained in Chapter 3 and by equations 3.73 and 3.75). This implies that to maintain the coherency of the digital correlation process, the phase given by equation 4.33 should contain an error of less than that given by equations 4.14, 4.15 and 4.19. At the input of the digital processor, a particular phase error is generated which is the result of the amplitude quantisation of the analogue channels and the uncertainty which exists in the amplitudes of 4 and Q_i in equation 4.33. In section 4.4, the relationship between the number of digital bits and the phase error of the digital chirp generator was given (equation 4.21). For example, having only one digital bit for the minimum level of the signal, there is 45° uncertainty in the digital interpretation of phase. Consequently, for coherent digital signal processing two conditions exist which determine the number of bits for the ADCs. Firstly, the minimum number of bits (n_i) required for translating the minimum received signal into a digital number which is governed by the acceptable phase error of the synthetic aperture process given by equations 4.14, 4.15 and 4.19. Secondly, to cover the signal dynamic range at the input of ADCs, the minimum number of bits (n_2) required for translating all the signal levels into digital numbers is given by equation 3.67. These are depicted in the complex plane of figure 4.26, from which the minimum number of bits (n) required for the ADCs to satisfy both the above conditions is given by:

$$n = n_1 + n_2 \quad \text{bits} \qquad \text{...4.34}$$

For the above expression, instead of equation 3.67, a more accurate equation for the number of digital bits to give a particular dynamic range, DR, is used. This is on the basis of quantisation noise power of a uniform ADC which results in the following well-known expression for DR, (Bellanger, 1984):

$$\mathrm{DR(dB)} = 6.02 \times n + 1.76 \qquad \text{...4.35}$$

This more accurate equation for the dynamic range has a difference of only 1.76dB compared to the simple result of expression 3.67. Now using equations 4.21 and 4.35 in equation 4.34 provides:

$$n = \frac{1}{6.02}\left[\mathrm{DR(dB)} - 1.76 + 20\log\left[1 + \frac{1}{\tan(4)}\right[\right| \qquad \text{...4.36}$$

Knowing the dynamic range DR of the radar, and the allowable phase error 64 per spatial sample for the synthetic aperture process, the minimum number of bits n for the ADCs can be easily calculated from equation 4.36. For the experimental system DR is 33dB and AO is 0.12 Radians. Inserting these numbers in equation 4.36 shows that ADCs should have at least 8 bits.

Once the output signals of the quadrature channels are properly digitised and recorded, an off-line computer will be used to process the stored data. This will be explained in Chapter 5, but to conclude Chapter 4, figures 4.27, 4.28 and 4.29 show the master frequency generator, the receiver and the receiver/transmitter chirp generator built for the prototype experimental synthetic aperture radar altimeter [N.B. the complete circuit diagrams of all sections of the prototype radar are given in Appendix 4].

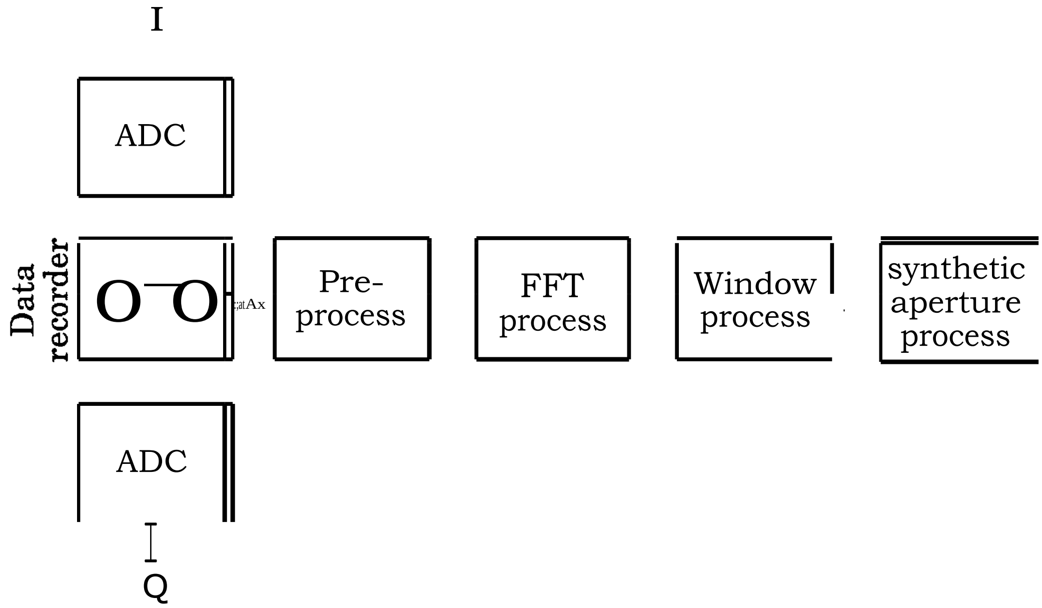

Figure 4.25- Signal processing steps for the experimental radar altimeter.

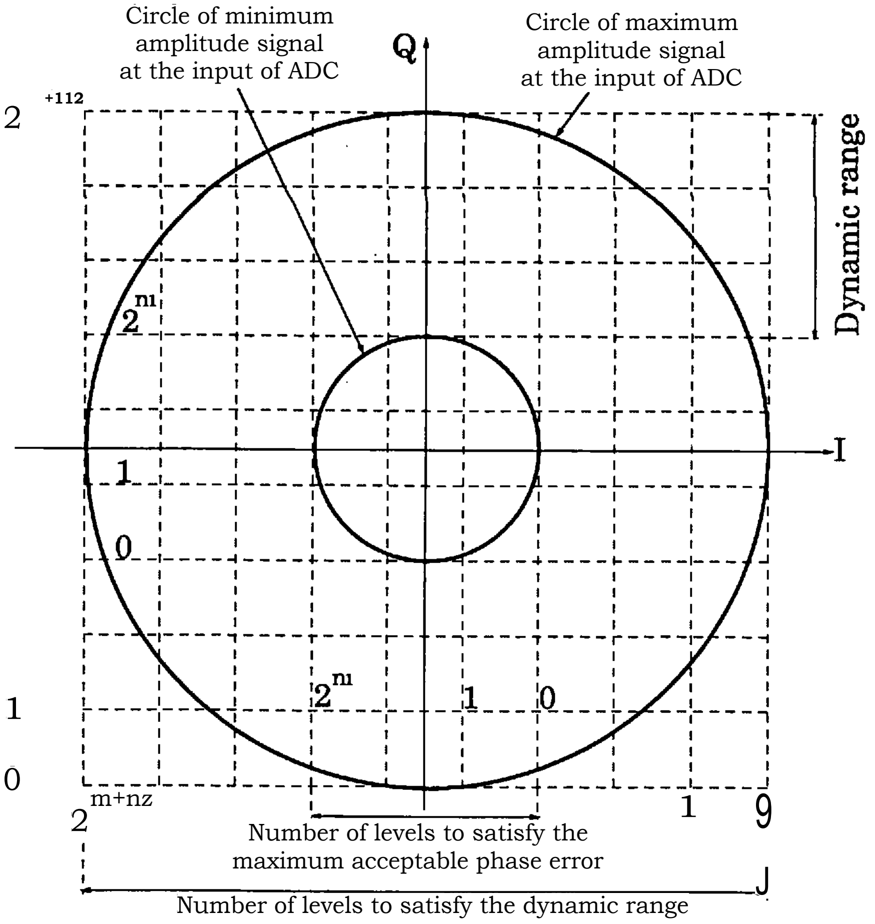

Figure 4.26- I/Q Amplitude quantisation in a coherent radar in order to preserve phase information.

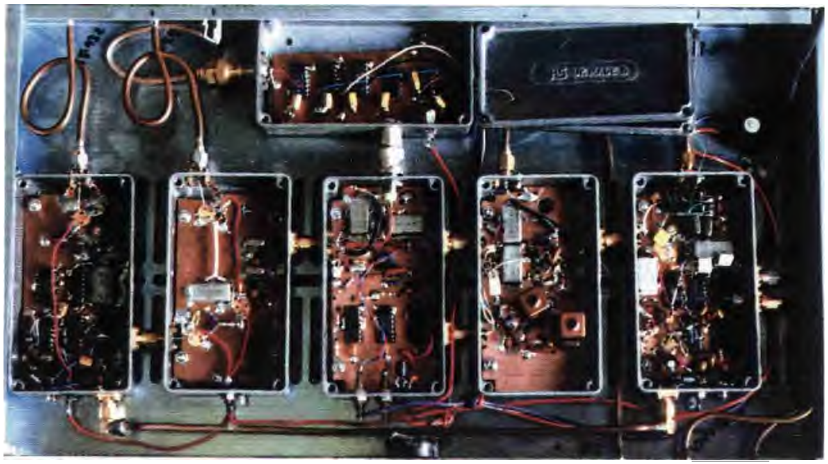

Figure 4.27- Master frequency generator.

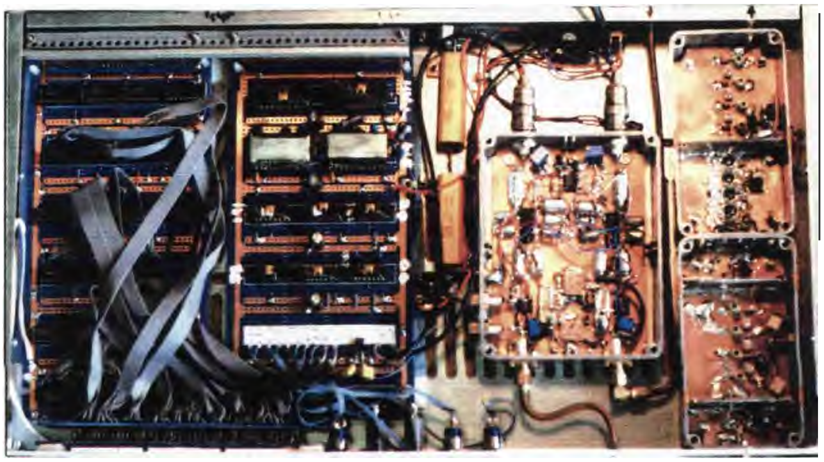

Figure 4.28- Receiver.

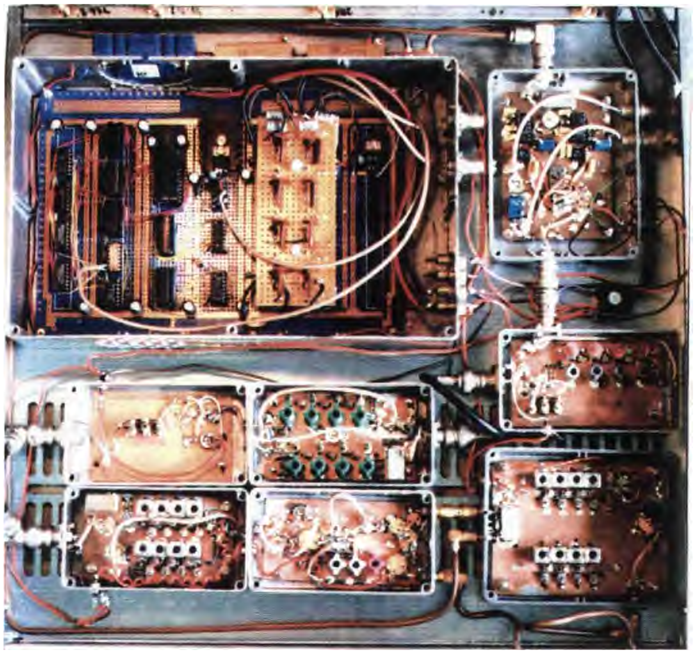

Figure 4.29- Receiver/transmitter chirp generator.

Chapter 5

Experiments and signal processing

Following the design, construction and laboratory testing of the prototype synthetic aperture altimeter, this chapter explains some fundamental experiments arranged for the instrument and signal processing of the acquired data, to examine the performance of the radar and the validity of the signal processing results.

5.1 *Synthetic phased array and its signal processing*

The ultimate test of the experimental synthetic aperture altimeter has to be carried out in a real environment on board a low-flying aircraft. However, it is possible to arrange a series of simpler 'out-of-window' experiments to evaluate the fundamental properties of the prototype system, since this particular synthetic aperture processing can be considered as a phased array radar (explained in Chapter 3). The main difference between the out-of-window and aircraft-borne experiments is that the latter has an inherent Doppler frequency shift during the sampling interval caused by the relative velocity of the platform with respect to targets, whereas in the former no Doppler effect is involved. However, in Chapter 3, it was explained that this Doppler effect for a synthetic aperture altimeter is insignificant and the fictitious stop-start pattern of the platform motion is valid. The stop-start assumption is even valid to a high degree of precision for normal spacecraft-borne SARs such as the one carried by SEASAT (Barber, 1985).

For the out-of-window experiments, the radar is installed on a triangular optical bench at a suitable distance from the targets. The radar is then moved along the optical bench in equal length steps (simulating the stop-start pattern). At any spatial step, a chirped pulse is transmitted and the received signal is digitised and stored. Thus at the end, a series of spatial samples have been collected for synthesising a narrow along-track beam. This method of generating a narrow beam can be called a 'sequentially sampled phased array radar' or a 'synthetic phased array radar'.

In a real (aperture) phased array radar, figure 5.1, N transmit/receive elements exist, sending pulses towards and receiving echoes from a target at a distance such that the wavefront can be assumed planar. The echo of a pulse transmitted by any individual transmit element is received by all N receive elements each having a different delay (because of the off-boresight angle, 0,of the target). Hence the total received voltage by the nth received element caused by all the transmit elements is:

$$v_n = \mathrm{exP.j}[\ \mathbf{f\text{-}}\,(\mathbf{Ri}+\mathbf{R_n}) + \mathbf{R1} + 13_{\mathbf{n}}] + \mathrm{expj}[\ -\ ?\ (R_2 + Rd + R_2 + (^{3}{}_{\mathbf{n}}] + \cdots\cdots$$

$$+\ \mathbf{expj}[\ -2L^{1}(\mathbf{R_N} + R_n) + 13_{N}I - P_{\mathbf{n}}] = \mathrm{expj}[\ 2i\!\!-\,R_{\mathbf{n}} + I3_{\mathbf{n}}]\underset{i=1}{\overset{N}{\mathbf{I}}}\mathbf{expj}[\ ^{21}\mathbf{R}_i + D0$$

where $r3_n$ is the phase shift of the nth transmit/receive element and R_n is the distance of the nth element to the target. The total received voltage by the entire array v_n is the sum of the signals received by each element, which is:

$$V_o = \underset{n=1}{\overset{N}{\mathbf{1}_i}} v_n = \underset{n=1}{\overset{N}{\mathbf{1}_i}} \mathrm{expj}[\ -Zi\!\!-\,R_n + 13_n]\underset{i=1}{\overset{N}{\blacksquare_i}}\mathrm{expj}[\ in.\ R_i + D_i]] = [\underset{n=1}{\overset{N}{\mathbf{I}}}\mathbf{expj}[\ 2_{\lambda}\!-\,\mathbf{R}_n + R_n]\mathbf{l}$$

5.1

In a linear array R_n and O_n are given by:

$\mathbf{R_{n=}\ R_1 - (n-1).d.sin0}$ **and** $\mathbf{P_n = n.13_1}$ **(n=1,2,3, ..,N)** **...5.2**

Substituting from the above expression in equation 5.1 gives:

$$V_o = e\mathbf{xpj}[\ -\mathbf{ll}\ R_1 + 13_1]\underset{n=1}{\overset{N}{\mathbf{I}}}\mathbf{expj}[(n-1).T]$$

...5.3

where:

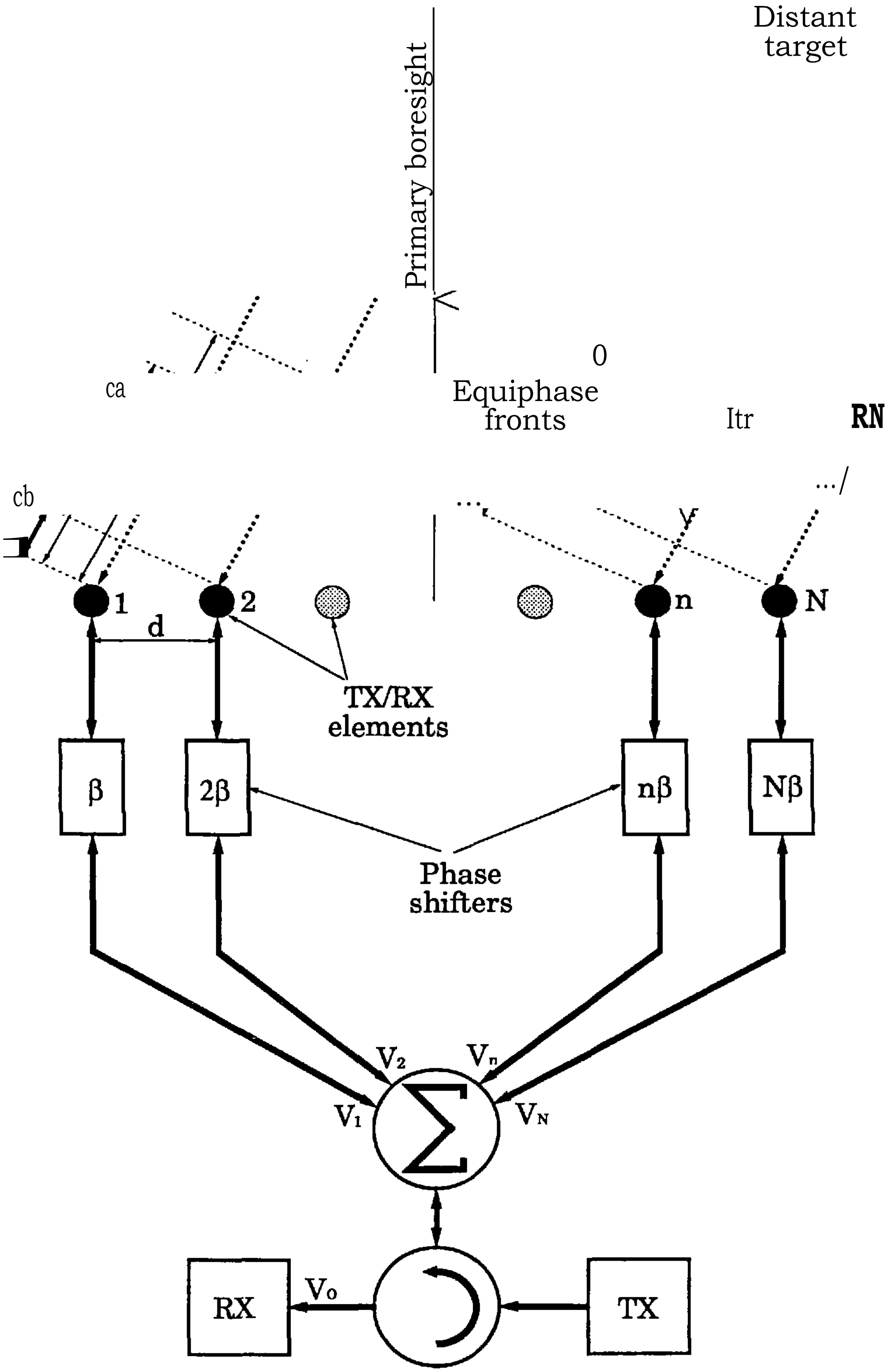

Figure 5.1- Real phased array

$$\mathrm{IP}= - \mathrm{IL}\ d\cdot\sin 0 + 13_1 \qquad ...5.4$$

Squaring the total output voltage given by equation 5.3, and knowing that the summation in equation 5.3 is a geometric series having a sinx/x closed form, yields the two-way power pattern of the phased array radar, and in its normalised form:

$$2\ \left| \frac{\sin \frac{\mathrm{WI}'}{2}}{N\cdot\sin \frac{\mathrm{IP}}{2}} \right|^{4} \qquad ...5.5$$

For a synthetic phased array radar (figure 5.2), there is only one transmit/receive element, which is moved along-track, sending pulses towards and receiving echoes from a target at a distance such that the wavefront can be assumed planar. The echo of a pulse emitted by the transmit element is received only by the accompanying receive element, because there is no other element. Thus the received voltage by the **nth** receive element caused by the **nth** transmit element has the following form:

$$v_{n=}\ \exp j[-\tfrac{2'}{2b}t\ 2R_n + 213_n] \qquad ...5.6$$

The summation of v_n over the entire synthetic phased array yields the total received voltage at the output which is (considering equations 5.2 and 5.4 as well):

$$\mathrm{NI}_{o=} \sum_{n=1}^{N} v_{n=}\ \exp j[\mathrm{AM}\ R_1 + 213_1] \sum_{n=1}^{N} \exp j R n - 1)2^{1}11$$

From the above expression, squaring the total output voltage yields the two-way power pattern of the synthetic phased array radar. This, after calculating the geometric summation and normalisation to unity, gives:

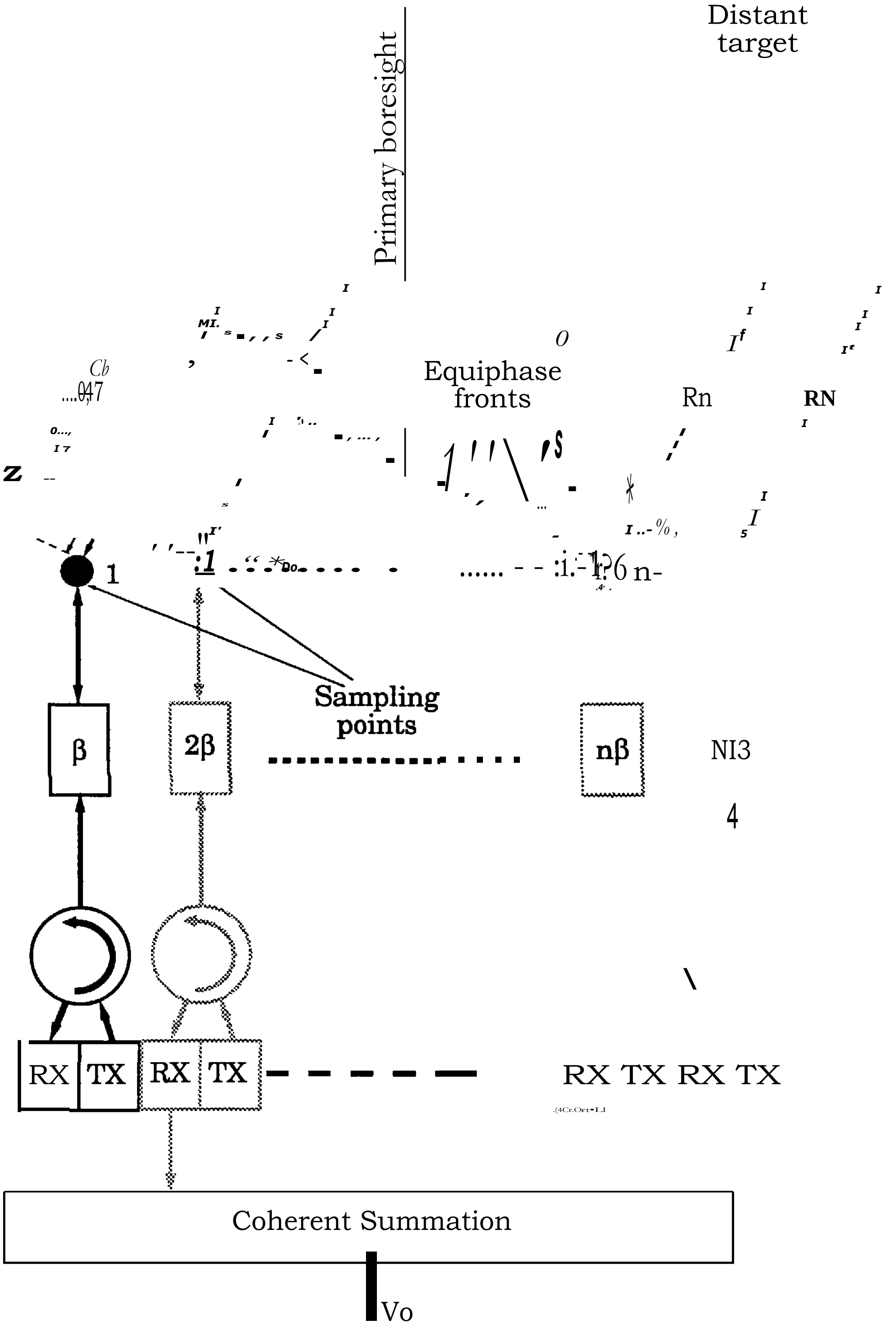

Figure 5.2- Synthetic phased array

$$\text{Geil} \quad \left. \frac{\sin N.}{N \cdot \sin T} \right|^{2} \qquad \ldots 5.7$$

This equation is the same as equation 3.26 which was obtained for the along-track power pattern of the synthetic aperture altimeter.

Comparing equations 5.7. with equation 5.5 shows that the beamwidth of the two-way power pattern of a synthetic array radar is twice as narrow as the beamwidth of the one-way power pattern of a real phased array of the same length. Also, as can be seen from equations 5.5. and 5.7, the first one is (sinNx)/(Nsinx) to the power of four but the second one is (sinNy)/(Nsiny) to the power of two. This means that in the case of uniform weighting, in a real phased array the maximum sidelobe level is about (-26dB) relative to the main lobe, whereas in a synthetic array the maximum sidelobe level is about (-13dB) relative to the main lobe. This implies that for a synthetic array, amplitude weighting of the along-track sample is more important than for a real phased array. Figure 5.3 illustrates the simulated patterns of a real array radar and a synthetic array radar, which confirm the above discussions about the two cases.

So far, the pattern analysis was on the basis of having isotropic elements. In a real situation, any individual element is a directive antenna. Assuming that all the elements have the same one-way power pattern $G_e(0)$, repeating the calculations shows that the only change in the results of equations 5.5 and 5.7 is that in both cases the two-way pattern is multiplied by the square of the elemental pattern [i.e. $G_e^2(0)$]:

$$G_{\mathrm{totai}}(e) = G_e^2(e) \cdot G \quad \{\text{where } \mathrm{Ill} = {}^{27c}\, \mathrm{dsinE}) + P_i \text{(equation 5.4)}\} \qquad \ldots 5.8$$

The beam of the elemental pattern is much broader than the beam of the

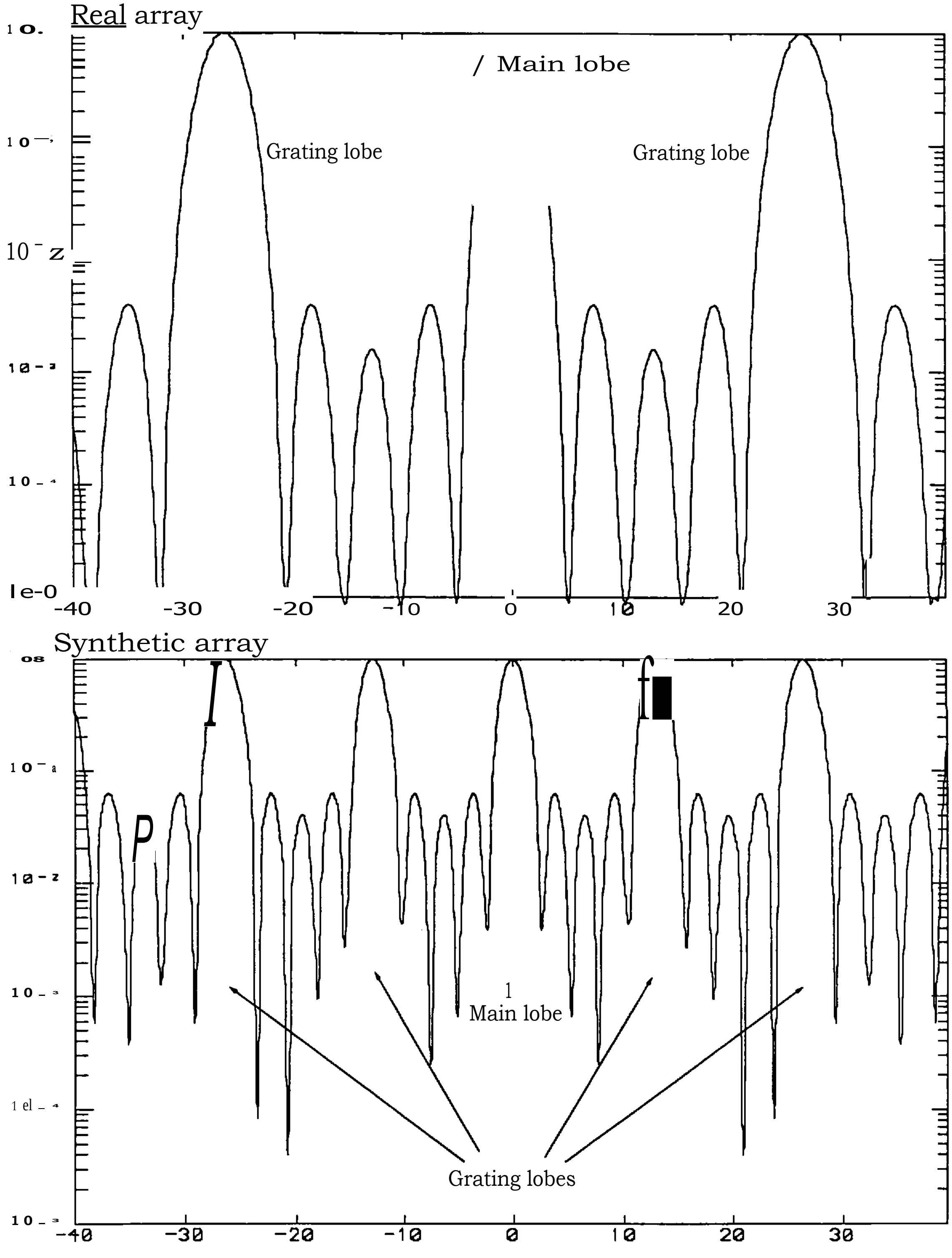

Figure 5.3- Beam pattern of real and synthetic array radars, (5 elements, 5cm spacing).

array pattern, therefore the elemental pattern has essentially no effect on the array main lobe and its surrounding sidelobes. In fact the main effect of the elemental pattern is attenuating the far-out sidelobes and grating lobes. This can be extremely useful in avoiding the reception of unwanted echoes through grating lobes which have the same power gain in the absence of the elemental pattern (figure 5.3). For the altimeter experiments, from equation 5.7 which provides the pattern of the synthetic array, the angular positions of the main beam and grating lobes are:

$$\mathrm{T.O} \qquad 0 \quad \sin^{1}[_{2d}(_{n} - m)] \; ; m = 0,+1,+2,+3,\ldots$$

...5.9

The above equation implies that the angular position of the main lobe can be scanned to a desired angle O. by properly choosing the amount of phase shift applied to the along-track samples. In other words, the required phase shifts 13_{n} to scan the main beam to angle 0_{0} are given by:

$$13_{n} = n.13_{1} = n\bullet[\,\overset{7}{2}-r\, d \sin 0_{0}] \qquad n = 1,2,3,,N$$

_5.10

Coherent summation of the along-track samples for $0_{0} = 0$ provides the normal synthetic aperture beam, and at the same time applying appropriate phase shifts to the samples provides the along-track scanning of the synthetic beam. Hence if the out-of-window experiments are arranged to cover both cases, in addition to exercising and assessing the along-track beam processing and beam scanning used in a real spaceborne synthetic aperture altimeter, (explained in Chapter 3) they will also provide experience applicable to across-track scanning.

The experimental radar does not have any hardware to generate phase shifts for the elements of the transmitter and receiver. Therefore both phase shifts will be generated digitally in the receiver signal processing software, and as a result twice the phase shift (i.e. 2%) has to be applied to the nth sample (equation 5.6). The nth along-track sample before phase shifting has an in-phase component A_n and a quadrature component B_n, therefore the nth phase shifted sample before coherent summation will be:

$$vas\ I_n+j(k= [A_n+jB_n][\cos 213_n+j\sin 213_n]$$

Inserting equation 5.10 in the above expression, the I and Q parts of the nth sample become:

$$In\ Ancos[\ _{2,}\ ndsin0_0]\ -B_{as}sin[\quad ndsin0_0]$$

$$Q_n= A_n sin[\overset{4}{p}\ ndsin0_0]\ +B_n cos[\quad ndsin0_0] \qquad ...5.11$$

Having the quadrature components of the nth sample (A_n and B_n), equations 5.11 provide the required calculations before coherent summation, in order to scan the synthetic beam to angle 0_0 After this stage, the processed synthetic pattern (coherent summation) has the following power at angle 0_0:

$$P^{o}:\ [\ ^{N}\ In]^{2}\ [\ Qn]^{2} \qquad ...5.12$$

Normally, the range processing of the synthetic aperture by the FFT method is carried out before the along-track processing, so equations 5.11 and 5.12 are applied to FFT processed output of the quadrature channels.

The out-of-window experiments are performed using corner reflector targets. This means that since the targets are easily recognisable from the background, there is no need to use a narrow across-track real beam, as would be required by a normal synthetic aperture altimeter (explained in Chapters 3 and 4). Therefore the sort of antenna required for an aircraft-borne design (2mx0.5m) can be simply replaced by a horn antenna similar to the receiver antenna of the aircraft-borne altimeter.

Almost any object capable of reflecting microwaves can be used as a test target for the radar experiments in a laboratory environment, but for field experiments where high directional accuracies are difficult to achieve, a test target should have a wide-angle scattering cross-section, insensitive to orientation (relative to the radar), (Ulaby et al., 1982). Table 5.1 gives a summary of the basic specifications of some normal test targets that are used for indoor and outdoor radar experiments.

Test target	Maximum radar cross-section (a)	Half-power beamwidth	Comments
Square flat plate	$47rA^{2}A^{2}$	0 .442Va	large a, very narrow beam
Circular flat plate	$4\ {}^{2}/)^{2}$	$o^{3}Alr$	large a, very narrow beam
Sphere	A	omniditectional	r > 2X, small a
Trihedral corner reflector	$71{:}b^{4}/3X.^{2}$	30°- 40°	large a, simple structure
Luneberg-lens reflector	$47cA^{2}/X^{2}$	max. 180°	large a, complex structure

Table 5.1: Specifications of the radar test targets (Ulaby et al., 1982)

In table 5.1, A represents the physical area for the flat plates and the cross-sectional area for the sphere and Luneberg-lens, a is the side of the square plate, b is the edge of the trihedral, and r is the radius of the circular plate.

In order to provide highly reflective, wide-angle and easy-to-make test targets, from table 5.1, the obvious choice is the trihedral corner reflector. For the field experiments, the cross-section of the trihedral corner reflectors is chosen as +30dB to overcome background reflections. Having a carrier frequency of 13.5GHz (X = 2.2cm) and a = +30dB, from table 5.1, the edge size of the trihedral reflector is 0.8m. For the field experiments, two such trihedral corner reflectors were made (figure 5.4).

Figure 5.5 shows the microwave head of the experimental radar, consisting of the transmitter and receiver horn antennas, microwave band-pass filters and isolators, a microwave amplifier to compensate for the attenuation of the signal by the coaxial cable which transfers the output of the PLL microwave oscillator placed inside the laboratory to the microwave head placed outside the window, the microwave transmit and receive chirp up-converters, the full-deramp mixer and the first stage of the 70MHz IF amplifier. The out-of-window experiments are concerned with the processing of the spatial samples of the test targets in range and along-track dimensions (i.e. a single processed aperture). This implies that the amount of digital data at the output of receiver ADCs is not significant and instead of using a digital data recorder, a digital memory can be employed inside the receiver to store the acquired data. As a result, two random-access-memories (RAMs) are installed at the output of the quadrature ADCs, and after storing individual spatial samples, the data are transferred to an off-line computer for digital signal processing (the circuit diagram of the receiver memories is given in Appendix 4). Figure 5.6 shows the prototype radar RF rack and the microwave head with their cabling ready for the experiments.

5.2 *Spectral structure of FMCW pulses*

Before starting the actual out-of-window experiments and their associated signal processing, it is worth considering the spectral structure of the received echoes from the test targets. The experimental radar altimeter transmits continuously a linear-frequency modulated carrier (centred at co_o) with chirp slope of Ix and time duration T. At the receiver, the echo signals are collected and mixed with the frequency shifted version of the same transmitted FMCW waveform in order to translate the range information into beat frequency components. In figure 5.7, the transmitted and received signals are illustrated in time-frequency coordinates, where the transmitted chirp leads the received waveform by the two-way time delay t_d. The nth transmitted pulse has the following frequency function:

Figure 5.4- Aluminium trihedral corner reflector

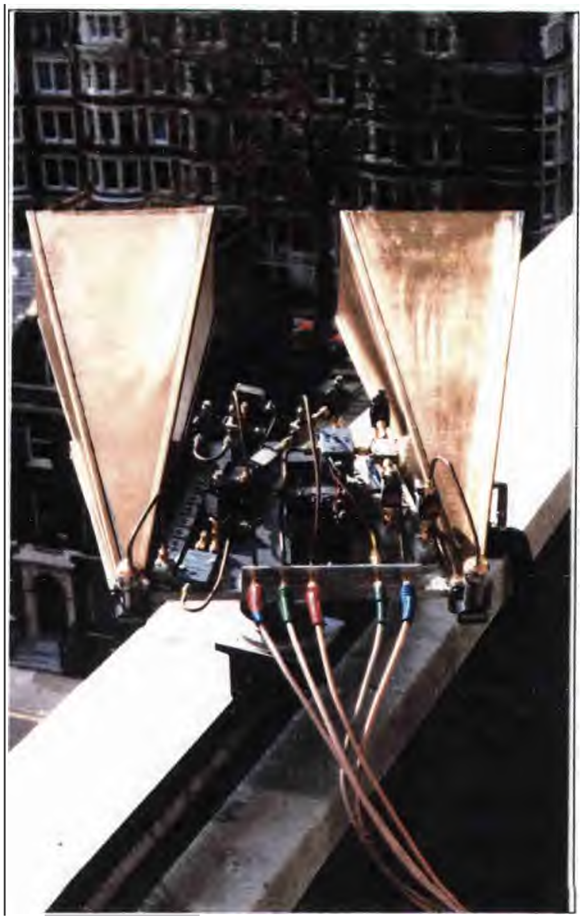

Figure 5.5- Radar microwave head on the optical bench

Figure 5.6- Radar rack and microwave head with their cablings

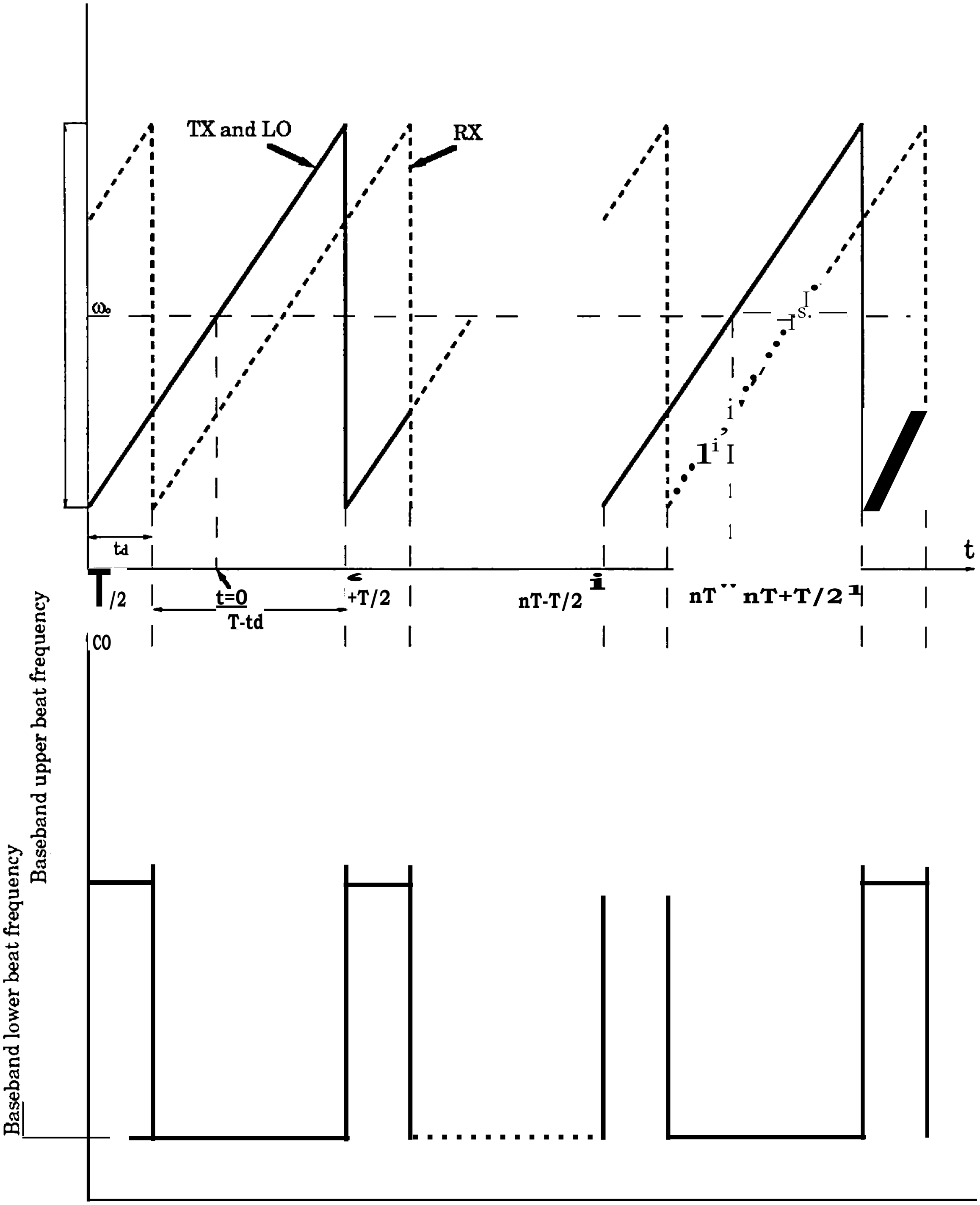

Figure 5.7- FMCW transmitted, received, local oscillator and demodulated baseband waveforms.

$$ca_r = co_o + 2irp,t_n \qquad -\frac{T}{2} < t_n < +\frac{T}{2} \qquad ...5.13$$

where:

$$t_n = t - nT \qquad 5.14$$

Substituting equation 5.14 in equation 5.13, the phase of the transmitted chirp is given by:

$$(D_T\ 4co_v dt = co_o t_n + itp.t_n^2 + nco_o T \qquad -\frac{T}{2} < t_n < +\frac{T}{2} \qquad ...5.15$$

From figure 5.7 the time interval belonging to the nth receiver LO signal (or transmitted signal) coincides first with the remainder of the (n-1)th received chirp and then with the nth received chirp for the rest of the period. Therefore the phase of received signal can be expressed by the following equations:

$$(D_{\underline{R}}\ co_{o(tn-1} - td + 7Cp.(t_{n\_i} - t_d)^2 + (n-1)\ o)T \qquad -\frac{T}{7} < t_{il} < -\frac{T}{7} + t_d$$

$$\text{OR } w_o(t_n - t_d) + ng(t_n - t_d)^2 + n\ co_0 T \qquad -\frac{T}{I} + t_d < t_n < i - _T \qquad ...5.16$$

The output of the full-deramp mixer provides the beat signals at the IF frequency. However after IF amplification, a constant frequency local oscillator is used to down-convert the IF signals to baseband. From equations 5.15 and 5.16, the baseband beat signal can be directly derived [V_B. expj(4_T -O_R)]:

$$V_{B1} = expj[co_o t_d - It\ g\ (T - t_d)^2 + 27rigt_d - T)t.] \_ \frac{T}{2} < t_n < -\frac{T}{2} + t_d$$

$$V_{/32} = expj[co_o t_d - /CPA_d^2 + 27CIIt_d t_n] \qquad -\frac{T}{2} + t_d < t_n < +\frac{T}{2} \qquad ...5.17$$

The Fourier transform of the baseband signal provides the range information:

$$\overset{+..}{} V(CO)\ 4(V_{il}e\,v_{B2}).eXpj[-cot].dt \qquad \text{...5.18}$$

Substituting expressions 5.14 and 5.17 in equation 5.18, and by applying the time limits, the Fourier transform becomes (Hymans and Lait, 1960):

$$'o))=\underset{-oo}{\overset{+\ .}{ex}}[-no)11.\ \left|\ \overset{-\frac{T}{1}+t_d}{\underset{\frac{T}{2}}{\mathbf{I}}}V_{Bi}expj[-ca_n].dt_n+\overset{+\frac{T}{2}}{\underset{2+t_d}{\mathbf{S}}}V_{B2}expj[-cot_n].dt_n\right| \qquad \text{...5.19}$$

The summation in the above equation is equivalent to an impulse comb (Bellanger, 1984):

$$\underset{n=-o.}{/}expj[-n.27cf.T1=\frac{1}{T}\underset{n=-.o}{1},8[1-\frac{1}{T}I$$

Inserting the above expression in equation 5.19, calculating the Fourier transforms and filtering out the higher beat frequency term, since it is far removed from the range window, and also knowing that the received signal is almost overlapped in time on the LO signal (i.e. T - t_d - T), the normalised amplitude of the Fourier transform output becomes:

$$V(0=\underset{n=-...}{/}S[f-\frac{121}{T}\frac{\sin[7c(gt_d-\ f)(T\ -t\,d]}{pc(Ilt_d-f)(T-t_d)]}\ \_\overset{i^{o}}{}\underset{n=-0..}{8[f}\ \ \frac{n_i}{T}\frac{\sin[it(gt_d-07}{[7cOit_d-fin} \qquad \text{...5.20}$$

The above expression provides the baseband spectrum corresponding to the full-deramp down-conversion of a point target echo. The (sinx/x) factor of equation 5.20 (having a maximum at f =1.tt$_d$) carries the range information of the point target. The existing impulse comb in equation 5.20 is the result

of the periodic FMCW signal and irrelevant to the location of the point target this part always remains stationary. Thus it can be said that the point target response of the FMCW radar consists of a stationary impulse comb with 111' frequency spacing and a sliding (sinx/x) envelope on top of the impulse comb (figure 5.8). This means that if the distance of the target to the radar is such that its associated beat frequency is an integer multiple of the PRF (PRF = VT), the main lobe of the sliding envelope will be centred on an impulse of the stationary comb and ideally all the other impulses will be nulled by the nulls of the sliding envelope. However, if the above situation does not exist, there will be two impulses in the main lobe and one impulse in any sidelobe. As an example, for the experimental radar altimeter, if the range of the point target is an integer multiple of the range resolution, nx 3 metres, after normalising to OdBm, the level of main lobe will be OdBm and there will be no sidelobes (i.e. sidelobe level will be -0. dBm). Now if the point target is displaced by only 0.6metres, there will be two impulses in the main lobe having levels of -0.5dBm and -13dBm and the levels of the first sidelobes will be -16.5dBm and -20dBm. If the target is displaced by half the range resolution, 1.5m, there will be two equal impulses in the main lobe each having a level of -4dBm and the level of the first sidelobes will be -13.5dBm.

Here it is worth mentioning that the (sinx/x) factor of equation 5.20 is exactly the same as equation 3.18, which was obtained for the range compression of a point target signature in a synthetic aperture altimeter. However in that analysis nothing was mentioned about the impulse comb, which is the result of the repetitive nature of the transmitted signal with a periodicity of PRI = T. In any case, if required, it is only a matter of multiplying the sinx/x response by the proper impulse comb. Although considering the impulse comb might be important for signal processing of point targets, to distinguish between two targets placed in successive range bins and one target placed at the boundary of the same range bins (this matter will be explored in one of the experiments), in the real altimeter, the range window consists of a bank of FFT filters each having one resolution cell width. This means that the number of FFT points per range bin is not important and for any range bin even one FFT point is sufficient.

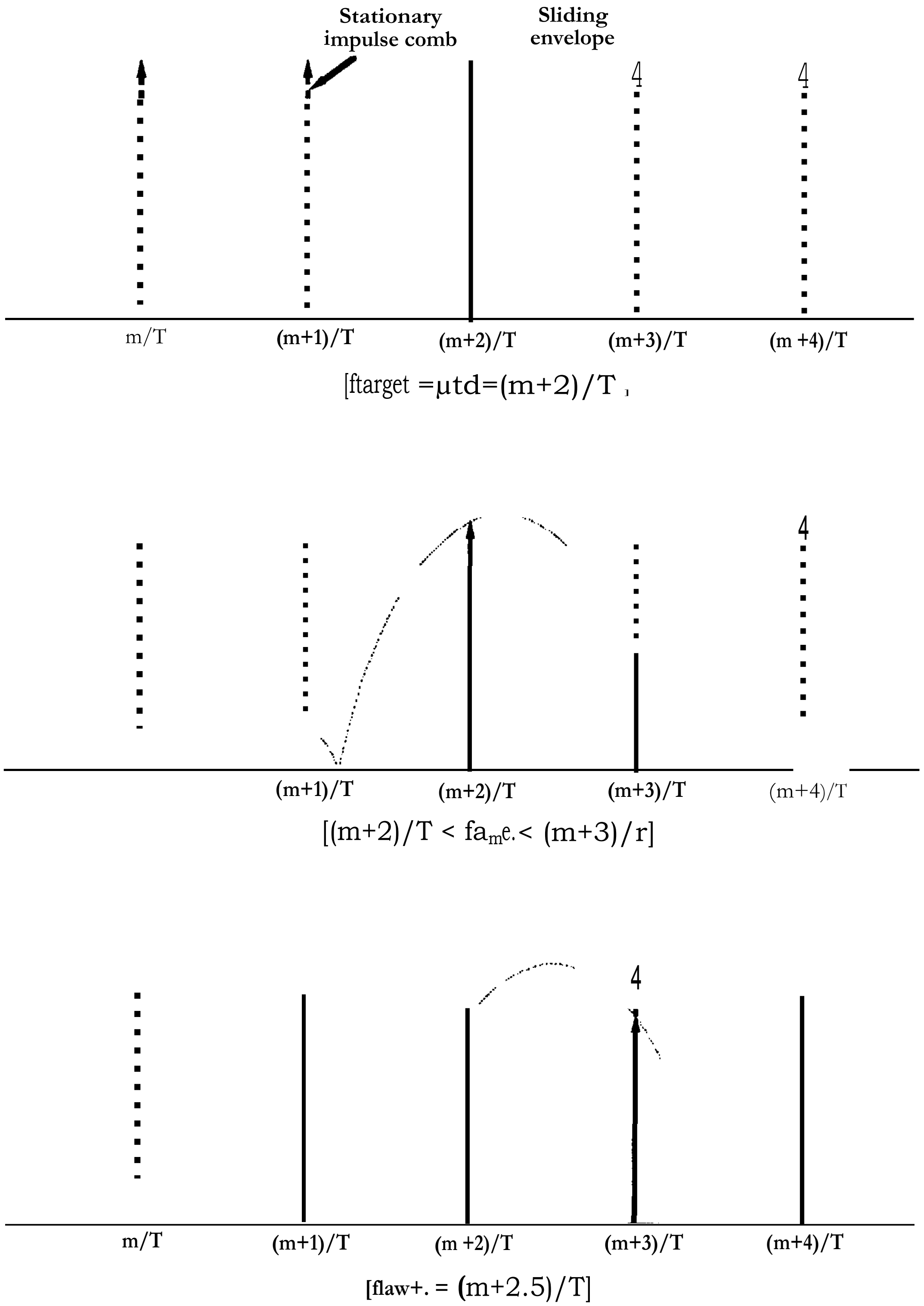

Figure 5.8- Range signature of a point target in the frequency domain

5.3 *Fundamental experiments*

In this section the out-of-window experiments are explained and at the end the obtained results are discussed.

To consider firstly the deployment of targets and the radar set-up, the two trihedral corner reflectors were placed on the roof of the Science Library (DMS Watson building) of University College London (as a suitable test site), and the radar microwave head which carries the transmitter and receiver antennas was placed on an optical bench outside a window (in the line-of-sight of corner reflectors) on the tenth floor of the Engineering building of University College. The slant range between the position of the trihedral reflectors and the radar antennas could be changed between —40-50 metres. The total length of the optical bench was 1 metre and 90 centimetres of this length was used for synthetic aperture processing. The spatial sampling was taken in 5 cm steps, so 19 along-track samples (1+90/5=19) were available. The trihedral reflectors were placed not on the boresight of the optical bench but with an angle of about 12° from boresight. This provided the opportunity to process the acquired data both for generating the synthetic beam and scanning of this beam along-track. To transmit and receive within the real beam, the boresight directions of the horn antennas were turned to be parallel with the directions of the trihedral reflectors.

Figure 5.9 illustrates the isotropic, elemental and total gain patterns (in along-track) at a boresight angle of -12° relative to optical bench boresight simulated for the arranged experiments. From this simulation, the synthetic pattern provides a beamwidth of 0.7° and the transmitter/receiver horn antennas provide 7.2° real beamwidth. Figure 5.10 depicts the scanning simulation of the synthetic beam for two scanning angles of -8.5° and -15.5° (by applying appropriate phase shifts to the individual along-track elements 'spatial samples'). Since the direction of the elemental pattern is unchanged and is still centred at -12°, the peak level of the scanned synthetic main lobe at any angle is determined by the level of the

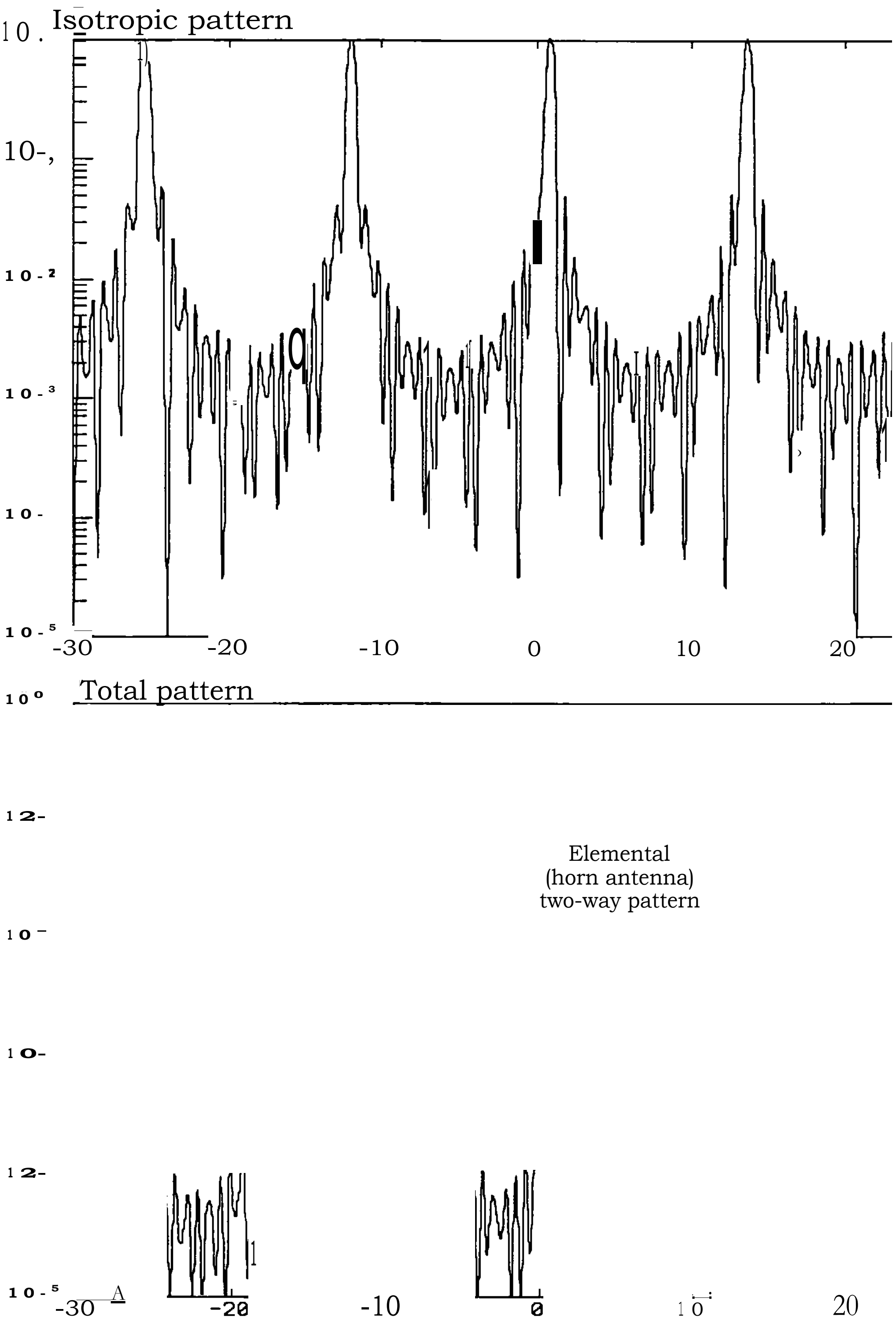

Figure 5.9- Simulation of the experimental radar along-track pattern, (horizontal axis:azimuth angle in degrees, vertical axis: normalised power level).

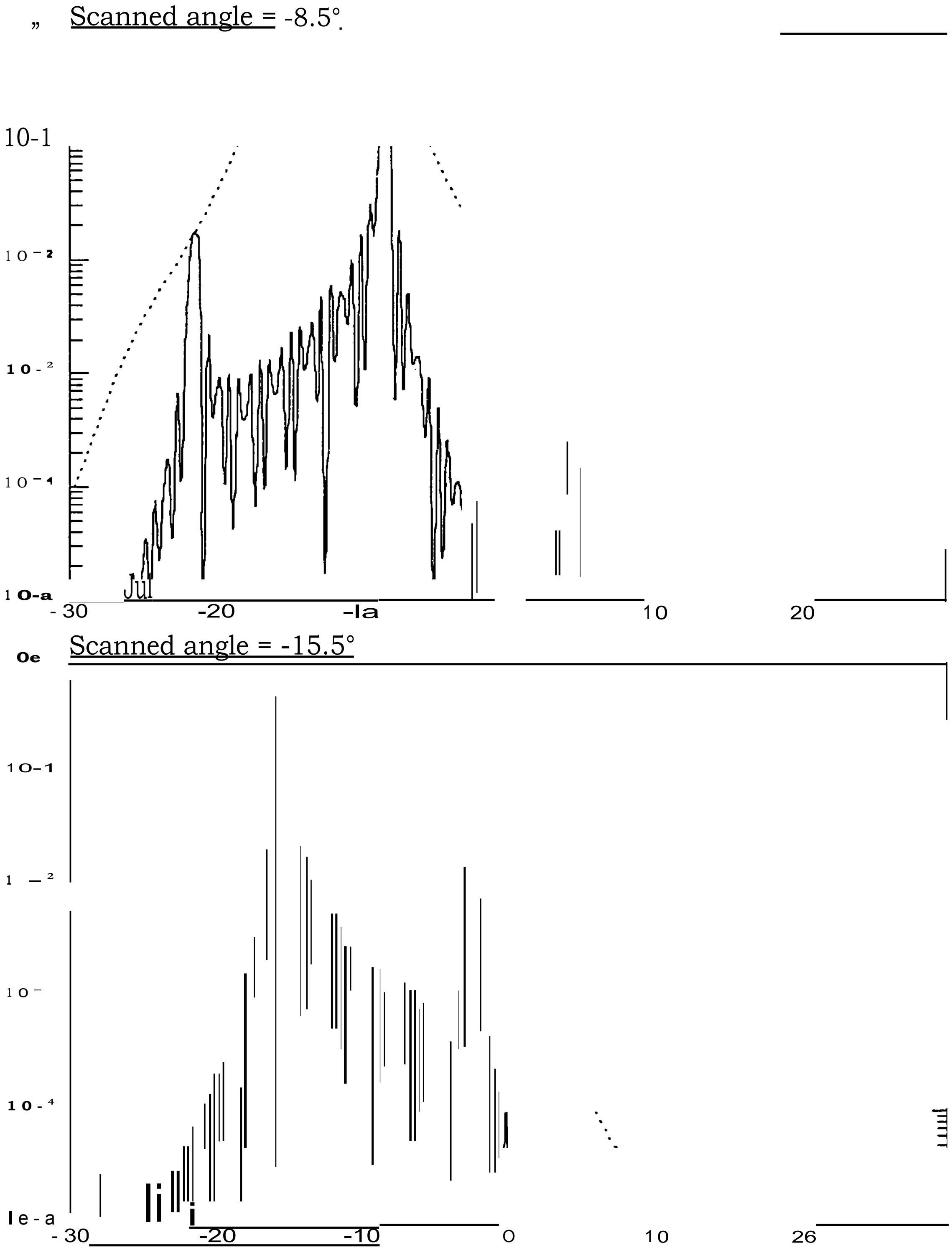
Scanned angle = -8.5°

Scanned angle = -15.5°

Figure 5.10- Simulation of along-track scanning of the synthetic beam for the experimental radar, (primary boresight angle = -12°, horizontal axis: azimuth angle in degrees, vertical axis: beam level in dB).

real pattern at that particular scanning angle. Therefore to avoid reduction of the main lobe level, the scanning angle has to be limited to the usable beamwidth of the elemental pattern.

In the experimental radar, the transmitted chirp signal has a 69.9MHz offset from the receiver LO chirp, and as was explained in Chapter 4 this particular offset frequency provides an IF beat signal at 70MHz for a target with a distance of 300 metres from the radar. Therefore the radar second local oscillator frequency is 70MHz. For the out-of-window experiments, since the distance of the targets to the radar is about 50 metres, this 70MHz local oscillator is not useful. Therefore an external frequency synthesiser synchronised to the master oscillator of the radar was used. By setting the correct frequency on this frequency synthesiser, the range window of the radar could be simply centred at any desired range.

5.3.1 *Experiment 1*

For this experiment, an almost arbitrary configuration of the trihedrals was chosen to see whether in principle they are distinguishable from each other. Figure 5.11 shows the geometry of the trihedrals on the test site in an x-y-z coordinate system which is centred at the centre of the array radar (i.e.centre of the optical bench) along with directly measured geometrical dimensions. From the geometry, the range and the angular separation between the centre of trihedrals with respect to the centre of the array can be calculated:

$$r_1 = \sqrt{x_1^2 + y_1^2 + z_1^2} = \sqrt{7^2 + 43.5^2 + 18^2} = 47.6 \text{ metres}$$

$$r_2 = \sqrt{x_2^2 + y_2^2 + z_2^2} = \sqrt{8.5^2 + 40^2 + 18^2} = 44.7 \text{ metres}$$

$$\theta = \tan^{-1}\frac{[y_1^2 + z_1^2]^{1/2}}{x_1} \quad \tan^{-1}\frac{[y_2^2 + z_2^2]^{1/2}}{x_2} - 2.5^\circ \qquad \ldots 5.21$$

By moving the microwave head along the optical bench, 19 spatial samples with 5cm spacings were collected for off-line signal processing. Figure 5.12

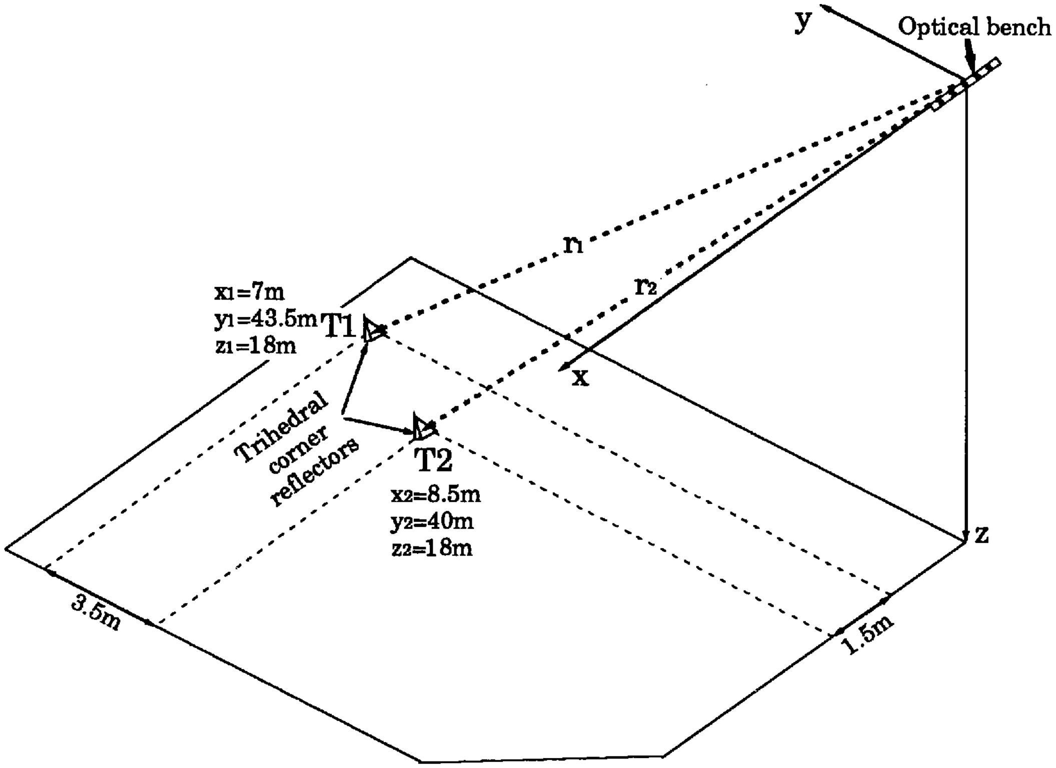

Figure 5.11- Geometry of the targets in Experiment 1

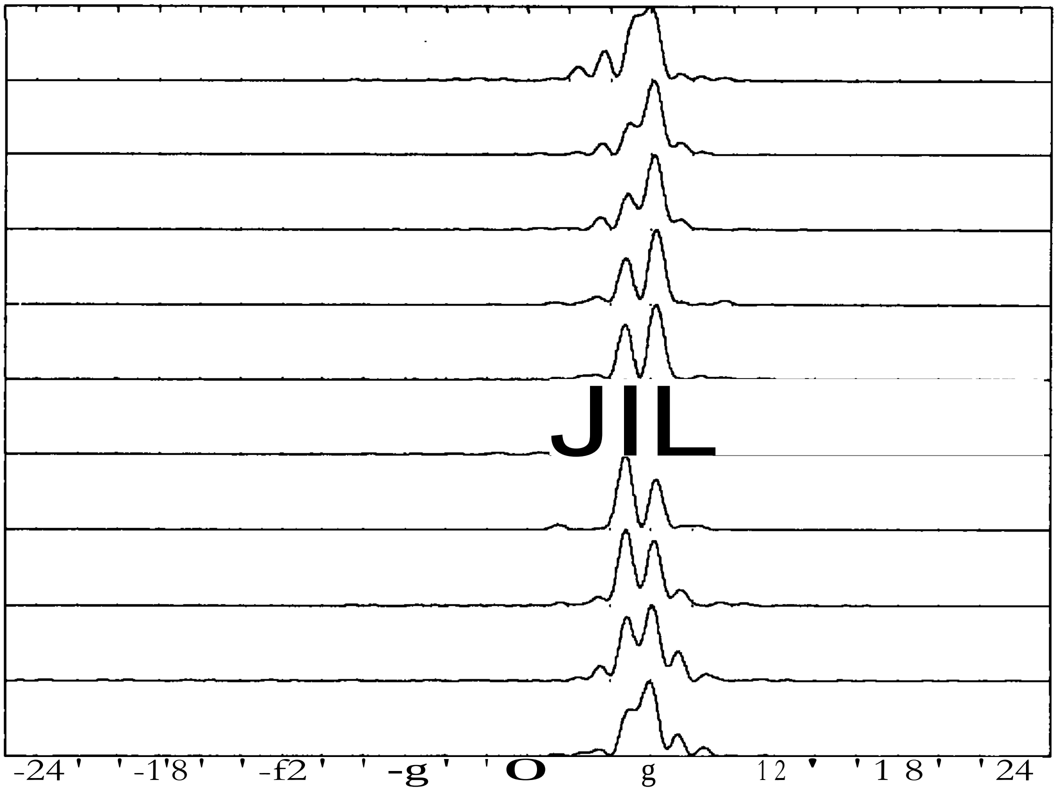

Figure 5.12- Unprocessed spacial samples (different frames correspond to different along-track points, horizontal axis: range bins from -25kHz to 1-25kHz; vertical axis: normalised power level, linear scale).

illustrates some examples of the received waveforms for different spatial samples after fast Fourier transformation and before any along-track signal processing. As can be seen, these single frames (snap-shots) provide a few spectral lines giving some range information about the existence of reflecting targets within the real beam of the transmit/receive horn antennas. However, as these separate frames have not been related to each other yet and also the targets are all well within the real beam of the horn antennas, it is not easy to say how many targets are on the test site and what their range/along-track separations are. Now the collected along-track samples are applied to the signal processing software, which provides range FFT, along-track correlation and along-track synthetic beam scanning. The first output of the processor is a series of frames illustrated in figure 5.13. Any single frame is a two-dimensional (range/along-track) processed waveform for a particular synthetic scanning angle, from -10° to -14.75° (20 scanning steps with 0.25° angular spacing). From this figure it can be clearly seen that as the synthetic beam is scanned at a particular angle a peak appears on the waveform and as the scanning continues this peak disappears. At another angle a second peak appears and then disappears later. Therefore there must be two dominant bright targets within the processing domain.

Now to find the details of the signatures, the processor provides two individual frames for the targets (depicted in **figure** 5.14), giving the along-track and range information. From these frames it is found that the range difference between the two trihedrals is 6kHz-5kHz = 1kHz which is equal to 3 metres, and as the LO frequency synthesiser was set to map 48 metres range at 6KHz baseband, target T_1 has to be at a range of 48m and target T_2 at 45m. Also from figure 5.14, the along-track angular separation between the two targets is 13.75°-10.9°=2.85°.

The third output of the processor is a three dimensional (3-D) plot which gives the received power level of the targets in the range/along-track domain. Figure 5.15 provides this 3-D plot which clearly shows that there are two targets (separated in range and along-track) on the test site.

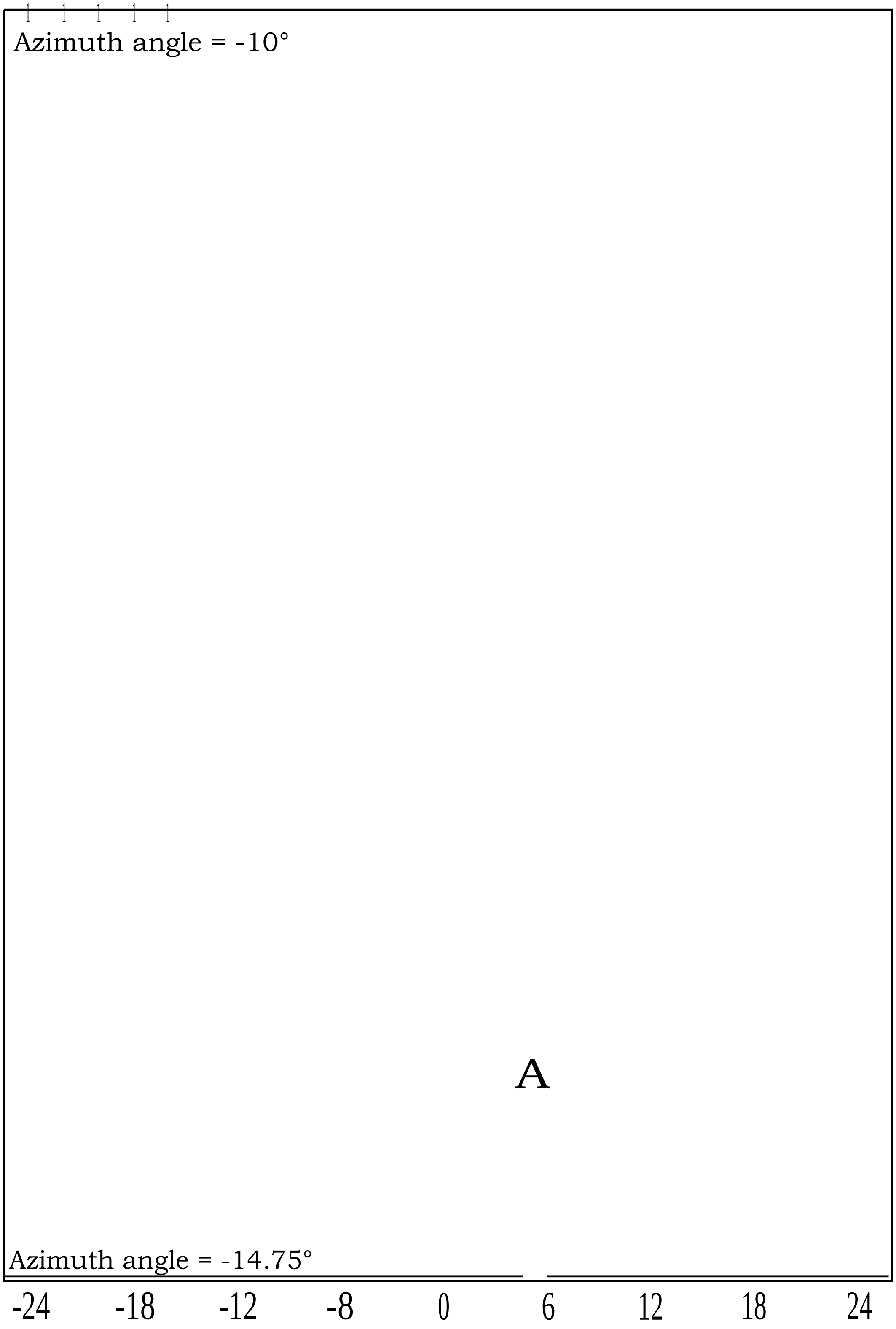

Figure 5.13- Processed waveforms for Experiment 1 (azimuth angle from -14.75° to -10° in 0.25° steps, horizontal axis: range bins from -25kHz to +25kHz; vertical axis: normalised power level, linear scale).

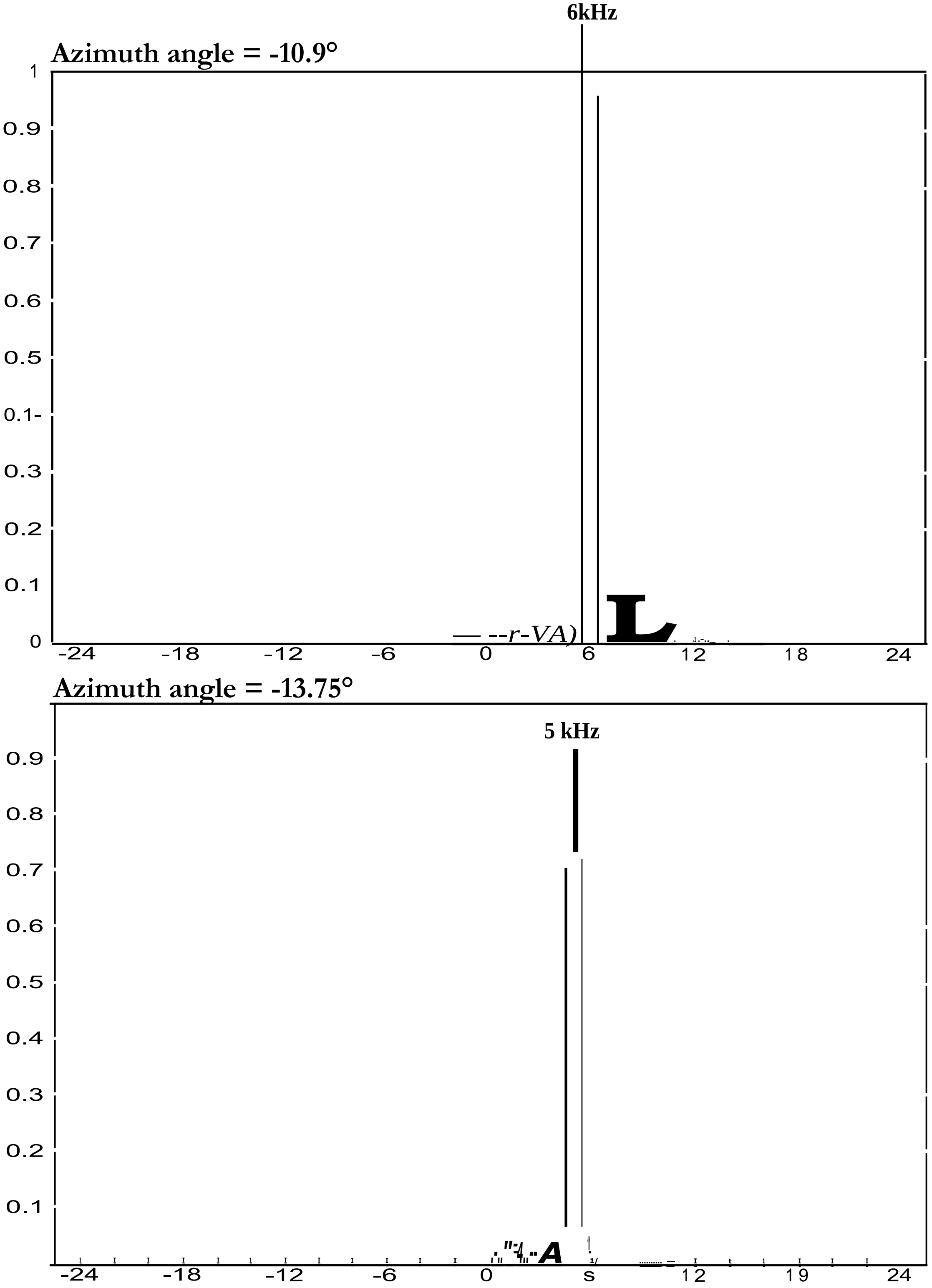

Figure 5.14- Detailed processed waveforms for Experiment 1 (horizontal axis: range bins from -25kHz to +25kHz, vertical axis: normalised power level, linear scale).

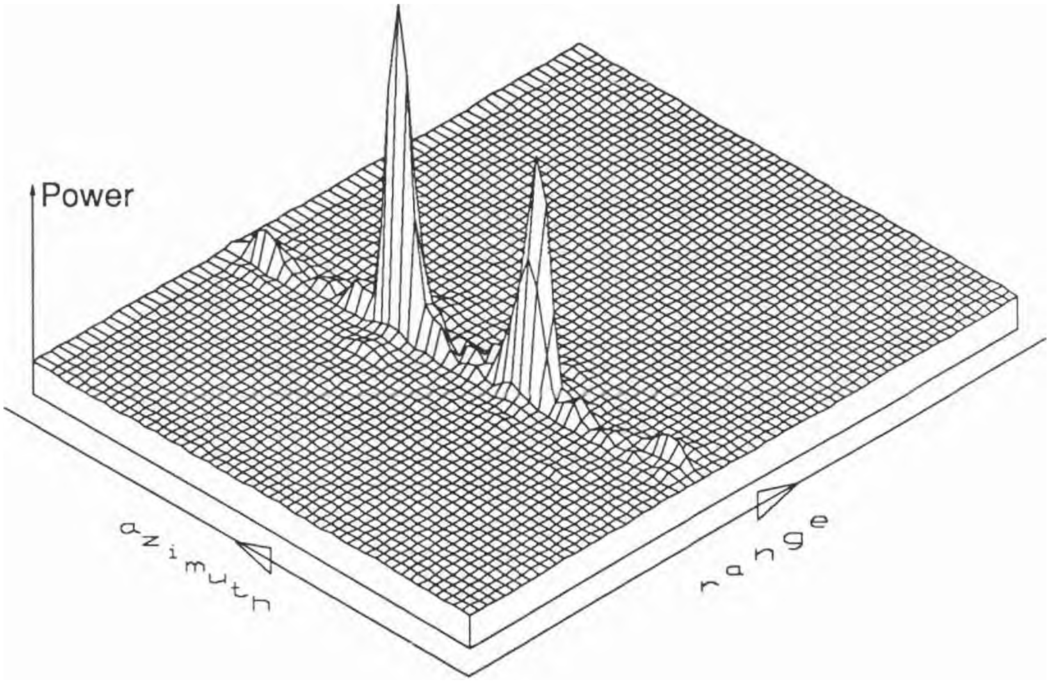

Figure 5.15- 3-D processed result for Experiment 1 (the linear scale normalised power levels of two targets, range grid spacing: 2.34m, azimuth grid spacing: 0.16m).

5.3.2 *Experiment 2*

For this experiment, the configuration of the targets was such that their angular separation with respect to the radar was very close to the theoretical synthetic beamwidth. Figure 5.16 shows the geometry of the two trihedrals along with directly measured geometrical dimensions. From the geometry, the range of the targets and their angular separation can be calculated, equations 5.21, giving: r_1 = 47.3m, r_2 = 44.6m and 0 = 0.6°.

The collected along-track samples of this experiment were applied to the signal processing software. The first output of the processor is a series of frames illustrated in figure 5.17. Again, any single frame is a two-dimensional (range/along-track) processed waveform for a particular synthetic scanning angle, this time from -11.2° to -15° (20 scanning steps with 0.2° angular spacing). From this figure the formation of signatures can be observed. Here as the targets are nearer to each other, the change in the processed waveform is faster than that of the first experiment. It is still possible, though, to distinguish two dominant bright targets within the processing domain.

Now to find the details of signatures, the processor provides two individual frames for the targets (depicted in figure 5.18), giving the along-track and range information. From these frames it is found that the range difference between the two trihedrals is again 6kHz-5kHz = 1kHz which is equal to 3 metres. Hence, similar to Experiment 1, target T_I has to be at a range of 48m and target **T_2** at a range of 45m. Also from figure 5.18, the along-track angular separation between the two targets is 13.8°-12.8°. 1°.

The third output of the processor is the 3-D power/range/along-track plot. Figure 5.19 provides this 3-D plot which clearly shows that there are two very closely-separated targets.

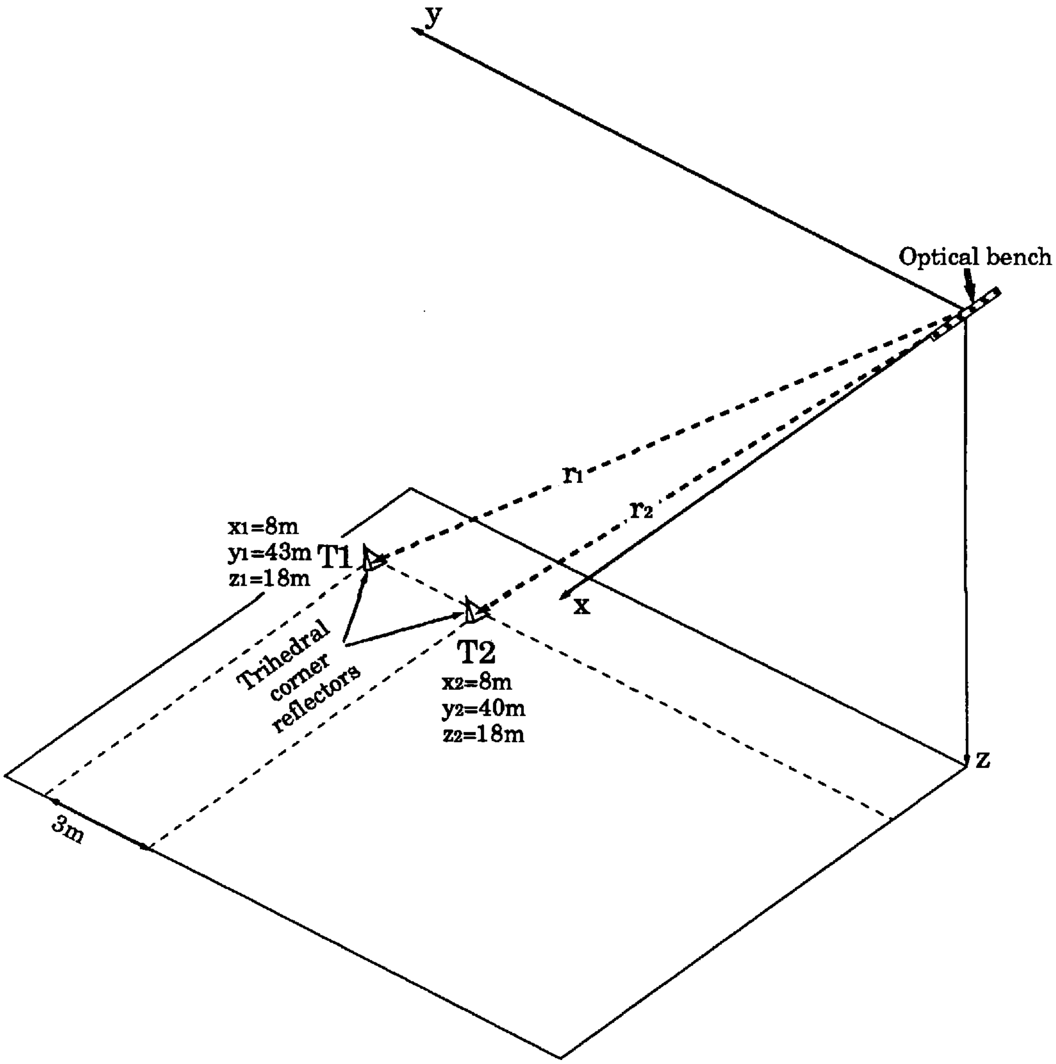

Figure 5.16- Geometry of the targets in Experiment 2.

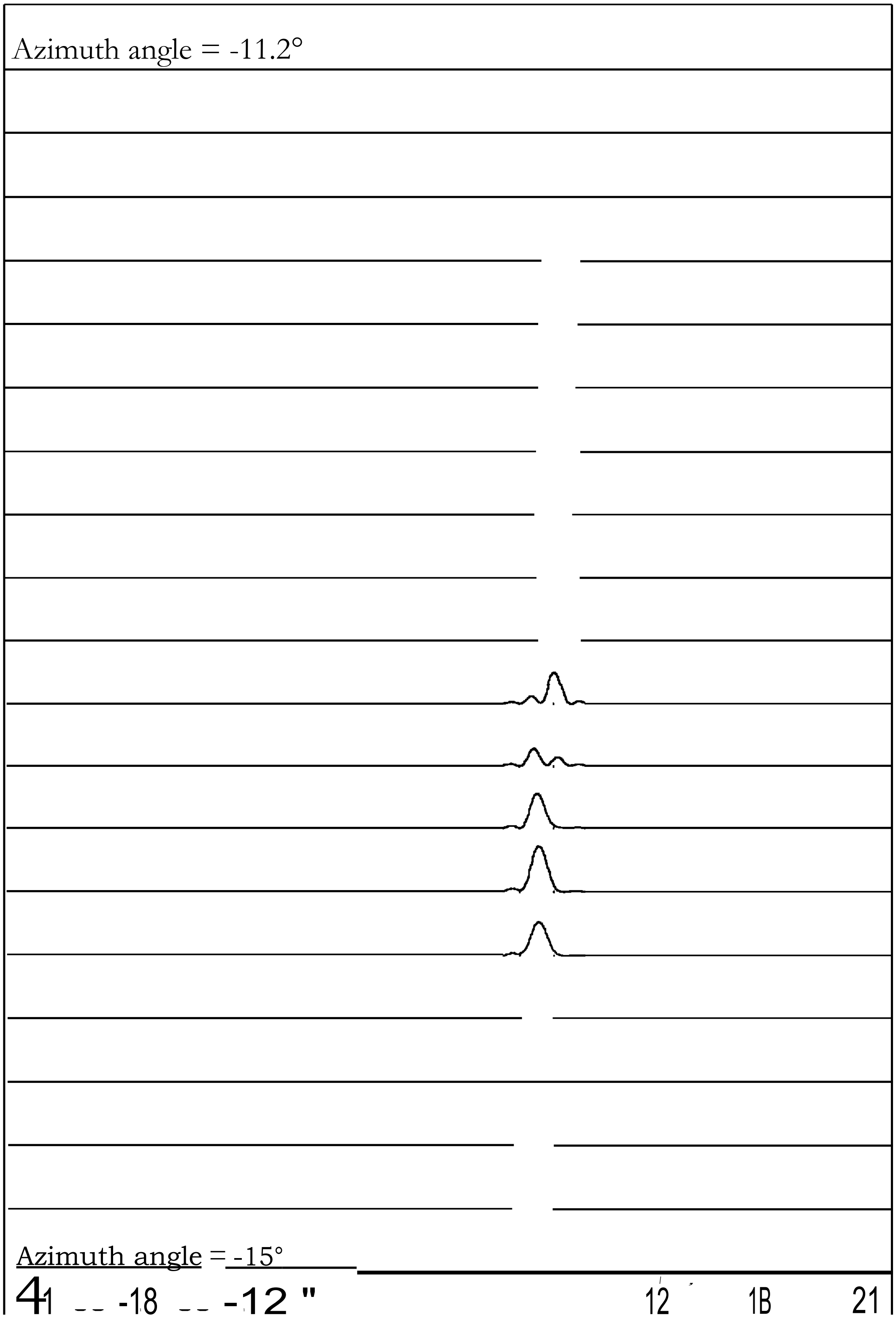

Figure 5.17- Processed waveforms for experiment two (azimuth angle from -15° to -11.2° in 0.2° steps, horizontal axis: range bins from -251(1-1z to +25kHz; vertical axis: normalised power level, linear scale)

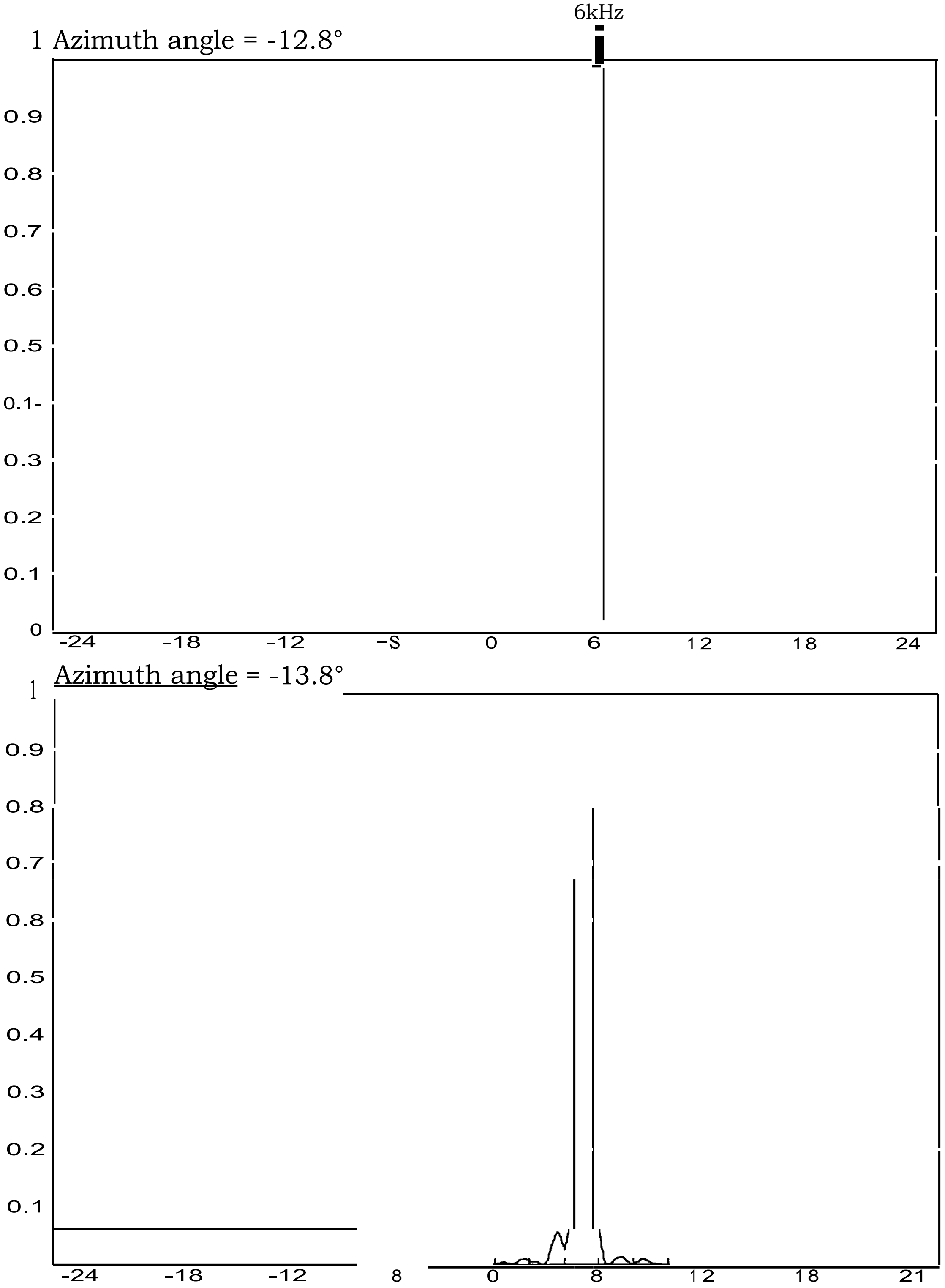

Figure 5.18- Detailed processed waveforms for Experiment 2 (horizontal axis: range bins from -25kHz to +25kHz, vertical axis: normalised power levels, linear scale)

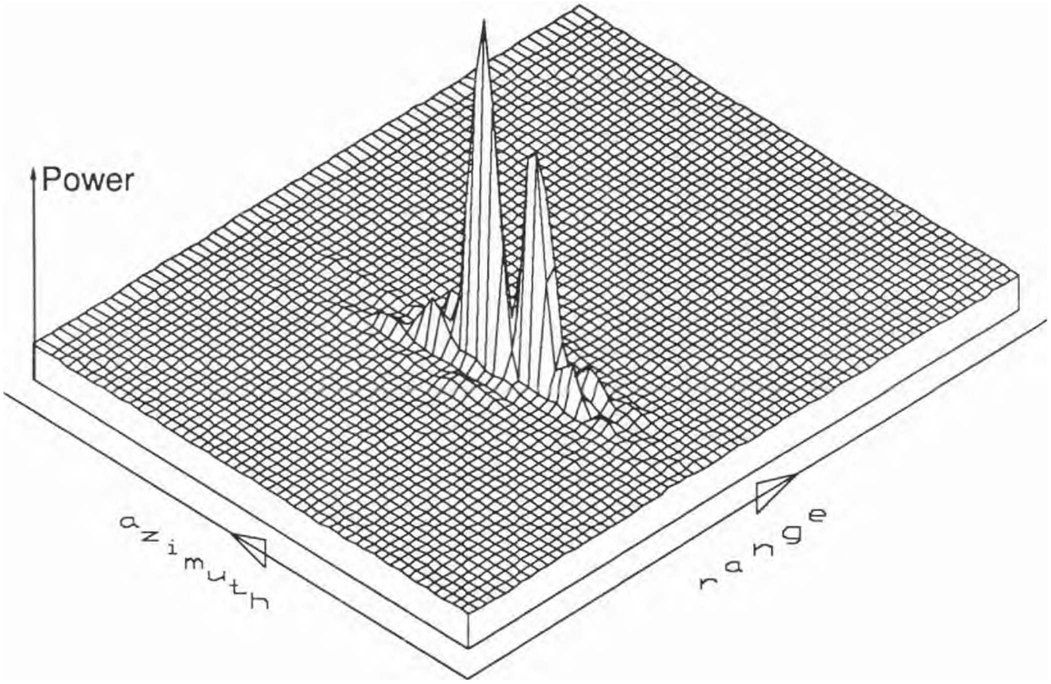

Figure 5.19- 3-D processed result for Experiment 2 (the linear scale normalised power levels of two targets, range grid spacing: 2.34m, azimuth grid spacing: 0.16m).

5.3.3 *Experiment 3*

For this experiment, the two trihedrals were placed side-by-side, so both of them provide the same range information and only by means of along-track processing can they be distinguished from each other. Figure 5.20 shows the geometry of the trihedrals along with directly measured geometrical dimensions. From the geometry the range of the targets and their angular separation can be calculated, giving: r_1 = 44.4m, r_2 = 44.6m and 0 = 1.3°.

The collected along-track samples of this experiment were applied to the signal processing software. The first output of the processor is illustrated in figure 5.21 showing the range/along-track processed waveforms for synthetic scanning angles from -11.2° to -15° (20 scanning steps with 0.2° angular spacing). From this figure, the formation of signatures can again be observed providing two dominant bright targets within the processing range, even though their range to the radar is almost the same.

Then the processor provides detailed signatures of the targets (depicted in figure 5.22), giving the along-track and range information. From these frames it is found that the range difference between the two trihedrals is 5kHz-5kHz = 0 . Therefore both target T_1 and target $\mathbf{T_2}$ are at the same range of 45m. However, from figure 5.22 it can be realised that they have an along-track angular separation of 13.75°-12.55°= 1.2°.

The third output of the processor, which is the 3-D plot, is illustrated in figure 5.23, and shows two targets on the test site which are at the same range but at different along-track angles.

5.3.4 *Discussion of the results*

In this section the results of the out-of-window experiments are discussed. First it should be mentioned that the error in the direct geometrical measurement of the coordinates of the targets is estimated to be of the order of ±1m (i.e. a_z= a_y= a_z= 1m). Applying equations 5.21 to equation 3.93,

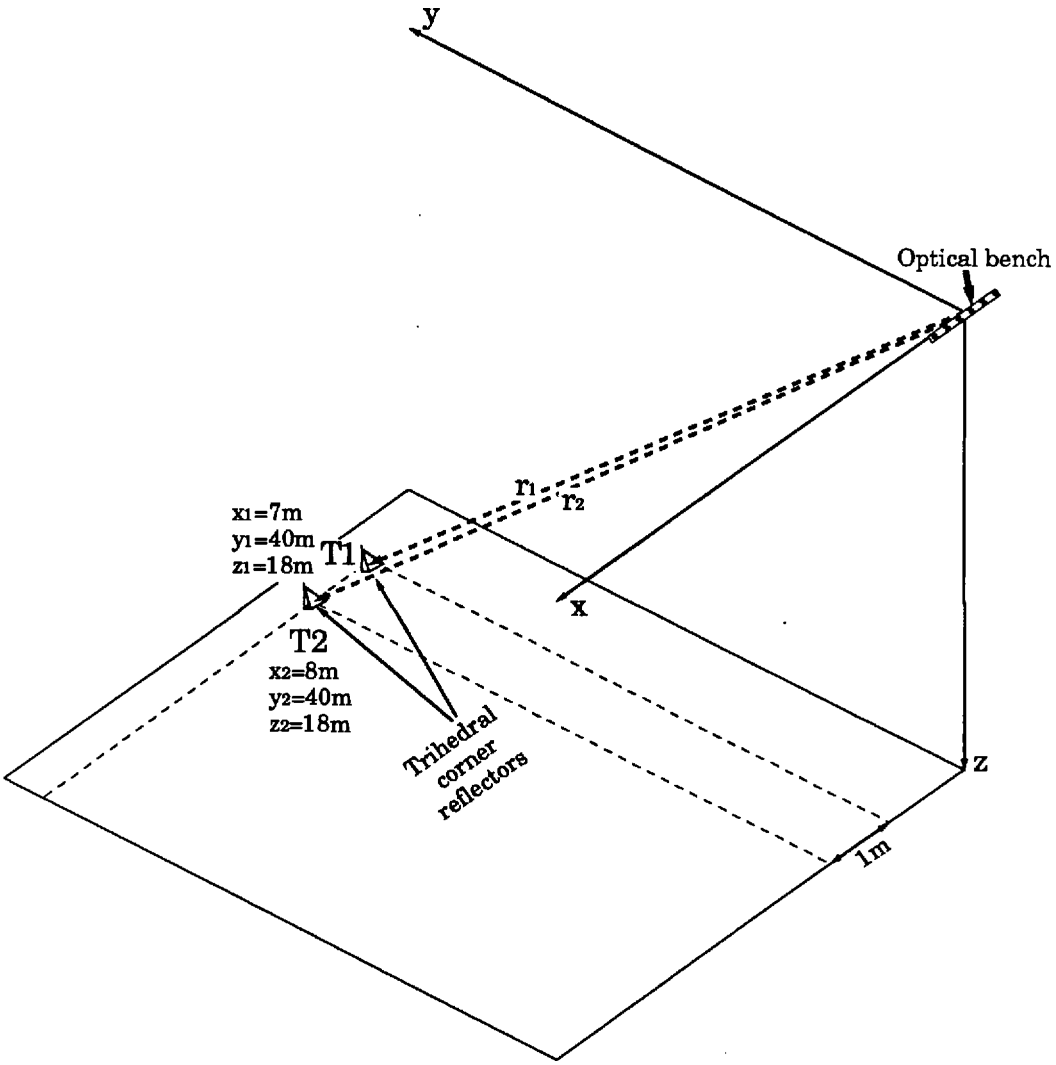

Figure 5.20- Geometry of the targets in Experiment 3.

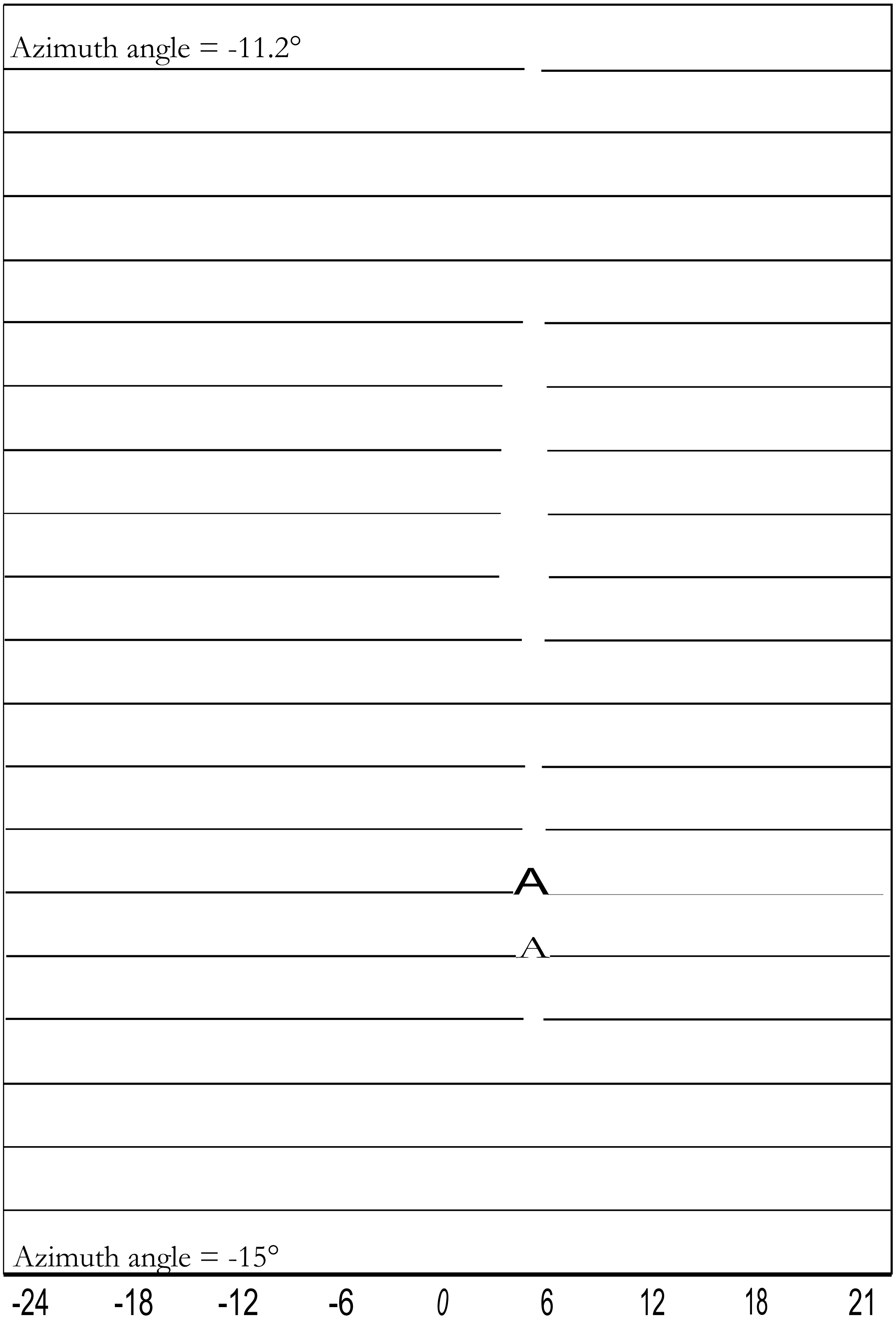

Figure 5.21- Processed waveforms for Experiment 3 (azimuth angle from -15° to -11.2° in 0.2° steps, horizontal axis: range bins from -25kHz to +25kHz; vertical axis: normalised power level, linear scale).

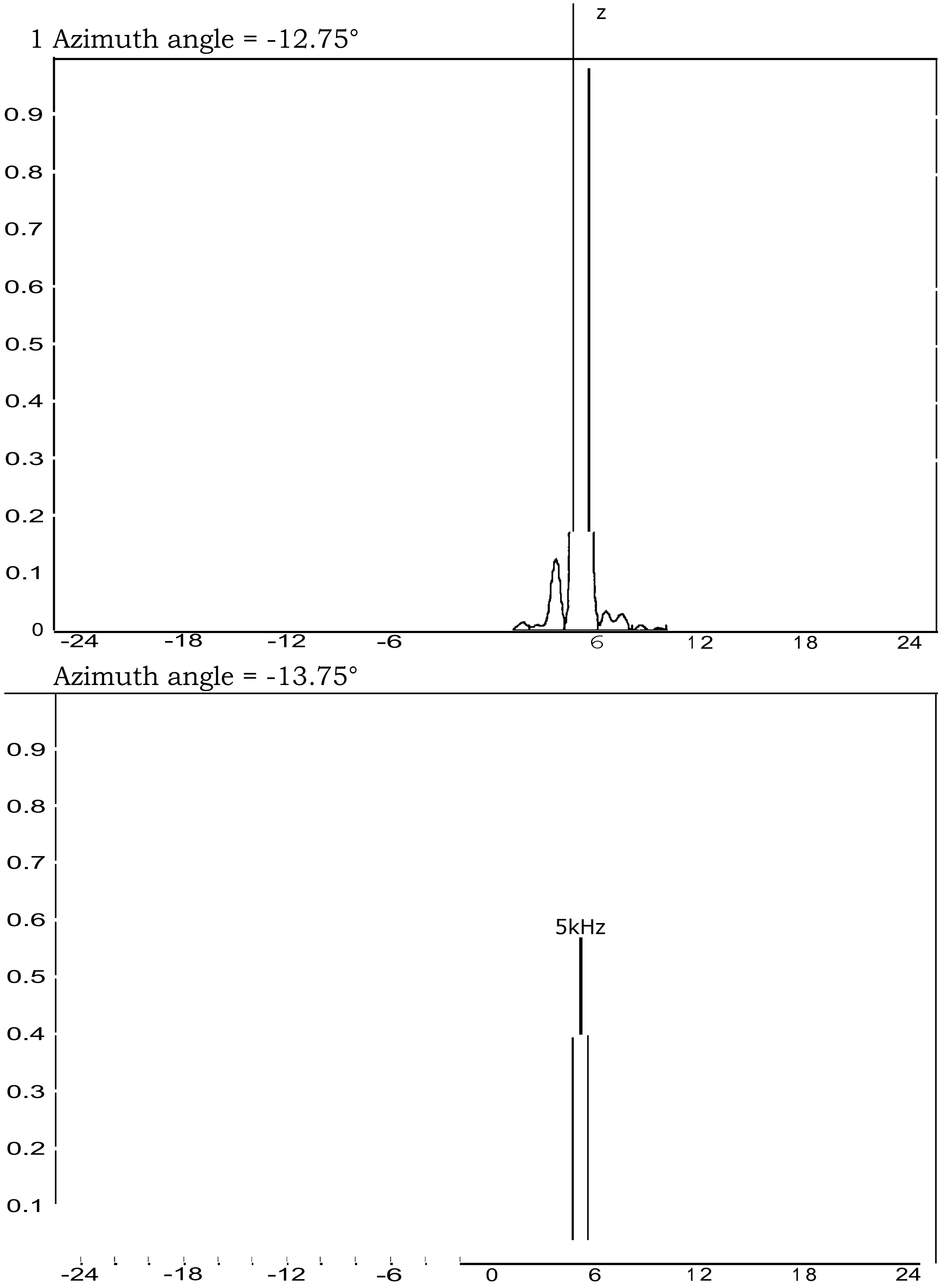

Figure 5.22- Detailed processed waveforms for Experiment 3 (horizontal axis: range bins from -25kHz to +25kHz, vertical axis: normalised power levels, linear scale)

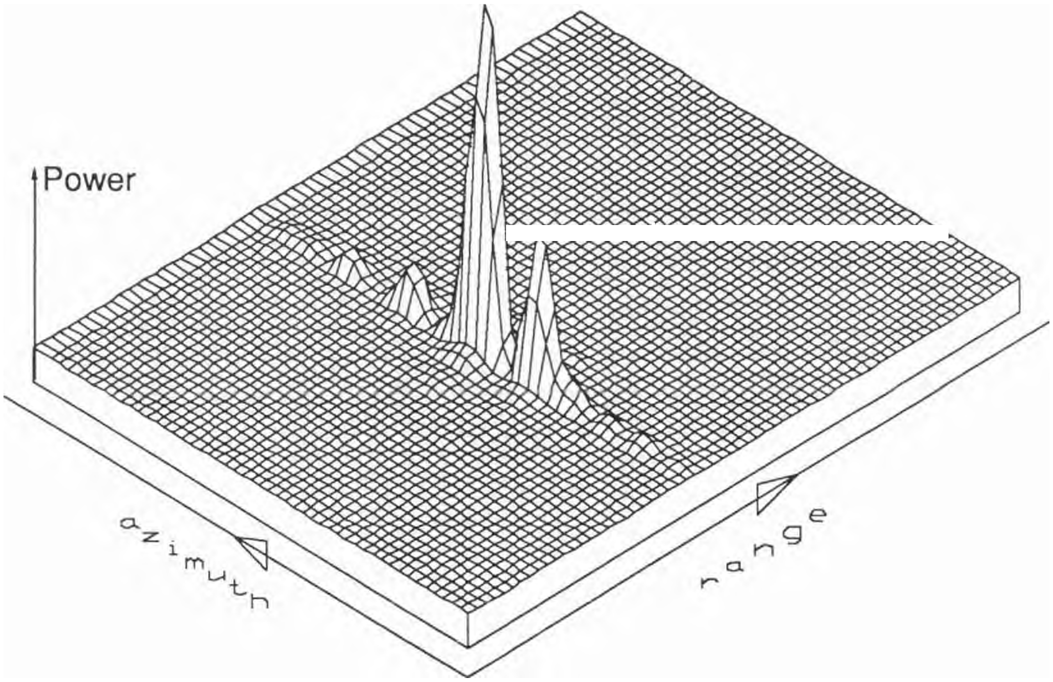

Figure 5.23- 3-D processed result for Experiment 3 (the linear scale normalised power levels of two targets, range grid spacing: 2.34m, azimuth grid spacing: 0.16m).

(propagation of errors) the error in the range calculation from direct geometrical data will be of the order of a_r= 1.1 metres. This error is less than the range resolution of the experimental radar (o_r= 3m). Table 5.2 summarises the range of the trihedral corner reflectors in the three experiments obtained by signal processing of the received waveforms, and also by calculating from direct geometrical measurement of the coordinates of the targets.

	Radar results		Geometrical results	
	Target1	Target2	Targetl	Target2
Experiment 1	48m	45m	47.6m	44.7m
Experiment 2	48m	45m	47.3m	44.6m
Experiment 3	45	45m	44.4m	44.6m

Table 5.2: Comparison of range information results.

Considering the existing range error of 1.1 metres, the radar results and geometrical calculations are in very good agreement, showing that the range information of the targets has been correctly extracted, and although the range difference of the targets is only one range bin, they have been distinguished in range by the processor.

Having coordinate errors of about 1 metre when the absolute coordinates of the targets are much larger than one metre does not change the range calculation very much, and as was shown, the associated range error is about 1.1 metres. However, a 1 metre error in the direct geometrical measurement of the target coordinates may have a drastic effect on the calculation of the angular separation between the targets. For instance, in Experiment 3, if the coordinate of target T_1 along the x-axis is changed from 7 metres to 8 metres (= x-Fa_x), its estimated location will be exactly on target $\mathbf{T_2}$ and this implies zero angular separation between the two targets instead of 1.4° which was calculated in the experiment. To alleviate this problem, as an alternative to direct coordinate measurements, a field telescope (Telescope AA, made by BE Ltd) capable of measuring the angle between two distant points with an accuracy of about 0.05° (i.e. 3 arcmin) was employed to measure the angular separation between the centres of two trihedral corner reflectors. Table 5.3 summarises the angular separation between the two test targets obtained by signal processing of the received waveforms, by calculation from direct geometrical measurements of the coordinate of targets, and also by using the field telescope.

	Angular separation between the two targets		
	Radar results	Geometrical results	Telescope results
Experiment 1	2.85°	2.5°	3.1°
Experiment 2	1°	0.6°	1.1°
Experiment 3	1.2°	1.3°	1.3°

Table 5.3: Comparison of along-track information results.

The results of all three methods are near to each other. Particularly, the direct angle measurements by telescope which are more accurate than the geometrical calculations show discrepancies of less than 10% in comparison with the signal processing results. Consequently, synthetic array processing and beam scanning in the experimental radar has shown that the along-track information of targets has been correctly extracted.

5.3.5 *Double spectral line target*

A separate experiment has been carried out to examine the evolution of the signature of a target when its range is not an integer multiple of the range resolution (as explained in section 5.2).

The range of an individual target can be examined before any signal processing by looking at its IF beat signal on the screen of an on-line spectrum analyser. Having a spectrum analyser in the experimental radar set-up connected to the IF output, the locations of trihedrals were chosen in such a way that one of them provided one spectral line and the other one two lines. After signal processing of the collected spatial samples, the three dimensional plot of the results is illustrated in figure 5.24 giving the received power level of targets in the range/along-track domain. This figure confirms the discussion of section 5.2, and clearly shows that when the range of a target is not an integer multiple of the range resolution, as the along-track processing is performed the two corresponding spectral lines rise together and then fall together.

5.4 *Further discussions*

Chapter 4 has provided the theoretical and practical aspects of the design, construction and testing of the experimental radar, and Chapter 5 has examined the field test of the prototype system as a synthetic aperture altimeter. Since the prototype radar outputs the raw baseband signals for processing by an off-line computer, this suggests that it can be also useful as a conventional radar altimeter for experimental purposes.

If the opportunity becomes available to use the experimental radar in a real test over topographic surfaces, the range and along-track processing will be exactly similar to what was explained and applied in this chapter. However, the output processed waveforms have to be used in height and roughness estimations. Since over topographic surfaces no models for the return signal or algorithms for waveform analysis have been introduced, the processed waveform is initially treated as a basic histogram consisting of several range bins, for which a mean value and a variance can be defined and the results can be considered as the mean height and surface roughness within the altimeter footprint.

To conclude this chapter, the results of the out-of-window experiments show that for the relatively simple and cheap prototype instrument, the coherency of the radar system was fully maintained and without any noticeable problems, the signature of the test targets were correctly extracted demonstrating good agreement with actual measured range and angular separation data.

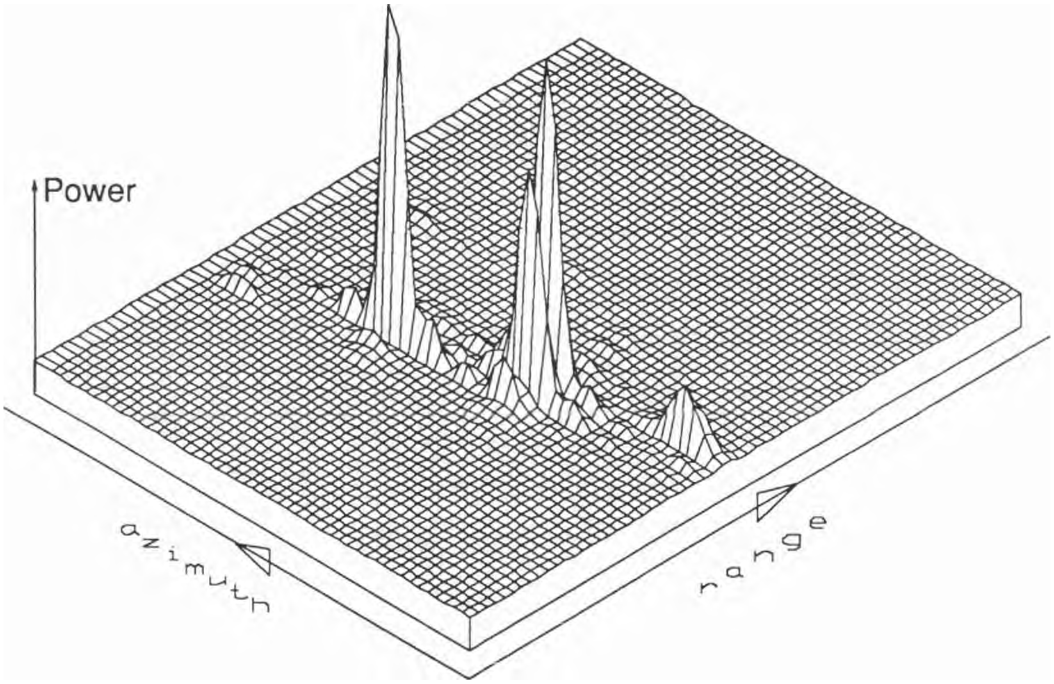

Figure 5.24- 3-D processed result for two targets, one having one spectral line, and the other two spactral lines (linear scale normalised power levels, range grid spacing= 2.34m, azimuth grid spacin= 0.16m)

Chapter 6

Summary and conclusions

6.1 *Summary and discussion*

Radar altimetry over the ocean is now a well established discipline of satellite remote sensing, providing high precision mean height measurements of the ocean surface, with errors of less than 10cm, from an orbital altitude of about 800km. In contrast, satellite radar altimetry over land has not been yet globally attempted, but there is much interest among scientists in using radar altimeters over topographic surfaces. If such instruments are introduced to remote sensing satellites, they can provide a wealth of topographic data to be used in all disciplines of Earth sciences.

The design of an altimeter depends on the type of the surface under its observation. Generally, the ocean surface can be considered as a smooth and homogeneous surface. This enables an altimeter with a relatively wide beam antenna to reveal the mean height and surface roughness with significant precision. A topographic surface, however, cannot be normally treated as a homogeneous and smooth surface and even for a small area, the variation in the elevation of land features can be so large that a conventional ocean altimeter encounters serious problems, such as interpretation error and misregistration of a measured range, which cannot be normally corrected. In order to alleviate these problems and to obtain meaningful altimetric measurements over land, and hence to provide as closely as possible, undistorted information about the topography within the footprint of the radar altimeter, the antenna beam has to be restricted to a very small portion of the total area under observation.

A radar altimeter may employ different techniques to restrict the illuminating area and to obtain information about the geometry of the targets. The range information can be obtained by measuring the two-way time delay of a transmitted pulse. In order to obtain high range resolution without increasing the peak transmitted power and maintaining sufficient signal-to-noise ratio, the transmitted pulses are phase coded signals, (conventionally linear FM chirps), rather than pulses of unmodulated carrier. One of two methods are normally applied to a received chirp signal for extracting its range information, matched filtering and full-deramp technique. For the case of an altimeter, both methods are identical in terms of range resolution and transmitted power, but there is an important difference between them. In the matched filter method, the time domain compressed output has the same bandwidth as the transmitted chirp signal. This implies that very high sampling rates and very high speed processing hardware are required. In contrast, the full-deramp process compresses the bandwidth substantially, which permits the use of much simpler and very much slower signal processing hardware.

The high range resolution provided by the full-deramp technique allows precision height measurement for a land altimeter. On the other hand, to obtain a narrow illuminating beam, and consequently high spatial resolution, very large, complex and costly antennas would be needed. It is, however, possible to employ a thin, long antenna for the altimeter to provide a narrow across-track beam. Then by means of aperture synthesis, a narrow along-track beam is also created.

The high resolution requirements for the land altimetry are not only because of the need to localise the beam and to avoid the measurement errors, but are also dictated by the demands of different disciplines of Earth sciences. Correlating these requirements with the available radar techniques reveals that of vertical resolution, along-track resolution and across-track resolution, the third is the hardest to improve. The across-track resolution has to be generated by a real beam. A fine across-track resolution needs a narrow beam, and a narrow beam requires very short wavelengths and very long antennas. Even for a 10m to 20m long antenna, the operating frequency of the radar altimeter has to be of the order of tens of Gigahertz in order to provide a decent pixel size. A suitable frequency for this purpose has to be chosen, taking into account the windows of low atmospheric attenuation such as: 37GHz, 96GHz, 140GHz and 220GHz. The present state of millimetre-wave technology and its trend of advancement for the near future implies that the most likely choice in terms of the availability of the space qualified components will be the 37GHz band. A 10m to 20m long antenna at 37GHz generates an across-track resolution of a few hundred metres, which falls in the upper limit of the high resolution regional scale altimetry.

Other techniques have been also proposed for the extraction of the land topography, namely: optical stereo imagery, stereo SAR, interferometric SAR and laser altimetry. Optical stereo imagery and stereo SAR provide high resolution pixels adequate for the remote sensing purposes, but their height resolution is coarse (of the order of 10m) which is not sufficient for most of the purposes defined. Intereferometric SAR needs extensive signal processing in terms of image generation, phase extraction and phase unwrapping, and in the end the obtainable height resolution is not better than the normal pulse compression techniques used in radar altimeters. Laser altimetry offers very high ground and height resolutions, as well as simple signal processing requirements,.but the obvious problem with laser altimetry is the obstruction of the laser beam whenever the area under observation is covered by clouds. Apart from this, the important concern is the short lifetime of laser sources, which at present makes laser altimeters unsuitable for regional and global scale applications.

The assessment of the merits and drawbacks of different methods of high resolution topographic mapping shows that the synthetic aperture altimetry is the one which can provide the maximum benefits, as a single remote sensing instrument, and in terms of resolution and coverage, to the greatest number of activities of Earth sciences. For this purpose, a technologically reasonable trade-off for near future satellite-borne altimetry, is to design a radar to provide -500mx500m resolution cells and a few metres (say 3m) height resolution, operating in the 37GHz frequency band. This instrument would orbit at 800km altitude to provide permanent monitoring of the Earth's surface, and other complementary methods, particularly laser altimetry, may be used for the purpose of local scale topographic mapping of selected areas of the Earth's surface.

The theoretical study of synthetic aperture altimeter has shown that the aperture synthesis and full-deramp techniques are two orthogonal processing steps providing along-track and range resolutions. The required aperture that has to be synthesised for the altimeter is very short, which implies that unfocused processing is quite sufficient for this particular case.

It is clear that even having a single-beam synthetic aperture altimeter cannot be sufficient, because its illuminating footprint is so small that providing a database of global altimetric information would need several years. Hence in order to reduce the mapping time (which is important for the study of the dynamic phenomena of the Earth's surface), the technique of wide swath scanning is introduced. In this method both the real across-track beam and the synthetic along-track beam of the altimeter are scanned, the first one electronically and the second one by means of signal processing. An important problem of this type of altimeter is the amount of data which has to be collected and processed, and the discussion has shown that with the present technology in optical storage systems and signal processing hardware, the use of scanning synthetic aperture altimeter is quite feasible.

The other problem with a synthetic aperture altimeter, which is common in all the proposed high resolution altimeter techniques, is that altimetric measurements with high spatial resolution will not provide any useful information, unless the acquired data are referenced to the geometrical coordinates of the illuminated footprint. In other words it is important not only to employ the high spatial resolution techniques that have been described, but also to determine and control the exact location of the antenna beam on the surface. The required angular precision is of the order of tens of arcseconds, which is difficult to maintain by inertial navigation systems. However, star trackers can certainly provide excellent results. In addition to star trackers, an idea based on the NAVSTAR global positioning system (GPS) was also presented, in which it was explained that by using a series of interferometric GPS receivers it should be possible to measure and control the baseline angle with the precision adequate for synthetic aperture altimetry.

Following the theoretical study of the application of aperture synthesis to satellite radar altimetry, it is proposed that the next stage in the development of such an instrument would be an aircraft-borne 'proof-of-concept' synthetic aperture altimeter which can be realised rather simply and cheaply. Therefore in the second part of this study an experimental instrument was introduced, and theoretical and practical aspects of such a radar, which consequently led to the construction of a complete prototype system were examined. This radar altimeter includes a number of novel features, such as aperture synthesis with full-deramp range processing, digital chirp generation and bistatic FMCW operation. It also uses an off-line computer which offers significant ease and flexibility in performing range processing, synthetic aperture processing and along-track synthetic beam scanning. After design, construction and laboratory testing of the prototype radar, to explore the capabilities of the system, a series of out-of-window experiments were arranged. These experiments attempted to construct the range/along-track signature of the backscattered signals of two trihedral corner reflectors, when spatial samples were taken by moving the radar in along-track on a triangular optical bench. By processing the collected data and comparing the outputs with the geometrical calculations and also with angle measurements made by a special field telescope, the results of the out-of-window experiments showed that for this relatively simple and cheap prototype instrument the coherency of the radar system was fully maintained and without any noticeable problems, the signatures of the test targets were correctly extracted demonstrating good agreement with the true location of trihedral corner reflectors on the test site.

6.2 ***Further work***

This thesis has presented the results of the study on the application of aperture synthesis to satellite radar altimetry which was carried out at University College London in parallel with work by scientists at the Jet Propulsion Laboratory, California Institute of Technology, on the feasibility study of the LORA instrument (Land and Ocean Radar Altimeter), with the aim of deploying a scanning radar altimeter in orbit.

The very wide nature of these kinds of studies which overlap several disciplines of science and engineering, leave many questions which have to be answered and thoroughly explored. Although it has not been possible to cover these in a limited time scale, it is worth mentioning some extra investigations which may be carried out if there is any further interest in the achievements of this particular work.

1- From what has been investigated throughout this thesis, it is realised that several specifications required by a synthetic aperture altimeter are technologically feasible, but whether it is possible to control the attitude of all parts of a long antenna with high angular accuracy is uncertain. Even the installation of high precision star trackers or interferometric GPS receivers in a number of locations over the antenna surface cannot guarantee that all the elements of the antenna structure have the proper location and orientation and the antenna beam illuminates the right section of terrain. Therefore one of the main challenges of pursuing the design of such an altimeter is the detailed structural and mechanical analysis of long antennas in orbit. To simplify the design, one approach is to limit the capabilities of the altimeter by sacrificing the spatial resolution to some extent in order to reduce the length of the antenna. Another method is to use two smaller antennas across-track in an interferometer configuration with suitable length of the baseline to obtain narrow intereferometric fringe lobes. This can provide across-track resolution similar to the long across-track antenna of the synthetic aperture altimeter. Although attitude stabilisation and control of two small antennas is much

simpler than that of a long antenna, this type of altimeter, which can be called an interferometric synthetic aperture altimeter, has its own difficulties such as more complex signal processing requirements and much more importantly the problem of how a particular lobe may be recognised and tracked from all the lobes of the interferometric fringe. These important problems need to be investigated and compared with the difficulties of a long antenna synthetic aperture altimeter before any final decision making.

2- The across-track real beam scanning is one of the necessities of a wide swath synthetic aperture altimeter which requires the use of a phased array antenna in the across-track direction. To do this, three methods are envisaged. First, the conventional use of antenna elements along with controllable phase shifters for each element. For this method the form of phase control, the optimum design of the phased array and the switching speed of phase shifters with such a high pulse repetition frequency can be investigated. As was demonstrated in Chapter 5, it is possible to scan the beam by digital signal processing, so for the second method the phased array elements do not need to be accompanied by phase shifters, and the received signal of each across-track antenna element can be processed in a separate channel and at the end, the outputs combined together after proper phase shifting of any individual output through signal processing software. This method seems more complex than the first one, but if separate LO frequencies are applied to separate channels and all the outputs are added together, it might then be possible to handle all the signals by only one receiver. The third method is a multiple across-track beam configuration by means of separate antenna feeds or antenna elements for each swath angle. This makes the beam scanning irrelevant but on the other hand its hardware is more complicated.

3- In contrast to the ocean surface which is relatively smooth and homogeneous and for whose backscattered waveforms very effective detection algorithms exist, virtually an infinite number of topographic surfaces with different complexities and backscattering properties exist

which make it very difficult to find general algorithms which can provide high precision results. Therefore it is worth arranging several field experiments or simulation programs for a variety of topographic surfaces, and by considering the range window as a simple histogram, trying to find its mean and variance as measures of height and roughness. These results can then be compared with the true geometrical properties of the area under observation. This might provide considerable information about the sort of algorithms which have to be developed.

4- It is believed that the proposed aircraft-borne proof-of-concept altimeter represents a cost-effective way of demonstrating the principle of synthetic aperture altimetry in a real environment and gaining experience in building the hardware and processing data for the ultimate spaceborne system, in a relatively short time scale. Hence the next stage in the development of the existing experimental synthetic aperture altimeter can be the construction of a prototype system suitable of being installed in an aircraft. The experimental system has been designed in such a way that transmitter and receiver LO chirp signals are up-converted and multiplied in the VHF band and then at the same time a common microwave signal is applied to two parallel mixers to up-convert both VHF chirp signals to the final microwave band. Therefore it is quite easy to change the carrier frequency of the radar from 13.5GHz to 37GHz which is the carrier frequency of the proposed spaceborne synthetic aperture altimeter. For this purpose, the only modifications in the radar hardware will be the replacement of the two up-converting mixers and their accompanying filters along with providing a suitable mm-wave band signal source. The benefits of increasing the carrier frequency to the mm-wave band are considerable reduction of the size of the aircraft-borne radar antenna, and also providing valuable information about the sort of backscattering which an altimeter might encounter in the mm-wave band over topographic surfaces, for which at the present time there is little information.

References

Abbott, S., 'A wider vision of optoelectronics'; ***IEE Review,*** June, 1989.

Barber, B.C., 'Theory of digital imaging from orbital synthetic aperture radar'; ***International Journal of Remote Sensing,*** Vol.6, No.7, 1985.

Bellanger, M., 'Digital processing of signals, theory and practice'; Wiley, 1984.

Berlin, P., 'The geostationary applications satellite'; Cambridge University Press, 1988.

Bevington, P.R., 'Data reduction and error analysis for the physical sciences'; McGrow-Hill, 1964.

Bierman, H., 'Improved devices and circuitry reduce front-end noise level'; ***Microwave Journal,*** August, 1988.

Bierman, H., 'mm-wave devices and subsystems meet military/space demands'; ***Microwave Journal,*** July, 1989.

Brigham, E.O., 'Fast Fourier Transform and its applications'; Prentice-Hall, 1989.

Brooks, R.L. el al., 'Ice sheet topography by satellite altimetry'; ***Nature,*** Vol 274, 10 August, 1978.

Brus, E., 'Ambition marks global plans for remote sensing'; ***Microwaves & RF,*** January, 1988.

Burke, K. and Dixon, T.H., 'Topographic science working group report'; NASA contract NASW-4066, 1988.

Carter, D.J.T. and Challenor, P.G., 'Satellite remote sensing and wave studies into the 1990s'; ***International Journal of Remote Sensing,*** Vol 9, Nos 10 & 11, 1988.

Chase, R.P., 'Earth Observation System', Volume IIh, Altimetric system; NASA, 1987.

Clark, A.N., 'Longman Dictionary of Geography; Longman', 1985.

Cook, C.E. and Bernfeld, M., 'Radar Signals, an introduction to theory and application'; Academic Press, 1967.

Curtis, T.E. and Rees-Roberts, T.M., 'A systolic node processor for real time high throughput SAR signal processing'; IEE Colloquium on Synthetic Aperture Radar, London, November, 1989.

Elachi, C., 'Spaceborne radar remote sensing: applications and techniques'; IEEE Press, 1987.

Fitch, J.P., 'Synthetic aperture radar'; Springer-Verlag, 1988.

Francis ,C.R., 'The ERS-1 altimeter, an overview'; Proc. ERS-1 Radar Altimeter Data Products workshop, Frascati; ESA SP-221, May, 1984.

Freese, R.P., 'Optical disks become erasable'; ***IEEE Spectrum,*** February, 1988.

Griffiths, H.D. et al., 'A study of antenna signal processing techniques for radar altimeters'; ESA contract report 6001/84/NL/GM, December, 1985.

Griffiths, H.D., 'Studies of radar altimetry over topographic surfaces'; Ph.D. thesis, University of London, 1986.

Griffiths, H.D., 'WP 1207-SAR mode'; Technical note STN/ATTA/351/UCL/EE, Synthetic aperture altimetry, December, 1987.

Griffiths, H.D. and Purseyyed, B., 'A study of advanced radar altimeter techniques'; ESA contract report 7088/87/NL/JG(SC), January, 1988.

Griffiths, H.D. and Purseyyed, B., 'A radar altimeter with synthetic aperture processing'; Proc. *European Microwave Conference,* **London september, 1989.**

Gutshull, R.L. and Deters, R.A., 'A survey of attitude sensors'; *The Journal of the Astronautical Sciences,* **Vol XXVII, No 3, 1979.**

Harris, F.J., 'On the use of windows for harmonic analysis with the discrete Fourier transform'; Proc. *IEEE,* **No.1, January, 1978.**

Hymans, A.J. and Lait, J., 'Analysis of a frequency-modulated continuous-wave range system'; Proc. *./EE,* **July, 1960.**

Jabra, A.A., 'Tailoring HEMTs for low-noise amplifier designs'; *Microwaves & **RF,*** **October, 1988.**

Kamal, A.K., 'Millimetre wave radar'; Proc. *International Conference on Radar,* **Paris, 1989.**

Kolldge, J.C. and Sand, J.A., 'Advanced star tracker design using the charge injection device'; *Automatica,* **Vol 20, No 6, 1984.**

Khosrowbeygi, A.,' SSB modulators and frequency multipliers for digital chirp generator circuits'; M.Sc. project report, Department of Electronic and Electrical Engineering, University College London, September, 1988.

Klauder, J.R. et al., 'The theory and design of chirp radars'; *The Bell System Technical Journal,* **July, 1960.**

Levanon, N., 'Radar principles'; Wiley, 1988.

Long, M.W., 'Radar reflectivity of land and sea'; Lexington Books, 1975.

McGoogan, J.T. and Walsh, E.J., 'Real-time determination of geographical parameters from a multibeam altimeter'; AIAA/NASA Conference on Smart Sensors, November, 1978.

Measures, R.M., 'Laser remote sensing, Fundamentals and applications'; Wiley, 1984.

Mishra, U.K. et al., 'The AlInAs-GaInAs HEMT for microwave and millimeter-wave applications'; ***IEEE** Transactions on Microwave Theory and Techniques,* Vol.37, No.9, September, 1989.

Morgan, D.P., 'Surface-wave devices for signal processing'; Elsevier Science Publishing, 1985.

Pettai, R., 'Noise in Receiving Systems'; Wiley, 1984.

Purseyyed, **B.** and Griffiths, **H.D.,** 'A synthetic aperture altimeter'; Proc. *TGARSS-88,* ESA SP-284, Edinburgh september, 1988.

Quasius, G. and McCanless, F., 'Star trackers and system design'; Spartan Books, 1966.

Robin, G.de Q., 'Mapping the Antarctic ice sheet by satellite altimetry'; *Canadian Journal of Earth Sciences,* Vol.3, 1966.

Robins, W.P., 'Phase noise in signal sources, theory and applications'; Peter Peregrinus Ltd., 1982.

Robinson, I.S., 'Satellite oceanography'; Ellis Horwood, 1985.

Sabins, F.F., 'Remote sensing principles and interpretation'; Remote Sensing Enterprises, Inc., 1987.

Skolnik, M.I., 'Introduction to radar systems'; McGraw-Hill, 1985.

Somma, R. and Thompson, A., 'Radar altimeter phase A study Final report'; European Space Agency contract 4428/80/F/DD/SC, 1981.

Spilker, J.J., 'GPS signal structure and performance characteristics'; *(Navigation) Journal of The Institute of Navigation,* Vol.25, No.2, 1978.

Steinberg, B.D., 'Principles of aperture and array system design'; Wiley, 1976.

Thomas, J.K. et al., 'Computer-derived height from SIR-B stereo radar images'; Proc. *IGARSS-86,* ESA SP-254, Zurich, September 1986.

Ulaby, F.T., et.al., 'Microwave remote sensing, active and passive', Vol II; Addison-Wesley, 1982.

Wehner, D.R., 'High resolution radar'; Artech House, 1987.

Wingham, D.J. and Rapley, C.G., 'A new approach to topographic altimetry'; Proc. *IGARSS-88,* Edinburgh; ESA SP-284, Vol.2, Sept, 1988.

Wolf, P.R., 'Elements of photogrammetry'; McGraw-Hill, 1983.

Yunck, T.P. et al., 'GPS-based satellite tracking system for precise positioning'; *IEEE Transactions on Geoscience and Remote Sensing,* Vol GE23, July, 1985

Zavrel, R.J., 'Digital modulation using the NCMOTM'; *RF Design,* March, 1988.

Zebker, H.A. and Goldstein, R.M., 'Topographic mapping from interferometric synthetic aperture radar observations'; *Journal of Geophysical Research,* Vol. 91, No. B5, April, 1986.

Appendixl

Impulse response of the linear chirp matched filter

The chirp pulse signal to be processed has the following form:

$$v_i(t) = a.\exp j \Big\rceil 2/c(f_0 + \tfrac{1}{2} 11^* \qquad , -\tfrac{T}{T} < t < + {}_{2}$$

This signal is passed through a lossless filter having an impulse response h(t) which is the time inverse of the signal, and is given by the following expression, in which k is an unknown amplitude factor:

$$h(t) = k.\exp j[211(f_o - 2\ gt)ti$$

Therefore the output of the matched filter can be written as:

$$v_o(t) = v_i(t)*h(t) \int_{\frac{T}{2}}^{+\frac{T}{2}} \qquad - t).dt = kaT \frac{\sin(icifft)}{(ngeft)} .\exp jeo(t)$$

The conservation of energy property in a lossless system implies that the total energy at the input and output of a matched filter should be the same. The total energy under the pulse envelope of the input signal is given by:

$$E.=f \qquad {}^{2}dt = \int_{\frac{T}{2}}^{T} a^2 dt = a^2 T$$

and the total energy under the sinx/x envelope of the output signal is given by:

$$r. \quad {}^{2}dt \quad \overset{+a^{\circ}}{1}[\ kaT\ \frac{\sin(npTt)}{7C1.111}\ ]^{2} dt = (\ \frac{Ica\ 2}{7\mu\_}\ )^{\cdot}\ f_{r} \sin(np.T)t\ \dot{j}^{2}dt \qquad ...A1.1$$

The integral of a squared sinc function is equal to:

$$^{+}\ \frac{\sin^{2} px}{x^{2}}\ d_{x} = {}^{+}\ \frac{\sin^{2} px}{0\ x^{2}}\ d_{x}$$

therefore the result of equation A1.1 will be:

$$E_{0} = 2.(\frac{ka}{})^{2}.(\ mfr.\ \frac{1}{2}.\ ) = \ {}^{k\ a}_{\ 22T}$$

Equating the input and output energies gives:

$$E_{0} = E_{1} \longrightarrow \frac{k^{2}a^{2}T}{1^{1}} = a\ \mathbf{T} \qquad k$$

So the impulse response of the linear chirp matched filter is given by:

$$h(t) = fiT.expj[2n(f.- 2\ pad$$

Appendix2

Speckle noise in the synthetic aperture processing

This appendix summarises the speckle or fading noise which is the result of the coherent processing involved in the aperture synthesis.

The radar, which is mounted on a platform, passes over the terrain, and at every pulse repetition interval (PRI) transmits a pulse towards the surface which consists of many scattering points. The received signal by the radar at any spatial point is the vectorial (coherent) sum of the backscattered signals from all the individual scatterers. This gives rise to a variation in the return signal from the same area, corresponding to different transmitted pulses emitted at different spatial positions of the platform. This phenomenon is known as fading (Rayleigh fading). When many neighbouring scattering areas are processed, the resultant pattern shows a variation in the processed detected level per pixel (caused by fading) which is known as speckle noise. It should be noted that speckle noise consists of spatial, not temporal, variation of the pixel detected level.

Since there are many independent, randomly spaced scatterers within any illuminated area, the received signals at the I and Q channels corresponding to the i^{th} transmitted pulse will follow zero mean [E(I or Q)=0] Gaussian distributions with the variance $a_i{}^2$,[Var(I or Q)$-7.6_i{}^2$]:

$$p(I_i \text{ or } Q_i) = \frac{}{27c} \exp[-\frac{I_i^2 \text{ or } Q_i^2}{2,af}] \text{ and } [E(I_i \text{ or } Q_i) = 0 \text{ , } Var a_i \text{ or } Q_i) = a_i^2]$$

Therefore the amplitude of the received signal (i.e. $V_i = 1/I_i{}^2 + Q_i{}^2$) follows a Rayleigh distribution with mean E(V_i) and variance Var(Vi):

$$p(V_i) = {}^{V}\text{-}\exp[\overset{-V?}{2}]\ \text{and}\qquad E(V_i) - \frac{\overline{MT^2}\,{}^{1}}{2}, \ \mathrm{Var}(V_i) = 2af(1\text{Ii}) \Bigg|$$

...A2.1

and the power of the received signal (i.e. $P_i = l_i^{\,2} + Q_i^{\,2}$) follows an exponential distribution with the mean E(Pi) and variance Var(Pi):

$$P(Pi) = \overset{1}{27}\,\mathrm{exP}\overset{Pi}{\vee} \qquad \text{and } [\ E(P_i) = 2a2\ ,\ \mathrm{Var}(P_i) = (2a2)^2\ ]$$

...A2.2

The signal-to-fading (or speckle) noise ratio of one received waveform is defined as the square of the mean value of the output amplitude (considered as the ideal received amplitude without fading) divided by its variance (considered as the superimposed fading noise), so from equation A2.1:

$$(sNR)_{speckle} = \frac{E^2(v)}{v_a 7\backslash 7} = 3.66 \text{ or } 5.6\text{dB}$$

It should be noted that this is an inherent SNR irrespective of whether there is any thermal noise (due to the radar receiver). This implies that the best SNR which can be achieved in a radar system in the presence of Rayleigh fading is 5.6dB, even if the ratio of the received signal to system noise is very high. (It is however possible to achieve very high SNR for individual bright point targets because in this case the Rayleigh fading does not occur).

Normally in a radar after all the required processing, the I and Q channels are squared and added together, and the resultant power is used as the output processed waveform. In this case the signal-to-speckle noise has to be obtained on the basis of the output power statistics which are exponential (equation A2.2). So the signal-to-speckle noise ratio of one received waveform is the the mean value of the output power divided by the square root of the variance:

$$(SNR)_{specue} = \frac{E(P.)}{r(P_i)} = 1 \text{ or } OdB$$

...A2.3

In order to increase the signal-to-speckle noise ratio and as a result the net SNR, of the radar, N independent return signals are averaged. The combination of N independent exponential distributions follows a chi-squared distribution with the mean value E(PN) and the variance Var(PN), (Wehner, 1987):

$$P(PN) \quad \frac{(PN)^{N-1}}{(90)!\ (261)}\ {}_{2}\underline{N}\exp[\frac{\_p}{---_T}] \text{ and } E(P_N) = 2Na_i^2\ Var(PN) = ({}^2443^2)^2$$

and the signal-to-speckle noise for this case is given by:

$$({}^{SNR})_{speckle} \quad \frac{E(PN)}{Var(P_N)} \qquad or\ [10log,r97$$

...A2.4

Equation A2.4 shows a factor of „IN improvement in the signal-to-speckle noise ratio compared to the SNR of one waveform (equation A2.3).

In a SAR, speckle noise can be reduced by using independent data sets to estimate the same area of the terrain. When only one data set is available, multilook processing can be applied by dividing the available synthetic aperture into subapertures which generate independent looks at the target area, based on the angular position of the targets (Fitch, 1988).

Appendix3

Phase noise of the synthetic aperture altimeter master oscillator

This appendix provides the phase noise requirements of the master oscillator of the synthetic aperture radar altimeter. The phase modulated signal may be written as (Robins, 1982):

v(t) = .,fi sin[cot + 8(t)] ...A3.1

where *C* is the carrier rms power in Watts, and:

8(t) = 8.sin(pt) ...A3.2

which is the simplest form of phase noise modulation (i.e. sinusoidal representation of narrow band noise), where 0 is the peak phase noise on the carrier in radians, and:

$p = 21cf_m$ ...A3.3

where f_m is the offset frequency from the carrier. Substituting equation A3.2 into equation A3.1 and expanding the result in terms of Bessel functions, and assuming small values of peak phase noise 0, which occur in random noise modulation (i.e. small sideband to carrier ratios), gives:

v(t) = ,fiC[sin on + el sin(w+ot - $\frac{9-}{2}$ sin(co-p)t] ...A3.4

From equation A3.4, the peak amplitude of each resultant sideband at angular frequencies (co + p) and (w - p) is:

$$V_{Peak} = ,fiC \bullet \; 2 \qquad V_{rills} = 17.\,.€1 \; 2$$

Therefore the power in one sideband is given by:

$$^{P}SSB - \overset{2}{4} \qquad \text{...A3.5}$$

Due to the small value of the modulation index, and the resultant linearity of the modulation process, no amplitude modulation will be produced. Thus, the sideband power given by equation A3.5 is purely phase modulation power.

As mentioned in Chapter 4, in the experimental radar system there is only one (master) local oscillator to generate both the receiver LO and after a proper frequency shifting the transmitter carrier. Therefore the form of transmitted, receiver LO and received signals will be as follows:

$$V_{LO} = \exp j[q_o t + 27E\frac{L}{2}t^2 + 0(t)] \qquad \text{...A3.6}$$

$$V_{TX} = \exp j[(o).-co_i\ ,t + 27r\frac{11}{2}t^2 + OW] \qquad \text{...A3.7}$$

$$v_{Rx} = \exp j[(o)- co_{11})(t-t_d)+27t^{p.}\,0-t_d)^2+00-t_d)] \qquad \text{...A3.8}$$

where 0(t) is the spurious phase modulation of the single microwave oscillator, m. is the chirp slope, and td = 2R/c is the two-way time delay of a particular target. After mixing v_{LO} and v_{Rx}, the phase at the output of the full-deramp mixer or at the input of IF stage is:

$$0_{w}(t) = (1)_{LO}\text{-4:1}_{Rx} = Ro_{ir}t+(co_{(c}\,co_{1}dt_{d}-27t\,\frac{1}{2}(t_{d}^{2}-2t_{d}t)]+[0(t)\ -0(t-t_{d})] \qquad \text{...A3.9}$$

In the above equation the first bracket gives the familiar noiseless information used in the ideal radar signal processing, and the second bracket belongs to the spurious phase modulation at the IF stage due to master oscillator phase noise, now affected by the delay time. Thus:

$$^{o}\text{noise:}\ ^{e\ (t)}\ -^{0\ (t\ -td)} \qquad \text{...A3.10}$$

Adopting the classical phase noise evaluation of oscillators, it is assumed that the spurious modulation of the master oscillator is sinusoidal in nature:

$$= 8.\sin(pt+v) \qquad \text{...A3.11}$$

In other words 0(t) is the noise component in a 1Hz bandwidth at angular offset frequency p and xv is an arbitrary constant phase. Substituting equation A3.11 into equation A3.10, gives:

$$e_{lF} = 0\sin(pt+v)-0\sin[p(t-t_{d})+v] = 29\sin(\frac{pt_{d}}{7})\cdot\cos[pt+N-\text{[illegible]})] \qquad \text{...A3.12}$$

Equation A3.12 shows a time varying function of cos[....] with a peak phase modulation index of

$$0'(t_{d}) = 28\sin(\frac{pt_{d}}{2}) \qquad \text{...A3.13}$$

Equation A3.13 shows the peak phase noise at IF, when the relative delay of the two signals of receiver and transmitter is t_d = 2R/c seconds, and a is the peak phase noise of the master oscillator. If t_d was zero (i.e. zero time delay), since the v_{Rx} and v_{Tx} had the same instantaneous phase noise they would cancel each other and the IF signal would be spectrally pure.

Referring to equation A3.5, this equation gives the single sideband power due to a sinusoidal phase modulation with peak modulation index of 0, on a sinusoidal carrier with peak voltage amplitude of \/(2C). Now, if the phase modulation is assumed to be due to phase noise [i.e. exchanging **PSSB by** N_{op} to show the phase noise power], from equation A3.3 the single sideband phase noise density-to-carrier ratio at the offset frequency f_m can be found as:

$$\mathbf{P}_{\mathbf{SSB}} \text{-->} N_{op} = \frac{C0^{2}}{4} \qquad \left(\frac{N_{M}}{C}\right)_{fm} = \frac{e2}{4}$$

...A3.14

Now substituting for 0 from equation A3.13 in equation A3.14, the maximum permissible master oscillator phase noise sideband density at offset frequency f_m is given by:

$$\left(\frac{N_{op}}{C}\right)_{f_{(max)}} = \frac{1}{4}\left[\frac{e'(td)}{2\sin(\ ptd\ )}\right]^{2}$$

or more usefully, in logarithmic terms:

$$\left(\frac{N_{P}}{C}\right)_{f_{m(max)}} = 10\log\{\frac{1}{4}\left[\frac{eV_{d})}{2\sin(\frac{pt}{2})}\right]^{2}\} = \text{Mogi}\left\{\frac{0'4_{d})}{4\sin(\frac{pt_{1}}{2})}\right\} \text{dB/Hz}$$

...A3.15

Equation A3.15 gives the maximum permissible phase noise sideband density at frequency offset f_m. This means that if the maximum permissible phase noise at the IF stage $0'(t_d)$ which is equivalent to the acceptable phase error in the synthetic aperture processing, and also the time delay td are known, then the required phase purity at the master oscillator at any particular offset frequency f_m can be calculated from equation A3.15.

Appendix4

Circuit diagrams of the prototype experimental radar

This Appendix provides all circuit diagrams of the experimental radar altimeter which were explained thoretically in chapter five and have put together in block diagram illustrated below. These circuits are as follows:

Circuit 1: 70MHz reference crystal oscillator;
Circuit 2: 8MHz/10MHz frequency generator;
Circuit 3: 18.432MHz/69.9MHz frequency generator;
Circuit 4: 100kHz/50kHz/20kHz sampling frequency generator;
Circuit 5: 275.33MHz frequency generator for microwave PLL;
Circuit 6: Microwave head;
Circuit 7: Receiver IF amplifier;
Circuit 8: Receiver baseband I and Q generator;
Circuit 9: Receiver analogue to digital converters and memory;
Circuit 10: Baseband digital chirp generator;
Circuit 11: Baseband chirp low-pass filters;
Circuit 12: Baseband chirp to RF SSB up-converter;
Circuit 13: First chirp signal frequency quadrupler;
Circuit 14: Second chirp signal frequency quadrupler;
Circuit 15: TX/RX RF chirp translator.

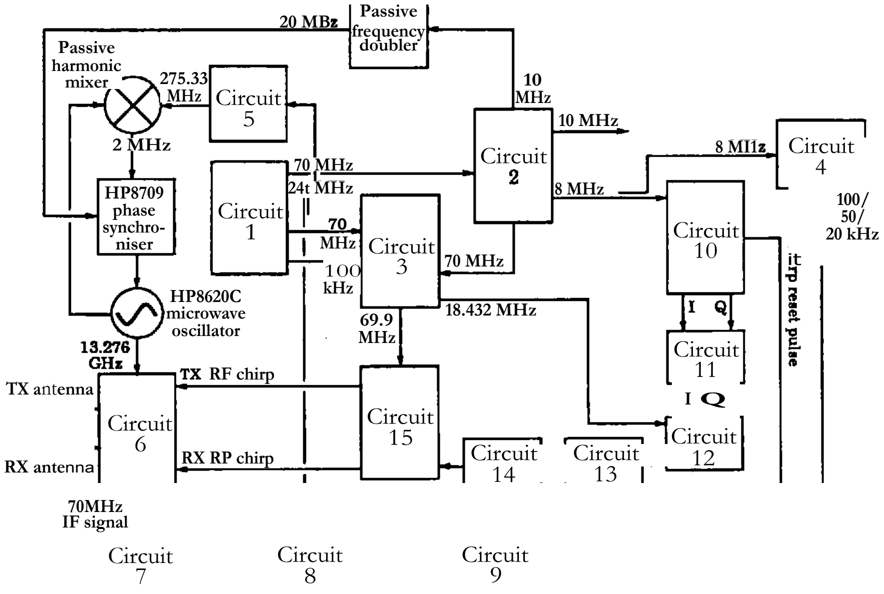

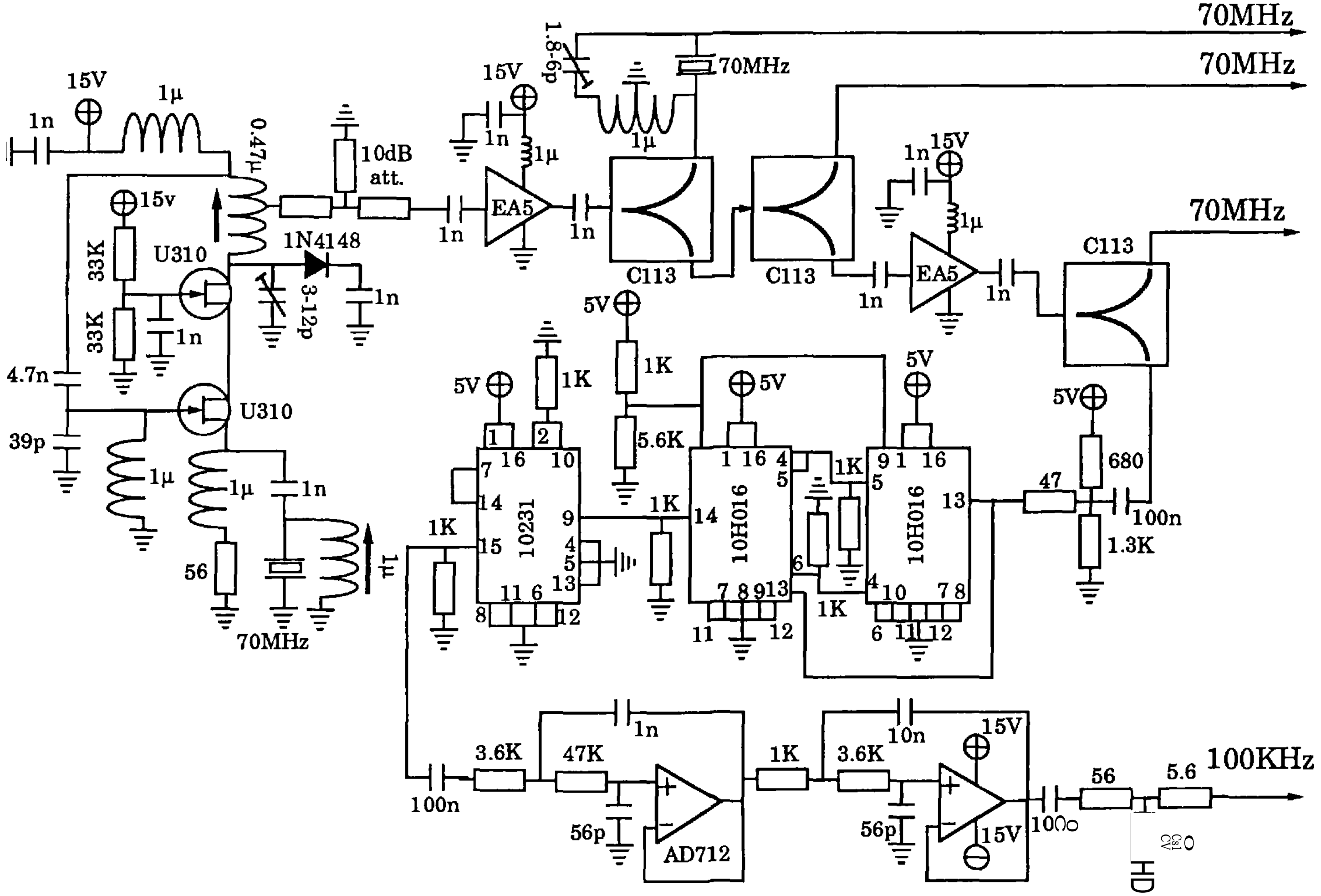

Circuit 1: 70MHz reference crystal oscillator.

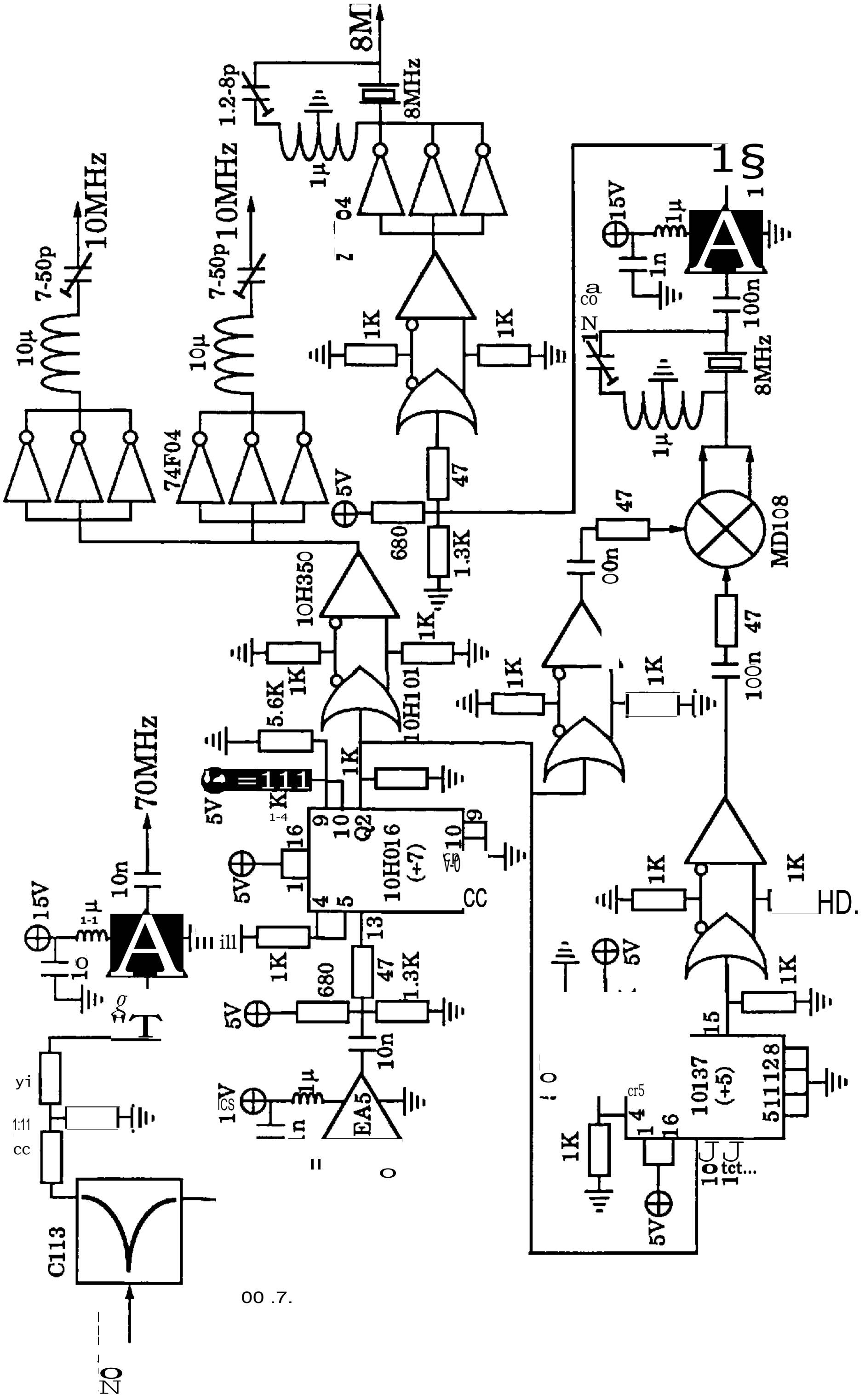

Circuit 2- 8MHz/10MHz frequency generator.

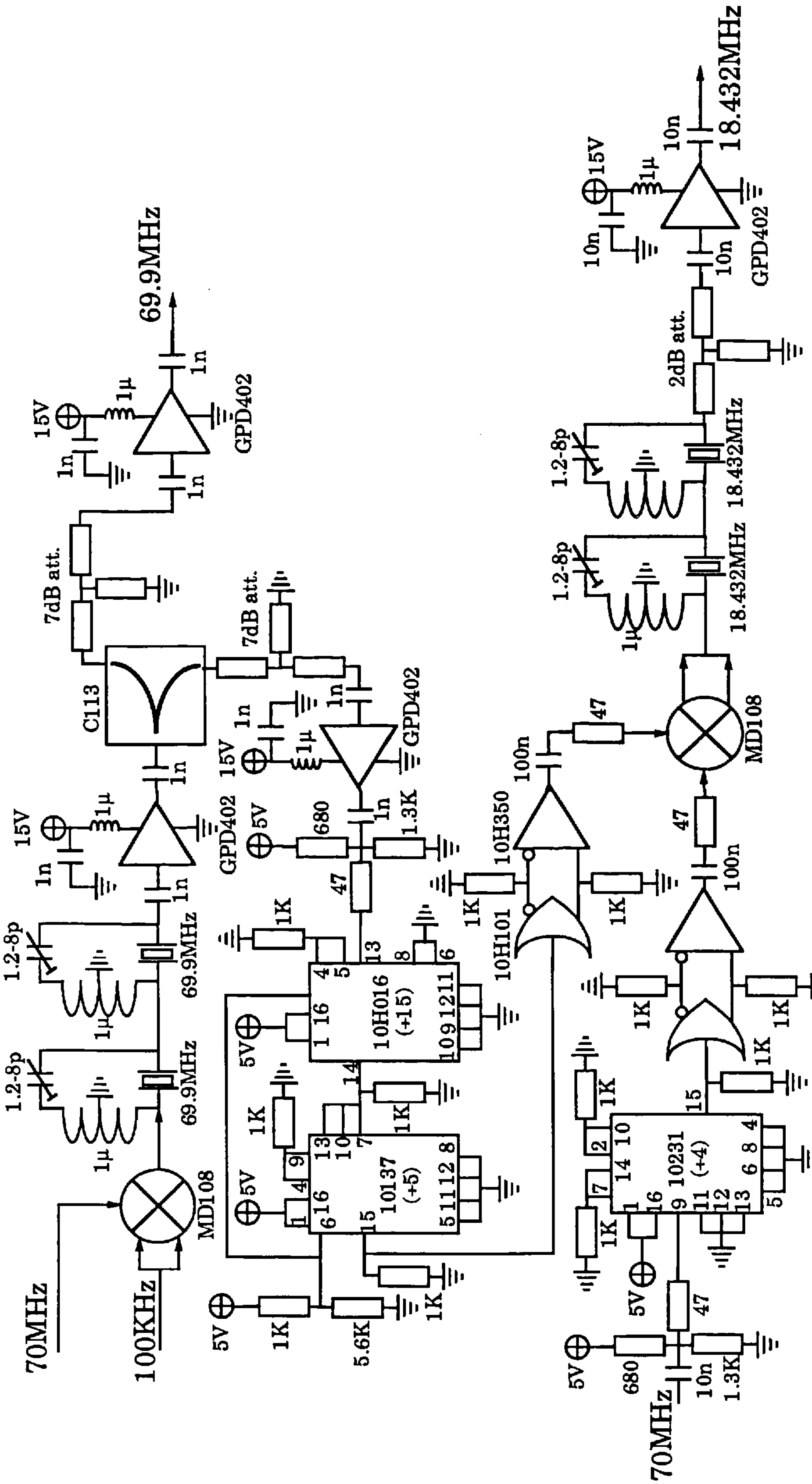

Circuit 3- 69.9MHz/18.432MHz frequency generator.

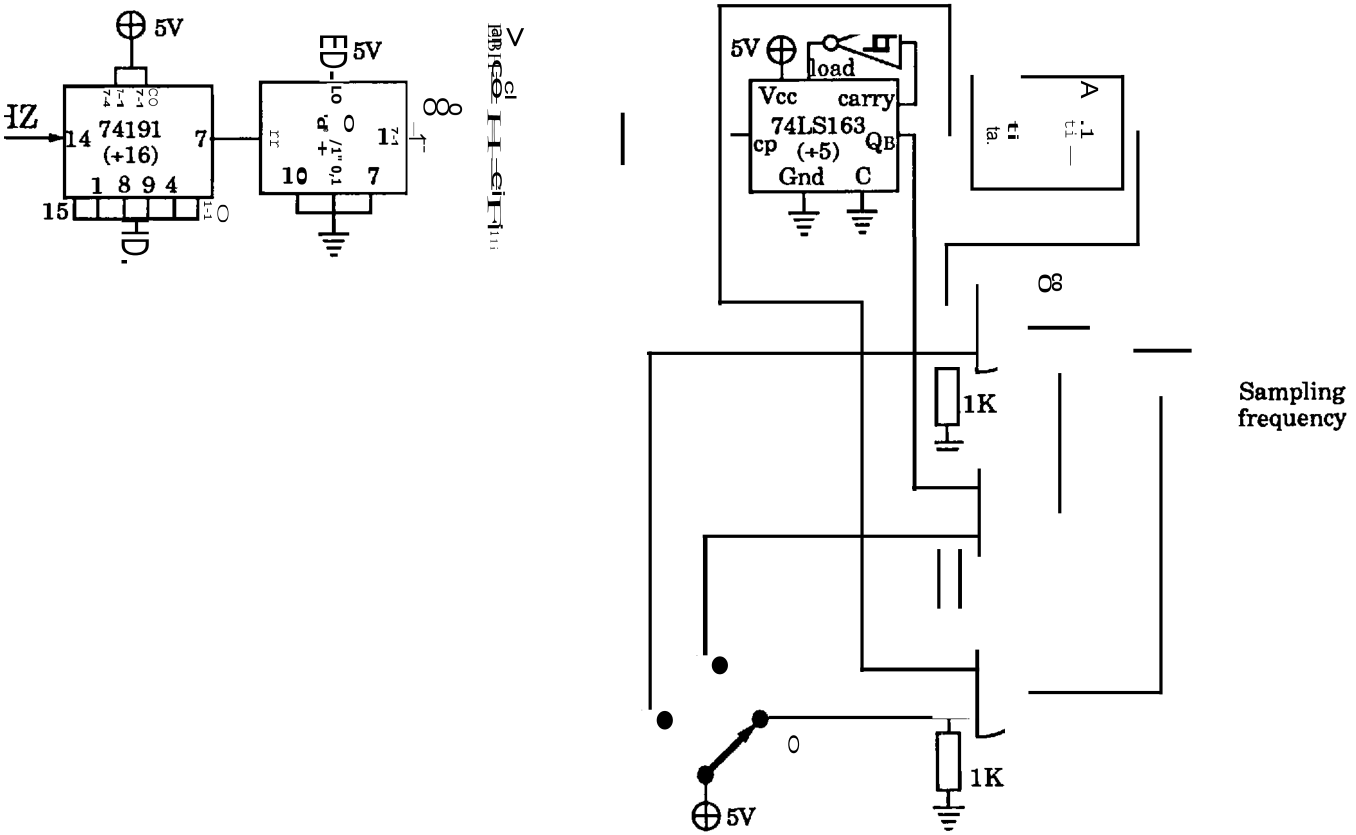

Cirrcuit 4- 100kHz/50kHz/20kHz sampling frequency generator.

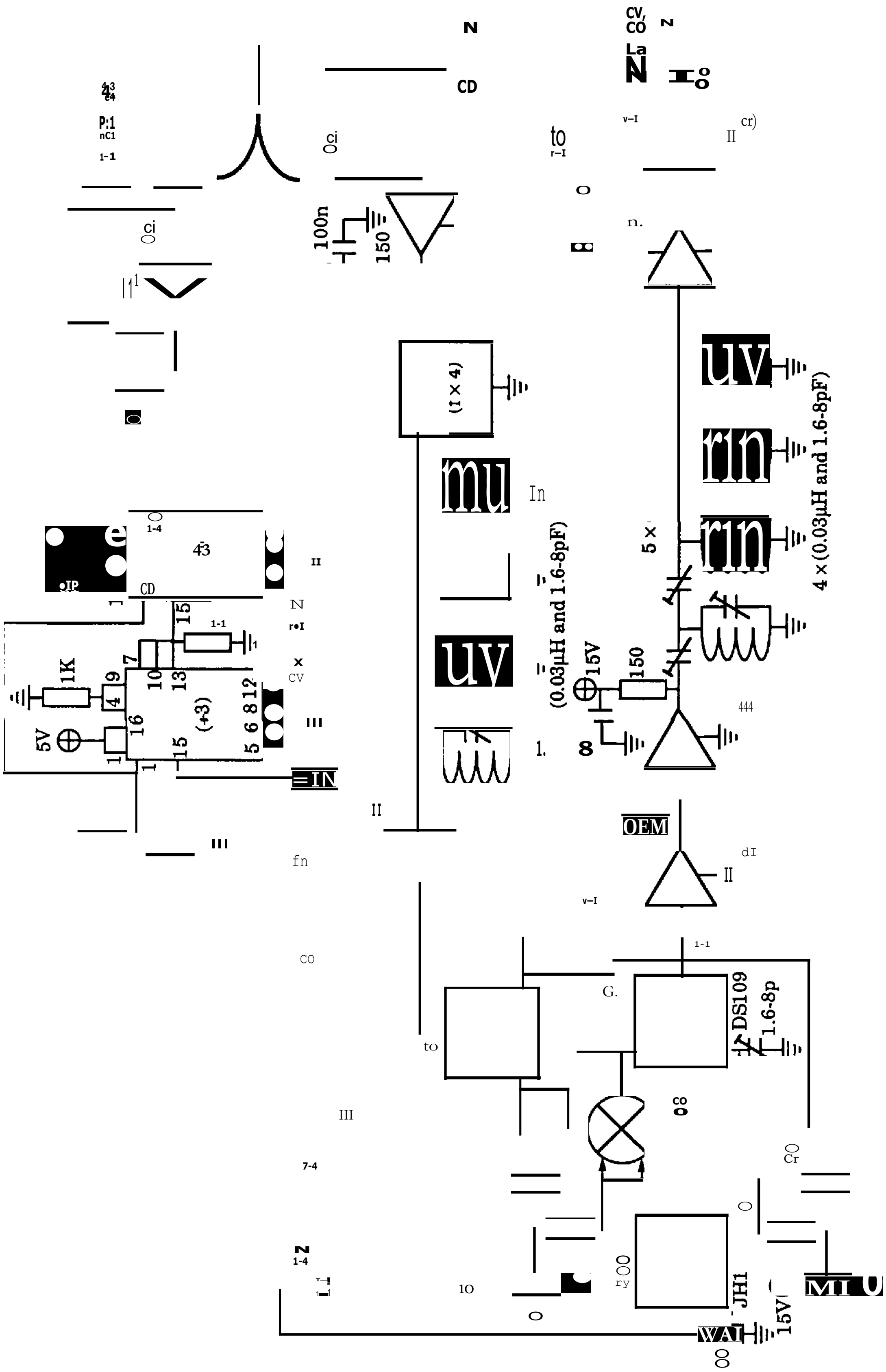
100n
150
(1 × 4)
1K
5V
(+3)
15V
150
(0.03µH and 1.6-8pF)
5 ×
4 × (0.03µH and 1.6-8pF)
DS109
1.6-8p
15V

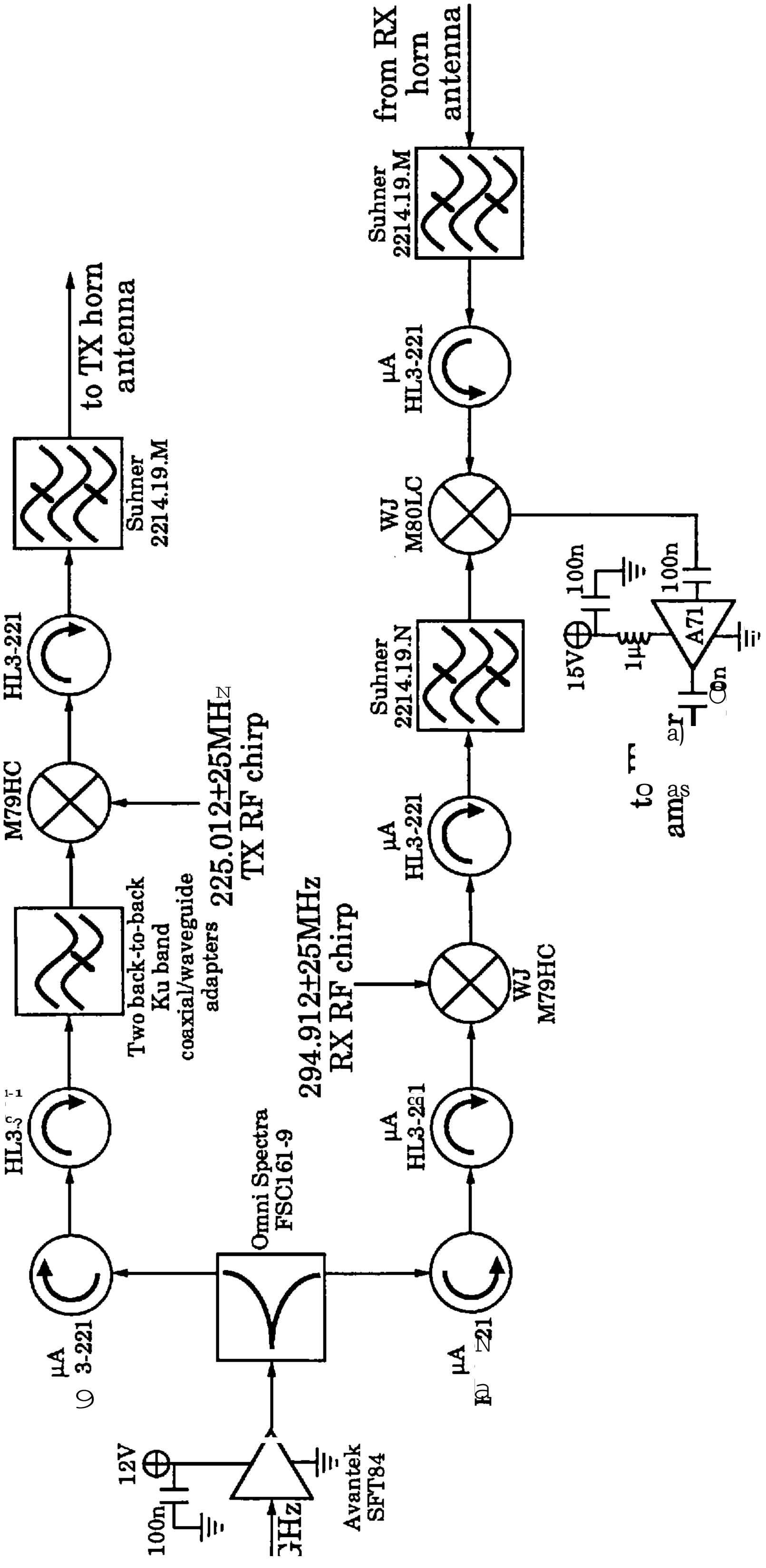

Circuit 6- microwave head.

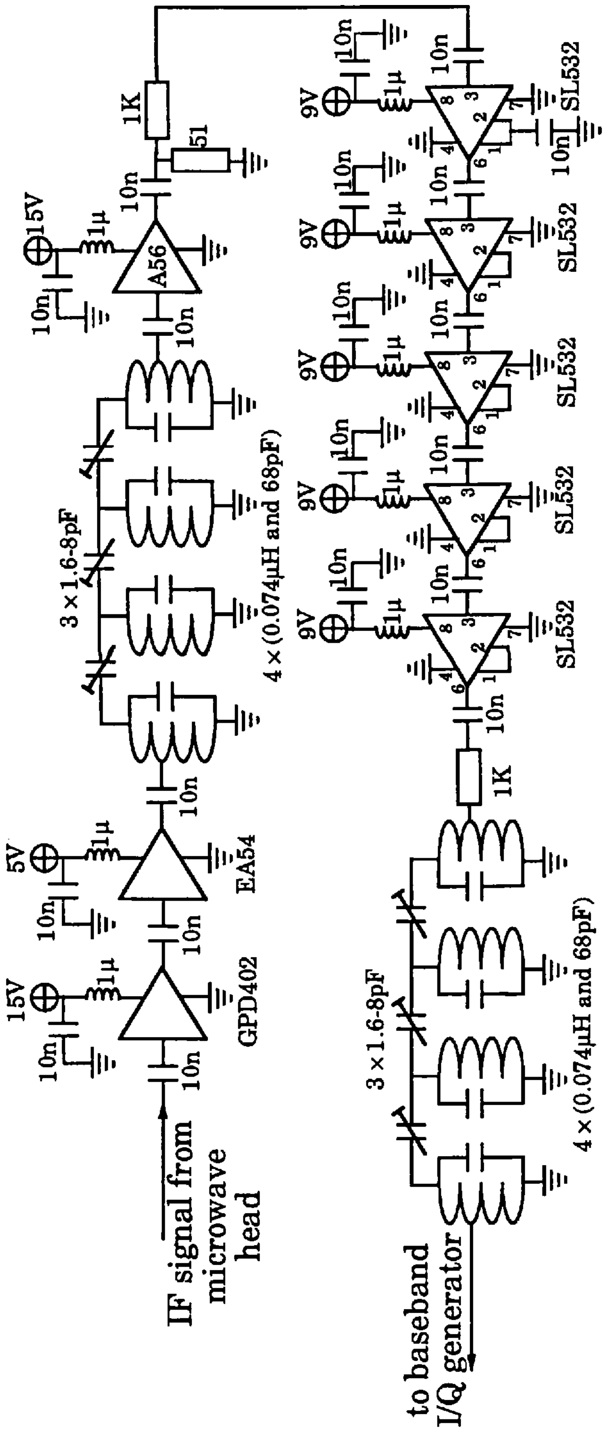

Circuit 7- Receiver IF amplifier.

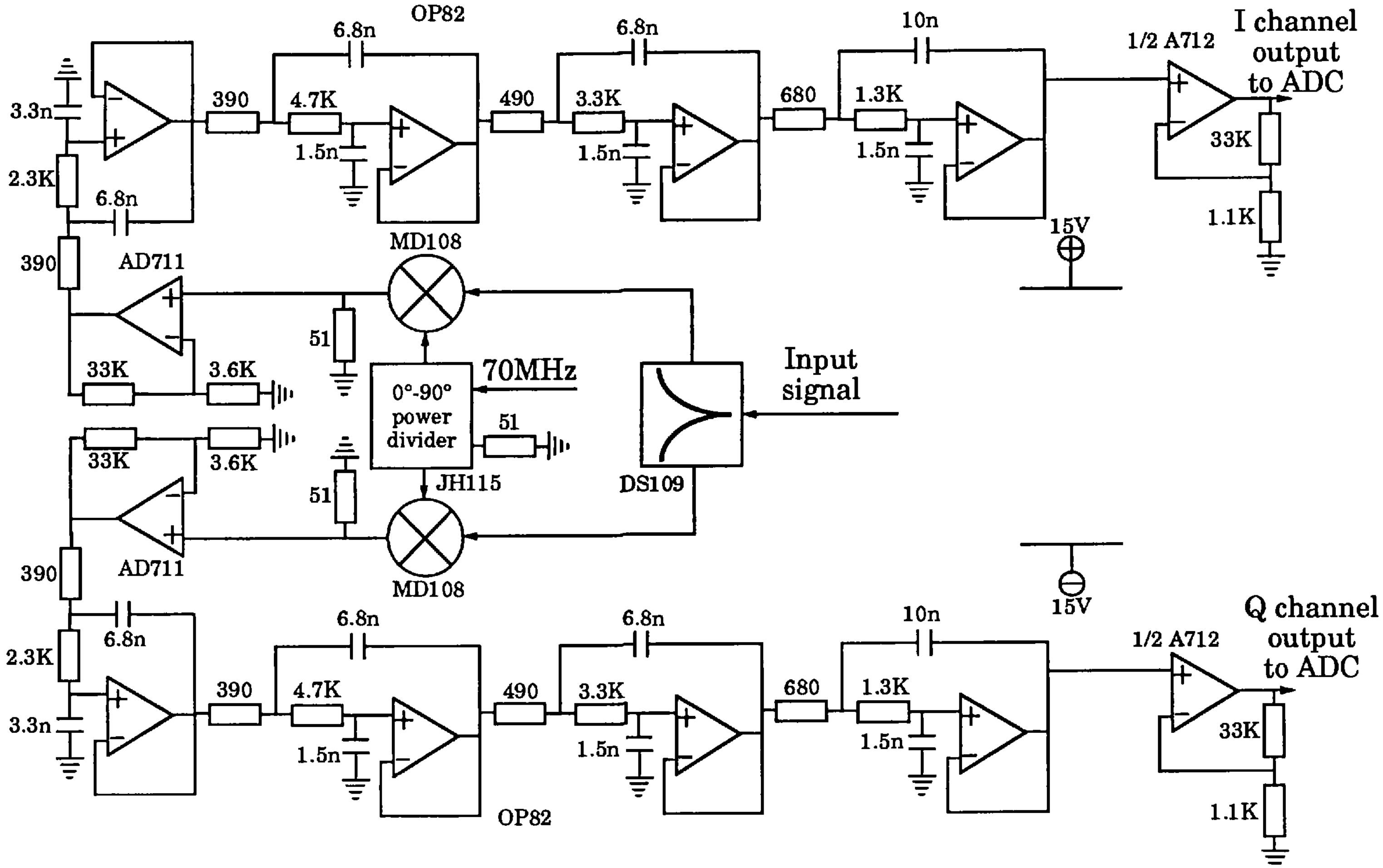

Circuit 8- Receiver baseband I and Q generator.

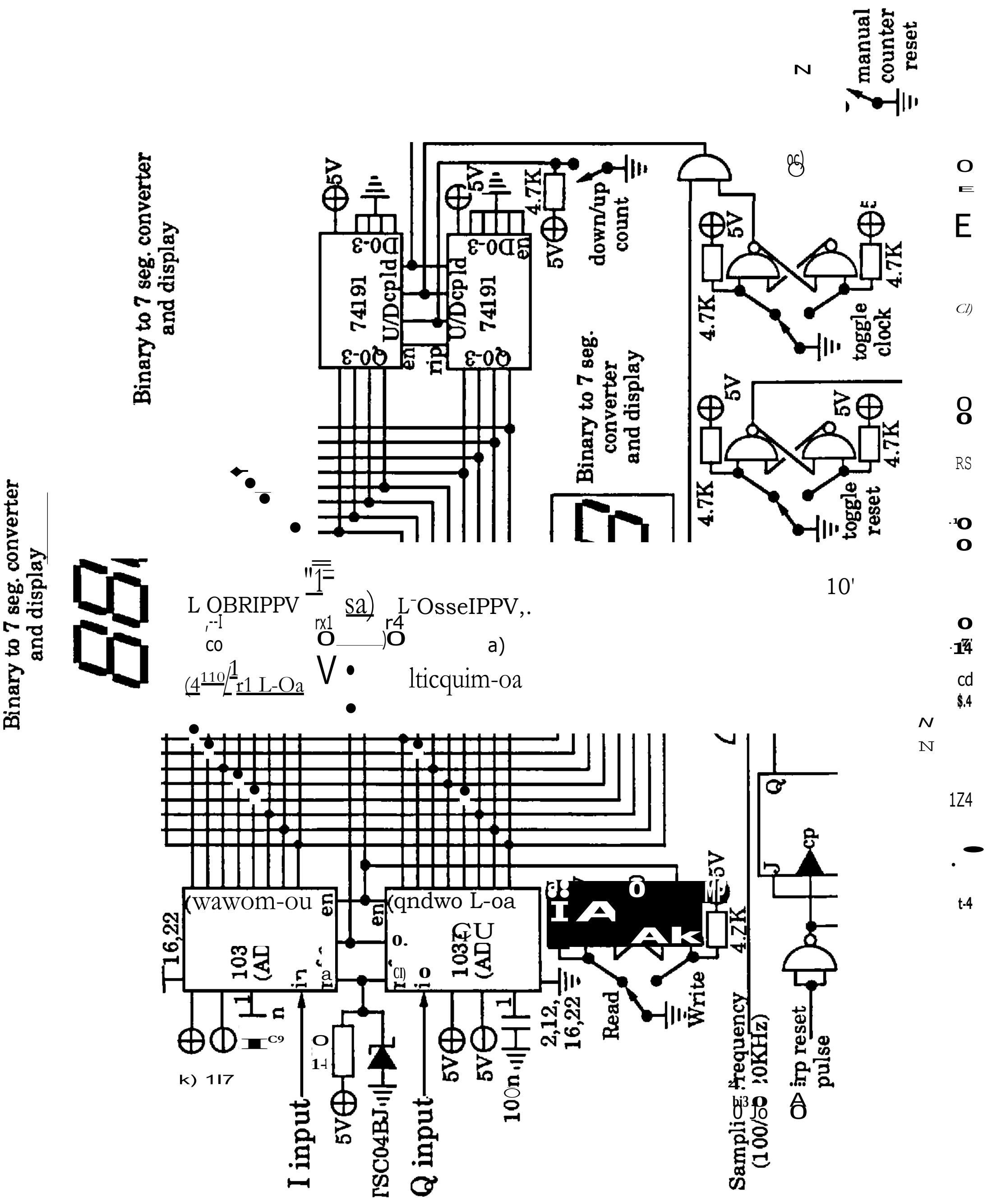
Binary to 7 seg. converter and display
Binary to 7 seg. converter and display
Binary to 7 seg. converter and display
5V
74191
74191
U/Dcpld
D0-3
Q0-3
en
rip
4.7K
down/up count
manual counter reset
toggle clock
toggle reset
103 (AD
en
16,22
I input
Q input
5V
FSC04BJ
100n
2,12, 16,22
Read
Write
Sampling frequency (100/50KHz)
chirp reset pulse
J
Q
cp

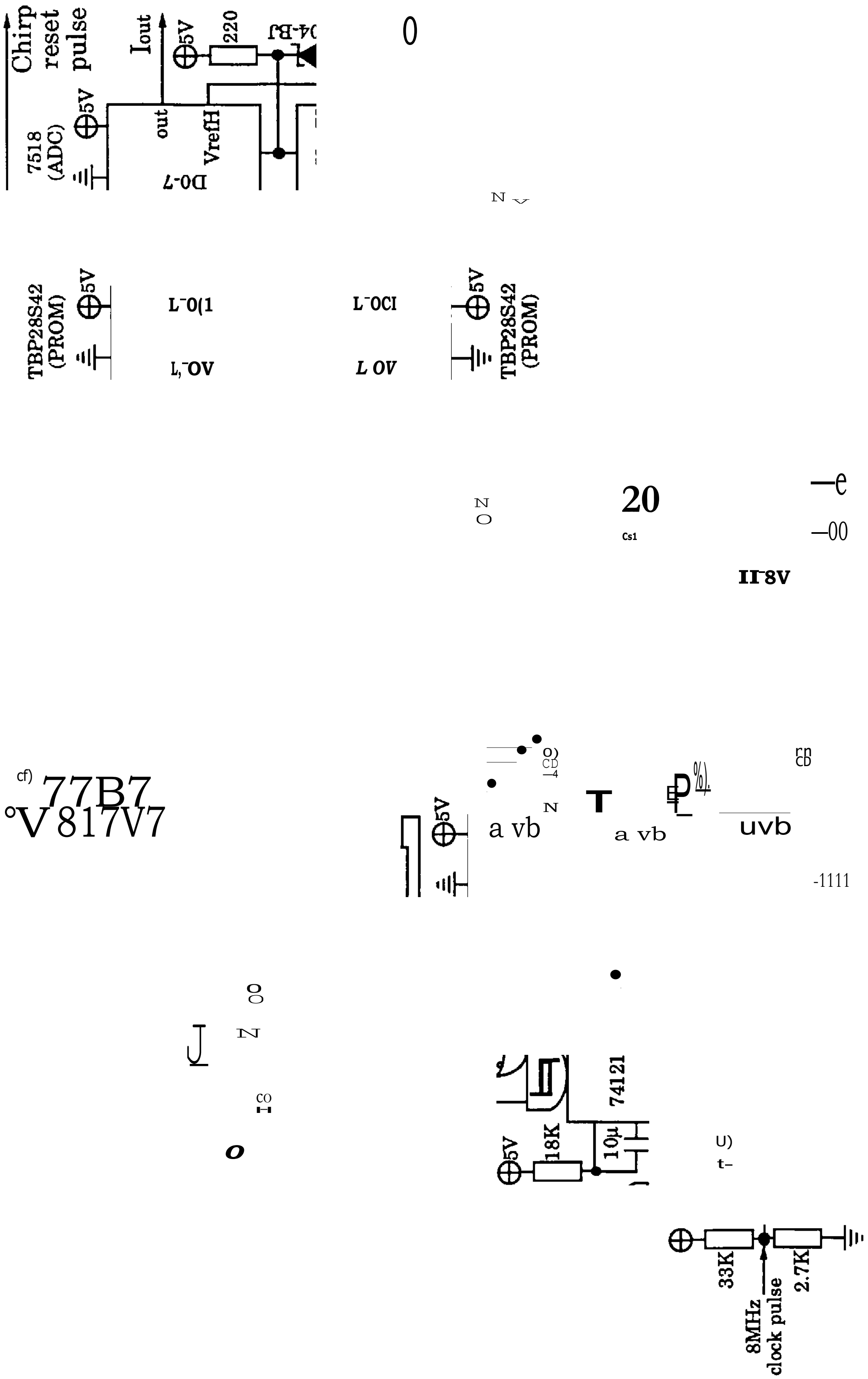

Circuit 10- Baseband digital chirp generator.

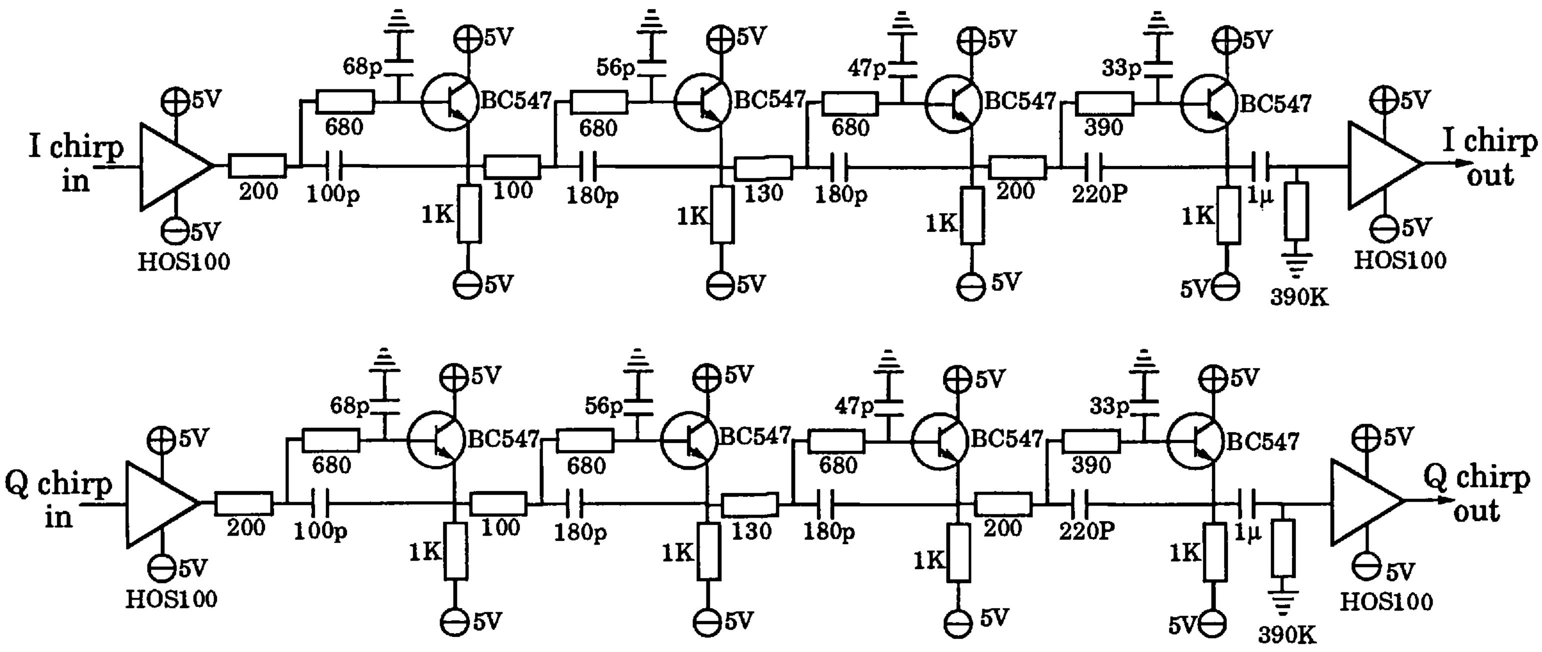

Circuit 11- Baseband chirp low-pass filters.

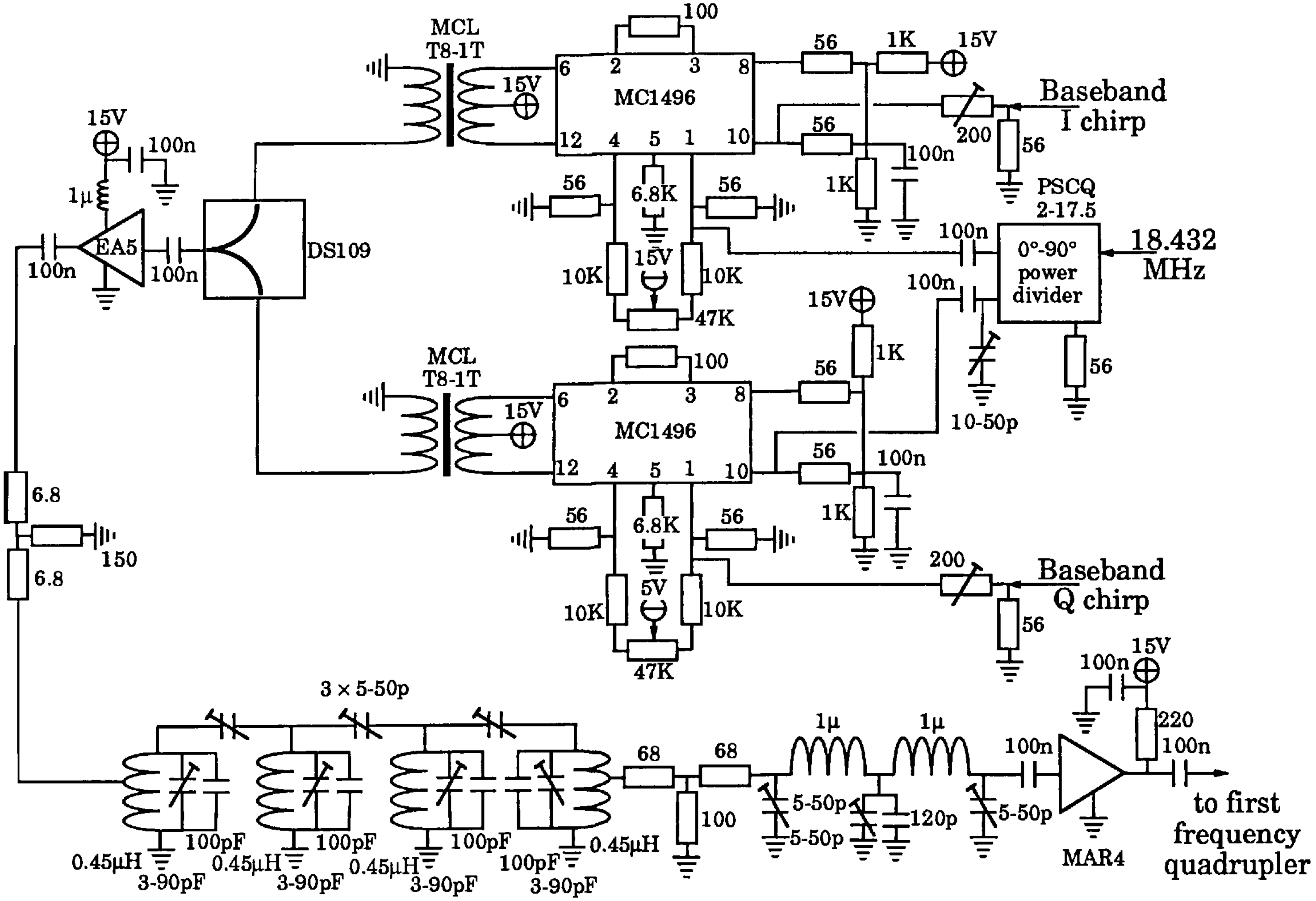

Circuit 12- Baseband chirp to RF SSB up-converter.

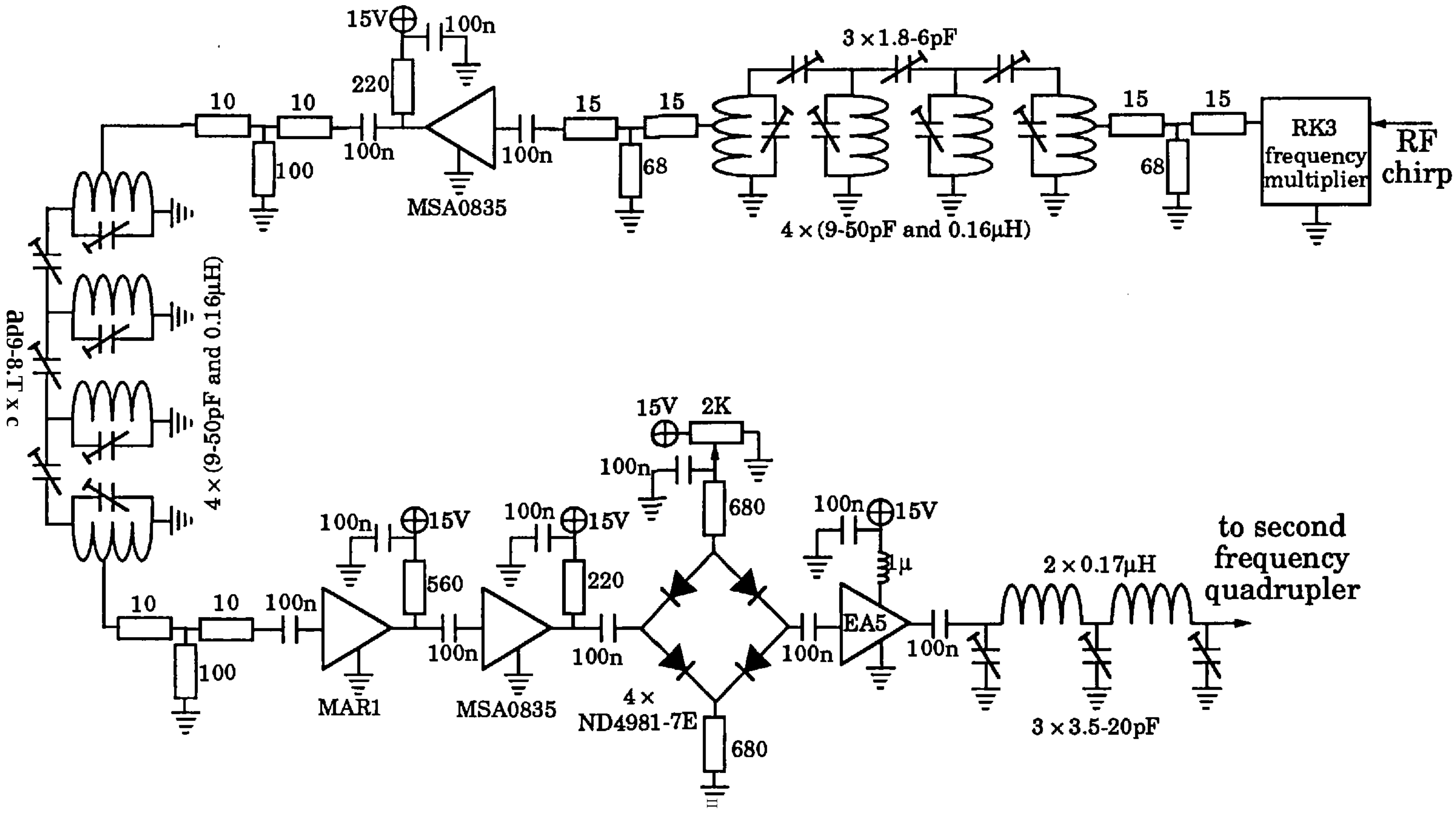

Circuit 13- First chirp signal frequency quadrupler.

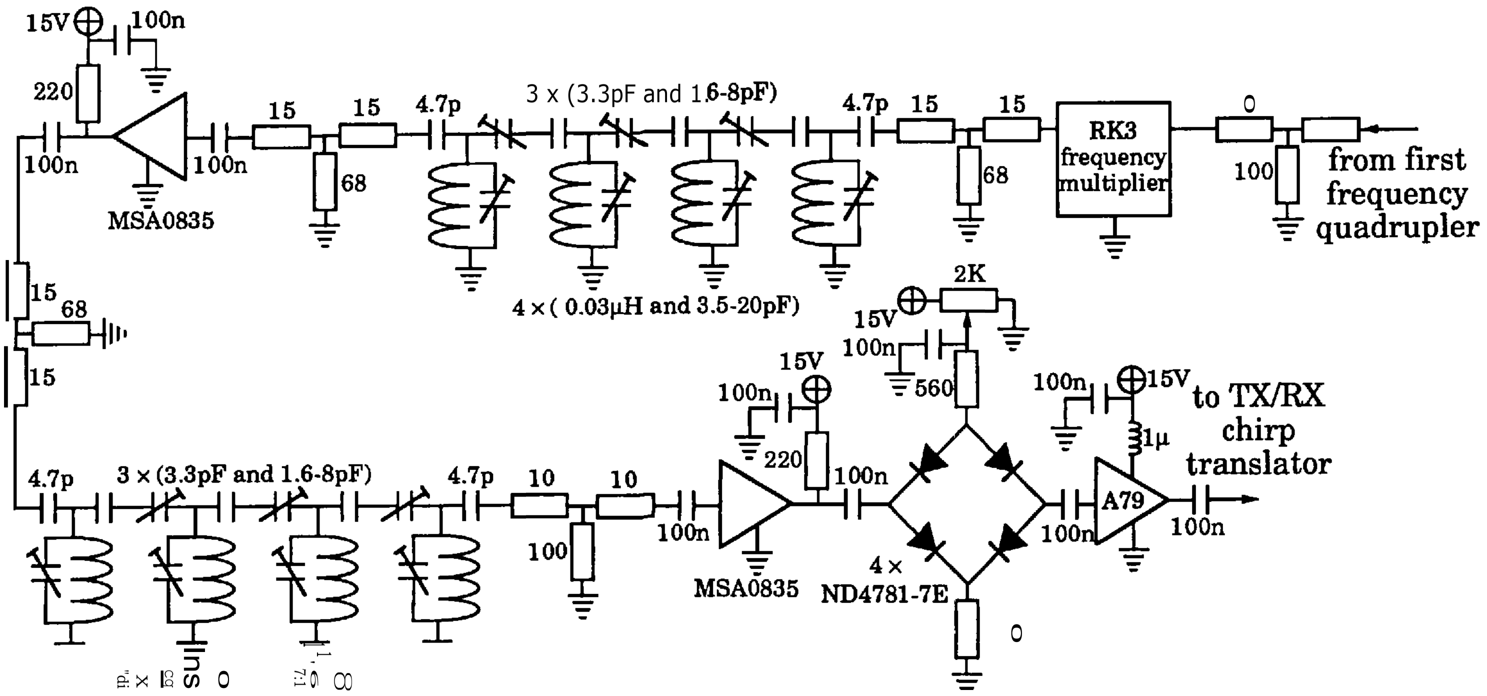

Circuit 14- Second chirp signal frequency quadrupler.

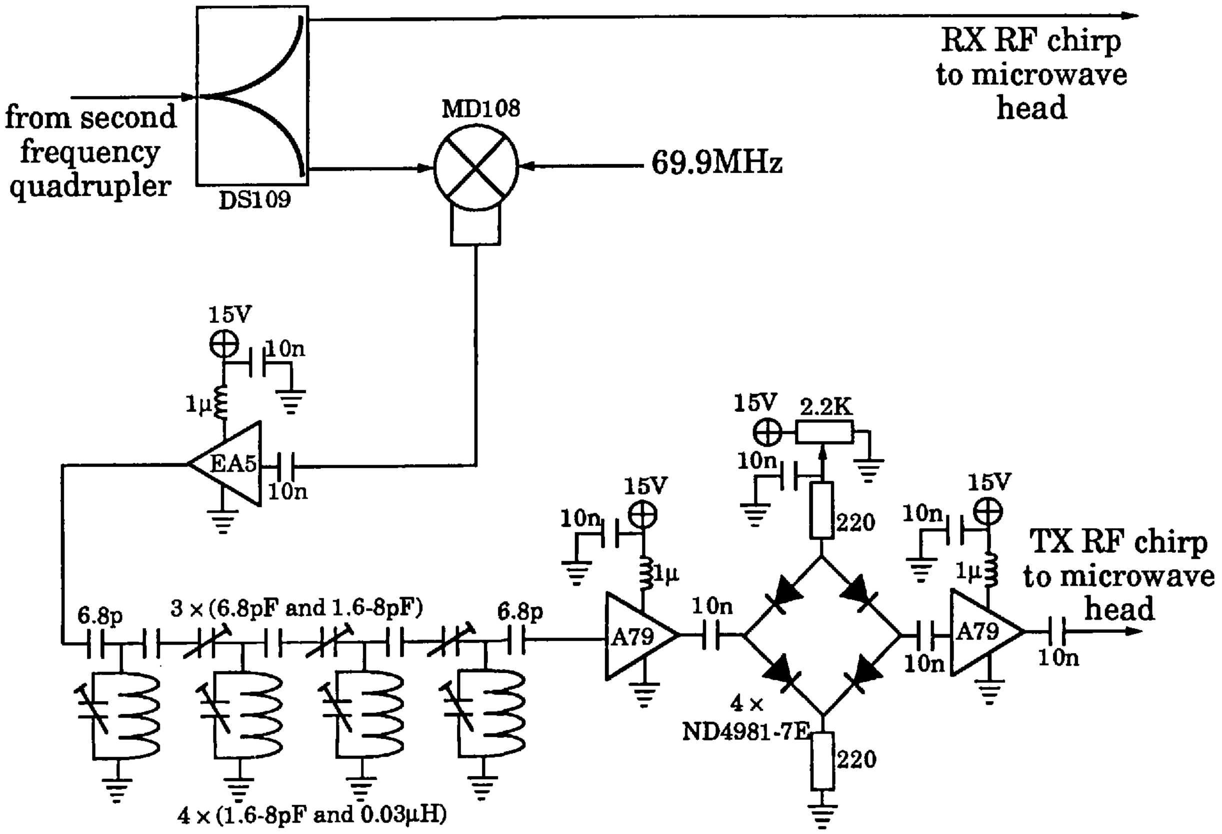

Circuit 15- TX/RX RF chirp translator.